Description des processus physiques pilotant le cycle de vie de brouillards radiatifs et des transitions brouillard–stratus basé de modèles conceptuels

Eivind Wærsted

université PARIS-SACLAY

NNT : 2018SACLX053

Thèse de doctorat

Description of physical processes driving the life cycle of radiation fog and fog–stratus transitions based on conceptual models

Thèse de doctorat de l'Université Paris-Saclay
préparée à École Polytechnique

Ecole doctorale n°579 Sciences mécaniques et énergétiques, matériaux et géosciences (SMEMAG)
Spécialité de doctorat : Météorologie, océanographie, physique de l'environnement

Thèse présentée et soutenue à Palaiseau, le 12.10.2018, par

EIVIND WÆRSTED

Composition du Jury :

Philippe Drobinski Directeur de recherche CNRS, LMD (UMR-8539)	Président
Marie Lothon Chargée de recherche CNRS, LA (UMR-5560)	Rapporteur
Pierre Gentine Professor Columbia University, EEE	Rapporteur
Gert-Jan Steeneveld Associate Professor, Wageningen University, MAQ	Examinateur
Christine Lac Ingénieur ICPEF Météo-France, CNRM (UMR-3589)	Examinatrice
Marjolaine Chiriaco Maître de conférences UVSQ, LATMOS	Examinatrice
Martial Haeffelin Ingénieur de recherche CNRS, IPSL (FR-636)	Directeur de thèse
Jean-Charles Dupont Physicien adjoint UVSQ, IPSL (FR-636)	Co-encadrant de thèse
Marie Vicomte Ingénieur Direction Générale de l'Armement	Invitée
Damien Vignelles Ingénieur Meteomodem	Invité

Acknowledgements

This PhD thesis has been a great experience for me, both professionally and personally. For the first time of my life, I have lived abroad for a longer time period, and I got the chance to live in a big city and be in touch with a large and diverse research environment of atmospheric sciences. One motivation for choosing this particular thesis was the possibility to work closer to the actual observations of the atmosphere and clouds. Being part of the SIRTA team, with occasional field work at the observatory, and the direct use of observational data, has been just the enriching experience I had hoped for. I would like to thank the financial organisms of my thesis, the Direction Générale de l'Armement, and the company Meteomodem, for granting me the scholarship that allowed me to study fog for the past 3 years.

I give a great thanks to my main supervisor, Martial Haeffelin, who has put a lot of time and energy into our weekly discussions of my work. He has always been available to answer my questions or help me find a new direction when everything seemed to be stuck. There has always been a vast amount of alternative angles of attack and pists to pursue, not least due to the very large and multi-instrumental fog dataset that has been at my disposal, and the clarifying discussions with Martial have been essential for keeping up the progress. I would also like to thank my co-supervisor Jean-Charles Dupont, who has followed my work closely as well and answered my questions to help me interpret my results. His practical knowledge about the SIRTA instrument park has been very important for being able to understand and correctly apply the observational data. The whole SIRTA team has also been helpful with processing the data we had particular need of and the deployment of specific instruments in the fog season. The comprehensive observations at SIRTA are supported through the ACTRIS-2 project, which is funded by the European Union's Horizon 2020 research and innovation programme under grant agreement No 654109. The BASTA cloud radar, which is one of the main tools used in my thesis, is maintained and developed by Julien Delanoë of LATMOS, and his help with understanding the radar has been very important for my work. Felipe Toledo also helped me understanding better the functioning of radars in general. I would also like to acknowledge those who participated in the early-morning balloon flights with the droplet-counting instrument LOAC, and Jean-Baptiste Renard for helping us understand and use the LOAC.

In spite of the large observational dataset, modelling has been an essential part of my thesis. I have needed the models to understand the mechanisms we observe and their sensitivities, and to estimate the variables that we do not directly observe, especially the processes at fog top. The application of the radiative transfer model ARTDECO allowed us to study the very important fog-top radiative fluxes. I thank Philippe Dubuisson from LOA at the University of Lille as well as Victor Winiarek, for their assistance in setting up the model runs with ARTDECO. Thanks to the ICARE Data and Services Center for providing access to the ARTDECO code and the associated datasets.

In addition to the radiation modelling, I also got the chance to study turbulent processes of fog in

this PhD thesis, using large-eddy simulations (LES). This was possible thanks to Gert-Jan Steeneveld, who welcomed me to a 3 months stay at his institute in Wageningen in the Netherlands, and to the WIMEK, who financed this stay. Gert-Jan has always been very positive and interested in our work with the large-eddy model and patient to explain the technical aspect to someone who had never worked with LES before. I learned a lot during the stay in the Netherlands, not least because of the new processes I had to understand, especially the surface energy balance and entrainment at the top of well-mixed boundary layers. The expertise of the Dutch researchers on atmosphere–vegetation interactions and boundary-layer turbulence was very valuable for me. In addition to Gert-Jan, I would especially like to thank Arnold Moene, Stephan de Roode, Chiel van Heerwarden, Jordi Vila, Huug Ouwersloot, Xabier Pedruzo Bagazgoitia and Fred Bosveld for important discussions on how best to understand the fog interactions with the surface and the layer above its top, and how to set up the LES in a good way. The simulations were also made possible thanks to the SURFsara supercomputer facilities with the financial support of the Netherlands Organisation for Scientific Research (NWO) Physical Science Division (project number SH-312-15). The ACTRIS Trans-National Access program funded a visit of Gert-Jan to Paris some time after the 3-months stay, which helped us continue our collaboration.

We also applied data from the reanalysis ERA5 in the fog analysis. These were provided through ECMWF, COPERNICUS Climate Change Service data, available from the ESPRI/IPSL data center.

There are also many colleges at LMD other than my supervisors who helped me understand and develop the concepts of my thesis. In particular, I had fruitful discussions with Jordi Badosa, Simone Kotthaus, Juan Antonio Bravo-Aranda, Thibault Vaillant de Guélis, Felipe Toledo, Olivier Atlan and Jan Polcher. I also want to thank Gaëlle Clain, Pauline Martinet, Maud Pastel and Julien Delanoë for participating in my monitoring committee, and Pierre Gentine and Marie Lothon for accepting to be reviewers for my thesis. Thanks also to all the other members of my defence committee for evaluating my PhD project: Christine Lac, Marjolaine Chiriaco, Philippe Drobinski, Gert-Jan Steeneveld, Damien Vignelles and Marie Vicomte.

A research project like mine requires a lot of work dedicated to writing, debugging and understanding programming code, as well as logging into various computers. I would here like to give a special thanks to Marc-Antoine Drouin for his help with computer technicalities, which he has always been very willing to give at almost any time. Julien Lenseigne has also helped me out with technical problems of a wide range, such as helping me make the printer print my thesis correctly, and providing me with a keyboard when the built-in one in my Macbook was broken.

Coming to work in France is specifically challenging due to the formalities involved, even when I did not need a visa or work permit. Thanks to the administration staff (Isabelle Ricordel, France-Lise Robin, Gaëlle Bruant, Grégory Boucher), my supervisor Martial, and Imma Bastida for helping me out with various forms. Thanks to Xavier Quidelleur and Kim Ho of the Smemag doctoral school for the good communication regarding my yearly re-registrations and validation of courses. Thanks also to Emmanuel Fullenwarth and Aurélien Arnoux for the very clear instructions and good communication regarding the intricate formalities required for the thesis defence and legal deposits of my dissertation.

On the wider aspect of living in France, I would also like to thank the organisation Science Accueil for preparing my stay in France by enabling me to open a bank account before I arrived and giving me explanations on which insurances I needed to get. I also very much appreciate being allowed to live at the excellent student house Maison de Norvège in Cité Universitaire for my whole stay. All of

the staff there has been very kind and helpful, and I have enjoyed staying with my fellow residents – thank you all first-floorers! Thanks also to my very nice fellow residents in the apartment where I lived during my stay in Wageningen. I am also thankful for the very inclusive Trinity International Church of Paris and the friendly young people I got to know there.

I very much appreciated the social activities among the PhD students and Post-docs at LMD, including football, board games and evenings out in Paris. Bastien, Nicolas, Oliver, Felipe, Aurore, Artemis, Stavros, Thibault, Adrien, Rodrigo, Xudong, Ariel, Sara, Fuxing, Erik, Trung, Alexis, I am going to miss you all.

A very special thanks goes to my girlfriend Beate, who has been patiently waiting for me back in Norway all this time. Thanks for our pleasant short holidays together every 2 months or so, which have been very nice breaks from life as a PhD student. Thanks also to Beate's family for welcoming me into their homes during the holidays and bringing me on their Europe road trip.

Finally, thanks to my own family for the regular contact during my stay in France and their interest in my work. Thanks in particular to my father Morten who is always available when I need encouragement and advice. I am also thankful for the care and concern of my grandmother Sigrun. My uncle Kristian and aunt Liv have always been very supportive, especially since the early death of my mother. I am also, as I always have been, very happy to have my large and fast growing Danish family, who I go to see every year at Christmas.

Abstract

Fog causes hazards to human activities due to the reduction of visibility, especially through the risk of traffic accidents. The fog life cycle is driven by radiative, dynamical, and microphysical processes which interact with each other in complex manners that are not yet fully understood. Improving our understanding of these processes and our ability to forecast fog formation and dissipation is therefore an objective for research. This thesis analyses the life cycle of continental fog events occurring in the Paris area, using several ground-based remote sensing instruments deployed at the SIRTA atmospheric observatory. We focus on understanding the dissipation after sunrise and the local processes involved. Over a 4-year period, more than 100 fog events are documented by observing cloud base height (CBH) (with ceilometer), cloud top height (CTH) and clouds appearing above the fog (with cloud radar), and the liquid water path (LWP) (with microwave radiometer (MWR)). When combined with the cloud radar, the MWR also provides estimates of the integrated water vapour (IWV) above the fog and the thermal stratification of the layer above fog top.

Most fog events dissipate by lifting of the CBH without a complete evaporation of the cloud, and sometimes even without a reduction in LWP. This is because an increase in the CTH can also trigger fog dissipation. In fact, by applying the model of Cermak and Bendix (2011), we find that the LWP and CTH are the principal parameters which determine the CBH and therefore fog dissipation. For each CTH, there is a critical fog LWP which must be exceeded if the fog should stay at the surface. This critical LWP increases more than linearly with CTH, and for a fog temperature of 5 °C it is estimated to 6 g m^{-2} for a CTH of 100 m, 29 g m^{-2} for 200 m, and 131 g m^{-2} for 400 m. In order to better understand fog dissipation, we therefore focus on the impacts of the physical processes on LWP and CTH. Using a radiative transfer code and large-eddy simulations (LES), we quantify the impacts on the two parameters by the processes of long-wave (LW) radiation, short-wave (SW) radiation, surface turbulent heat fluxes, fog-top entrainment, large-scale subsidence and droplet deposition, and we study the parameters which can cause important variability in these impacts. We also develop a conceptual framework based on a well-mixed assumption to be able to calculate the impacts that estimated heat and moisture fluxes have on the fog LWP.

Radiative processes are studied using the comprehensive radiative transfer code ARTDECO. The LW radiative cooling at fog top can produce 40–70 g m^{-2} h^{-1} of LWP when the fog is opaque (LWP $>\approx$ 30 g m^{-2}) and there are no clouds above. This cooling is the main process of LWP production and can renew the fog LWP in 0.5–2 h. Its variability is mainly explained by the fog temperature and the humidity profile above the fog. Clouds above the fog will strongly reduce this production, especially low clouds: a cloud with optical depth 4 can reduce it by 30 (100) % when located at 10 (2) km. When the fog is semi-transparent to LW radiation, corresponding to LWP $<\approx$ 30 g m^{-2}, which is the case for nearly half the fog dataset, the LWP production increases strongly with LWP. Loss of LWP by absorption of solar radiation by the fog is 5–15 g m^{-2} h^{-1} around midday in winter,

increasing with cloud thickness, but it can be enhanced by 100 % in case of important amounts of absorbing aerosols (case tested: a population of urban aerosols with dry aerosol optical depth of 0.15 and single scattering albedo of 0.82).

Heating of the fog due to solar radiation absorbed at the surface, through turbulent heat fluxes, is found to be the dominating process of LWP loss after sunrise and can reach 20–30 g m^{-2} h^{-1} (according to LES), but its magnitude is sensitive to the Bowen ratio. However, observations of the turbulent heat fluxes during fog are not precise enough to determine the Bowen ratio. Its importance for fog LWP budget shows that improved understanding and measurements of the Bowen ratio during fog should be a priority. Through its impact on the Bowen ratio, the liquid water on the surface can be important for fog persistence in the morning; in our LES study, fog dissipates 85 min later in a run with 50 % of the surface covered by liquid water, compared to a run with no surface water.

Observations by radiosondes reveal the variability of the thermal stratification and humidity of the layer above the fog top. Using the LES, we find a strong sensitivity of the vertical development of the fog top to this observed variability in stratification. By enhancing entrainment, a weak stratification at fog top can lead to earlier fog dissipation by (1) more depletion of LWP by entraining unsaturated air, especially if the air is dry, and (2) increase in CTH. Fog dissipation is 90 min earlier in an LES sensitivity test using a weak stratification relative to the baseline run with a strong stratification. The variability of this stratification in the radiosondes can be observed reasonably well with the MWR temperature profile, which allows continuous time series of this parameter. The variability in the humidity above fog top also has an important impact on the dissipation time: in our LES sensitivity test with dry overlying air, the fog dissipates 70 min earlier than in the baseline run with air above close to saturation. The drier air causes faster depletion of fog LWP, allowing the fog to lift earlier. However, the effect of humidity above is sensitive to the details of the humidity profile, since a dry atmosphere also increases LW radiative cooling.

In order to investigate the results presented above for a larger number of fog events, we develop a conceptual model which uses 12 parameters derived from cloud radar, microwave radiometer, ceilometer, broadband radiometer, sonic anemometer, soil fluxmeter and scatterometer measurements, and 2 parameters obtained from reanalysis data, to calculate the impacts on LWP and CTH from each of the six local processes (LW radiation, SW radiation, surface heat fluxes, entrainment, subsidence, deposition). It is applied to 45 observed fog events which are present at sunrise.

An important variability in radiation, entrainment rate and surface heat fluxes between the 45 cases is found, which can explain some of the observed differences between them. In particular, the observed seasonality in dissipation time, with fog lasting longer near winter solstice, sometimes the entire day, can be related to the weaker insolation near winter solstice, which limits the LWP loss processes related to solar radiation. We also find a correlation between the calculated entrainment velocity, for which we use the entrainment scheme of Gesso et al. (2014), and the observed vertical development of the CTH, although advection clearly has a strong impact on the CTH. The entrainment scheme also reproduces the effect of stratification on CTH found with the LES model, but it generally underestimates the entrainment velocity relative to the LES, showing that the scheme needs to be adjusted to the special case of fog. While fog events occur both during large-scale upward motion and subsidence, the persistent fog events systematically occur during subsidence. We show that the subsidence in itself does not favour fog persistence, because its effect on reducing the LWP (through adiabatic heating and divergence) is stronger than its reduction of critical LWP (through sinking

CTH). Thus, the correlation between persistence and subsidence is likely related to other synoptic factors that occur together with subsidence.

While the terms of radiation in the conceptual model are rather robust, several other terms suffer from significant uncertainties, leaving room for improvements in the future. We also find indications that horizontal advection and heterogeneity play an important role in the observed evolutions of LWP and CTH, because they often evolve in a way that we cannot explain by the local processes. We therefore suggest that the conceptual model should be extended to also account for observed or modelled horizontal advection.

Finally, the vertical profile of radar reflectivity in the fog, which we can study in detail thanks to the high vertical resolution and small blind-zone of our cloud radar, exhibits significant variability. The reflectivity is usually in the range -40 to -15 dBZ. The max value in the profile is in some situations located near the fog top; this often occurs right before or during dissipation by lifting of cloud base. This shape suggests a lack of bigger droplets in the lower levels of the fog. In other cases, the reflectivity is stronger and has a max near the middle of the fog layer, indicating more sedimentation of big droplets. We also show with three tethered balloon flights in fog of a droplet counter (0–300 m altitude) that an approximate relationship between radar reflectivity and liquid water content applies to fog, similarly as has previously been shown for other low clouds. The profile of radar reflectivity can therefore reveal information about fog microphysical properties.

Hence, Doppler cloud radars, microwave radiometers and ceilometers are three essential instruments to provide detailed measurements of key variables – at the base, inside, at the top and above the fog – that are critical to better understand the life cycle of continental fog.

Contents

Chapter 1

Introduction

1.1 Foreword

Fog is an interesting meteorological phenomenon in many ways. A fog is basically like a cloud, that is a humid airmass containing microscopic, activated water droplets (or, in cold areas, ice crystals). Unlike clouds, however, fog is in direct contact with the Earth's surface. This opens the possibility for more direct interactions with the surface and vegetation, and with human activities. Due to the scattering of visible radiation by droplets, the visibility is reduced during fog, which is hazardous for traffic, so that cars, ships and airports must take precautions (Tardif and Rasmussen, 2007). In addition to its impact on the visibility, fog has many effects on the environment. In many dry regions, especially near subtropical west coasts such as in Namibia and Chile, fog is an important source of freshwater to the ecosystems, because it occurs much more frequently than rain (e.g. Seely and Henschel, 1998). Using fog-collecting nets, it is even possible to provide freshwater for local populations from fog (Klemm et al., 2012). As the fog acts as a solvent for many atmospheric aerosols and gases, it impacts the atmospheric chemistry and can catalyse chemical reactions (e.g. Boris et al., 2018). Wet deposition of pollutants is more efficient through fog than rain due to the larger droplet surface area and the longer residence time near the surface, where the concentration of pollutants is highest, which can importantly increase the deposition of pollutants where fog frequently occurs (Dollard et al., 1983; Barrie and Schemenauer, 1986).

This thesis is mainly motivated by the impact that fog has on the visibility. The financial and human losses related to fog can be as large as for tornadoes and even storms due to the delays and increased risk of accidents in air, marine and land transportation (Gultepe et al., 2009). In order to manage and plan traffic efficiently according to the meteorological situation, forecasts of visibility are important (Tardif and Rasmussen, 2007). Fog has proven to be a difficult phenomenon to forecast, and current numerical weather prediction models (NWP) often fail to predict the time and location of the formation and dissipation of fog with sufficient accuracy (e.g. Steeneveld et al., 2015). Although the occurrence of fog and haze has decreased in Europe over the last decades, it still remains a frequent phenomenon in many areas of the continent (Vautard et al., 2009; van Oldenborgh et al., 2010). In particular, it occurs often in the Alpine region, such as the Po Valley. Northern Europe has more fog than the Mediterranean, and the winter has overall more fog days than the summer, with the number of days per winter season with visibility below 200 m (2 km) varying from >15 (>75) for some sites in the Alps and Eastern Europe to <3 (<15) in the Mediterranean and north-western United Kingdom, with most of Northern Europe having an occurrence in the middle of these two (van Oldenborgh et al.,

2010).

This thesis aims to advance the understanding of the different physical processes which govern the fog life cycle and lead to its dissipation. We will explore how ground-based remote sensing instruments that observe the atmospheric column can diagnose the variability of physical processes that are important for the fog evolution. This introduction chapter elaborates on the precise definition of fog (section 1.2) and gives an overview of the various situations in which fog may occur (section 1.3). The life cycle and key processes for the fog types studied in this thesis are then presented (section 1.4). The objectives of the thesis will be elaborated at the end of the chapter (section 1.5).

1.2 Definition of fog

Fog is defined as the reduction of visibility to below 1 km due to the presence of suspended water droplets in the vicinity of the Earth's surface (American Meteorological Society, 2017). Thus, two conditions must apply for fog to occur: (1) the reduction in visibility, and (2) that the main reason for this reduction in visibility is the presence of small, suspended droplets. These two aspects of fog are explained in this section.

1.2.1 Visibility

The definition of visibility from American Meteorological Society (2017) is: "The greatest distance in a given direction at which it is just possible to see and identify with the unaided eye 1) in the daytime, a prominent dark object against the sky at the horizon, and 2) at night, a known, preferably unfocused, moderately intense light source". This definition is by itself rather subjective, since it depends on the human capacity to observe, and a more objective formulation has therefore been developed based on the concept of the contrast between the object and its background (between 0 and 1). Due to the scattering of the light by the atmosphere between the object and the observer, the contrast decreases with distance according to the following formula (Duntley, 1948):

$$C = C_0 e^{-\alpha_{ext} \cdot d} \tag{1.1}$$

where C_0 is the contrast at close range, C is the contrast at distance d, and α_{ext} is the extinction coefficient of the atmosphere between the object and the observer. For a black object against a white horizon, $C_0 = 1$. The lowest contrast that the human eye is able to discern is conventionally set to $C = 0.05$ by the Commission on Illumination (Hautière et al., 2006). This is then used to derive the visibility distance by the Koschmieder formula:

$$Vis = -\frac{\ln 0.05}{\alpha_{ext}} = \frac{3.0}{\alpha_{ext}} \tag{1.2}$$

Although the theory used to derive this formula depends on several assumptions, such as a homogeneous, static atmosphere, a flat and diffuse surface, negligible absorption, and the observed object being small compared to the distance to it, the formula has been found to agree well with human observations (Horvath and Noll, 1969). To measure visibility, the quantity which needs to be observed is therefore the extinction coefficient α_{ext} of the atmosphere at visible wavelengths. To get below the fog threshold of 1 km, it follows that the extinction coefficient must exceed 3.0 km^{-1}.

1.2.2 Fog v.s. other phenomena that reduce the visibility

The second part of the fog definition specifies that the reduction of visibility is caused by suspended, microscopic droplets. In fact, there are several other ways the visibility may be reduced. These include heavy rain, blowing snow, smoke and sandstorms. Rain is not fog because the droplets are too big and therefore not suspended but falling from a cloud above. Conventionally the separation between cloud droplets and raindrops is at 200 μm, at which the fall speed is 0.7 m s^{-1} (American Meteorological Society, 2017). Smoke and sand are not fog because they are dry particles and not droplets. Snowflakes are not fog because they are too big and frozen. Although all of these phenomena can give the same effect on visibility as fog, the processes governing them are very different, and they require different approaches to understand and predict.

However, in cold environments fog may also consist of suspended ice crystals, which is referred to as ice fog (American Meteorological Society, 2017). Ice fog usually does not occur unless the temperature is below -10 °C (Gultepe et al., 2007). When fog made of water droplets occurs below 0 °C, the droplets will freeze when depositing on surfaces, so-called icing, and it is referred to as freezing fog.

If the relative humidity has not reached saturation, the hygroscopic aerosols will not activate into droplets, as explained by Köhler theory (Köhler, 1936), but they can still grow sufficiently large to reduce visibility. This phenomenon is referred to as haze, and the unactivated, hydrated aerosols are called haze particles (American Meteorological Society, 2017). Conventionally, it is assumed that the visibility in haze is higher than 1 km and that it only drops to below this threshold when the haze particles activate to droplets. An intermediate situation is referred to as mist, where relative humidity is close to 100 %, but the visibility is not below 1 km (American Meteorological Society, 2017). However, the distinction between fog and haze is not always sharp: the visibility may be reduced to below 1 km even without activation in very heavily polluted situations, such as extreme haze (e.g. Yang et al., 2015). The activation of cloud condensation nuclei (CCN) into droplets may occur at a smaller or larger diameter, typically in the range 1–4 μm, depending on the mass and chemical composition of the CCN (Rogers and Yau, 1989).

In many situations, several types of particles may contribute simultaneously to reduce the visibility. Fog may occur together with rain, and in industrial areas fog or haze may combine with smoke to form smog (American Meteorological Society, 2017). It has also been shown that haze particles may contribute a significant part of the extinction during fog (Elias et al., 2009).

1.2.3 Droplet size distribution

The fog consists of a large number of small water droplets of different sizes, which constitute a droplet size distribution (DSD). Both the droplet number and sizes are important because they affect how the fog interacts with radiation and the microphysical processes which lead to deposition. The initial number and sizes of the droplets depend on the formation mechanism of the fog (how high the supersaturation becomes) and the aerosol population which acts as CCN (Rogers and Yau, 1989). The distribution may evolve during the fog life cycle, due to the dynamics of the fog, which may lead to the appearance of bigger droplets (e.g. Price, 2011; Dupont et al., 2012).

The DSD is commonly expressed mathematically as a function $n(D)$, defined so that $n(D) \cdot dD$ is the number of particles in a unit volume of air with diameters between D and $D + dD$. The total

number of cloud droplets is found by integrating over all sizes:

$$N_c = \int_{D_{min}}^{D_{max}} n(D)dD \tag{1.3}$$

where D_{min} is the conventional threshold separating the droplets from haze particles (typically 2 μm). As mentioned above, the size D_{max} which separates cloud droplets from raindrops is conventionally set to 200 μm. However, most instruments that measure the DSD only capture the droplets smaller than 50 μm (Guyot et al., 2015). The liquid water content (LWC), i.e. the mass of droplets in a unit volume of air, can be calculated from the DSD as:

$$LWC = \int_{D_{min}}^{D_{max}} \frac{\pi \rho_l}{6} n(D) D^3 dD \tag{1.4}$$

where $\rho_l = 10^3$ kg m^{-3} is the density of liquid water.

In the visible part of the spectrum, cloud droplets efficiently scatter the radiation, while they only weakly absorb. The fraction of the radiation incident to the droplet that is scattered (or absorbed) is referred to at the extinction efficiency (Q_{ext}). The extinction coefficient is therefore:

$$\alpha_{ext} = \int_{D_{min}}^{D_{max}} \frac{\pi}{4} Q_{ext(D)} n(D) D^2 dD \tag{1.5}$$

For cloud droplets that are several times bigger than the visible radiation, a good approximation is $Q_{ext} = 2$ so that the extinction coefficient is (Hu and Stamnes, 1993):

$$\alpha_{ext} = \frac{3LWC}{\rho_l D_{eff}} \tag{1.6}$$

where D_{eff} is the effective diameter, defined as:

$$D_{eff} \equiv \frac{\int_{D_{min}}^{D_{max}} n(D) D^3 dD}{\int_{D_{min}}^{D_{max}} n(D) D^2 dD} \tag{1.7}$$

1.3 Fog types

Fog forms when the air near the surface becomes supersaturated with water vapour, which triggers the activation and growth of droplets to micrometer sizes. Since the saturation vapour pressure increases strongly with temperature, supersaturation of the air may be obtained from a reduction of the air temperature, from an increase in its water vapour content, or from a combination of the two (Rogers and Yau, 1989). There are therefore several meteorological conditions which may result in fog, and fog types have been defined according to the mechanism causing the fog to appear (Gultepe et al., 2007; Tardif and Rasmussen, 2007).

Radiation fog forms when the land surface is cooled through the emission of LW radiation, usually during the night in clear-sky conditions, leading to supersaturation of the air just above the surface (Haeffelin et al., 2010). This fog type is associated with anticyclones above land (Gultepe et al., 2007). The wind has been shown to be a critical factor for the formation of radiation fog; if the wind is too strong, turbulent mixing will dilute the cooling and moistening in a too thick layer for supersaturation to occur, while too little wind may result in dew deposition instead of fog (Zhou and Ferrier, 2008;

Haeffelin et al., 2013).

Another way to cool the airmass to saturation is by lifting. Upslope fog forms when moist air is forced to lift due to topography, and fog is therefore frequent on the upwind slopes of hills and mountain ranges, especially when the wind comes from a moist area, such as the sea (Błaś et al., 2002).

Fog may also form by a gradual lowering of the base of a pre-existing very low stratus all the way to the surface. Previous studies have identified the mechanisms of cloud-top radiative cooling, subsidence, and the moistening of the sub-cloud layer through evaporation of falling drizzle as possible explanation for this lowering of the cloud base (Koračin et al., 2001; Dupont et al., 2012). Another way that fog can form through moistening is through the evaporation of rain during precipitation events, so-called precipitation fog (Tardif and Rasmussen, 2007). If the precipitation is associated with the passage of a warm front, it can also be called frontal fog; the front may induce fog formation both through evaporation of precipitation and by the mixing of the warm and cold airmasses that meet at the front (Gultepe et al., 2007). Fog may also form due to the evaporation of dew from a wet surface due to heating from the sun right after sunrise, which can lead to saturation of the air. This phenomenon is called morning transition fog (Tardif and Rasmussen, 2007).

Advection fog is the result of the advection of a moist airmass above a colder surface. This is typical for fog formation above the ocean. When warm air is blowing over a colder sea surface, the mixing of the air parcels with different temperature can result in saturation, and it is especially frequent in areas of coastal upwelling (Koračin et al., 2014). Conversely, advection fog can also form when cold air is advected above a warmer surface. In high latitudes, this gives rise to a phenomenon called steam fog (Koračin et al., 2014).

This thesis studies fog events observed at the atmospheric observatory SIRTA near Paris (France). This is a continental mid-latitude site, where the fog events are mainly radiation fog or stratus-lowering fog (Dupont et al., 2016). These fog types will therefore be the focus of the rest of this introduction chapter.

1.4 Life cycle of continental radiation fog and stratus-lowering fog

Previous studies on radiation fog have identified that it goes through different evolutionary stages. Often three stages are described: the formation phase, the development phase and the dissipation phase (e.g. Bergot, 2013). During the formation phase, the surface layer is stable with limited vertical mixing, and it reaches saturation due to radiative cooling of the surface, allowing the formation of small cloud droplets. The fog may form as a very thin layer, just above the cold surface, and its horizontal extent is often broken by patches of clear air, due to heterogeneity of surface properties that impact humidity (Gultepe et al., 2007). This layer may remain thin, but often it develops vertically to become 100 m thick or more. This thicker fog will have a significant emissivity so that the radiative cooling is transferred from the surface to the fog top. This cooling at the top will eventually make the initially stable fog layer neutrally stratified, i.e. a saturated adiabatic lapse rate, which enhances vertical mixing (Price, 2011). This transition from "stable fog" to "adiabatic fog" is important for the fog internal dynamics: while the stable fog has little vertical mixing, the adiabatic fog can be strongly coupled between the surface and its top (e.g. Bergot, 2016). The phase of increasing vertical mixing and TKE is what is referred to by Bergot (2013) as the development phase. As the fog thickens, the initial distribution of small droplets is usually modified with the appearance of larger droplets of

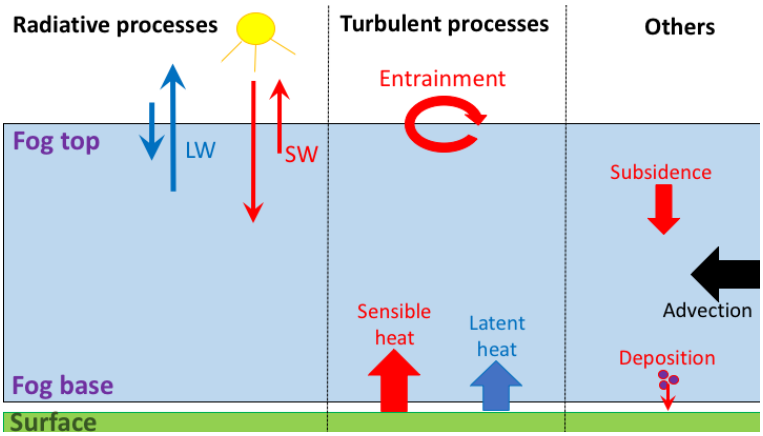

Figure 1.1: The physical processes which impact the liquid water of the fog layer. Those marked in blue will typically produce fog water while those marked in red will reduce fog water.

diameters 15–20 μm, which Price (2011) use to define the mature phase of the fog. However, Price (2011) shows that the appearance of the bigger droplets is not always related to the time when the stable temperature profile becomes saturated adiabatic.

Radiation fog does not always start as a thin layer at the surface, though. In many cases it forms at a few tens of metres of altitude, followed by a rapid downward thickening to the surface (e.g. Haeffelin et al., 2016). The large-eddy simulation (LES) study of Mazoyer et al. (2017) explained the elevated fog formation by the presence of obstacles such as trees, which enhances wind-driven turbulence and dew deposition on the surface and vegetation, thereby limiting the humidity close to the ground. The theoretical calculations of Zhou and Ferrier (2008) suggest that very thin radiation fog cannot persist unless the turbulence is very weak: the more wind-driven turbulence is present, the thicker the fog layer must be to persist. Consequently, the saturated layer needs to acquire a certain thickness before the fog may start to form. Stratus-lowering fog differs from radiation fog by already being thick when fog forms at the surface. In this case, the formation phase consists of an interaction between the stratus and the sub-cloud layer instead of the cooling of a stable layer. Dupont et al. (2012) identified the humidification of the sub-cloud layer by evaporation of droplets falling from the cloud base as a key process for the formation of stratus-lowering fog.

Once the fog has formed, several processes affect its profile of liquid water. This is shown schematically in Fig. 1.1. The contact with the surface allows droplets to deposit on the vegetation, both through the terminal fall velocity of the bigger droplets and through impaction on the vegetation and other obstacles. It has been found that the sedimentation process dominates the deposition under very weak wind speed (< 2 m s^{-1}), while impaction is the most important of the two when the wind is stronger (Katata, 2014). The vertical flux of LWC by sedimentation is essential to account for in order to simulate realistic LWC in fog (Brown and Roach, 1976; Bergot et al., 2007). The surface also exchanges heat with the fog. Due to the radiative cooling, the surface is initially colder than the fog in case of radiation fog formation. However, once the fog has become opaque to long-wave (LW) radiation, the surface is sheltered from the radiative cooling, which instead occurs at the fog top (e.g. Haeffelin et al., 2013). Due to heat diffusion from the soil, the surface temperature will typically become higher than the air temperature, so that the surface becomes a heat source rather than a heat sink for the fog (Roach, 1995; Price, 2011). This becomes much more pronounced once the sun has risen, as the surface is then heated also by solar radiation (Brown and Roach, 1976), so that the fog

is heated from below by turbulent sensible and latent heat fluxes.

The cooling from above and heating from below generates turbulence through buoyancy, so that the fog will contain convective structures (e.g. Nakanishi, 2000). The generated turbulence will promote mixing between the fog and the unsaturated air above the fog top, leading to evaporation of fog droplets (Gultepe et al., 2007) and to upward development of the fog top. However, the mixing at fog top is limited by the strong inversion that usually develops due to the cooling of the fog top (Nakanishi, 2000; Price, 2011; Price et al., 2015). Fog droplets will also evaporate as they approach the heated surface below (Nakanishi, 2000). Radiation fog therefore usually dissipates in the morning due to the heating from the surface, so-called fog burn-off (Tardif and Rasmussen, 2007; Haeffelin et al., 2010). The dissipation phase, as characterised by Bergot (2013), involves an intensification in the vertical mixing due to a further destabilisation of the fog layer by the appearance of solar radiation, or alternatively an increase in wind speed. The dissipation phase can also be characterised by an increase in visibility and a reduction of the LWC and droplet sizes near the surface (Maier et al., 2013).

This thesis focuses specifically on the developed phase of the fog layer and the processes that affect its dissipation. Fog dissipation is defined as the increase of visibility to above 1 km due to removal of the droplets at screen level. Note that dissipation therefore does not require a complete evaporation of the cloud; the cloud may be displaced vertically so that it no longer touches the surface. Radiation fog will typically dissipate after sunrise, but there is still an important variability of the time of dissipation (Dupont et al., 2016), and occasionally very persistent fog may last for the whole day (Price et al., 2015). Roach (1995) summarises the mechanisms that can disperse a fog layer in addition to the heating by solar radiation: (1) the appearance of a cloud layer above the fog, reducing the radiative cooling, (2) heating from the soil, more so in autumn than in winter, and (3) an increase in the wind speed, which enhances mixing. These mechanisms of dissipation of fog all act by modifying the balance between the processes controlling the liquid water of the fog (Fig. 1.1). The mechanisms have since been studied using numerical models and observational studies. Bergot (2016) showed with LES simulations that a stronger wind speed favours earlier dissipation, due to the increased turbulence and mixing with the air above. The results of Maronga and Bosveld (2017) indicate that high soil temperature mainly delays fog formation and does not affect dissipation as much. Soil moisture, however, impacts the dissipation time, with drier soil favouring earlier dissipation due to the reduction in latent heat flux (Maronga and Bosveld, 2017). Due to its impact on the fog optical depth and sedimentation rate, the fog droplet number concentration can also affect dissipation time, with fewer and larger droplets favouring earlier dissipation (Maalick et al., 2016; Mazoyer et al., 2017). Falling droplets can cause fog dissipation by collection processes and deposition, but they can also cause lowering of a low stratus cloud base to the ground to form stratus-lowering fog, as studied with Doppler cloud radar by Dupont et al. (2012). Large-scale advection also has impacts on fog dissipation. The observations of Price et al. (2015) show that warm advection can reduce the relative humidity in the air overlying the fog and therefore increase the loss by mixing, which can lead to dissipation. Thus, drying from mixing, contributing to dissipation, can be enhanced by both increase in wind speed and reduction in the relative humidity of the air above. It was found in LES studies (Bergot, 2013, 2016) that dry tongues of air which penetrate the fog from above, cause a large horizontal spread in the liquid water path (LWP) during the dissipation phase of fog, so that the time of fog dissipation can be variable in the horizontal even if the surface forcing is homogeneous. Circulations at the horizontal edge between fog and clear air, driven by temperature gradients, can be an important mechanism for dissipating the

fog, as observed by Price et al. (2015). However, they also found that such circulations at the fog edge can drive a rapid expansion of the fog layer when the clear air is close to saturation.

1.5 Context and objectives for the thesis

One reason that fog is challenging to predict is that it is a threshold phenomenon governed by many small-scale processes; subtle differences in these processes can impact the fog formation or dissipation (e.g. Zhou and Ferrier, 2008; Haeffelin et al., 2013). In numerical weather prediction (NWP) models, the small-scale processes must be parametrised. Bergot et al. (2007) compared the fog prediction by single-column models of fog and found important sensitivity of the results to which parametrisations were used for droplet sedimentation and soil-atmosphere interactions, and also to the correct representation of the nocturnal inversion.

As a supplement to NWP, statistical models are developed for sites for which fog forecasts are needed, in particular airports. The models relate the visibility to other meteorological observations, such as temperature, relative humidity, wind speed and cloud cover. Based on a long time period of continuous measurements, conditions preceding fog formation or dissipation can be statistically identified and give a probabilistic short-term forecast of the visibility (e.g. Pasini et al., 2001) or the time of fog formation (e.g. Fabbian et al., 2007). Most of the investigations have focused mainly on observations of near-surface conditions. These are easier to observe with ground-based instruments than the properties higher up in the fog. However, since once the fog has formed, many of the processes occur near the fog top, it is important to observe the whole vertical profile of the fog layer to understand its evolution and dissipation.

Ground-based remote sensing instruments such as cloud radars and microwave radiometers (MWR) are well suited for continuously measuring properties of the vertical profile of fog and clouds. Many algorithms have been developed, based on one or several instruments, to retrieve geophysical parameters of clouds from the observations, such as the LWP from the MWR (Rose et al., 2005), and LWC, ice content or particles sizes from the cloud radar, with or without combining it with the MWR (e.g. Dong and Mace, 2003; Delanoë et al., 2007; Martucci and O'Dowd, 2011). These instruments are currently becoming less expensive and with higher performance, and more commonly deployed on sites of interest. For example, the ceilometer, which is traditionally only used for cloud-base detection, is being improved to give information about the vertical profile of extinction, which can be used to track the hygroscopic growth of aerosols that may lead to elevated radiation fog formation (Haeffelin et al., 2016). The systematic use of observations from these remote sensing instruments is further being facilitated by the efforts to establish standardised conventions for quality control, calibration routines, data file formats and the sharing of data between institutions and between countries. In Europe, such collaboration is currently undertaken by the project ACTRIS (`www.actris.eu`). By retrieving properties of the whole atmospheric column in real-time, the remote sensing instruments have a great potential for contributing to weather forecasts. The observations may either be directly used to anticipate the evolution in the next hours (nowcasting) or they can be assimilated in NWP to improve the initial state of these models. Recent studies have shown that certain short-term NWP forecasts can be improved by assimilation of MWR temperature and humidity profiles (Caumont et al., 2016).

This thesis aims (1) to improve the understanding of the physical processes that play a role in fog dissipation, and (2) to investigate how the observations from ground-based remote sensing instruments

can be used to understand and possibly anticipate the fog dissipation. We have chosen to focus particularly on the fog events that persist until sunrise, on how they evolve during the daytime until their dissipation. We further focus on the local processes, by which we mean the processes that occur in the vertical column of the atmosphere on a small horizontal scale, and which do not depend on horizontal advection or heterogeneities. The investigations will be centred on the following questions:

- How much does each of the local processes contribute to the liquid water budget of the fog, in various conditions?
- What is the impact of the variability of the properties at and above the fog top on the liquid water budget and dissipation of the fog?
- What information can be derived from the cloud radar and MWR measurements about the current state of the different fog processes?
- How is the dissipation of fog related to the evolution of its LWP and its thickness?
- To what extent can the observed evolution of the fog be attributed to the local processes, and how much must rather be attributed to advection and other non-local effects?

To answer these questions, a dataset of 7 years of fog events at the SIRTA observatory is studied. The various geophysical properties that we retrieve from observations and their variability are presented in chapter 2. Numerical modelling tools are thereafter used to understand what impact the observed variability has on different processes. In chapter 3, a comprehensive radiative transfer code is applied to study the radiative processes in fog and quantify their impacts on the LWP of the fog through heating and cooling. This chapter incorporates our published paper on this topic (Wærsted et al., 2017, hereafter W17). The dynamical processes, including surface–fog interactions and the mixing between the fog and the air above, are studied using high-resolution LES in chapter 4, which contains our paper on this topic which was submitted in July 2018 (Wærsted et al., 2018, hereafter W18). Chapters 3 and 4 allow a quantitative analysis of the importance of various local processes for the evolution of the fog LWP and its dissipation. In chapter 5, these results are applied to analyse a much larger number of fog events (45) through a conceptual model. The analysis aims to quantify the variability of the impacts of the different processes among the observed events and to explain some of the differences we observe in the evolution and time of dissipation among the events. Finally, the conclusions are presented in chapter 6.

Chapter 2

Observed properties of fog events

This chapter presents the instrumentation used in this study and the various fog properties that can be retrieved from them. It also presents statistics of these properties from the large number of fog events observed on the SIRTA observatory.

2.1 Observational site SIRTA

SIRTA (Site Instrumental de Recherche par Télédétection Atmosphérique) is a multi-instrumental atmospheric observatory located 20 km south of Paris at the university campus of École Polytechnique, where a large number of atmospheric variables have been continuously recorded since 2002 (Haeffelin et al., 2005). Thanks to the elevated number of fog events occurring there each winter, this site is suited for fog observational research, which has been a scientific priority for the site since the ParisFog project started in 2006 (Haeffelin et al., 2010). Table 2.1 presents the instruments used in this thesis to study fog. Nearly all of these instruments are located in the main facility of the SIRTA observatory, hereafter referred to as "the platform", which is located on a grass field between a narrow wood to the north and a small lake to the south (Fig. 2.1). The larger surroundings are characterised by a patchwork of university buildings, small woods, agricultural and sports fields, and suburban houses.

Standard meteorological measurements (2-m temperature and humidity, 10-m wind speed, surface pressure) are recorded continuously at the platform. In addition, there are six levels of temperature

Figure 2.1: The SIRTA observatory main facility.

Instrument	Measured quantity	Vertical range and resolution	Temporal resolution	Available from
Remote sensing				
95 GHz Doppler FMCW cloud radar (LATMOS, BASTA)	Reflectivity (dBZ), Doppler velocity (m s^{-1})	RA 0-6(12) km, RE 12.5(25,100,200) m	12 s	July 2013
14-channel microwave radiometer (MWR) (RPG HATPRO)	LWP (g m^{-2})	Integrated	1 min	Feb 2010
	IWV (kg m^{-2})	Integrated	1 min	Feb 2010
	Temperature profile (K)	RA 0–10 km, 4–5 deg. of freedom	≈5 min	Feb 2010
	Humidity profile (g m^{-3})	RA 0–10 km, 2 deg. of freedom	≈5 min	Feb 2010
905-nm ceilometer (Vaisala CL31)	Attenuated backscatter (m^{-1} sr^{-1})	RA 0–7.6 km, RE 15 m	30 s	Dec 2010
Sodar (Remtech SFAS)	Wind speed profile (m s^{-1})	RA 10–200 m, RE 5 m	10 min	Nov 2015†
Granulometers				
Fog monitor (DMT FM-120)	Droplet concentration (cm^{-3}) in 30 size bins (2–50 μm)	At 4? m	1 s	Oct 2013
Aerosol counter (Meteomodem LOAC)	Particle concentration (cm^{-3}) in 19 size bins (0.2–50? μm)	Tether balloon profiles 0–300 m	1 s	IOP
Surface layer state				
550-nm scatterometer (Degreane DF20+)	Visibility (m)	At 3 m	60 s	Feb 2010
550-nm scatterometer (Degreane DF320)	Visibility (m)	At 4 m	60 s	Oct 2013
875-nm scatterometer (Vaisala PWD22)	Visibility (m)	At 20 m	60 s	Oct 2013
Thermometers (Guilcor PT100)	Air temperature (K)	At 1,2‡,5,10,20,30 m	60 s	Sept 2011
Barometer (Vaisala PTB110)	Surface pressure (Pa)	At 2 m	60 s	2005
Rain gauge 3070 (Precis-Mecanique)	Precipitation rate (mm h^{-1})	At 2? m	60 s	2005
Sonic anemometers (METEK)	Mean wind speed (m s^{-1}), momentum flux (m^2 s^{-2})	At 10,30 m	10 min	2007
Ground and soil state				
Thermometer (unsheltered)	Skin temperature (K)	At ground level	60 s	Jan 2014(?)
Soil thermometer (Guilcor)	Soil temperature (K)	At 5,10,20,30,50,100 cm depth	60 s	Feb 2007
Soil moisture sensor (ThetaProbe)	Soil moisture (m^{-3} m^{-3})	At 5,10,20,30,50,100 cm depth	60 s	Feb 2007
Surface energy budget				
Pyranometers (Kipp & Zonen CMP22)	Down- and upwelling irradiance in solar spectrum (W m^{-2})	At 10 m	60 s	Apr 2012
Pyrgeometers (Kipp & Zonen CGR4)	Down- and upwelling irradiance in terrestrial spectrum (W m^{-2})	At 10 m	60 s	Apr 2012
Heat flux sensor (Hukseflux HFP01SC)	Soil heat flux (W m^{-2})	At 5,20,100 cm depth	60 s	Jan 2014
GILL sonic anemometer and LI-7200 infrared gas analyser	Sensible and latent heat flux (W m^{-2})	At 2 m	10 min	Nov 2015†
Radiosondes (M10, Météo France, Trappes)	Temperature (K), relative humidity (%)	RA 0–30 km, RE ≈ 5 m	12 h	1999?

Table 2.1: Instruments used in this thesis for the study of fog. All the instrument apart from the radiosondes are located on the platform shown in Fig. 2.1. †The sodar and surface turbulent flux station were deployed for a longer period, but are only used for November 2015 in this study. ‡There is a separate thermometer at 2 m which is deployed from 2005.

and humidity measurements on the 30-m mast shown in Fig. 2.1. Wind speed is also measured by sonic anemometers at 10 m and 30 m, obtaining also the momentum flux, which allows the calculation of aerodynamic resistance (see section 5.3.2). Visibility is measured at screen level (3 or 4 m) and at 20 m.

The different terms of the surface energy budget are also measured. Two pairs of pyrano- and pyrgeometer measure global upwelling and downwelling short-wave (SW) and long-wave (LW) radiative flux at 10 m, and turbulent sensible and latent heat fluxes are measured at 2 m with the eddy covariance method using a GILL sonic anemometer and an LI-7200 closed-path infrared gas analyser. The ground heat flux is measured at 5, 20 and 100 cm depth. Soil temperature and moisture are measured at

these and three additional levels, and an unsheltered thermometer in the grass measures surface skin temperature.

Full atmosphere profiles of temperature and humidity are available from radiosondes launched from the Météo-France station Trappes twice a day, at around 11 and 23 UTC. Trappes is located 15 km to the west of SIRTA and is 12 m higher above sea level.

The fog monitor FM-120 (Droplet Measurement Technologies) is deployed at SIRTA every winter season since 2013. This instrument counts and sizes individual droplets using a forward scattering probe inside a small measurement chamber, which samples a steady flow of air using an active ventilation. Particles are categorised into 30 size bins in the range 2–50 μm (in diameter), which are mostly droplets. From October 2014, it is equipped with a swivel, which ensures that the air inlet faces the wind direction, giving a more reliable sampling of droplets.

Several remote sensing instruments useful for fog observations are also deployed at the platform. A Vaisala CL31 ceilometer operating at 905 nm provides a vertical profile of (attenuated) light backscatter with 15 m resolution (Kotthaus et al., 2016). This wavelength is highly sensitive to cloud droplets, giving reliable detection of clouds. Since the cloud rapidly attenuates the ceilometer beam, further characterisation of the cloud profile above the cloud base is performed by the 95 GHz cloud radar BASTA (Delanoë et al., 2016, `http://basta.projet.latmos.ipsl.fr/`), which is deployed in a vertically pointing position. Because this cloud radar uses the frequency-modulated continuous wave (FMCW) technique, rather than pulses, its components are less expensive than traditional cloud radars. BASTA is suitable for fog studies due to its high resolution (12.5 m) and small blind zone (40–60 m) compared to many other cloud radars. The prototype of BASTA has been operating at SIRTA since 2010, but its high-resolution product is only available from the summer 2013. In addition to the high-resolution mode, the cloud radar has three more modes with higher sensitivity but larger blind-zone and smaller vertical resolution, all of which give one profile every 12 s. In this thesis, we use the 100-m resolution mode for detecting clouds above the fog (or the 200-m mode in W17), while the 12.5-m mode is used for observing the fog. Finally, the 14-wavelength MWR HATPRO provides brightness temperature measurements in 7 oxygen and 7 water vapour bands. The vertically integrated liquid water path (LWP) and integrated water vapour (IWV) of the whole atmospheric column, as well as rough profiles of temperature and humidity up to 10 km can be retrieved from these measurements (Rose et al., 2005).

2.2 Fog events observed at SIRTA

Most of the instruments used in this thesis have been measuring at SIRTA almost continuously since 2010 (Table 2.1). This long time series captures a large number of fog events, which is valuable for a statistical study of the fog life cycle. However, since high-resolution cloud radar data is only available from October 2013, a particular focus will be given to the fog events occurring after this.

Most of the analysis performed in this thesis is based on averages of observations in 10-minute blocks. It is convenient to use blocks to get the same times for each observed quantity. The sample size of 10 min is chosen because most of the observations are given at least once every 10 min (Table 2.1). Although the spacing of observations is not always completely even, no weighting of observations are done when averaging.

Fog presence is detected using the visibility measured at 3 or 4 m altitude (the df20+ instrument is used until 30 Sept 2013, and the DF320 thereafter). If at least half of the visibility measurements

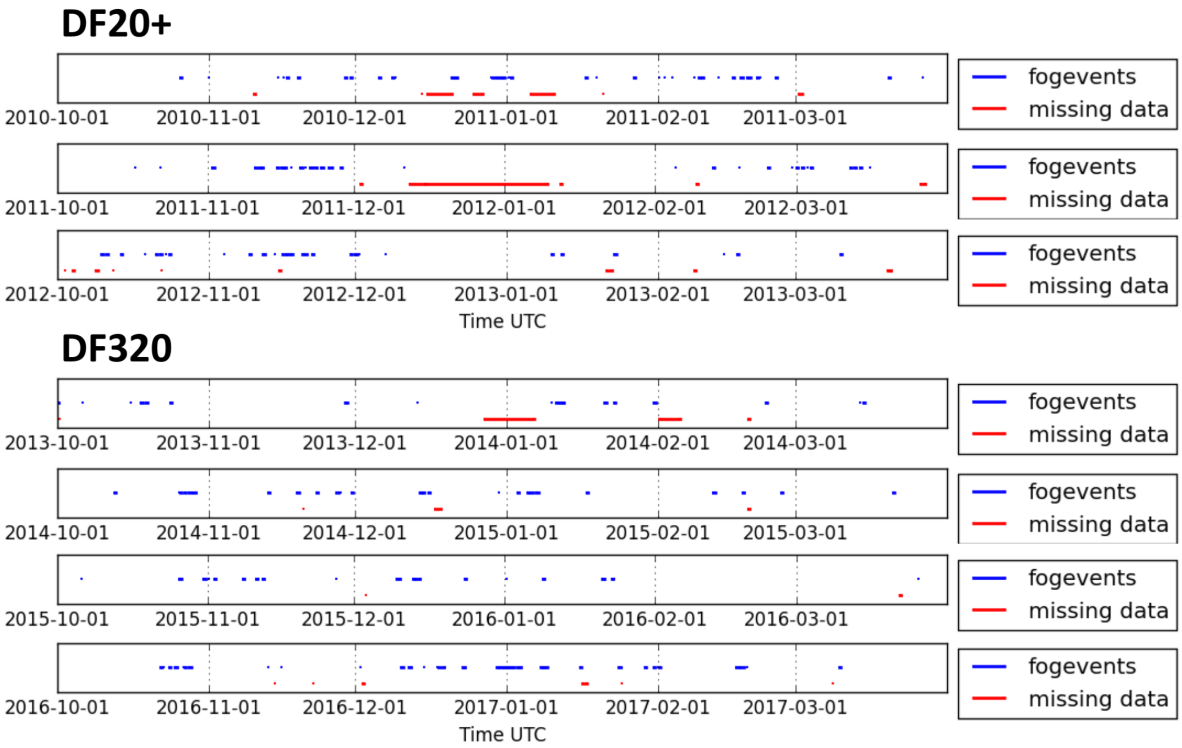

Figure 2.2: Fog events detected during seven winter seasons by visibility. The fog events are marked in blue, while red lines indicate periods where visibility data are missing. For the first three winter seasons, we use the visibility meter DF20+ and for the last four DF320 (see Table 2.1).

are below 1 km in a 10-min block, it is considered a fog block. No distinction is made between fog and other phenomena that could reduce the visibility to below 1 km; however, the only other possibility is heavy rain, since sandstorms, snowstorms or extreme haze does not occur at SIRTA. Most of the fog events are observed by the ceilometer, which confirms that a cloud base is present. Fog events are defined using a 3-of-5 rule similar to the algorithm of Tardif and Rasmussen (2007), but with 10-min blocks rather than hourly measurements. A positive construct is defined as a sequence of 5 blocks where the middle block and at least 2 others are fog blocks. A negative construct is defined as a sequence of 5 blocks where the middle block is a fog block, but less than 2 of the others are. A fog event begins with the first fog block within a positive construct. It ends when a negative construct or 3 consecutive non-fog blocks are detected; the end of the fog is then set to the last fog block in the previous positive construct. After detecting fog events in this way, we merge neighbouring events that are closer than 60 min. Finally, events shorter than 60 min are discarded.

This fog detection algorithm identifies 250 fog events in the period 1 Oct 2010 – 30 Sept 2017, of which 218 occur in the winter half-year (October to March). In the period 1 October 2013 – 30 September 2017, which is the main focus of the thesis, there are 129 fog events. 114 of these have data from both the cloud radar BASTA and the MWR HATPRO. Figure 2.2 shows the occurrence of fog events during the seven winter seasons. It is clear that the fog events are not evenly distributed, but often occurring in clusters lasting up to a week. This clustering is probably related to periods where synoptic weather conditions are favourable for radiation or stratus-lowering fog formation. Unfortunately, visibility data are missing in some extended periods, especially during the mid-winter of the two first seasons (Fig. 2.2), so that we likely are missing some fog events.

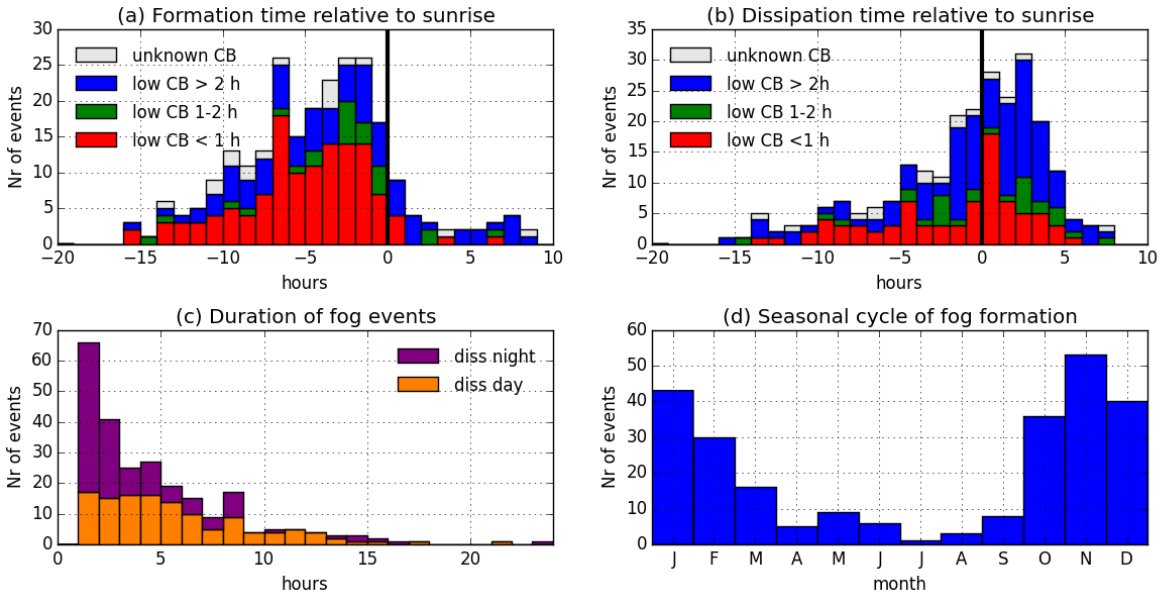

Figure 2.3: Fog events detected from 1 Oct 2010 to 30 Sept 2017: (a) Time of formation and (b) time of dissipation relative to sunrise. The different colours mark how long a cloud base is present below 400 m before formation (in a) and after dissipation (in b), ignoring cloud absence lasting less than 30 min. For some events it is unknown, due to missing ceilometer data. (c) Duration of the fog events, for those dissipating in night and in day. (d) The number of fog events forming in each month.

Figure 2.3a shows the distribution of fog formation time relative to sunrise among the 250 events. The colour classification corresponds to the time that a low cloud base is present before fog formation time (for detection of cloud base, see section 2.3). The fog events for which it is 2 h or more can be considered as stratus-lowering fog events (83 events), while the others are likely radiation fog events (150 events). Fog most frequently forms in the last 5 hours of the night (Fig. 2.3a), which is consistent with previous studies of radiation fog (Tardif and Rasmussen, 2007; Dupont et al., 2016), because radiative cooling accumulates throughout the night. There are also a few cases of formation after sunrise, but these are mainly due to stratus-lowering. Dissipation is most frequent around sunrise or up to 4 h after sunrise (Fig. 2.3b), as expected for radiation fog and stratus-lowering fog (Tardif and Rasmussen, 2007). There is also an important number of fog events which dissipate at night. These are significantly shorter in duration than those dissipating in the day: while more than half of the fog events dissipating at night last less than 3 h, the same holds true for only a quarter of those dissipating in day (Fig. 2.3c). Figure 2.3b also distinguishes the events where a low cloud remains for more than 1 h and more than 2 h after dissipation. It is common that a cloud remains for at least 2 h (at least half of the events), indicating that the fog usually dissipates at ground level prior to the complete dissipation of the cloud. This dissipation after sunrise by lifting of cloud base is also the behaviour found in several LES studies (e.g. Nakanishi, 2000; Bergot, 2013; Mazoyer et al., 2017). Finally, Fig. 2.3d shows that there is a strong seasonal cycle in the occurrence of fog, with most of the events in October–February, which is typical for northern Europe (section 1.1).

Figure 2.4 shows the variability of the surface meteorological variables during the fog events. The visibility usually reaches a minimum value in the range 100–300 m (Fig. 2.4b), but with important duration of higher visibilities (Fig. 2.4a). The temperature has a large range of variability, with some events warmer than 15 °C and several events with temperatures below 0 °C, while most of the events

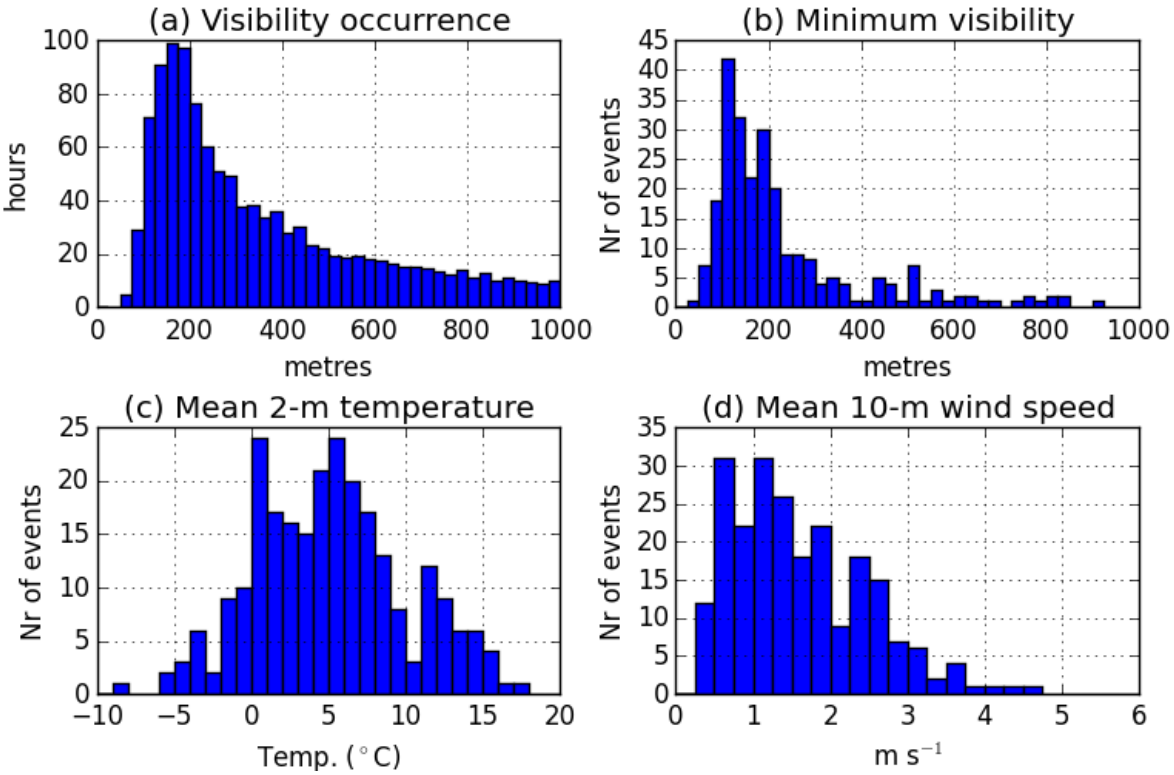

Figure 2.4: Surface meteorological conditions during the 250 fog events observed during Oct 2010 – Sept 2017 (based on 10-min blocks within each fog event): (a) duration of 10-min median visibility during all fog events (excluding blocks with visibility above 1 km); (b) minimum value of the 10-min median visibility in each fog event; (c) mean temperature during each fog event; (d) mean wind speed (from sonic anemometer at 10 m) during each fog event.

have temperature in the range 0–10 °C (Fig. 2.4c). The 10-m wind speed (Fig. 2.4d) is usually below 3 m s^{-1} with a few events having higher wind speed (up to 5 m s^{-1}). This is in agreement with previous studies finding that radiation fog typically forms when wind speeds is below 3 m s^{-1} (e.g. Menut et al., 2014), and the average values of 1.5 and 1.8 m s^{-1} during radiation fog and stratus-lowering fog, respectively, found by Dupont et al. (2016).

2.3 Cloud base and top

The cloud base height (CBH) is detected using the ceilometer. Following Haeffelin et al. (2016), it is set to the first gate in the profile where the attenuated backscatter signal exceeds the threshold of 2 $\cdot 10^{-4}$ m^{-1} sr^{-1}. The visibility at 3 or 4 m is used to detect when the CBH is at the surface (fog): when the visibility is less than 1 km, the CBH is set to 0 m. While the ceilometer is excellent for detecting the base of the cloud, since its laser beam interacts very strongly with droplets, the rapid attenuation of the signal means it cannot observe the whole cloud profile. Here the cloud radar BASTA comes of use. By using microwave radiation, the signal interacts only weakly with the clouds and is able to penetrate even thick clouds to give a full atmospheric profile of cloud occurrence.

The backscattered signal from hydrometeors which are hit by the cloud radar beam increases strongly with the size of the particle. When observing liquid droplets, the backscattered power is

proportional to the sixth power of the diameter[1] (Rogers and Yau, 1989). The range-corrected signal received by the cloud radar can therefore be used to estimate the radar reflectivity, defined as:

$$Z = \int_0^\infty n(D) D^6 dD \tag{2.1}$$

Z has units of $\mathrm{mm}^{-6}\ \mathrm{m}^{-3}$, but is usually given in dB scale, with unit $\mathrm{dBZ} = 10 \cdot \log_{10}(Z)$. The cloud radar BASTA retrieves this product, assuming the target are cloud droplets. The values of Z are studied in section 2.4.2. For ice clouds, a similar relationship holds, but the signal is slightly weaker for similar sized particles due to ice having a smaller refractive index than water (Rogers and Yau, 1989).

To detect the cloud top height (CTH), we use the automatic signal detection analysis of the cloud radar software, which is based on the signal-to-noise ratio (Delanoë et al., 2016) and evaluates whether each measurement is good signal or noise. In a 10-min block, if at least half the measurements at a radar gate is considered good signal by this analysis, that gate is assumed to have a cloud signal. Searching upwards from the detected CBH, the CTH is set to the base of the first gate without cloud signal, provided that the following 2 gates do not have cloud signal either, and that a cloud signal was detected in the gate below. Four examples of the detection of cloud base and top are shown in Figs. 2.5–2.8.

Since the backscattered signal increases with the particle diameter in the sixth power, the signal from clouds containing only small droplets may be too weak to be detected by the cloud radar. Due to the dispersion of the radar beam, the sensitivity threshold (i.e. the lowest value of Z that can be detected) increases proportionally with the square of the range (i.e. the distance between the cloud radar and the target), which means an increase of 6 dBZ for every doubling of the range. The sensitivity at 1 km range of the cloud radar prototype operating at SIRTA until 2016 (BASTA-SIRTA) is about -27.5, -32, -38 and -41 dBZ with the 12.5-m, 25-m, 100-m, and 200-m modes, respectively, although it may vary with the atmospheric conditions (Delanoë et al., 2016). However, from October 2016 to June 2017 a more sensitive prototype was deployed (BASTA-MOBILE), and from June 2017 BASTA-SIRTA was again deployed but with an improved sensitivity similar to that of BASTA-MOBILE. The improvement in sensitivity is at least 10 dBZ (Delanoë et al., 2016).

The 12.5-m mode of the cloud radar is used for cloud top detection, because it has the highest vertical resolution and the smallest blind-zone. Nevertheless, the 3 lowest gates cannot be used, and the following 2 gates almost always have some signal even if there is no cloud, due to the noise effect in the 3 first gates actually extending to a lesser extent into these next gates, making it hard to automatically distinguish a weak cloud signal from the instrumental noise (see examples in Fig. 2.5a, Fig. 2.7a). Therefore, the estimated fog top has a lower limit of 60–80 m when retrieved by the cloud radar. However, we may use the visibility meter at 20 m to determine whether the fog top is below 20 m or not. If the median visibility measured at 20 m is higher than 1 km while fog is detected below, we know that CTH $<$ 20 m. In these cases, CTH is set to 10 m (in case of cloud base detected at 7.5 m, it is set to 14 m). An example is the early stages of the fog on 27 Oct 2014, when the visibility at 20 m stays well above 1 km while the 4-m visibility shows periods of fog (Fig. 2.5d). The cloud radar signal may sometimes also detect signals which are not cloud, such as after fog dissipation on 27 Oct 2014; after 9:30 UTC it is clear from the ceilometer that there is no cloud below 500 m (Fig.

[1]For raindrops that are not much smaller than the cloud radar wavelength (3 mm), this power-law is not valid, although the signal still increases with drop size

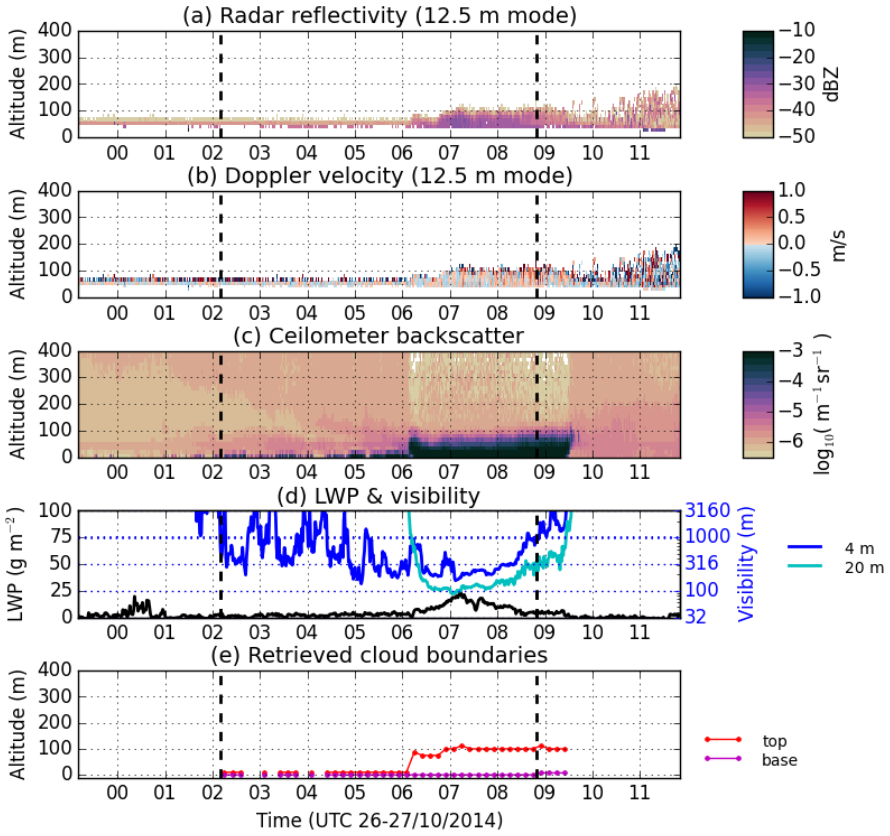

Figure 2.5: Time series of the fog event on 27 Oct 2014. Vertical lines mark fog formation and dissipation times (see section 2.2). (a) The profile of radar reflectivity (Z) and (b) Doppler velocity from the cloud radar (showing only data remaining after noise filtering), (c) the attenuated backscatter of the ceilometer, (d) LWP retrieved by the MWR (see section 2.5.1) and visibility at 4 m and 20 m, and (e) the retrieved CBH and CTH.

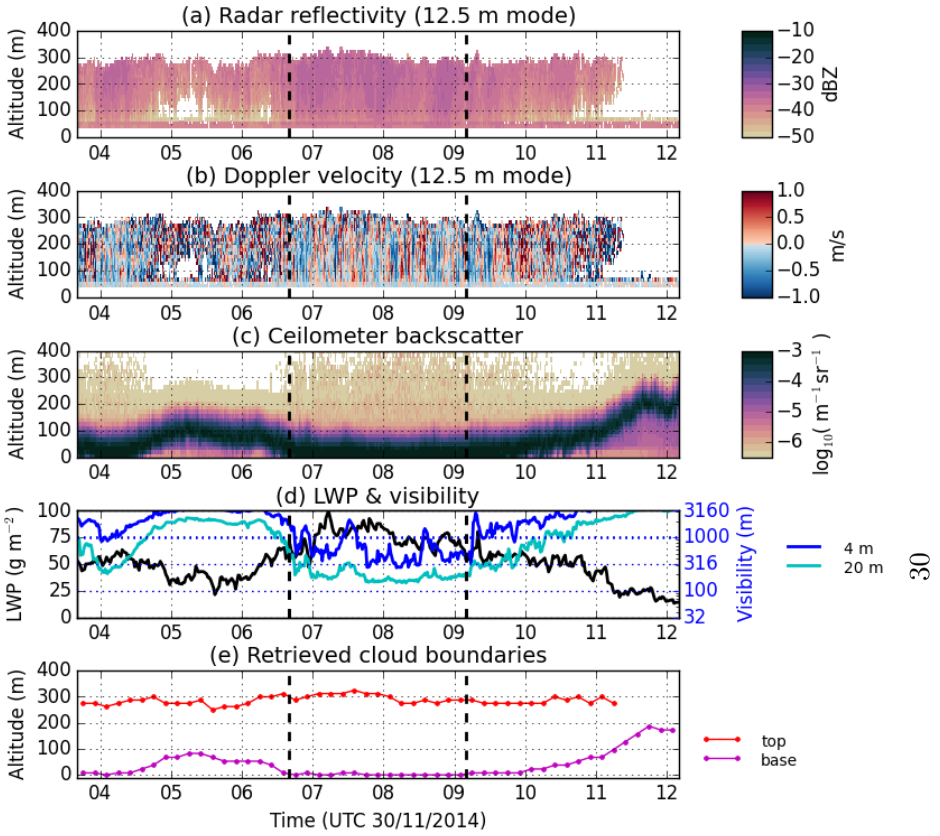

Figure 2.6: Time series of observations and retrieval of cloud boundaries for the fog event on 30 Nov 2014. See Fig. 2.5 for a further explanation.

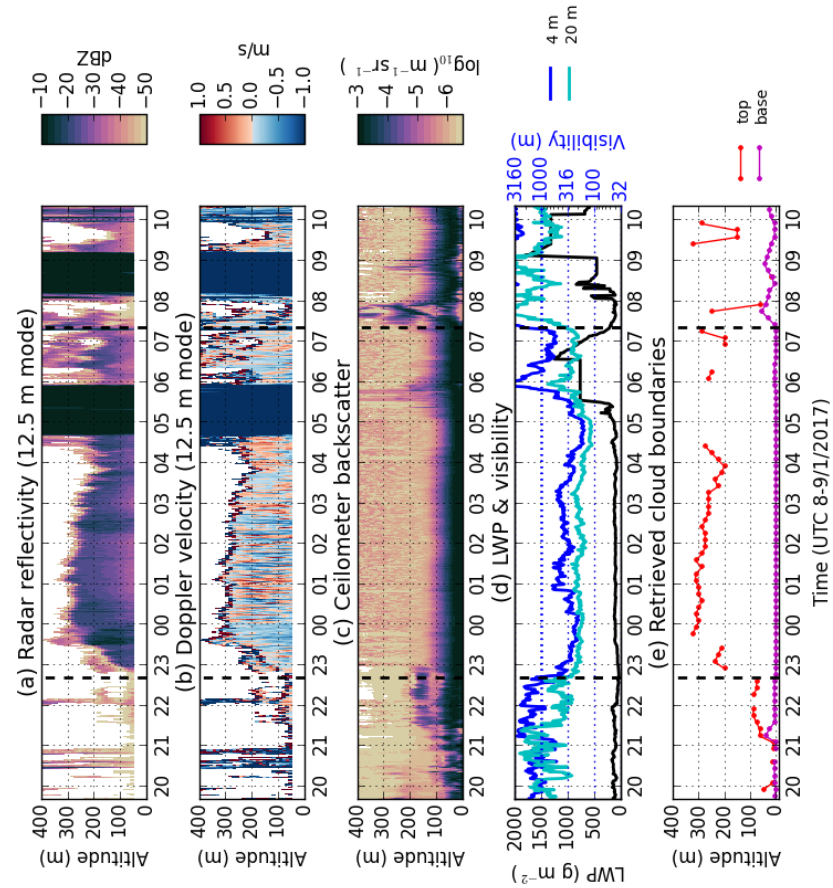

Figure 2.8: Time series of observations and retrieval of cloud boundaries for the fog event on 8-9 Jan 2017. See Fig. 2.5 for a further explanation.

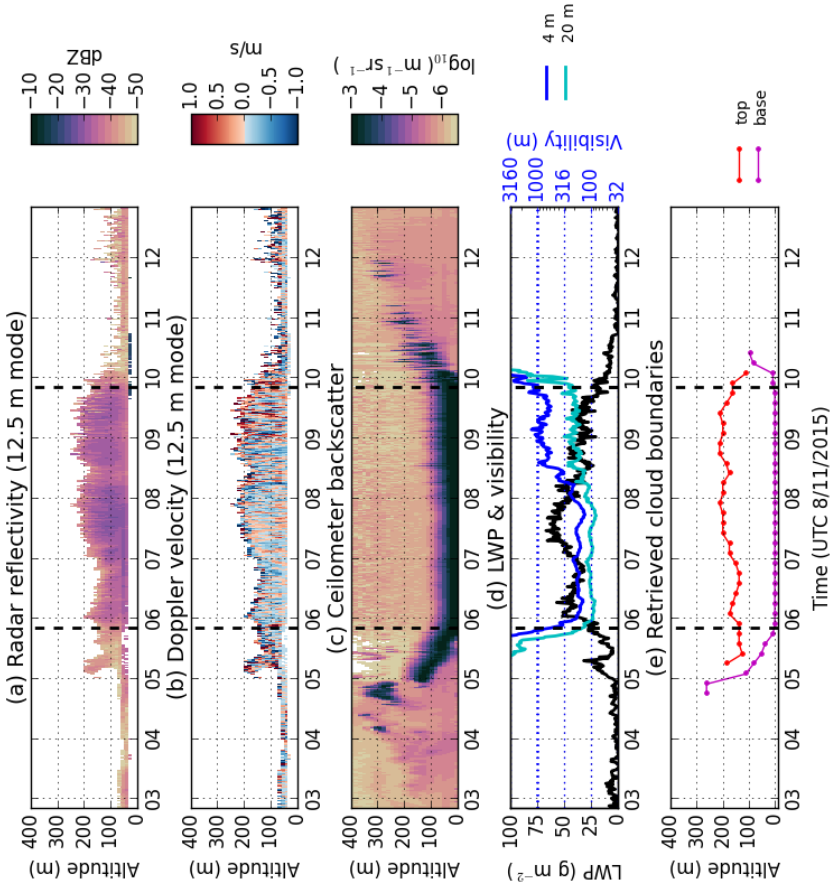

Figure 2.7: Time series of observations and retrieval of cloud boundaries for the fog event on 8 Nov 2015. See Fig. 2.5 for a further explanation.

2.5c), but the cloud radar still observes a signal up to 200 m (Fig. 2.5a). A similar behaviour can be observed on 8 Nov 2015 after 10:30 UTC (Fig. 2.7ac). It is therefore important to have the ceilometer to determine whether or not there is a cloud. it also occurs that the cloud radar is not able to detect the low stratus cloud. An example of this is on 30 Nov 2014 (Fig. 2.6), when the fog base lifts from the surface around 9 UTC and the stratus base gradually ascends over the next hours, which can nicely be tracked by the ceilometer (Fig. 2.6c). The reflectivity is relatively weak (<-35 dBZ) and it weakens as the cloud lifts, indicating that the cloud droplets are getting smaller (Fig. 2.6a). The cloud radar signal stops right after 11 UTC, but the ceilometer indicates that there is still a cloud, and also the MWR detects an important liquid water path (Fig. 2.6d). Likely the droplets are too small to create a signal to be detected by the cloud radar. Thus, the increased sensitivity is important to be able to detect the vertical extent of fog and low stratus.

The cloud radar signal decreases gradually with height at the cloud top, indicating a transition from cloud to clear air by gradual decrease of the droplet sizes (panel (a) in Figs. 2.5–2.8). The detected CTH therefore depends on the sensitivity of the cloud radar. Due to the improvement in sensitivity from October 2016 (going from the prototype BASTA–SIRTA to the prototype BASTA–MOBILE), a higher CTH will be retrieved with BASTA–MOBILE than with BASTA–SIRTA for the same cloud. As an example, the fog on 8–9 Jan 2017 (Fig. 2.8) includes a thin layer of reflectivity of below -40 dBZ (Fig. 2.8a), which would not be observed with BASTA-SIRTA; the fog top on 30 Nov 2014, which is similarly thick, does not have such a layer (Fig. 2.6a). This is not only an effect we get due to a change of the cloud radar components, though, since the sensitivity is also a function of altitude. The thin fog on 27 Oct 2014 also has a gate or two with Z < -40 dBZ when it is 100 m thick (Fig. 2.5a). Thus, the cloud-top detection will underestimate the CTH increasingly with altitude, and the effect may be a few tens of metres. During the fog on 9 Jan 2017 there are 1–3 gates, i.e. a ≈25-m thick layer, with Z < -40 dBZ (Fig. 2.8a). However, it is possible that some of these gates are in reality dominated by noise and therefore that the CTH is overestimated. An indication of this is the very strong positive and negative values in the Doppler velocity in the uppermost gates (Fig. 2.8b), which is a typical pattern of the background noise (Delanoë et al., 2016). This layer, of seemingly retained noise, is not as prominent in the other examples, and it indicates that the BASTA-MOBILE prototype has a less strict algorithm for removing noise. Thus, the CTH detection can be sensitive both to the sensitivity of the cloud radar and to the noise detection technique.

In the presence of rain (falling from a higher cloud), the raindrops will dominate the cloud radar signal, and it is therefore impossible to detect the cloud top with the cloud radar. To detect rain presence, a threshold in the Doppler velocity of -0.5 m s^{-1} is used. If, during the search for the cloud top, the average Doppler velocity at a gate is more negative than this threshold, the rest of the profile is discarded and no cloud top is found. An example of rain during fog is shown for 9 Jan 2017: Between 4:30 and 6 UTC, no information about the cloud droplets or the fog top can be retrieved due to the presence of the rain falling from a higher cloud, which gives a very strong reflectivity (>-10 dBZ, Fig. 2.8a). The very strongly negative Doppler velocity (<-1 m s^{-1}, Fig. 2.8b) shows clearly that the signal is rain.

Figure 2.9a shows the statistics of CTH retrieved during all the fog events of 2013–2017 when the fog cloud is touching the surface. Out of 579 h, 52 h is fog thinner than 20 m. A further 77 h has CTH < 100 m. The exact value of CTH for these periods is uncertain due to the above mentioned limitation of the cloud radar. CTH in the range 100–300 m occurs 317 h with uniformly distributed

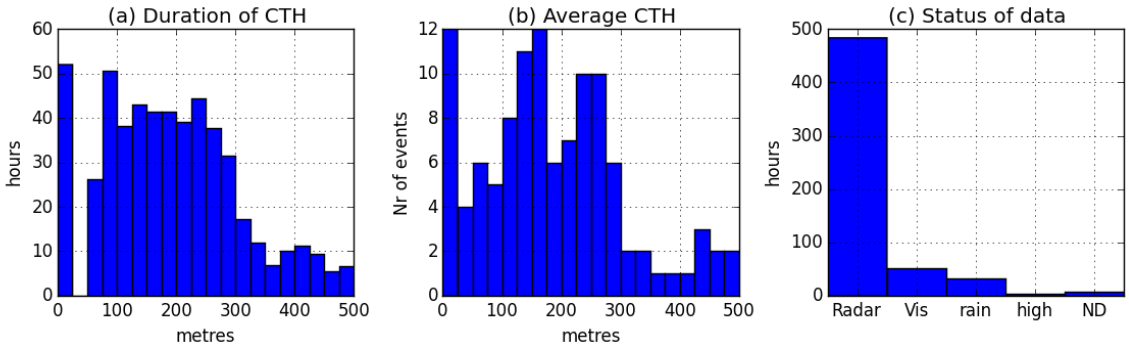

Figure 2.9: Statistics of cloud top height (CTH) retrieved for the 114 fog events in the period 1 Oct 2013 to 30 Sept 2017 for which cloud radar and MWR data are available. (a) The total number of hours with different CTH values during all the fog events, (b) the mean CTH from formation to dissipation in each fog event, and (c) Occurrence of the status of the CTH retrieval during all the fog events (see text for explanation). Periods within the fog events when the cloud does not touch the surface have been excluded, which concerns about 24 h.

occurrence. There is a marked drop-off in occurrence for CTH beyond 300 m, with only 78 h of CTH in 300–500 m, and 12 h of CTH $>$ 500 m (not shown). The mean CTH (Fig. 2.9b) shows the same patterns as the CTH duration. 12 of the events have mean CTH below 25 m, which indicates that all or a large part of the event is thinner than 20 m. Out of the 114 events, 2 fog events have a higher mean CTH than 500 m (577 m and 694 m), and for 1 event no data could be used (due to rain).

Figure 2.9c shows the frequency of each status of the CTH retrieval. 92.5 % of the time, the CTH is retrieved using the cloud radar ("Radar") or using visibility at 20 m ("Vis"). When the CTH cannot be determined, it is most often due to the presence of rain ("rain", 5.7 % of the time). It is only rarely because of missing data (in the cloud radar or ceilometer, "ND", 1.2 % of the time). We also do not search for the cloud top higher than 1 km, which causes a few occurrences of undetermined CTH when the fog is very thick ("high", 0.6 % of the time). All in all, the periods with missing CTH, mainly due to rain, cover only a small part of the fog events.

2.4 Fog microphysics

2.4.1 In situ observations at 4 m

The fog monitor FM-120 measures the droplet concentration in 30 size bins in the range 2–50 μm and therefore allows a detailed study of the fog DSD. However, since the FM-120 is deployed only at 4 m, it can only give the DSD at this level. Both the number and sizes of the droplets may change with altitude, due to various processes such as adiabatic cooling in updrafts, dry intrusions at the top, droplet aggregation and sedimentation. It is nevertheless useful to study the DSD near the surface, since it is here that the fog deposition takes place.

As is common for granulometers, the FM-120 is calibrated with respect to the measured sizes, but not to the number concentration due to various factors (Guyot et al., 2015). Additionally, in some cases the measurements may be invalid due to pump or laser diode problems. Before using the FM-120 data for a given fog event, a quality control and normalisation using the visibility from DF320 is therefore performed. From the DSD measured by FM-120, we can calculate the extinction coefficient

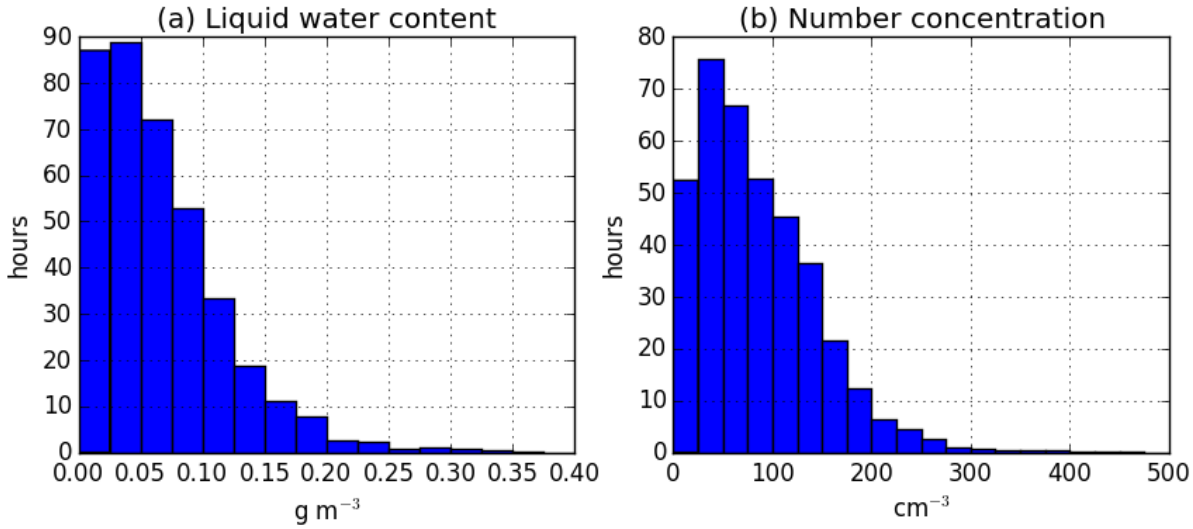

Figure 2.10: Occurrence of (a) LWC and (b) N_c observed by FM-120 at 4 m during the 64 fog events where the FM-120 data could be used, after visibility normalisation.

by summing over the contributions from all the 30 size bins:

$$\alpha_{ext,FM} = \sum_{i=1}^{30} N_i Q_{ext} \frac{\pi}{4} {D_i}^2 \tag{2.2}$$

where N_i and D_i are the number concentration and diameter, respectively, of the droplets in each size bin. For visible light, we may estimate $Q_{ext} = 2$ for droplets. The extinction coefficient from DF320 is calculated from Koschmieder's equation (see Eq. 1.2):

$$\alpha_{ext,DF} = \frac{3.0}{Vis} \tag{2.3}$$

The extinction coefficients are averaged in 5-min blocks from formation to dissipation of the fog event. Then, periods where the $\alpha_{ext,DF} < 3$ km^{-1} are discarded (visibility above fog threshold). Based on the remaining data, a linear regression slope between the 5-min averages of $\alpha_{ext,DF}$ and $\alpha_{ext,FM}$ in the fog event is calculated ($y = \alpha_{ext,FM}$, $x = \alpha_{ext,DF}$), as well as the correlation coefficient. The FM-120 measurements are considered to be valid if the correlation is better than 0.8 and the slope larger than 0.1. The FM-120 measurements (N_i) are then normalised using the regression slope. With this method, 64 fog events with reliable FM-120 data in the period Oct 2013 – Sept 2017 are identified and normalised.

Figure 2.10 shows the occurrence of N_c and LWC in all the 64 fog events with reliable FM-120 data. The LWC is less than 0.1 g m^{-3} 79 % of the time, and 46 % of the time less than 0.05 g m^{-3}, and rarely above 0.2 g m^{-2} (2 %). The droplet concentration N_c is most often around 50 cm^{-3}, but all values up to 150 g m^{-2} occur frequently. It is rarely above 200 cm^{-3} (4 % of the time). These results can be compared with the findings of Mazoyer (2016), who studied the microphysics of 42 fog events in the three winter seasons 2010–2013 at SIRTA using the FM–100, an earlier version of the fog monitor. She found that N_c had a median of 30–100 cm^{-3} (depending on fog type), with most of the data in the range 20–160 cm^{-3}, and that LWC had a median 0.02–0.03 g m^{-3} and most of the data in 0.01–0.08 g m^{-3}. While the N_c is very similar to our results, the LWC is significantly lower. This

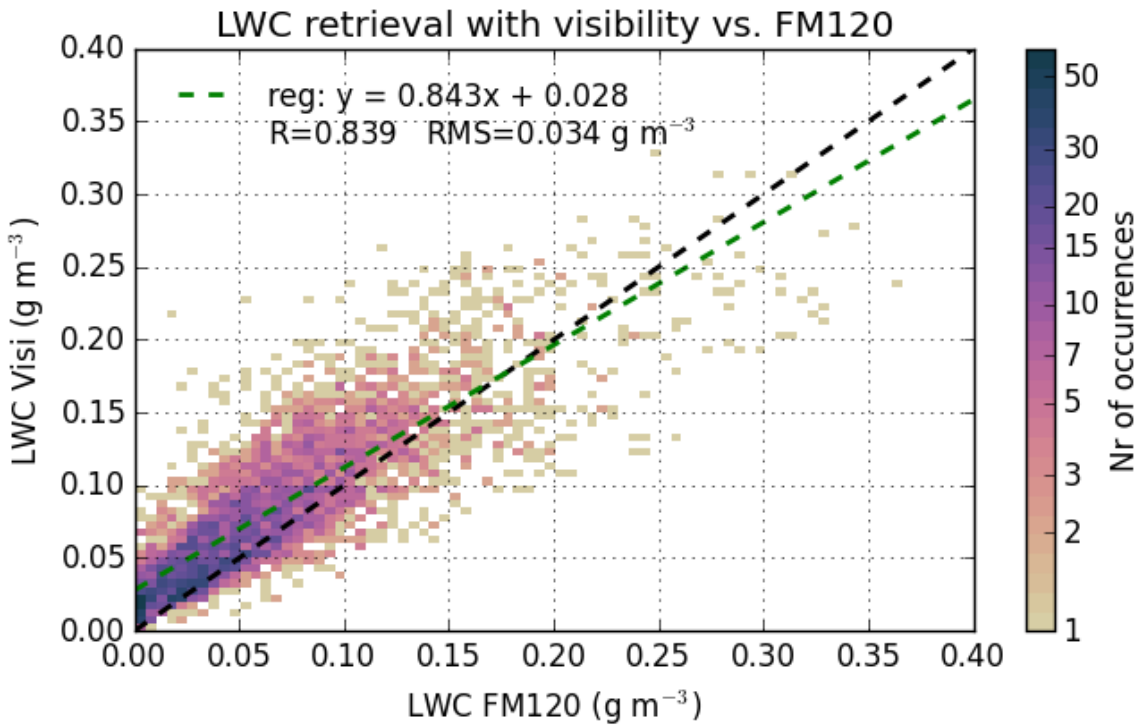

Figure 2.11: Comparison of LWC calculated from visibility using Eq. (2.4) and measured by the FM-120, both at 4 m, for 5-min averages. The data come from the 64 fog events in the period 2013–2017 with valid FM-120 data after visibility normalisation of the FM-120 data. The green dashed line indicates the linear regression on the data.

may in part be due to Mazoyer (2016) comparing events rather than all fog hours; however, when we consider the median LWC in each of our 64 events, we still get 33 of the events above 0.05 g m^{-2} and 8 above 0.1 g m^{-2} (not shown).

When detailed observations of the fog microphysics are not available, the LWC at screen level may be estimated from the visibility. One such empirical relationship is presented by Gultepe et al. (2006):

$$LWC = 0.0187 \cdot Vis^{-1.041} \tag{2.4}$$

with LWC in g m^{-3} and Vis in km. Figure 2.11 evaluates this relationship by comparing the LWC measured by FM-120 with the LWC calculated from the visibility of DF320. Although there is an important spread, there is clearly a linear relationship, which captures a large part of the LWC variability (correlation coefficient 0.84). The root-mean-square (RMS) deviation is 0.034 g m^{-3}, and the LWC is most often overestimated, especially when LWC $<$ 0.1 g m^{-3}, as is also indicated by the regression line.

2.4.2 Profiles of radar reflectivity

While the FM-120 can precisely observe the fog DSD at 4 m, it does not give information about its properties at higher altitudes in the fog. To get information about the microphysics higher up, remote sensing techniques which are able to observe the whole profile of the fog can be used. The radar reflectivity (Z) observed by the cloud radar is a function of the droplet numbers and sizes (Eq. 2.1), and it therefore may provide some information about the microphysics. In this section, the profiles of

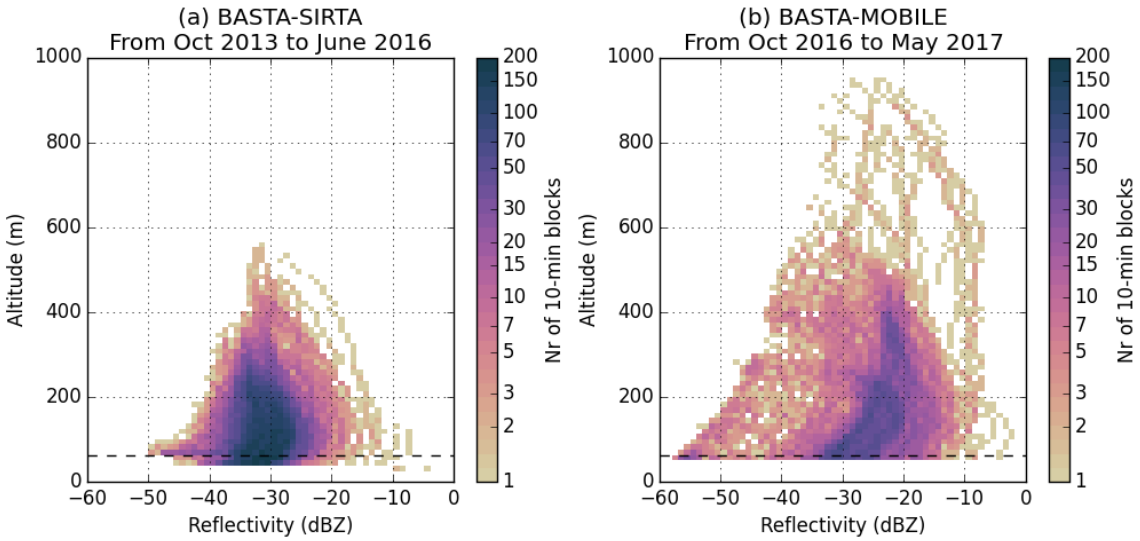

Figure 2.12: Occurrence of 10-min median reflectivity in each radar gate during all the fog events between October 2013 and May 2017 which have cloud radar and MWR data available (111 events). All 10-min blocks between formation and dissipation for which CBH=0 m and the cloud top is detected by the cloud radar are included (i.e. excluding periods of rain). (a) Fog events observed by the prototype BASTA-SIRTA (deployed until July 2016); (b) fog events observed by the prototype BASTA-MOBILE (deployed from Oct 2016 to Jun 2017). The dashed horizontal line marks the lower limit of the gates that are used for retrieval of the LWC profile (section 2.5.2).

Z are introduced, while the retrieval of LWC from Z is discussed in the following section.

Figure 2.12 shows the values of reflectivity measured during the fog events in 2013–2017 at different altitudes, separating the periods observed by the two different prototypes of the cloud radar. We see that Z is usually in the range -40 to -20 dBZ, and that the range of measured values decreases with altitude. The increase with height of the lowest measured value is due to the decreasing sensitivity with height (6 dBZ for every doubling of the altitude). The decreased range of values with height can also be explained by the smaller data sample at higher altitudes (fog is not so often thicker than 300 m, Fig. 2.9a). The signal is rarely stronger than -15 dBZ (note that periods with rain are not shown, since only blocks where the cloud top could be detected are included).

The old prototype BASTA-SIRTA (Fig. 2.12a) mainly observes reflectivity in the range -40 to -25 dBZ. The newer prototype BASTA-MOBILE (Fig. 2.12b) clearly has a larger dynamic range than the old one, measuring values from -50 to -10 dBZ relatively frequently at 200 m, while this range is only about half as large for BASTA-SIRTA. This is due to the improved sensitivity, which also allows the detection of a higher cloud top, which can possibly explain the larger amount of data in the range 400–600 m compared to BASTA-SIRTA. The values of Z that occur the most are shifted several dBZ in BASTA-MOBILE relative to BASTA-SIRTA. This difference can be attributed to the fact that the two cloud radars have not been inter-calibrated. In fact, cloud radars need to be calibrated for their retrieval to represent the physical Z in Eq. (2.1); before calibration, the logarithmic unit may have a constant offset in dBZ (Delanoë et al., 2016). The calibration is better for BASTA-MOBILE than for BASTA-SIRTA (Julien Delanoë, personal communication), which indicates that the Z measured by BASTA-SIRTA has a negative offset of a few dBZ. However, some of the differences between Fig. 2.12a and Fig. 2.12b can also be due to actual year-to-year variability, as the new prototype was only deployed for one season. The wider dynamic range in BASTA-MOBILE is probably also impacted by

Dataset	α	β	A	B
Fox and Illingworth (1997)	0.031	1.56	9.27	0.0641
Atlas (1954)	0.048	2	4.56	0.05
6 Jan 2015	0.020	1.91	7.75	0.0524
19 Dec 2016	0.049	2.06	4.32	0.0485
3 Jan 2017	0.097	2.51	2.53	0.0398

Table 2.2: Coefficients for Eq. 2.5 found by regression from observations, in two previous cloud studies, and in the tethered balloon flights which we carried out in fog at SIRTA.

the less strict noise filtering, for which we found evidence in Fig. 2.8, giving a layer of low reflectivity at fog top that may be dominated by noise. Overall, both cloud radars capture an important variability in Z, and the two prototypes observe a similar pattern of reflectivity occurrence once calibration and sensitivity difference are considered.

2.4.3 Retrieval of LWC using radar reflectivity

Several papers have studied the relationship between radar reflectivity (Z) and LWC (Atlas, 1954; Sauvageot and Omar, 1987; Fox and Illingworth, 1997), using the following empirical formula:

$$Z = \alpha LWC^{\beta} \tag{2.5}$$

with Z in mm^6 m^{-3} and LWC in g m^{-3}. Since LWC is the 3rd moment of the DSD and Z is the 6th, we might expect $\beta = 2$, if the number concentration and shape of the DSD do not change with LWC. From in situ measurements of the microphysics, Atlas (1954) found that the relationship could indeed fit with $\beta = 2$, and $\alpha = 0.048$. Later, Fox and Illingworth (1997) fitted the relationship to data from flights in stratocumulus clouds, finding $\alpha = 0.031$, $\beta = 1.56$. However, neither of these studies were carried out in fog, so it is not given that they give good results for fog.

To study this relationship in fog, we carried out balloon flights in three different fog events with the Light Optical Aerosol Counter (LOAC) (Renard et al., 2016). This instrument functions in a similar way to the FM-120, but it is much smaller, allowing it to be lifted by a balloon, and it also measures sub-micron particles down to 0.2 μm diameter. Its air pump is much weaker than that of FM-120, though, which makes the measurements more vulnerable to bias from wind. Each of the balloon campaigns lasted several hours, during which the instrument was lifted in the altitude range 0–300 m. This allows a comparison between 2-min averages of microphysical properties measured by the LOAC and the radar reflectivity retrieved by the cloud radar in the closest gate to the position of LOAC. The details are described in Dupont et al. (2018).

The resulting coefficients are shown in Table 2.2 and visualised in Fig. 2.13, together with the relationships found by Fox and Illingworth (1997) and Atlas (1954). The table also shows the equivalent coefficients A and B, which are used to calculate the LWC in g m^{-3} from reflectivity Z^* in dBZ:

$$LWC = A \cdot 10^{B \cdot Z^*} \tag{2.6}$$

($A = \alpha^{-\beta/2}$ and $B = \frac{1}{10\beta}$). As the analysis of the LOAC balloon flights was not so straightforward, due to various instrumental corrections that had to be carried out, the analysis leading to the publication of Dupont et al. (2018) was not finalised until near the end of the work with this thesis. The coefficients

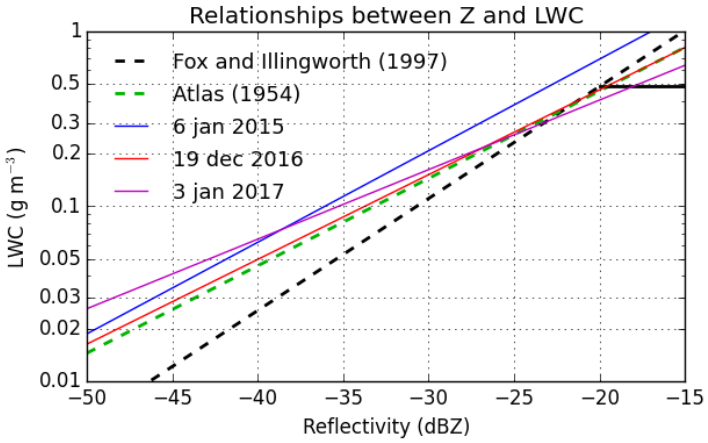

Figure 2.13: Relationships between radar reflectivity (Z) and LWC as estimated by two previous studies of cloud measurements and from three tethered balloon flights carried out by us at SIRTA during fog.

of Fox and Illingworth (1997) were therefore used for the analysis in the thesis.

In the presence of drizzle droplets, we cannot use the relationship between Z and LWC, since these droplets will dominate Z while not necessarily contributing importantly to LWC. We therefore let the LWC stop at the predicted value at -20 dBZ for all higher values of reflectivity (indicated by the black line in Fig. 2.13), as drizzle typically may occur when Z > -20 dBZ (e.g. Matrosov et al., 2004). The cut-off at -20 dBZ is also reasonable because the data of Fox and Illingworth (1997) do not cover higher values than about -20 dBZ, and our own balloon flights cover values up to -17 dBZ. We see from Fig. 2.12 that most of the time the reflectivity in fog is below -20 dBZ so that we can apply the Z–LWC relationship without cut-off.

2.5 Liquid water path

If the LWC is integrated in the vertical from fog base to fog top, we obtain the liquid water path (LWP) of the fog, in g m^{-2}. This total column of liquid water present in the fog will affect its radiative properties, and it is also important because it is a measure of how much water needs to evaporate before the fog cloud disappears. In the next chapters, the liquid water budget of the fog will be quantified by attributing production and removal of LWP to various processes. It is therefore important to quantify the fog LWP and its rate of change from observations.

2.5.1 Microwave retrieval of LWP

The MWR retrieves the LWP of the whole atmospheric column. If the fog is the only liquid cloud, the MWR thus provides a direct estimate of the fog LWP. If there are higher clouds containing liquid, the MWR retrieval will also include the LWP of these.

The uncertainty of the MWR LWP is ±20 g m^{-2} according to the manufacturer. However, we find using radiation closure that for fog forming in clear-sky conditions with LWP < 40 g m^{-2}, the uncertainty is more likely in the order of 5–10 g m^{-2} (see W17 for details). When the fog forms from clear sky, we have the advantage of being able to detect any systematic offset in the LWP, which ought to be zero in clear sky. If the pre-fog LWP bias is corrected for, the precision in the LWP retrieval during

fog will be importantly improved, since much of the uncertainty is related to incomplete knowledge of temperature and humidity profiles (Gaussiat et al., 2007), which change rather slowly with time. Nevertheless, the LWP retrieval is not precise enough to be used when the fog is very thin. When the (corrected) LWP is below 10 g m^{-2}, a retrieval based on the cloud radar and visibility, which will be described in section 2.5.2, is applied instead.

To correct for the clear-sky offset in LWP, we consider the LWP retrievals averaged in 1-h periods of clear sky. The probability that a cloud contains liquid decreases with height, due to the increased efficiency of ice nucleation processes with decreasing temperature (Rogers and Yau, 1989), and we have therefore not considered clouds above 7 km when detecting clear sky. 7 km is also the highest altitude observed by the CL31 ceilometer. To detect clear sky, the 12 μm brightness temperature ($T_{B,12}$) measurement of the MWR is applied. Since this wavelength is in the atmospheric window region, $T_{B,12}$ is expected to be low when no clouds are present below 7 km. In periods of fractional cloud cover, $T_{B,12}$ is expected to have a large variability. By comparing with the ceilometer, we find that 1-h periods of clear sky (below 7 km) can be well detected by the MWR by applying the following threshold values: mean($T_{B,12}$) $<$ -25 °C, std($T_{B,12}$) $<$ 1.5 °C, and std(LWP) $<$ 3 g m^{-2} (std means standard deviation). We thus obtain a time series of clear-sky offsets of LWP, which can be used to correct the LWP measurements for nearby fog events. Figure 2.14 shows the LWP offsets in the period October 2013 to December 2015. The offsets are mostly in the range 0–40 g m^{-2}, but in some periods they are much higher. However, neighbouring offsets tend to be relatively close to one another in their LWP value, which indicates that by using the closest offset to the fog event, we should be able to correct its offset reasonably well. It is more problematic if the fog event occurs between two offsets which are very different. This is the case for a fog event at the end of January 2014; however, its LWP value is less than 30 g m^{-2} which makes it obvious that we should use the lower offset. In October 2015, the manufacturer installed an improved software for the MWR which recalibrates better the LWP measurement in clear sky. From this time on, only insignificant offsets in clear sky are observed (in the order of 1 g m^{-2}). The clear-sky offset correction is therefore only performed for fog events until the end of October 2015.

The MWR retrieval is biased during rain, because the wet radome of the instrument perturbs the measurements (Rose et al., 2005). The data include a flag which indicates when this occurs. However, we found that this flag often marks data during fog which do not appear to be biased when there is no rain according to the Doppler velocity. We therefore instead rely on the cloud radar for detecting rain presence (see section 2.3).

To study the statistics of LWP of the fog observed by the MWR, we should be careful to consider the bias that can be introduced due to rain and clouds above. We consider that cloud (or rain) are present above the fog when 50 % of the cloud radar measurements (in a 10-min block) at a gate above fog top is considered good signal by the automatic signal analysis (similar as the method for detecting the fog with the cloud radar). For simplicity, we assume that if a signal above the fog is detected below 7 km, it may contain liquid and cause bias to the fog LWP retrieved from the MWR. However, due to the limited sensitivity of the cloud radar, we cannot rule out the possibility that there may still be undetected liquid clouds in the periods which remain. In total, during the 114 fog events which have cloud radar and MWR data, there are 3617 10-min periods, of which 546 has a cloud or rain signal detected above the fog.

Figure 2.15a shows the LWP retrieved from the MWR during all fog events for which we have

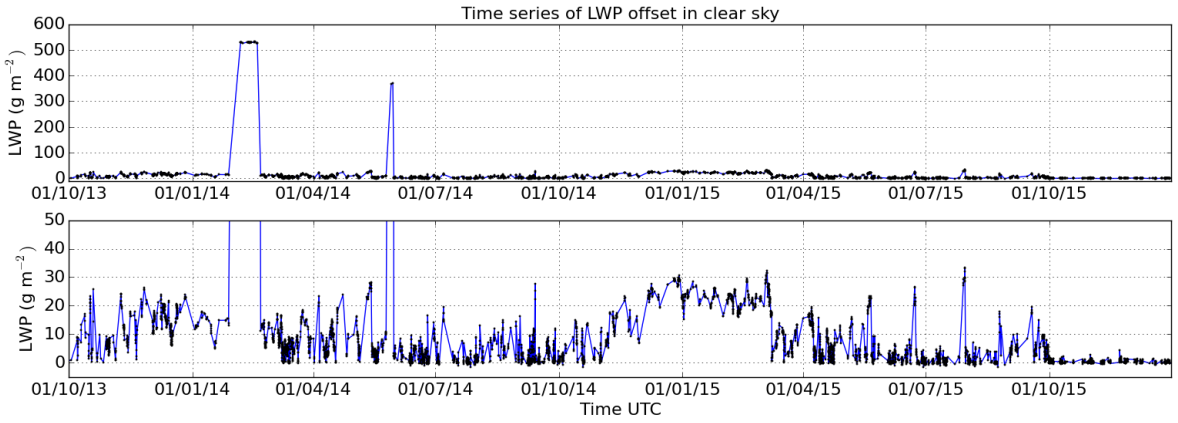

Figure 2.14: Clear-sky offsets in the MWR time series of LWP from October 2013 to December 2015.

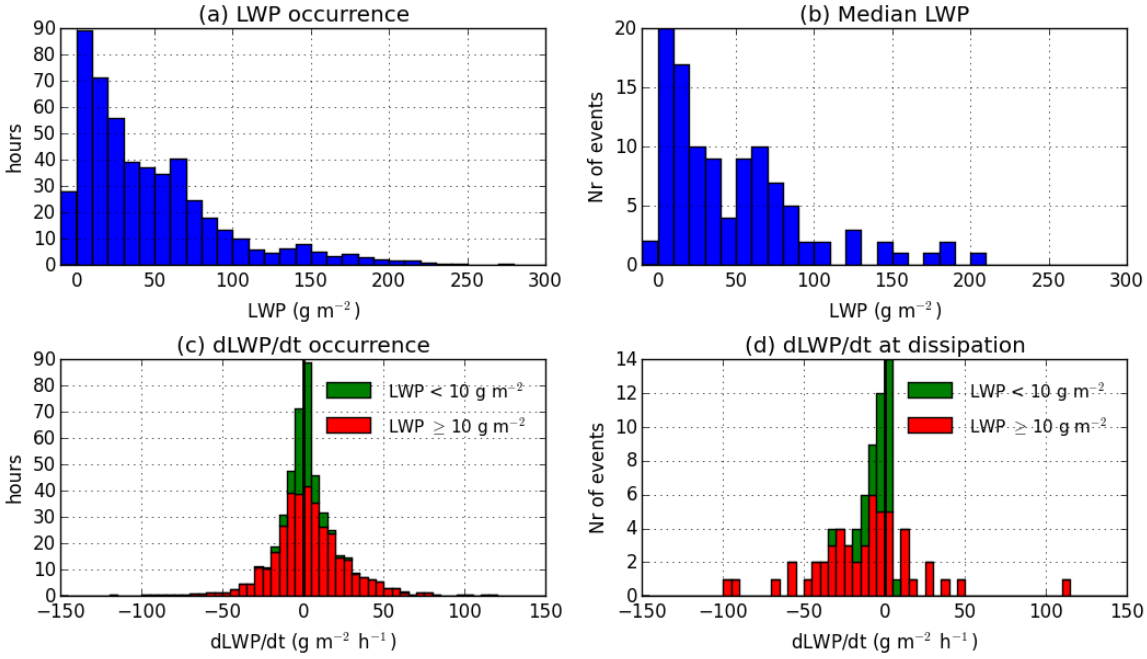

Figure 2.15: Statistics of LWP retrieved from the MWR for the 114 fog events in the period 1 Oct 2013 to 30 Sept 2017 for which MWR and cloud radar data are available. (a) The occurrence of LWP during all the events; (b) the median of LWP between formation and dissipation in each event; (c) the occurrence of rate of change of LWP, and (d) the rate of change at dissipation. In (c-d), the periods when LWP < 10 g m^{-2} are shown in a separate colour (NB: the green bars are stacked on top of the red bars). In all panels, the data affected by periods when higher clouds (or rain) are detected by the cloud radar have been excluded. Outliers which are not shown: 2 10-min periods are far outside the range in (a), and 4 in (c). In (d), there is 1 event outside the upper limit.

MWR and cloud radar data, excluding the periods with detected cloud radar signal above the fog. The LWP is nearly always less than 200 g m^{-2} (99 % of the time), and also mostly below 100 g m^{-2} (89 % of the time). The weakest values of LWP occur most frequently, which can be explained by the many thin fog events forming in clear sky without thickening during their lifetime. The LWP is 46 % of the time below 30 g m^{-2}, which we show in W17 is approximately the value of LWP where the fog becomes opaque to LW radiation. The median LWP for each event (Fig. 2.15b) shows a similar distribution to the duration of LWP.

Figure 2.15c shows the temporal rate of change of the LWP during the fog events. This quantity is calculated by first performing a 5-block running average (i.e. 50 min) on the LWP time series to remove rapid variability, and then calculating the derivative by the difference between the LWP of the block before and after the current block. Thus, each value is based on the LWP of 7 consecutive blocks. The value is excluded if a cloud signal is detected above the fog in any of these 7 blocks, which eliminates 743 of 3617 blocks. This distribution of the rate of change of LWP on hourly scale indicates that the balance between the processes affecting fog LWP should normally add up to a rate of change in the range $\pm$30 g m^{-2} h^{-1} (86.5 % of the time). As could be expected, weak changes in LWP occurs predominantly when the fog is very thin (green area). When these periods are not considered, the values of $\pm$10 g m^{-2} h^{-1} occur with almost uniform frequency.

Figure 2.15d shows the rate of change in the last time block before dissipation, which is available for 78 events (in the remaining 36 events, a cloud above or rain perturbs the retrieval). We note that the LWP decreases at dissipation in the majority of the fog events (67 %) and that the distribution of dLWP/dt at dissipation is clearly shifted towards negative values relative to the distribution for all of the fog (Fig. 2.15c), which is nearly centred at zero. This is what is expected from the hypothesis that dissipation is linked to a reduction in the LWP from evaporation of the fog. However, there are also many cases where LWP does not change significantly or even increases at dissipation (14 % of the events have increase above 10 g m^{-2} h^{-1}). Many of the events with weak LWP tendency at dissipation are events where LWP is already less than 10 g m^{-2} h^{-1} (green area in Fig. 2.15d), but also half of the events with higher LWP than this do not have a strong negative LWP tendency at dissipation (dLWP/dt $>$ -10 g m^{-2} h^{-1}). Although some of the cases may have increasing LWP at dissipation due to undetected clouds above the fog top, the frequent occurrence of LWP tendency close to zero or positive at dissipation indicates that the fog dissipation is not merely a question of the fog losing LWP, but could also be a vertical displacement of the liquid layer. The relationship between LWP and CTH at dissipation will be explored further in chapters 4 and 5.

Figure 2.16a shows the LWP as a function of geometric thickness (i.e. CTH). Following the main cluster of points, the LWP increases more than linearly with the thickness, indicating that the vertical mean LWC (LWP divided by CTH) increases with fog thickness. This is expected for a convective layer, since the saturated plumes will increase their LWC as they rise higher by adiabatic cooling (e.g. Brenguier et al., 2000). The mean LWC is in 0.1–0.3 g m^{-3} 61 % of the time, with peak occurrence around 0.2 g m^{-3}. For fog thicker than 100 m, mean LWC less than 0.1 g m^{-3} occurs only 7 % of the time (Fig. 2.16c). This is much higher than the LWC $<$ 0.1 g m^{-3} typically measured at 4 m by the FM-120 (Fig. 2.10a), which is consistent with an important increase of LWC with height. We also note the much smaller values of mean LWC for fog thinner than 100 m at 4 m (Fig. 2.16b)[2] relative

[2]Note that Figure 2.16b has higher uncertainty than Fig. 2.16c due to the cloud radar blind-zone for thin fog (overestimation of CTH) and the higher relative uncertainty of weak MWR LWP (which in particular explains the negative values)

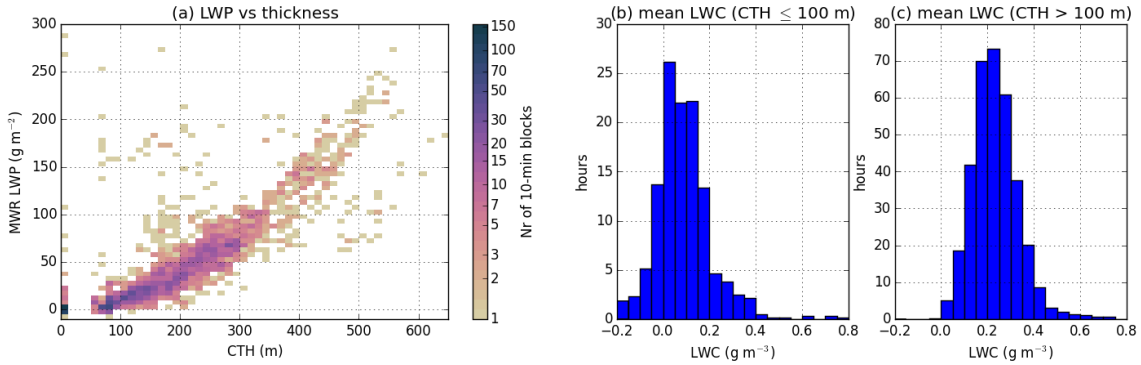

Figure 2.16: (a) LWP retrieved from the MWR plotted against fog geometric thickness (retrieved from the cloud radar). The data come from the 114 fog events in Oct 2013 – Sept 2017 which have both MWR and cloud radar data, including only time blocks when there is really fog at the surface (visibility < 1 km), no contamination of the fog signal by rain, and the cloud radar does not detect a signal between the fog and 7 km. (b-c) The vertical mean LWC, obtained by dividing LWP by the CTH (using the same data as in (a)), for periods when the fog is 100 m or thinner, and for periods when it is thicker than 100 m. Only 6 blocks are outside the plotted range in (a).

to thicker fog (Fig. 2.16c). This all indicates that LWC increases strongly with altitude in the fog. There are some outliers with high LWP and low thickness in Fig. 2.16a, which likely correspond to multilayer cloud cases when the cloud radar does not detect the cloud above. Even when discarding these outliers, the spread of LWP at a given CTH is large (e.g., LWP values from 25–70 g m^{-2} occur frequently for a thickness of 200 m), and this variability can be expected to be of importance for the fog dissipation: since convection tends to move the liquid towards the top of the mixed layer, the likelihood of the cloud base lifting from the ground should be higher if the LWP is small relative to the thickness. This hypothesis is explored further in section 5.2.

2.5.2 LWP retrieval from radar reflectivity and visibility

Although it is a powerful retrieval, the LWP of the MWR has some weaknesses, such as the confusion of the fog LWP with that of higher clouds and the high relative uncertainty for low values. Moreover, it would be useful to be able to estimate LWP also if the MWR is not available. The MWR also does not give information about the vertical profile of LWC. The retrievals of LWC using visibility (Eq. 2.4) and radar reflectivity (Eq. 2.6) are therefore interesting in order to get the profile of LWC and also an estimate of the LWP.

The profile of LWC is estimated using Eq. (2.6) in each radar gate, starting from the 6th gate (at 69 m, as the signal may be biased at the first gates), using the Fox and Illingworth (1997) coefficients (Table 2.2) and limiting to the values obtained for Z $<$ -20 dBZ (see section 2.4.3). Below gate 6, the visibilities measured at 4 m and 20 m are used to estimate the LWC, using Eq. (2.4). By vertical interpolation, the complete profile of LWC can be generated from these retrievals. Its integral gives an estimate of the LWP of the fog layer. This method has the advantage of working also when there are clouds above, except during rain.

Figure 2.17 evaluates the estimated LWP from visibility and cloud radar ("Parametrised LWP") with the MWR LWP retrieval, for the periods of fog thicker than 20 m when no cloud is detected between the fog and 7 km. The periods with the two different cloud radar prototypes are shown

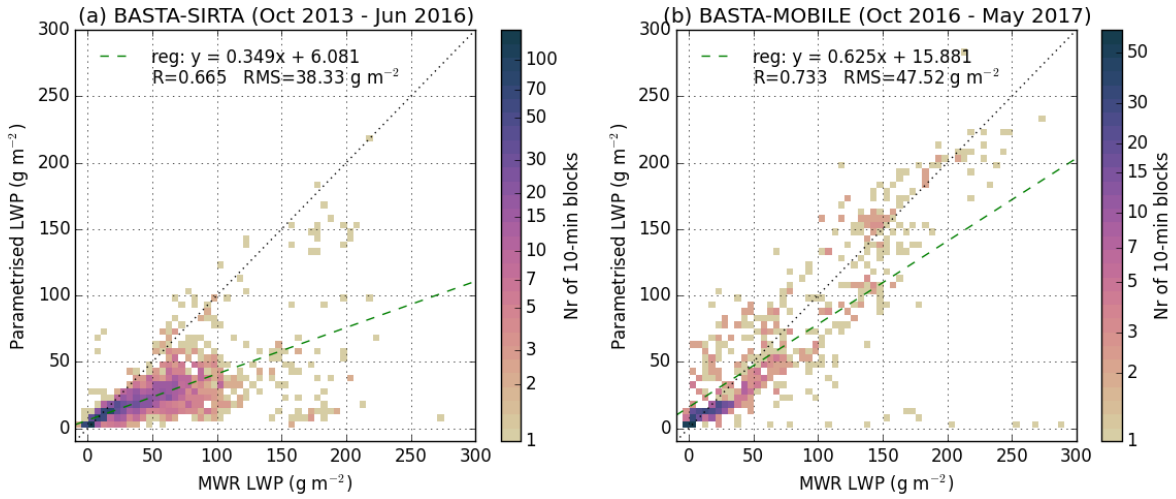

Figure 2.17: Comparison of the LWP calculated from the LWC profile retrieved by Eqs. (2.4),(2.6) with the retrieval of the MWR, including 10-min blocks in fog when no cloud is detected above the fog by the cloud radar and CTH $>$ 20 m. The periods documented by the prototypes BASTA–SIRTA (a) and BASTA–MOBILE (b) are shown separately. Very few blocks are outside the plotted range (none in (a), 4 in (b)). Also shown are regression lines (green, dashed), correlation coefficient (R) and RMS deviation between the two LWP's.

separately. The correlation is 0.67 for BASTA-SIRTA and 0.73 for BASTA-MOBILE. In the period of BASTA-SIRTA there is a systematic underestimation, while in the period of BASTA-MOBILE the data are more centred around the 1-1 line. The underestimation of BASTA-SIRTA is probably due to its lack of calibration (section 2.4.2), thereby underestimating Z and thus LWC. There are probably also some cases where higher clouds are present but undetected by the cloud radar, and this is the likely explanation for the outliers with very low parametrised LWP when MWR LWP is above 100 g m^{-2}. The better correlation for BASTA-MOBILE could be due to its higher sensitivity, which both allows higher clouds to be detected more often (fewer biased data points in MWR LWP included) and to better detect all the vertical extent of the fog (better parametrised LWP).

Figure 2.13 may indicate that using the coefficients of Atlas (1954) would give better agreement than using those of Fox and Illingworth (1997). However, this only gives marginally better agreement with the MWR LWP (not shown). As discussed by Maier et al. (2013), the Z–LWC relationship can be expected to change importantly during a fog life cycle. It is therefore not surprising that the reproduction of the MWR LWP by our parametrised profile of LWC does not have better accuracy than we see in Fig. 2.17 when using only a single pair of coefficient values in Eq. (2.6). Nevertheless, the parametrised LWP is useful in situations where LWP is weak so that the MWR LWP is not reliable. For LWP smaller than 10 g m^{-2}, the parametrisation is applied instead of using the MWR. When MWR LWP is above 10 g m^{-2}, it can be used to normalise the LWC profile from the parametrisation, i.e. increasing all values of LWC so that the integral becomes equal to the MWR LWP.

2.6 Temperature and humidity profiles

Temperature and humidity profiles, both in the fog and the atmosphere above, are required for calculating the impact of radiative processes on the fog (for details, see W17). The temperature profile in the fog is also important for the fog dynamical processes, with particularly the distinction of stable

and adiabatic fog profile (see section 1.4).

Since radiosondes are only available at about 00 and 12 UTC, the MWR is used to get continuously updated profiles of temperature and humidity from the surface to 10 km, above which the last radiosonde (8–20 km) and a climatology (above 15 km) is used, including some overlap to ensure smooth transitions (see W17 for details). However, since the MWR uses passive remote sensing, the resolution of the temperature and humidity profiles is limited. The retrieved information represents the average temperature of layers rather than specific levels in the atmosphere. The MWR has 4–5 degrees of freedom in the temperature profile, its resolution being best in the lowest 1 km or so due to the use of several scanning angles (Löhnert et al., 2009). Nevertheless, we have found that the resolution is not sufficient to capture the fog-top inversion or distinguish between a stable and adiabatic profile within the fog layer. We have therefore chosen to modify the lower part of the MWR temperature profile according to the assumption that the fog has a saturated adiabatic temperature profile. The lower boundary condition is either the temperature measurements at the 30-m mast (in the radiation calculations in W17) or the 2-m temperature (in the conceptual model in section 5.3). Above the fog top, the temperature profile is joined to the MWR profile by an inversion of 0.1 K m^{-1} (in the radiation calculations in W17, we use 0.05 K m^{-1}).

The methodology is illustrated in Fig. 2.18a for a case of thick fog on 28/10/2014 at 6 UTC. The previous radiosonde is launched 7 h earlier, before the fog forms, and shows an inversion close to the ground. This profile therefore cannot be used for the later time when the fog has formed and caused important modifications to the profile. In this case, the MWR captures a part of the decreasing temperature with height inside the fog, but the inversion is too low compared to where the actual cloud top is observed.

To evaluate the applied temperature profile method, comparisons with radiosondes were carried out. Unfortunately, the radiosondes are not launched at the times of day with the most frequent fog occurrence (late night and early morning), so that the number of radiosondes launched during fog is very limited. In addition, the launch being at Trappes rather than SIRTA means that both the cloud boundaries and the temperature may differ. A direct validation is therefore not possible, but we may validate indirectly by considering the shape of the temperature profiles at Trappes during low stratus, near in time to the fog events. We chose to consider all radiosondes launched closer than 6 h to a fog event at SIRTA during cloud-base below 130 m at SIRTA, in the period Oct 2013 – Sept 2017. These are in total 58 launches, 47 of which have both cloud radar and MWR data available. Figure 2.19 shows the temperature profile in eight of these radiosondes, compared with the profile obtained with our method. These eight sondes are the first four at night and the first four during the day starting from 28 Oct 2014.

In most of the cases, the vertical temperature gradient in the fog agrees well between the radiosonde and our adiabatic assumption, although there is a constant shift of ≈1 °C in some cases. The inversion is often displaced by several tens of metres at Trappes relative to SIRTA, though, which is probably due to the cloud-top height varying in space and time. The observed inversion at fog top is not always as sharp as our assumed 0.1 K m^{-1}, and the transition from adiabatic profile to inversion may be more gradual, such as in profile (d). Profile (b) is a very thin fog which is still stable (seen from the profile on the 30-m mast, not shown). When only the 2-m temperature is used as lower boundary condition, our method will in this case put the inversion at the fog top, while it should be directly at the surface. However, since the fog is so thin, it does not give an important impact on the temperature. Profile

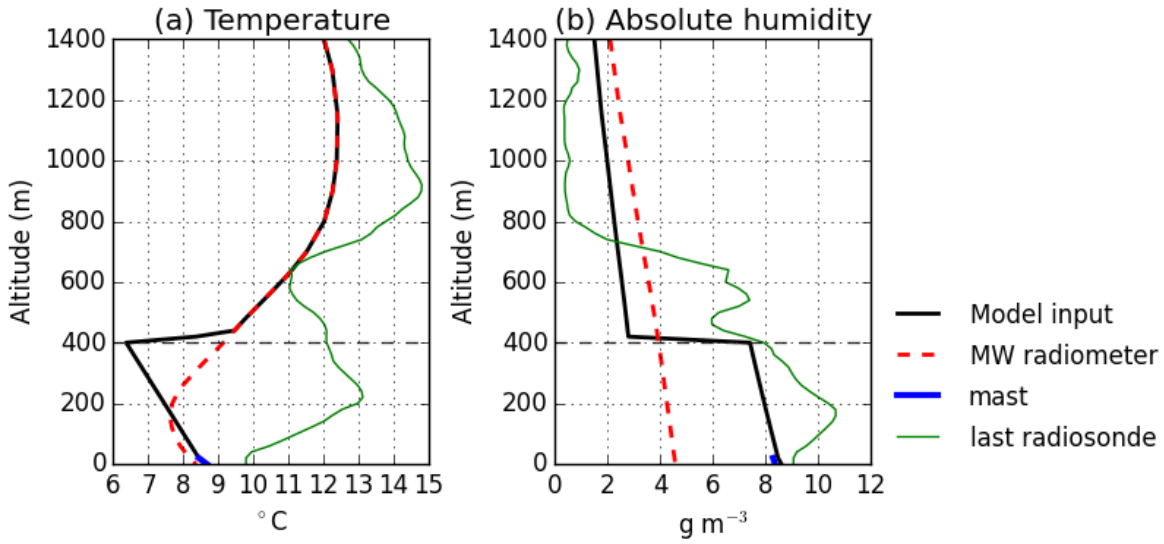

Figure 2.18: Example of the derivation of (a) the temperature profile and (b) the humidity profile in the fog and above, for 28/10/2014 at 06 UTC. The horizontal dashed line marks the fog top, observed by the cloud radar. The black line is the profile that we apply, which is a combination of ground-based in situ measurements (blue), the MWR profile (red), and assumptions on the shape of the profile in the fog (see text for details). The previous radiosonde launched at Trappes (green) (in this case at 23:15 UTC on 27/10) is only used above 8 km (except for in the LES input, when it is used for humidity starting from the fog top, see W18).

(g) is intriguing since the stratification is so weak above fog top. Here, our method does not produce any inversion at all, since the adiabatic profile has already encountered the MWR profile at the cloud top, and it reflects the very weak stability in this situation, which is confirmed by the radiosonde. The strength of the capping inversion is important for the interaction of the fog with the air above. This is investigated in W18. Even though the MWR cannot directly detect the inversion, it distinguishes well the variability in stratification above fog top, as we see from these four examples, and it also holds when all the radiosondes are considered (Fig. 2.20a).

The humidity profile from the MWR has less vertical resolution than the temperature profile, only 2 degrees of freedom (Löhnert et al., 2009). The example shown in Fig. 2.18b is very typical: the change in humidity between the boundary layer and free atmosphere cannot be resolved, and a very gradual decrease with height is retrieved, with a strong underestimation of the humidity within the fog, which should be at saturation. However, the integral is much more reliable, with an uncertainty of 0.2 kg m^{-2} according to the manufacturer. Comparisons of IWV retrieved from the MWR and calculated from the radiosonde humidity profiles, using the same 58 sondes as described above (Fig. 2.20b), gives a RMS deviation of 1.0 kg m^{-2}. The slightly higher deviations between the MWR and radiosonde than the uncertainty in the MWR can likely be attributed to the horizontal distance between SIRTA and the balloon trajectory (the two instruments do not measure exactly the same profile), the fact that the first level in the radiosonde typically is 50–100 m above SIRTA ground (see Fig. 2.19), and uncertainties in the radiosonde measurements.

Since the fog is known to be saturated with water vapour, in the radiation calculations we increase the humidity to saturation between surface and CTH, and we reduce the humidity in the atmosphere above by the same integrated amount so that the total IWV is unchanged. This is illustrated in Fig. 2.18b. In this particular case the adjustment of the above-fog humidity is rather strong, since the

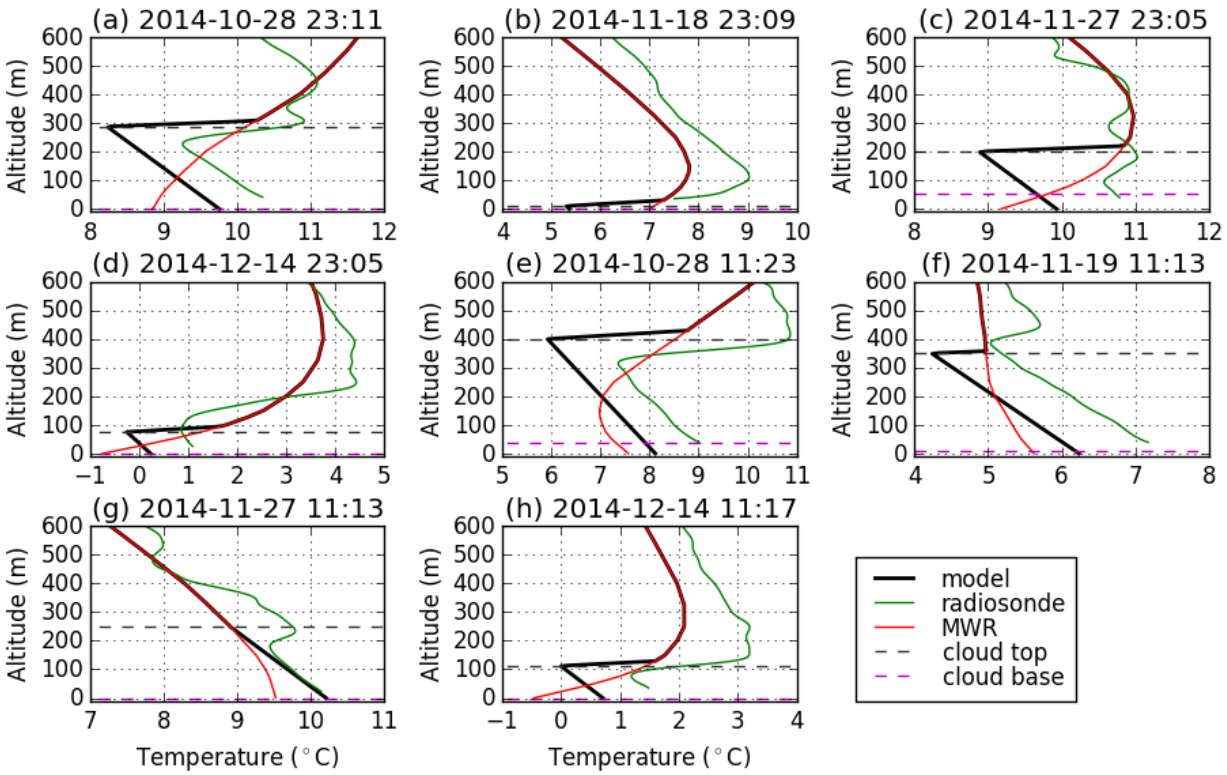

Figure 2.19: Comparison of the temperature profile obtained with our method, using the MWR, the adiabatic assumption and the 2-m temperature as lower boundary condition ("model"), with simultaneous radiosonde profiles at Trappes, for four night sondes and four day sondes released at Trappes during fog or very low stratus at SIRTA (time of the launch (UTC) is indicated above each plot). The cloud top (observed by cloud radar) and cloud base (observed by the ceilometer) are also indicated.

fog is thick and the IWV is low; in most cases the adjustment is smaller. We thus obtain a very reliable estimate of the IWV in the atmosphere above fog top, which is fortunate since the IWV is an important factor for the radiative processes of the fog (chapter 3). In the dynamical modelling of fog in W18, the humidity directly above is important, and we therefore use a radiosonde to initialise the model. This allows to take into account the layer of humid air that often is present between the fog top and the top of the residual layer, as can clearly be seen in Fig. 2.18b, although it is only approximate since both the thickness and humidity of this layer may change during the 12 h between two radiosondes.

2.7 Synthesis

This chapter explored the retrievals of fog properties from ground-based instruments at the SIRTA observatory, studying statistics of fog events in the period 2010–2017, but focussing mostly on the period 2013–2017 due to more data being available in these last 4 years. The large number of events (250 in all 7 years, 129 in the 4 years) has allowed several patterns to be revealed. The main points to retain are:

- Fog at SIRTA mainly occurs in the winter season (October – March). Fog forms most frequently in the last 5 hours before sunrise, and it dissipates most frequently around sunrise or up to 5 hour after sunrise. The fog events dissipating after sunrise statistically last longer than those

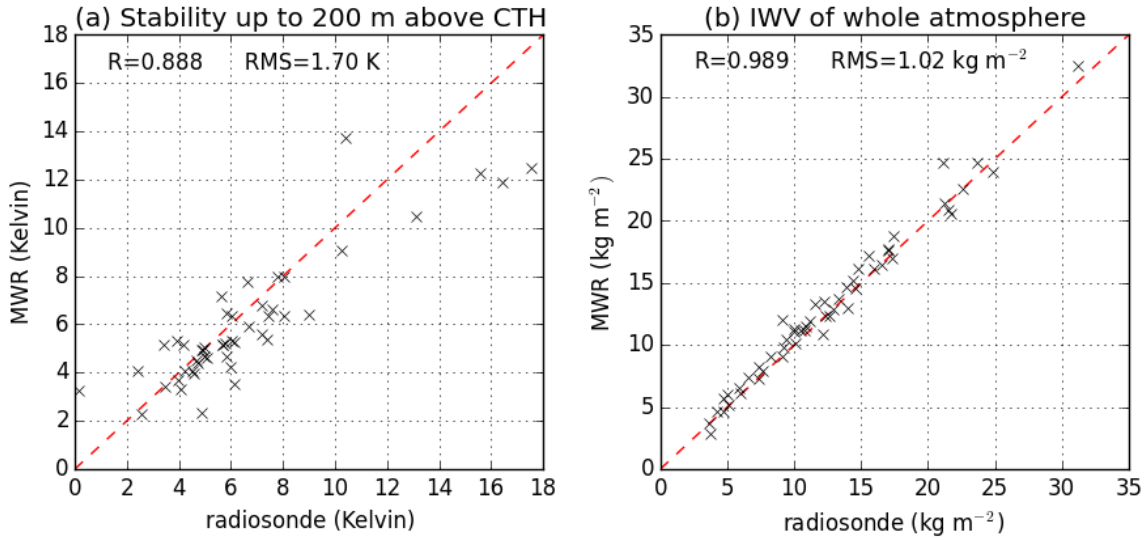

Figure 2.20: Comparison of retrievals using the MWR vs radiosondes: (a) Stability: potential temperature difference from surface to 200 m above (radar-observed) fog top; (b) full atmosphere IWV. The data represents all the radiosondes launched within 6 h of a fog event and during very low cloud at SIRTA (CBH $<$ 130 m) in the period Oct 2013 – Sept 2017 when MWR data are available, giving 52 sondes in (a) (also requiring cloud radar data) and 58 sondes in (b). The MWR retrieval of temperature 200 m above fog top is averaged over 30 min centred at the time of launch, while its retrieval of IWV is averaged in the 30 min following the radiosonde launch. The surface temperature used in (a) is the 2-m temperature (at Trappes for the radiosonde, and at SIRTA for the MWR). Correlation coefficient (R) and RMS deviations are indicated for both quantities.

dissipating in the night.

- The fog events dissipating after sunrise transition into a stratus cloud which lasts for at least 2 h in the majority of cases. Also, there is often no strong decrease of LWP at the time of dissipation. This suggests that fog dissipation can be better described as a vertical displacement of the liquid than a complete evaporation of the fog cloud.
- The cloud radar BASTA gives a reliable estimate of the CTH when it is higher than 60–80 m, except for periods of rain, which only occur 5.7 % of the time. The increased sensitivity of the prototype BASTA-MOBILE, installed from October 2016, gives improved cloud-top detection, although we should be aware of the impact that the signal-detection algorithm may have on the altitude of the cloud top. Using the cloud radar, we found that the fog thickness is usually 0–300 m (in 83 % of the periods when the cloud radar could be used), and the visibility measurement at 20 m shows that the fog is thinner than 20 m 10 % of the time.
- The radar reflectivity measured by the cloud radar is most often in the range -40 to -20 dBZ during fog outside of rain, sometimes as high as -10 dBZ. The BASTA-MOBILE prototype measures a larger dynamic range of reflectivity than the BASTA-SIRTA prototype, by at least 10 dBZ, due to its improved sensitivity.
- The LWP product of the MWR is a reliable estimate of the fog LWP in absence of rain and higher liquid clouds, as long as the LWP is not too weak ($>$10 g m^{-2}). The statistics of this retrieval show that LWP in fog is mostly below 100 g m^{-2} (89 % of the time), and nearly half the time below 30 g m^{-2} (the approximate value at which it becomes opaque to LW radiation,

see W17). The change in LWP on an hourly scale is mostly within ±30 g m^{-2} h^{-1} (87 % of the time), with a rather flat peak occurrence from -10 to +10 g m^{-2} h^{-1} for fog with LWP > 10 g m^{-2}. The processes affecting fog LWP can therefore be expected to balance to a value of ±0–30 g m^{-2} h^{-1}.

- To detect periods when the MWR retrieval of fog LWP is not reliable due to rain or clouds above, the cloud radar is needed.
- When LWP < 10 g m^{-2}, an LWP parametrisation using radar reflectivity and visibility is applied instead. The retrieval of LWC profiles in fog from radar reflectivity (Z) can be performed with a similar formula as used for stratus clouds (Eq. 2.5). We evaluated this formula using LWP closure with the MWR, obtaining a correlation between the MWR LWP and parametrised LWP of 0.67 for BASTA-SIRTA and 0.73 for BASTA-MOBILE. The LWP is systematically underestimated when using BASTA–SIRTA, while BASTA-MOBILE gives less systematic underestimation. This can be explained by the better calibration and higher sensitivity of the latter cloud radar.
- In situ measurements at 4 m indicate that predominantly the droplet concentration $N_c < 200$ cm^{-3} (96 % of the time) and LWC < 0.1 g m^{-3} (79 % of the time), with values around 50 cm^{-3} and 0.05 g m^{-3} being the most frequent. The LWC at 4 m can be roughly retrieved from visibility (RMS deviation of 0.034 g m^{-3}).
- LWC increases strongly with height, evidenced by the vertical mean LWC obtained from the MWR LWP and fog thickness, which has peak occurrence of 0.2 g m^{-3} for fog thicker than 100 m, while it is closer to 0.1 g m^{-3} for fog thinner than 100 m. The LWP thus increases more than linearly with the fog thickness, but there is important variability in LWP for a given fog thickness.
- To estimate the temperature profile, we assume a saturated adiabatic lapse rate inside the fog, above which we impose a strong inversion in order for the profile to join the MWR temperature profile. This agrees reasonably well with radiosondes in the majority of cases. The observation of the fog top from the cloud radar is essential for this retrieval, in order to know at which altitude to impose the inversion.
- The MWR retrieval of temperature profile observes the variability in above-fog stratification reasonably well, judging by the comparisons to 52 radiosondes (correlation coefficient 0.89), and the IWV is retrieved very well. These two parameters are therefore available as continuous time series to be used to study the fog processes. In contrast, the humidity profile is not sufficiently resolved to get information about the relative humidity in the layer immediately above the fog top, and we must rely only on radiosondes, available only at midnight and midday 15 km away.

Chapter 3

Radiative processes

This chapter is devoted to the study of radiative cooling and heating in fog and its impact on the fog LWP. As mentioned in section 1.4, the radiative processes are very important for the fog life cycle, especially for radiation fog. The objective of the investigations is to identify which atmospheric properties cause important variability in the impact of radiation on fog LWP budget, through variability in (1) LWP production through LW cooling, (2) evaporation from absorption of SW radiation inside the fog, and (3) radiative heating of the surface. The SIRTA observatory is a good site for studying these radiative processes since it has high-quality measurements of up- and downwelling radiative fluxes near the surface and remote sensing instruments which observe important parameters for the radiation transfer (profiles of temperature, humidity and clouds).

Section 3.1 presents the paper W17, in which the radiative processes are quantified using a comprehensive radiation code. The utilisation of such a code permits sensitivity studies which can identify the important parameters that determine the radiative impacts on the fog, and consequently how strong the radiative cooling and heating are in different situations. Section 2 in the paper presents the radiation model and how the impacts on fog LWP can be calculated from the radiative fluxes that the model provides. Section 3 gives more details on the way observations are used to provide input data to the radiation model (much of this is also covered in chapter 2 of this thesis). We then proceed to analyse seven observed fog events in section 4, showing how the differences in thickness, LWP, temperature and humidity profiles between these events cause differences in the radiative processes. In one of the seven cases, clouds appear above the fog, and the radiative effect of these clouds are studied. In section 5, we perform several sensitivity studies which systematically investigate how strongly the radiative processes change when each parameter is varied. In section 5.3 of the paper, we discuss how much the uncertainties in the input profiles, which come from remote sensing, impact the calculated radiation. This part also includes an estimate of the impact of absorbing aerosols. Conclusions are given in section 6.

After the paper, in section 3.2, parametrisations which can quantify the radiative processes directly from a small number of observations are introduced and compared with the comprehensive calculations. These parametrisations are introduced in order to quantify the radiative processes faster and simpler, and to reduce the number of inputs required. While the comprehensive code is necessary to study the nature of the radiative processes, the detailed input data which it uses are not available when we want to quantify the radiation for a particular observed situation, so that simple parametrisations are a more practical method. These parametrisations are used in the conceptual model presented in

section 5.3. In section 3.3, we use the simplified SW parametrisation together with the measurements of SW radiative flux at the surface to roughly estimate the main unknown parameter: the (vertically representative) fog droplet number concentration.

3.1 Published paper: Radiation in fog: quantification of the impact on fog liquid water based on ground-based remote sensing

Atmos. Chem. Phys., 17, 10811–10835, 2017
https://doi.org/10.5194/acp-17-10811-2017

Atmospheric Chemistry and Physics
Open Access
EGU

Radiation in fog: quantification of the impact on fog liquid water based on ground-based remote sensing

Eivind G. Wærsted[1], Martial Haeffelin[2], Jean-Charles Dupont[3], Julien Delanoë[4], and Philippe Dubuisson[5]

[1]Laboratoire de Météorologie Dynamique, École Polytechnique, Université Paris-Saclay, 91128 Palaiseau, France
[2]Institut Pierre Simon Laplace, École Polytechnique, CNRS, Université Paris-Saclay, 91128 Palaiseau, France
[3]Institut Pierre-Simon Laplace, École Polytechnique, UVSQ, Université Paris-Saclay, 91128 Palaiseau, France
[4]Laboratoire Atmosphères, Milieux, Observations Spatiales/UVSQ/CNRS/UPMC, 78280 Guyancourt, France
[5]Laboratoire d'Optique Atmosphérique, Univ. Lille – UMR CNRS 8518, 59000 Lille, France

Correspondence to: Eivind G. Wærsted (ewaersted@lmd.polytechnique.fr)

Received: 31 March 2017 – Discussion started: 10 May 2017
Revised: 23 July 2017 – Accepted: 25 July 2017 – Published: 14 September 2017

Abstract. Radiative cooling and heating impact the liquid water balance of fog and therefore play an important role in determining their persistence or dissipation. We demonstrate that a quantitative analysis of the radiation-driven condensation and evaporation is possible in real time using ground-based remote sensing observations (cloud radar, ceilometer, microwave radiometer). Seven continental fog events in mid-latitude winter are studied, and the radiative processes are further explored through sensitivity studies. The longwave (LW) radiative cooling of the fog is able to produce 40–70 $g\,m^{-2}\,h^{-1}$ of liquid water by condensation when the fog liquid water path exceeds 30 $g\,m^{-2}$ and there are no clouds above the fog, which corresponds to renewing the fog water in 0.5–2 h. The variability is related to fog temperature and atmospheric humidity, with warmer fog below a drier atmosphere producing more liquid water. The appearance of a cloud layer above the fog strongly reduces the LW cooling relative to a situation with no cloud above; the effect is strongest for a low cloud, when the reduction can reach 100 %. Consequently, the appearance of clouds above will perturb the liquid water balance in the fog and may therefore induce fog dissipation. Shortwave (SW) radiative heating by absorption by fog droplets is smaller than the LW cooling, but it can contribute significantly, inducing 10–15 $g\,m^{-2}\,h^{-1}$ of evaporation in thick fog at (winter) midday. The absorption of SW radiation by unactivated aerosols inside the fog is likely less than 30 % of the SW absorption by the water droplets, in most cases. However, the aerosols may contribute more significantly if the air mass contains a high concentration of absorbing aerosols. The absorbed radiation at the surface can reach 40–120 $W\,m^{-2}$ during the daytime depending on the fog thickness. As in situ measurements indicate that 20–40 % of this energy is transferred to the fog as sensible heat, this surface absorption can contribute significantly to heating and evaporation of the fog, up to 30 $g\,m^{-2}\,h^{-1}$ for thin fog, even without correcting for the typical underestimation of turbulent heat fluxes by the eddy covariance method. Since the radiative processes depend mainly on the profiles of temperature, humidity and clouds, the results of this paper are not site specific and can be generalised to fog under different dynamic conditions and formation mechanisms, and the methodology should be applicable to warmer and moister climates as well. The retrieval of approximate emissivity of clouds above fog from cloud radar should be further developed.

1 Introduction

Fog is defined as the presence of droplets in the vicinity of the Earth's surface reducing the visibility to below 1 km (American Meteorological Society, 2017). Reduced visibility associated with fog is a major concern for traffic safety, in particular for airports, where delays caused by low-visibility procedures cause significant financial losses (Gultepe et al., 2009). In spite of significant advances in the skills of numerical weather forecast models in recent decades, the timing of the appearance and dissipation of fog is poorly forecasted

(Bergot et al., 2007; Steeneveld et al., 2015). Fog is difficult to model with numerical weather forecast models because of its local nature and the subtle balance between the physical processes that govern its life cycle, which must be parameterised in the models (Steeneveld et al., 2015). Detailed ground-based observations of a fog condition in real time therefore have a potential for capturing information which is missed by the models and which could help estimate whether the fog will dissipate or persist in the near future.

Continental fog often forms by radiative cooling of the surface under clear skies (radiation fog) or by the lowering of the base of a pre-existing low stratus cloud to ground level (Gultepe et al., 2007; Haeffelin et al., 2010). Once the fog has formed, its evolution depends on the physical processes that impact the liquid water. A delicate balance between radiative cooling, turbulent mixing and droplet sedimentation has been found in observational and modelling studies of radiation fog (Brown and Roach, 1976; Zhou and Ferrier, 2008; Price et al., 2015). While radiative cooling produces liquid water by supersaturation, turbulent mixing usually is a loss mechanism for liquid water through the mixing of the fog with drier air or turbulent deposition of liquid water on the surface (Gultepe et al., 2007).

Three radiative processes affect the evolution of the fog by cooling or heating it. Firstly, the cooling from the emission of thermal (longwave, LW) radiation at the fog top produces liquid water by condensation, which maintains the fog against the processes that deplete the liquid water. The advection of a cloud layer above existing fog will shelter the fog from this radiative cooling and can therefore be an efficient dissipation mechanism (Brown and Roach, 1976). Secondly, solar (shortwave, SW) radiation will be absorbed by the fog droplets, mainly in the near-infrared spectrum (Ackerman and Stephens, 1987), which causes heating and subsequent evaporation and loss of liquid water. Finally, heating of the ground by absorption of SW radiation can cause a sensible heat transfer to the fog, causing the fog to evaporate from below (Brown and Roach, 1976). Fog therefore often forms during the night, when thermal cooling dominates, and dissipates a few hours after sunrise due to the increasing heating from solar radiation (Tardif and Rasmussen, 2007; Haeffelin et al., 2010).

The radiative cooling of fog not only drives condensation, but also turbulent processes. Once a fog contains a sufficient amount of liquid water, it becomes optically thick to LW radiation. It will then cool strongly at its top, while the lower part of the fog is shielded from cooling (Haeffelin et al., 2013). This cooling from above (and possibly heating from below) destabilises the fog layer and gives rise to convective motions; the cold air sinks and the warm air rises. The fog layer will therefore be turbulent, since convection constitutes a buoyant production of turbulent kinetic energy (e.g. Nakanishi, 2000). Entrainment of warmer, unsaturated air from above the fog is therefore enabled, which will cause evaporation as it mixes with the fog (Gultepe et al., 2007). At the same time, turbulent eddies near the surface can deposit droplets onto the vegetation (Katata, 2014), and droplets transported downwards can evaporate when approaching the warmer surface (Nakanishi, 2000). In addition to vertical destabilisation, the wind shear can contribute significantly to the generation of turbulence in fog (Mason, 1982; Nakanishi, 2000; Bergot, 2013).

In this study, we focus on the radiative aspect of this dynamical fog system. We aim to quantify the cooling (or heating) of the fog layer induced by the each of the three radiative processes introduced above, based on continuous observations of the atmospheric column from ground-based remote sensing instruments. From the cooling rate, we can estimate the condensation (or evaporation) rate that must occur in response for the fog to stay at saturation. Even though these condensation rates will be modified by the dynamical processes inside the fog, they still indicate how strongly the radiative processes influence the fog liquid water budget. We search answers to the following questions. How large is the rate of condensation or evaporation induced by each of the three radiative processes? How much does this vary from one case to another, and which atmospheric parameters are responsible for this variability? How can the magnitude of these impacts be quantified using ground-based remote sensing, and how large are the uncertainties?

In Sect. 2, we define the quantitative parameters used to describe the three radiative processes and how they are calculated, and we present the instruments, the radiative transfer code and the fog events studied. Section 3 provides a detailed description of how the observations are used to provide input to the radiative transfer code. In Sect. 4, we present the results when applying the methodology to the observed fog events. In Sect. 5, we discuss the uncertainties of the methodology and explore how sensitive the radiative processes are to different aspects of the atmospheric conditions. We also discuss the implications of our findings for the dissipation of fog. Finally, our conclusions are given in Sect. 6.

2 Data and methodology

2.1 Overview of the approach

Each of the three radiative processes in the fog is studied using a quantitative parameter. For the process of cooling due to LW emission, we calculate the rate of condensation in the whole of the fog (in $\mathrm{g\,m^{-2}\,h^{-1}}$) that would occur due to this radiative cooling if no other processes occurred, and we call it C_{LW} for short. Similarly, we calculate the evaporation rate due to SW heating inside the fog (in $\mathrm{g\,m^{-2}\,h^{-1}}$) and call it E_{SW}. The third process is the radiative heating of the surface, which will stimulate a sensible heat flux from the surface to the overlying fog when the surface becomes warmer than the fog. With this process in mind, our third parameter is the net radiative flux (SW+LW) absorbed at the surface (in $\mathrm{W\,m^{-2}}$),

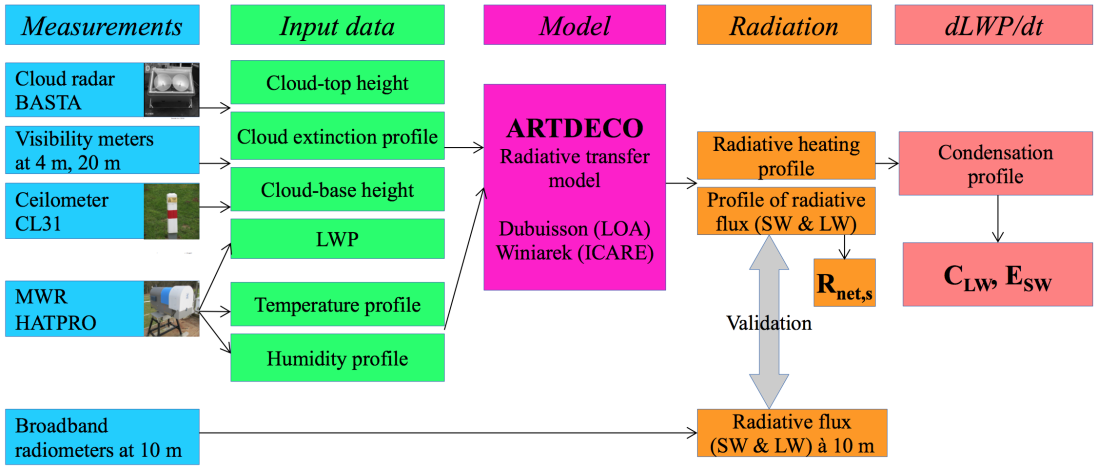

Figure 1. Schematic overview of the methodology.

$R_{\mathrm{net,s}}$ for short. The relationship between $R_{\mathrm{net,s}}$ and the sensible heat flux is also studied (Sect. 4.2).

Figure 1 shows schematically how the three parameters are calculated. Measurements from several in situ and remote sensing instruments (presented in Sect. 2.2) are used to estimate the input data of a radiative transfer model (presented in Sect. 2.3). The input data involve vertical profiles of clouds, temperature and humidity. The details of how we go from measurements to input data are presented in Sect. 3. The radiative transfer model calculates the profile of radiative fluxes and heating rates. The computed fluxes can be compared to measured fluxes at 10 m above ground level for validation. From the radiative heating rates, we can calculate the rates of condensation or evaporation in $\mathrm{g\,m^{-2}\,h^{-1}}$ (explained in Sect. 2.4).

2.2 Observational site and instrumentation

The multi-instrumental atmospheric observatory SIRTA in Palaiseau, 20 km south of Paris (France), provides routine measurements of a large number of meteorological variables since 2002 (Haeffelin et al., 2005). In situ and remote sensing observations taken at this site have been used to study the fog life cycle since 2006 in the framework of the ParisFog project (Haeffelin et al., 2010). An advantage of SIRTA is the continuous measurements by several ground-based remote sensing instruments. Such instruments have been proven useful for the study of the fog life cycle: the attenuated backscatter from a ceilometer can detect the growth of aerosols preceding fog formation (Haeffelin et al., 2016), while a cloud radar can provide information about the fog vertical development and properties once it has formed (Teshiba et al., 2004; Boers et al., 2012; Dupont et al., 2012). In this study, we use the observations from several instruments of SIRTA (Table 1) to analyse periods when fog occurred. The observatory is located in a suburban area, with surroundings characterised by small-scale heterogeneities including an open field, a lake and a small forest.

In situ measurements of (horizontal) visibility, air temperature, wind speed, surface skin temperature and SW and LW radiative fluxes are continuously recorded in the surface layer at the observatory. Radiosondes measuring the temperature and humidity profiles between ground level and 30 km are launched twice a day from the Météo-France Trappes station, located 15 km west of SIRTA. Measurements of sensible heat flux taken at 2 m using the eddy correlation method based on CSAT-3 sonic anemometer are applied to study the relationship between surface radiation budget and surface sensible heat flux.

A Vaisala CL31 ceilometer operating at 905 nm provides the profile of (attenuated) light backscatter at 15 m vertical resolution (Kotthaus et al., 2016), from which the cloud-base height can be determined (see Sect. 3.1).

The 95 GHz cloud radar BASTA is a newly developed cloud radar, the first prototype of which has been successfully operating at SIRTA since 2010 (Delanoë et al., 2016), observing the vertical profile of clouds in zenith direction. Unlike traditional radars, which emit short, powerful pulses of radiation, BASTA instead uses the frequency-modulated continuous wave technique, which makes it much less expensive than traditional radars (Delanoë et al., 2016, http://basta.projet.latmos.ipsl.fr/). Unlike the ceilometer pulse, the signal of the radar is only weakly attenuated by clouds and can therefore observe thick and multilevel cloud layers. However, the signal weakens with the distance to the target, which limits the ability of the radar to detect clouds with small droplets. BASTA therefore operates at four different modes, with vertical resolutions of 12.5, 25, 100 and 200 m. The radar switches systematically between the four modes so that each of them produces a measurement every 12 s based on 3 s of integration time. Better vertical resolution comes at the cost of sensitivity. The BASTA prototype

Table 1. Vertical and temporal resolution of the observations used in this study. All instruments are located at the SIRTA observatory main facility, apart from the radiosondes which are launched at Trappes (15 km west of the site) at approximately 11:15 and 23:15 UTC. The measurements by the cloud radar, ceilometer and microwave radiometer are obtained from remote sensing, while the other instruments measure in situ.

Instrument	Measured quantity	Vertical range and resolution	Temporal resolution
Cloud radar BASTA	Reflectivity (dBZ)	RA 0–6 km, RE 12.5 m RA 0–12 km, RE 25 m RA 0–12 km, RE 100 m RA 0–12 km, RE 200 m	12 s
Microwave radiometer	Liquid water path ($g\,m^{-2}$)	Integrated	60 s
	Temperature profiles (K)	RA 0–10 km, 4–5 degrees of freedom	$\approx$ 5 min
	Humidity profile ($g\,m^{-3}$)	RA 0–10 km, 2 degrees of freedom	$\approx$ 5 min
Ceilometer CL31	Attenuated backscatter	RA 0–7.6 km, RE 15 m	30 s
Visibility metres	Horizontal visibility (m)	At 4 m, 20 m	60 s
Thermometers on 30 m mast	Air temperature (K)	At 1, 2, 5, 10, 20, 30 m	60 s
Thermometer (unsheltered)	Surface skin temperature (K)	At ground level	60 s
Cup anemometer	Wind speed ($m\,s^{-1}$)	At 10 m	60 s
CSAT-3 sonic anemometer and LI-7500 infrared gas analyser	Sensible heat flux and latent heat flux ($W\,m^{-2}$)	At 2 m	10 min
Radiosondes	Temperature (K) and humidity ($g\,m^{-3}$) profiles	RA 0–30 km, RE $\approx$ 5 m	12 h
Pyranometers	Down- & upwelling irradiance in the solar spectrum ($W\,m^{-2}$)	At 10 m	60 s
Pyrgeometers	Down- & upwelling irradiance in the terrestrial spectrum ($W\,m^{-2}$)	At 10 m	60 s

used in this study can detect clouds at 1 km range (i.e. altitude) with reflectivities (see Sect. 3.2) above -27.5, -32, -38 and -41 dBZ with the 12.5, 25, 100 and 200 m modes, respectively. This lower limit for detection increases approximately with the square of the range, i.e. with 6 dBZ when the range increases by a factor of two. However, a new prototype that has recently been developed has improved the sensitivity with about 12 dBZ relative to the first prototype on all levels. The lowest ≈ 3 altitude levels in the radar data cannot be used because of coupling (direct interaction between the transmitter and receiver), which corresponds to the first ≈ 40 m when we use the 12.5 m mode to study the fog layers.

The multi-wavelength microwave radiometer (MWR) HATPRO (Rose et al., 2005) is a passive remote sensing instrument that measures the downwelling radiation at 14 different microwave wavelengths at the surface. These radiances are inverted using an artificial neural network algorithm to estimate the vertical profiles of temperature and humidity of the atmosphere in the range 0–10 km and the total amount of liquid water in the atmospheric column (liquid water path, LWP, $g\,m^{-2}$). As the profiles are based on passive measurements, the vertical resolution is limited; however, in the boundary layer the measurements at different elevation angles enhance the resolution of the temperature profile, giving 4–5 degrees of freedom for the full temperature profile. The humidity profile only has about 2 degrees of freedom (Löhnert et al., 2009). The integrated water vapour (IWV) is more reliable with an uncertainty of $\pm 0.2\,kg\,m^{-2}$, while the estimate of LWP in general has an uncertainty of $\pm 20\,g\,m^{-2}$, according to the manufacturer. However, for small LWP ($< 50\,g\,m^{-2}$), investigations by Marke et al. (2016) indicate that the absolute uncertainties are smaller, with a root mean square (rms) error of $6.5\,g\,m^{-2}$. Moreover, much of the uncertainty in retrieving LWP is due to uncertainties in atmospheric conditions, such as cloud temperature and humidity profile (e.g. Gaussiat et al., 2007), which usually will not change dramatically during one fog event. In the absence of higher liquid clouds, the detection limit of changes in fog LWP should therefore be smaller, probably of the order of $5\,g\,m^{-2}$ (Bernhard Pospichal, personal communication). To reduce the constant bias in MWR LWP, we subtract the mean LWP retrieved during the 1 h period of clear sky that is nearest in time to the fog event of interest. For the three fog events in 2014 studied in this paper (see Sect. 2.5), the imposed corrections are 1.1, 5.2 and $23.9\,g\,m^{-2}$. An improvement of the instrument algorithm provided by the manufacturer in 2015 reduced this clear-sky bias to less than $1\,g\,m^{-2}$ for the rest of the fog events. An approximate evaluation of the LWP uncertainty using LW radiation measurements suggests an rms error in LWP of about 5–10 $g\,m^{-2}$ during fog with LWP $< 40\,g\,m^{-2}$ (Appendix A).

2.3 Radiation code ARTDECO

The radiative transfer is calculated using ARTDECO (Atmospheric Radiative Transfer Database for Earth Climate Observation), a numerical tool developed at LOA (Lille University) which gathers several methods to solve the radiative

transfer equation and data sets (atmospheric profiles, optical properties for clouds and aerosols, etc.) for the modelling of radiances and radiative fluxes in the Earth's atmosphere under the plane-parallel assumption. Data and a user guide are available on the AERIS/ICARE Data and Services Center website at http://www.icare.univ-lille1.fr/projects/artdeco. In this paper, the radiative transfer equation is solved using the discrete-ordinates method DISORT (Stamnes et al., 1988) in the solar spectrum (0.25–4 µm) and the thermal spectrum (4–100 µm). The spectral resolution is $400\,\mathrm{cm}^{-1}$ in 0.25–0.69 µm, $100\,\mathrm{cm}^{-1}$ in 0.69–4 µm and $20\,\mathrm{cm}^{-1}$ in 4–100 µm, which gives 303 wavelength bands in total. Gaseous absorption by H_2O, CO_2 and O_3 is taken into account and represented by the correlated k-distributions (Dubuisson et al., 2005; Kratz, 1995). In ARTDECO, the coefficients of the k-distribution are calculated using a line-by-line code (Dubuisson et al., 2006) from the HITRAN 2012 spectroscopic database (Rothman et al., 2013). The use of correlated k-distribution makes it possible to accurately account for the interaction between gaseous absorption and multiple scattering with manageable computational time. In addition, the impact of the absorption continua is modelled using the MT_CKD model (Mlawer et al., 2012). Optical properties of water clouds are calculated for a given droplet size distribution (DSD) using Mie calculations. In this study, the DSD is parameterised using a modified gamma distribution, applying parameter values presented by Hess et al. (1998) for fog and continental stratus. The effective radius is 10.7 µm for fog and 7.3 µm for stratus, but we modify the effective radius in the fog according to the radar reflectivity (see Sect. 3.2). Ice clouds are represented by the Baum and Co ice cloud parameterisation implemented in the ARTDECO code (Baum et al., 2014), using an ice crystal effective diameter of 40 µm.

Radiative fluxes are calculated on 66 vertical levels spanning 0–70 km, 28 of which are located in the lowest 500 m in order to resolve fog layers well. A Lambertian surface albedo in the SW is applied, with a spectral signature representative of vegetated surfaces. However, as we observed that this albedo parameterisation generally overestimates the observed albedo by $\approx 25\,\%$, we downscale the albedo at all wavelengths to better fit the median albedo of 0.221 of October 2014–March 2015 observed at SIRTA. In the LW, a constant emissivity of 0.97 is used.

2.4 Calculation of radiation-driven liquid water condensation and evaporation

The radiation-driven condensation (or evaporation) rate is calculated assuming the air remains at saturation while cooling or warming from SW or LW radiation only, neglecting all adiabatic motions or mixing, but taking into account the latent heat of condensation. The derivations below are based on the thermodynamics of a saturated air parcel, which are described by e.g. Wallace and Hobbs (2006).

For N model levels at height h_j ($j = 1, \ldots, N$), ARTDECO calculates the radiative heating rate in each of the $N-1$ layers between these levels, $\left(\frac{\mathrm{d}T}{\mathrm{d}t}\right)_{\mathrm{rad},\,j}$ ($j = 1, \ldots N-1$). We assume that if the jth layer contains cloud, its water vapour content will always be at saturation with respect to liquid water. To satisfy this, the condensation rate C_{rad} due to the radiation must be as follows:

$$C_{\mathrm{rad},\,j} = -\frac{\mathrm{d}\rho_{\mathrm{s}}}{\mathrm{d}T}\left(\frac{\mathrm{d}T}{\mathrm{d}t}\right)_j, \tag{1}$$

where ρ_{s} is the saturation vapour concentration ($\mathrm{g\,m^{-3}}$) and $\frac{\mathrm{d}\rho_{\mathrm{s}}}{\mathrm{d}T}$ its change with temperature. $\left(\frac{\mathrm{d}T}{\mathrm{d}t}\right)_j$ is the total air temperature tendency, which under the above assumptions equals the radiative heating rate plus the latent heat of condensation:

$$\left(\frac{\mathrm{d}T}{\mathrm{d}t}\right)_j = \left(\frac{\mathrm{d}T}{\mathrm{d}t}\right)_{\mathrm{rad},\,j} + \frac{L_{\mathrm{v}}}{\rho_{\mathrm{a}} c_p} C_{\mathrm{rad},\,j}, \tag{2}$$

where L_{v} is the specific latent heat of condensation, ρ_{a} the air density and c_p the specific heat capacity of air at constant pressure. We estimate $\frac{\mathrm{d}\rho_{\mathrm{s}}}{\mathrm{d}T}$ by combining the ideal gas equation for water vapour ($e_{\mathrm{s}} = \rho_{\mathrm{s}} R_{\mathrm{v}} T$) and the Clausius–Clapeyron equation ($\frac{\mathrm{d}e_{\mathrm{s}}}{\mathrm{d}T} = \frac{L_{\mathrm{v}} e_{\mathrm{s}}}{R_{\mathrm{v}} T^2}$), which yields

$$\frac{\mathrm{d}\rho_{\mathrm{s}}}{\mathrm{d}T} = \frac{e_{\mathrm{s}}}{R_{\mathrm{v}} T^2}\left(\frac{L_{\mathrm{v}}}{R_{\mathrm{v}} T} - 1\right), \tag{3}$$

where R_{v} is the specific gas constant of water vapour, and e_{s} is the saturation vapour pressure, which we estimate from the formula presented by Bolton (1980):

$$e_{\mathrm{s}}(T) = 611.2 \exp\left(\frac{17.67\,(T - 273.15)}{T - 29.65}\right), \tag{4}$$

with T in K and e_{s} is Pa. Combining Eqs. (1) and (2), we get an expression for the radiation-driven condensation rate:

$$C_{\mathrm{rad},\,j} = -\frac{\frac{\mathrm{d}\rho_{\mathrm{s}}}{\mathrm{d}T}}{1 + \frac{L_{\mathrm{v}}}{\rho_{\mathrm{a}} c_p}\frac{\mathrm{d}\rho_{\mathrm{s}}}{\mathrm{d}T}}\left(\frac{\mathrm{d}T}{\mathrm{d}t}\right)_{\mathrm{rad},\,j}. \tag{5}$$

We calculate this condensation rate for all layers within the fog and finally integrate it into the vertical to obtain the total condensation rate in the whole of the fog (in $\mathrm{g\,m^{-2}\,h^{-1}}$), thus obtaining C_{LW} and $-E_{\mathrm{SW}}$. It is worth noting that the gradient $\frac{\mathrm{d}\rho_{\mathrm{s}}}{\mathrm{d}T}$ increases strongly with temperature. This implies that a warmer fog condensates more liquid water than a cold fog given the same radiative cooling rate. In fact, the condensed water per radiative heat loss increases almost linearly from 0.55 to $0.90\,\mathrm{g\,m^{-2}\,h^{-1}}$ per $\mathrm{W\,m^{-2}}$ when the fog temperature increases from −2 to 15 °C (not shown).

Thus, the vertical integral of Eq. (5) allows the immediate effect of radiation on the fog LWP budget to be calculated from the output of the radiative transfer model. This is

possible because we have neglected all air motion. In reality, negative buoyancy induced by the radiative cooling will lead to downdraughts and turbulence, which favours entrainment, droplet deposition and other LWP sink processes, as described in Sect. 1. These indirect effects of radiation on the LWP budget are not studied in this paper, as a dynamical model taking into account forcings such as the wind and surface properties would be required in order to quantify them. When interpreting the results of this paper, it is important to keep in mind that the condensation rates C_{LW} and $-E_{SW}$ are not the actual condensation rates that occur in the fog, but rather the immediate condensational tendency to stay at saturation induced by the radiative temperature tendency, which could rapidly be modified by either drying or warming through mixing processes. Nonetheless, C_{LW} and E_{SW} are good indicators for how strongly the radiation impacts the fog LWP.

To improve the calculation of condensation rates, we could have taken into account that fog is often vertically well mixed due to destabilisation (Nakanishi, 2000), so that the whole of the fog layer cools at the same rate. However, we found that C_{LW} and E_{SW} only change marginally ($< 2\,\%$) if we apply the fog-layer vertical average radiative heating rate in Eq. (5) (not shown), which would not significantly affect our results.

2.5 Overview of the analysed fog cases

We calculate the radiation at 15 min intervals in seven fog events that occurred at SIRTA during the winter seasons 2014–2015 and 2015–2016. An overview of the atmospheric conditions during each of these fog events is given in Table 2. The fog events were chosen to cover an important range of variability in atmospheric conditions such as 2 m temperature and IWV, as well as fog properties such as geometric thickness and LWP, and we have included one fog event where cloud layers above the fog were observed. Considering all fog events at SIRTA in the winter seasons 2012–2016 with reliable LWP measurements from the MWR (e.g. excluding cases with liquid clouds above), in total 53 events, the 10th, 25th, 50th, 75th and 90th percentiles of the LWP distribution are 6.6, 16.4, 40.2, 68.0 and 91.2 g m^{-2}, respectively (not shown). The chosen fog events thus cover the typical range of fog LWP. Fog types can be defined by the mechanism of formation (Tardif and Rasmussen, 2007). At SIRTA, radiation fog and stratus-lowering fog occur with about the same frequency, while other fog types are less common (Haeffelin et al., 2010; Dupont et al., 2016). Fog during rain occasionally occurs, but such cases have been avoided in this study because rain or drizzle drops generate very large radar reflectivities, yielding cloud property retrievals highly uncertain (Fox and Illingworth, 1997), and because of the wetting bias in the MWR retrievals in rain (Rose et al., 2005).

Fog presence is defined by the 10 min average visibility at 4 m being below 1 km (American Meteorological Society, 2017). For a 10 min block to be part of a fog event, the visibil-

Table 2. Main characteristics of each fog event studied in this paper. Dissipation time is relative to sunrise (− is before, + is after). The fog events are classified as radiation fog (RAD) or stratus-lowering fog (STL), as defined by Tardif and Rasmussen (2007). Pressure is measured at 2 m and is indicated for the time of formation, while the bracketed value indicates how much higher (+) or lower (−) the pressure is 24 h later.

No	Time of formation (UTC)	Duration (hh:mm)	Diss. time rel. to sunrise (h)	Fog type	Pressure (hPa)	Higher clouds (y/n)	Min. visibility (m) at 4 m	Median (max) LWP (g m^{-2})	Max thickness (m)	2 m temp. range (°C)	IWV range (kg m^{-2})
1	27 Oct 2014, 04:30	4:20	+2.3	RAD	1006(−5)	n	135	6 (22)	110	7.2–9.4	≈ 9–13
2	28 Oct 2014, 00:50	8:20	+2.5	RAD	1001(−3)	n	145	130 (209)	450	7.0–9.8	≈ 7–9.5
3	14 Dec 2014, 06:00	17:10*	−8.6	RAD	999(+0)	n	103	18 (56)	210	(−1.1)–2.5	≈ 6–9
4	2 Nov 2015, 05:00	9:20	+7.6	RAD	1007(-8)	n	74	62 (105)	275	5.1–8.5	≈ 9–11
5	8 Nov 2015, 05:50	4:00	+2.9	RAD	1009(−1)	n	128	40 (61)	210	13.7–14.4	≈ 22–28
6	13 Dec 2015, 06:20	29:20*	+3.9	STL	1003(−3)	n	72	69 (135)	360	2.8–5.7	≈ 10–14
7	1 Jan 2016, 07:00	5:20	+4.5	RAD	1006(−17)	y	125	67 (154)	410	4.6–5.9	≈ 12–15

* The cloud base lifted to a few tens of metres on 14 December 2014 during 13:40–15:10 and on 13 December 2015 during 12:20–15:00.

ity should be below 1 km for at least 30 min of the surrounding 50 min period, based on the method proposed by Tardif and Rasmussen (2007), thus defining the fog formation and dissipation time of each event. From this definition, fog event numbers 3 and 6 should each be separated into two events; however, we have chosen to regard them as single events because the cloud base lifts only a few tens of metres for 2–3 h before lowering again.

3 Retrieval of geophysical properties

This section describes how the measurements at SIRTA are used to prepare the input data to the radiative transfer code: profiles of cloud properties, temperature and humidity. Before they are used, the data from all the instruments, except the temperature and humidity profiles from the radiosonde and MWR, are averaged in a 10 min block around the time of interest.

3.1 Fog and cloud boundaries

The fog or low stratus is searched for in the lowest 500 m of the atmosphere. Its cloud-base height is found using a threshold value in the attenuated backscatter from the ceilometer of 2×10^{-4} m^{-1} sr^{-1}, following Haeffelin et al. (2016). The cloud-base height is set to 0 m if the horizontal visibility at 4 m is below 1 km. The cloud-top height is set to the altitude where the 12.5 m resolution radar data no longer detect a signal above noise levels. If the visibility at 4 m is below 1 km but the visibility at 20 m is above 1 km, the cloud-top height is set to 10 m.

The presence and vertical extent of higher cloud layers is determined from the radar. The clouds are assumed to extend over the gates where a signal is detected above the background noise.

3.2 Fog microphysical properties

We assume that the fog contains only liquid droplets and no ice, which is a reasonable assumption as the screen temperature during the fog events studied here is a minimum of −1 °C (Table 2) and ice crystals in fog rarely occur at temperatures above −10 °C (Gultepe et al., 2007). The optical properties of the fog then depend only on the liquid water content (LWC) and the DSD. Only the extinction coefficient at 550 nm is required as model input in addition to the DSD, since ARTDECO can determine the optical properties at all 303 wavelengths by Mie calculations from this information (Sect. 2.3). The extinction coefficient of cloud droplets at visible wavelengths (including 550 nm) is well approximated by

$$\alpha_{\text{ext,visible}} = \frac{3\,\text{LWC}}{2\varrho_{\text{l}}\, r_{\text{eff}}}, \tag{6}$$

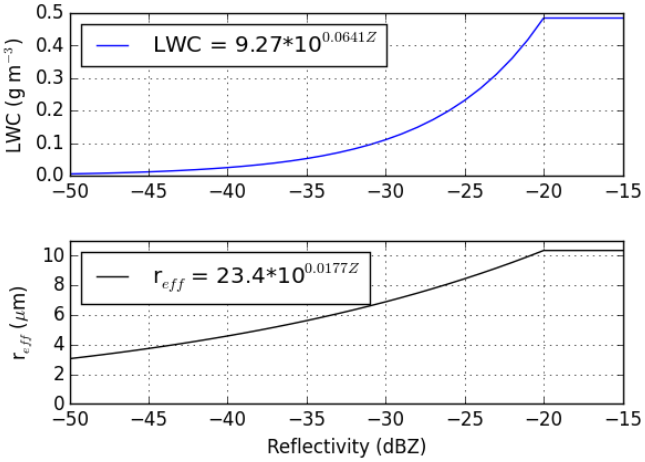

Figure 2. Empirical relationships between radar reflectivity (Z) and LWC and effective radius used in this study, based on Fox and Illingworth (1997).

with LWC in g m^{-3}, r_{eff} the effective radius in µm and ϱ_{l} the density of liquid water in g cm^{-3} (Hu and Stamnes, 1993). The optical depth at visible wavelengths (OD) is obtained by integrating $\alpha_{\text{ext,visible}}$ in the vertical.

The 12.5 m resolution mode of the radar is used to estimate LWC and r_{eff} at each level in the fog. For liquid droplets, the backscattered radar signal is proportional to the sixth moment of the DSD, a quantity known as radar reflectivity Z:

$$Z = \int_0^\infty D^6 n(D)\mathrm{d}D, \tag{7}$$

where $D = 2r$ is the droplet diameter and $n(D)\mathrm{d}D$ is the number concentration of droplets with diameter between D and $D + \mathrm{d}D$. Z has units mm^6 m^{-3}, but is usually expressed in units of dBZ, defined by $\text{dBZ} = 10 \cdot \log_{10}(Z)$. We have chosen to apply the empirical relationships of Fox and Illingworth (1997) relating the radar reflectivity Z (dBZ) to LWC (g m^{-3}) and r_{eff} (µm):

$$\text{LWC} = 9.27 \cdot 10^{0.0641\,Z} \tag{8}$$

$$r_{\text{eff}} = 23.4 \cdot 10^{0.0177\,Z} \tag{9}$$

These relationships were derived from aircraft measurements of the droplet spectrum in stratocumulus clouds, covering the range −40 to −20 dBZ. The relationships are not valid in the presence of drizzle, which strongly increases Z as droplets grow larger. Drizzle presence typically occurs when $Z > -20$ dBZ (e.g. Matrosov et al., 2004). We therefore use the value of LWC and r_{eff} obtained at $Z = -20$ dBZ for higher Z. The relationships are plotted in Fig. 2.

LWC and r_{eff} are estimated in each radar gate from cloud base to cloud top using these relationships, assuming no attenuation of the radar signal. For the lowest altitudes, where

the radar data cannot be used, we apply the reflectivity of the lowest usable gate (usually at ≈ 50 m). The LWP of the MWR is then applied as a scaling factor to improve the estimate of LWC. This scaling is not performed if the MWR LWP is less than $10\,\mathrm{g\,m^{-2}}$. If a higher cloud that may contain liquid is detected, the LWP should be partitioned between the fog and this cloud (see Sect. 4.3). Having obtained LWC and r_{eff}, the profile of $\alpha_{\mathrm{ext,visible}}$ can thus be determined using Eq. (6). Below 30 m, we instead use the visibility measurements, which relate to visible extinction through Koschmieder's formula (e.g. Hautiére et al., 2006):

$$\alpha_{\mathrm{ext,visible}} = -\frac{\ln 0.05}{\mathrm{Vis}} \approx \frac{3.0}{\mathrm{Vis}}. \quad (10)$$

Examples of the profiles of Z, LWC, r_{eff} and $\alpha_{\mathrm{ext,visible}}$ are shown in Appendix B. Uncertainties in the retrievals of microphysical properties are also discussed in Appendix B. To reduce the computational cost, only four different DSDs are given to the radiative transfer code, with effective radii of 4.0, 5.5, 8.0 and 10.7 µm. In one model run, the same DSD is used at all altitudes, and it is selected by applying Eq. (9) on the vertical median of Z.

3.3 Profiles of temperature and gases

The radiation code requires the vertical profiles of temperature and the concentrations of the gaseous species (H_2O, CO_2, O_3) as input. For CO_2, a vertically uniform mixing ratio of 400 ppmv is used, while for O_3 we use the AFGL mid-latitude winter standard atmospheric profile (Anderson et al., 1986) which is provided in ARTDECO. This standard atmosphere is also used for temperature and humidity (i.e. H_2O) above 20 km. Below 10 km, the temperature and humidity from the MWR is applied, while the previous radiosonde at Trappes is used in 10–20 km. The measured surface skin temperature is used for surface emission temperature, while the in situ measured air temperature is used in the 0–30 m layer. When there is no cloud base below 50 m, the MWR temperature profile is modified in the lowest 200 m of the atmosphere to gradually approach the temperature measured at 30 m.

Due to fog top radiative cooling and subsequent vertical mixing, the temperature profile is often characterised by a saturated adiabatic lapse rate inside the fog, capped by a strong inversion above the fog top (Nakanishi, 2000; Price et al., 2015). This vertical structure was also observed by the majority of the 12 radiosondes launched during four fog events in the ParisFog field campaign of 2006–2007 (not shown). If a cloud base is present below 50 m, we therefore let the temperature decrease adiabatically with height from the measured value at the top of the mast and then impose an inversion of 5 K per 100 m from the fog top until the temperature profile of the MWR is encountered. This inversion strength corresponds to what was typically observed by the aforementioned radiosondes. When a cloud base is present below 50 m, we also increase the humidity within the whole of the fog layer to saturation and decrease the humidity in the atmosphere above with the same integrated amount, thus improving the estimate of the humidity column above the fog top.

4 Results

We will now present the results obtained by applying the methodology described above to the seven fog events in Table 2. We first describe two contrasting fog events in some detail (Sect. 4.1), then we study the statistics of the radiative properties in all six fog events without clouds above (Sect. 4.2), and finally we study the impacts of the clouds appearing above the last fog event (Sect. 4.3).

4.1 Quantitative analysis of two contrasting fog events

Figure 3 shows the time series of several observed and calculated quantities during the fog event on 27 October 2014. The visibility and LWP time series (Fig. 3a) reveal that this fog has two distinct stages. From 02 to 06 UTC, intermittent patches of very thin fog exist, seen from the fluctuating 4 m visibility and the 20 m visibility remaining well above the fog threshold. After 06 UTC, the fog develops in the vertical, causing the visibility at 20 m to drop. The fog grows to a thickness of about 100 m, as can be seen by the radar (Fig. 3b), reaching a maximum LWP of about $20\,\mathrm{g\,m^{-2}}$ just after sunrise, at 07 UTC. A minimum visibility at 4 m (155 m) and at 20 m (87 m) is also reached at 07 UTC. After sunrise, the visibility steadily improves, fog dissipating at the surface at 08:50 UTC and nearly 1 h later at 20 m.

Figure 3c–d shows the time series of temperature, wind speed and the net SW and LW downward radiation observed at 10 m. Before fog formation, the ground undergoes radiative cooling of $\approx 60\,\mathrm{W\,m^{-2}}$, which gives rise to the observed strong temperature inversion in the first 20 m of the atmosphere. The surface radiation budget stays unchanged during the period of intermittent fog, indicating that the fog is restricted to below the 10 m level where the flux is measured. Once the fog starts developing in the vertical, however, the 10 m net LW radiation increases and becomes close to zero at the fog peak time at 07 UTC, indicating that the fog is nearly opaque to LW radiation at this time. In the same period, from 06 to 07 UTC, the stable temperature profile evolves into a near-isotherm layer. After sunrise, strong SW absorption at the surface (reaching $> 100\,\mathrm{W\,m^{-2}}$) is associated with a sharp rise in temperature, which likely explains the dissipation of the fog.

Figure 3e–h shows quantities that are calculated using our methodology. Until 06 UTC, the fog OD is based on the observed 4 m extinction and an assumed thickness of 10 m, resulting in a very low fog OD. The estimated fog OD increases strongly from 06 to 07 UTC, reaching 4 at 07 UTC. This is associated with a distinct increase in downwelling LW

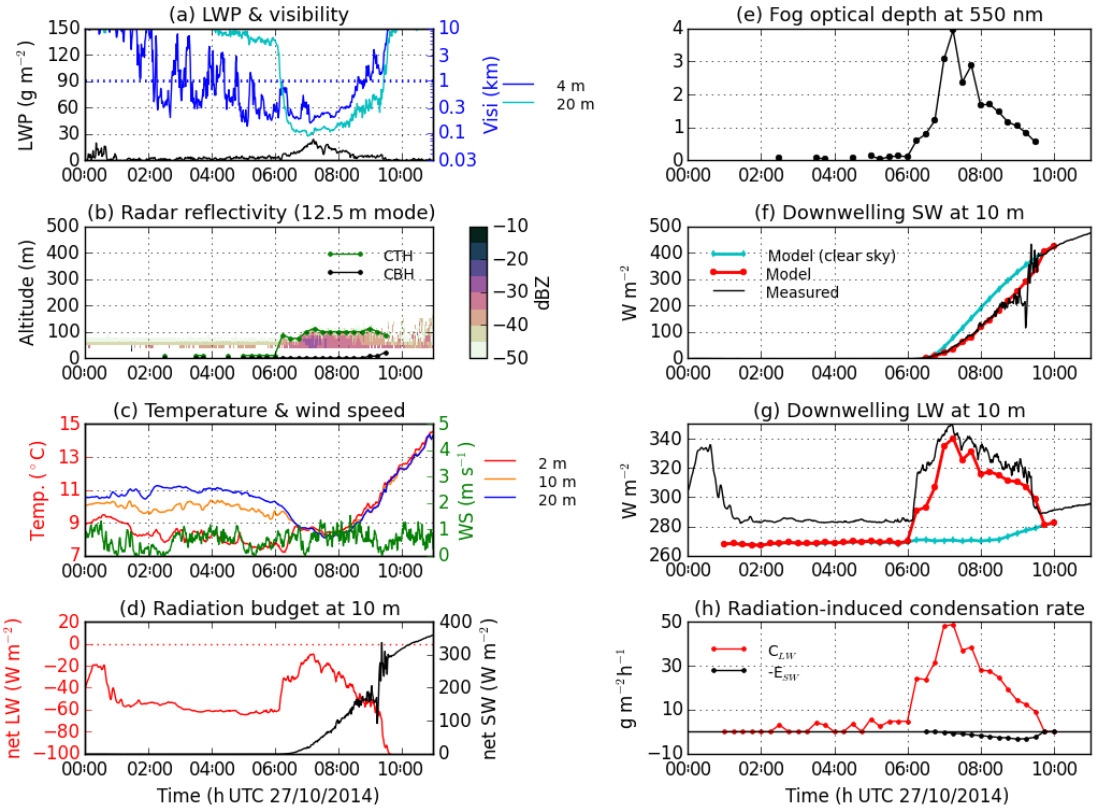

Figure 3. The fog event on 27 October 2014. **(a–d)** Time series of observed variables: **(a)** LWP from MWR ($g\,m^{-2}$) and visibility (m) at 4 and 20 m; **(b)** profile of radar reflectivity (dBZ), and estimated cloud-base height (CBH) and cloud-top height (CTH); **(c)** temperature (°C) at 2, 10 and 20 m, and wind speed ($m\,s^{-1}$) at 10 m; **(d)** net downwelling SW and LW radiative flux ($W\,m^{-2}$) at 10 m. **(e–h)** Time series of calculated variables: **(e)** fog optical depth at 550 nm; **(f)** downwelling SW flux ($W\,m^{-2}$) at 10 m, comparing model runs including the fog, model runs not including the fog (clear sky) and the measurement; **(g)** as **(f)**, but for the downwelling LW flux; **(h)** the vertically integrated condensation rates ($g\,m^{-2}\,h^{-1}$) due to LW and SW radiation (C_{LW} and E_{SW}, defined in Sect. 2.1).

at 10 m, which is qualitatively consistent with the observations (Fig. 3g). As the LW emissivity of the fog increases, the radiative cooling is transferred from the surface to the fog, causing an increase in the calculated C_{LW}, which reaches a maximum of $50\,g\,m^{-2}\,h^{-1}$ (Fig. 3h). The magnitude of this parameter indicates that the radiative cooling process can produce the observed maximum in fog LWP is less than 1 h, which is consistent with the observed increase in LWP. The underestimation of the downwelling LW at 10 m after 06 UTC can indicate that the calculated LW emissivity of the fog is slightly underestimated, and thus also C_{LW}. The calculation also underestimates the LW flux by about $15\,W\,m^{-2}$ before 06 UTC, which is probably due to uncertainties in the vertical profile of temperature and humidity (see Sect. 5.3). E_{SW} is small, at only $\approx 2\,g\,m^{-2}\,h^{-1}$ (Fig. 3h). The heating of the fog via surface absorption is probably much more important for evaporating the fog.

Figure 4 shows the same quantities as Fig. 3, but for the fog event on 13 December 2015. In contrast to the fog on 27 October 2014, this fog forms from the gradual lowering of the cloud-base of a pre-existing low stratus, which is already much thicker than the fog on 27 October 2014. During the whole day, this fog has an LWP of 50–100 $g\,m^{-2}$ and a thickness of 250–300 m and thus remains optically thick. A transition from fog to low stratus occurs at 12:20 UTC, but the cloud base rises only to ≈ 20 m before descending again to form fog at 15 UTC (not shown). As the fog is opaque to LW, the good agreement between the modelled and observed downwelling LW at 10 m (Fig. 4g) only reflects the temperature of the fog. More interesting is the good agreement between the modelled and observed downwelling SW radiation at 10 m (Fig. 4f), which indicates that the estimated fog OD is rather precise. C_{LW} is around $50\,g\,m^{-2}\,h^{-1}$ with little variability. The ratio of the fog LWP and C_{LW} has units of time, and it can be interpreted as a characteristic timescale for the renewal of the fog by radiative cooling; it is the time in which C_{LW} could produce the same amount of liquid water that is currently in the fog. This timescale is 1–2 h in this fog event. E_{SW} reaches $9\,g\,m^{-2}\,h^{-1}$ around midday and is thus of less importance. This thicker fog also reflects more SW radiation than the fog 27 October 2014 so that less SW

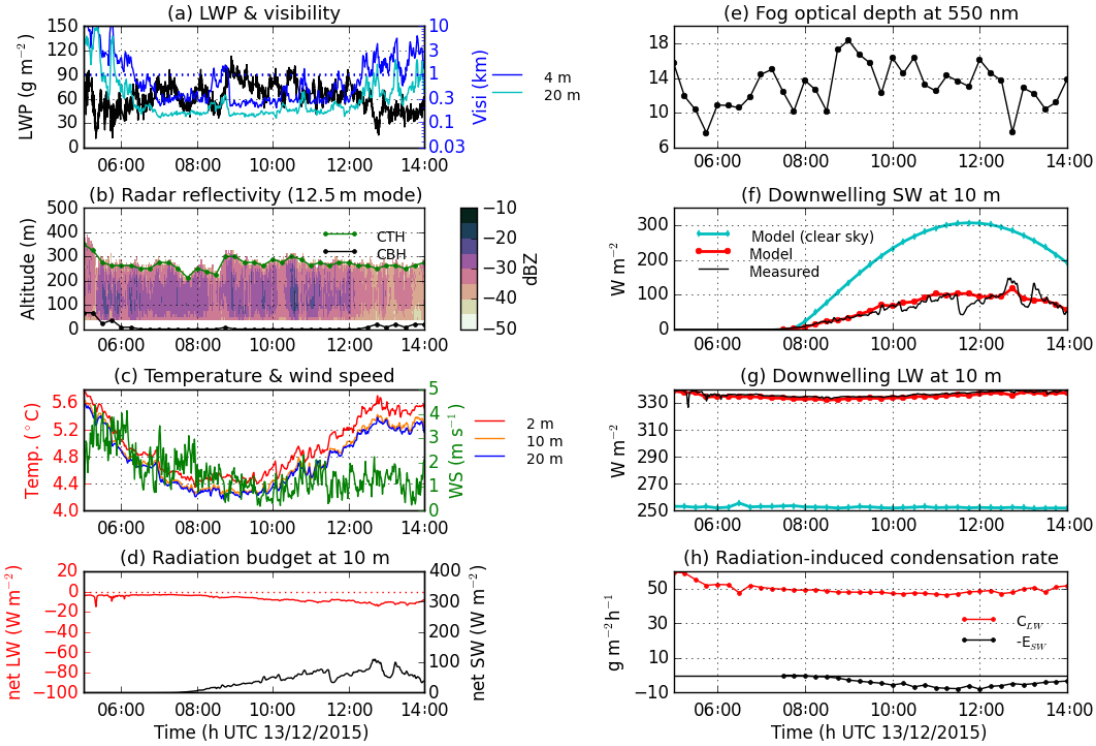

Figure 4. Same as Fig. 3 but for the fog event on 13 December 2015.

reaches the surface (Fig. 4f), which probably helps the fog to persist, although the LWP decreases during the day.

4.2 Radiation-driven condensation and evaporation in six fog events without clouds above

Figure 5 shows the values of our three radiation parameters calculated every 15 min during the six fog cases without higher clouds (Table 2). C_{LW} varies significantly, from 0 to 70 g m^{-2} h^{-1} (Fig. 5a). Firstly, when the fog is not opaque to LW radiation, C_{LW} is smaller, because the fog emits less than a blackbody. The optical depth of a cloud in the LW is principally determined by its LWP (Platt, 1976). We therefore plot C_{LW} against the MWR LWP in Fig. 5a, which shows that C_{LW} increases strongly with LWP when LWP is smaller than 20–30 g m^{-2}. Remember, though, that the MWR LWP is not used in the input data to the radiation code when it is less than 10 g m^{-2} (Sect. 3.2). When the fog is opaque (LWP $> \approx 30$ g m^{-2}), the radiative cooling is restricted to the uppermost 50–100 m of the fog (Appendix B), in agreement with previous studies (Nakanishi, 2000; Cuxart and Jiménez, 2012). C_{LW} then is in the range 40–70 g m^{-2} h^{-1}, varying significantly between fog events and to a lesser degree ($\approx$ 5–15 g m^{-2} h^{-1}) within the same event (Fig. 5a). This variability is not related to LWP since the LW emissivity is already close to 1 at an LWP of 30 g m^{-2}. We can interpret from Fig. 5a that the timescale of renewal by LW cooling (introduced in Sect. 4.1) in opaque fog is in the range 0.5–2 h, being longer for fog with higher LWP and even reaching 3 h for parts of the fog on 28 October 2014. This is similar to the typical timescale for observed major changes in the fog LWP (not shown). The magnitude of C_{LW} can be compared to the results of Nakanishi (2000), who studied the liquid water budget of fog in a large-eddy simulation. His Fig. 14a shows the domain-averaged profile of condensation rate in a 100 m thick fog with LWP of about 15 g m^{-2} (seen from his Fig. 5b) in the morning. Condensation occurs in the upper 50 m of the fog, and the integral over these 50 m gives roughly 30–40 g m^{-2} h^{-1}, which is similar to our results (Fig. 5a).

To investigate possible causes for the observed variability of C_{LW} in opaque fog, three cases of opaque fog (OD > 10) are compared in Fig. 6. C_{LW} are 63.4, 47.7 and 61.6 g m^{-2} h^{-1} (Fig. 6a). Since the fog is opaque, the budget of LW radiation at the fog top is the main determining factor for the radiative cooling. Figure 6b shows the LW fluxes at fog top in the three cases; the length of the vertical line indicates the net negative LW budget. The net LW budget is -73 W m^{-2} both on 2 and 8 November 2015, but the condensation rate is still higher by 14 g m^{-2} h^{-1} on 8 November 2015. This is explained by the higher temperature of the fog top on the latter date (Fig. 6c), causing a higher condensation rate with the same cooling (see Sect. 2.4). The fog conditions on 28 October 2014 and 2 November 2015 differ in condensation rate by 16 g m^{-2} h^{-1}. These two fog conditions have a very similar temperature, so the difference is

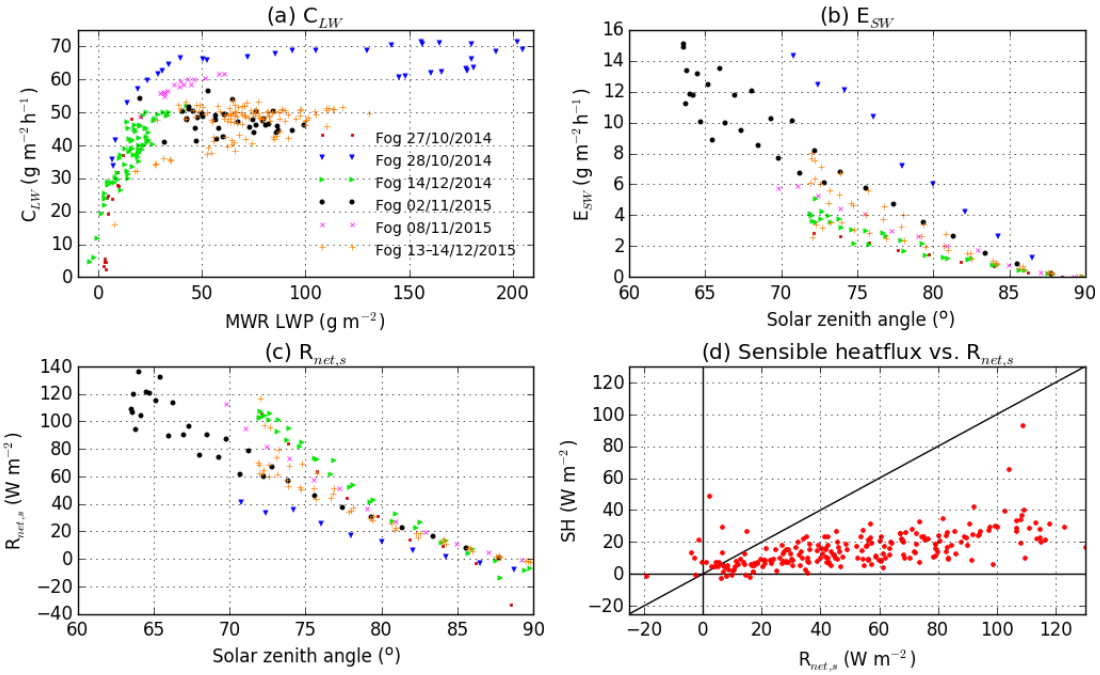

Figure 5. C_{LW} **(a)**, E_{SW} **(b)** and $R_{\mathrm{net,s}}$ **(c)** (defined in Sect. 2.1), calculated every 15 min from formation time to dissipation time for the six fog events without clouds above in Table 2. **(d)** Measured 10 min average sensible heat flux at 2 m vs. measured 10 min average $R_{\mathrm{net,s}}$ (at 10 m) during the daytime fog hours of all fog events in Table 2, excluding 28 October 2014 because the measurements are biased.

explained by the LW radiative budget at the fog top, which is $-100\,\mathrm{W\,m^{-2}}$ on 28 October 2014, i.e. $27\,\mathrm{W\,m^{-2}}$ more negative than on 2 November 2015. This higher LW deficit can be explained by the lower humidity above the fog (Fig. 6d) and possibly also the lower temperature in the first 1 km above the fog (Fig. 6c). Thus, C_{LW} in fog without a cloud above varies significantly both from differences in fog OD, the fog temperature and the LW emission from the atmosphere above.

Figure 5b shows E_{SW}, which varies in 0–15 $\mathrm{g\,m^{-2}\,h^{-1}}$. E_{SW} obviously depends on the amount of incoming SW radiation, so we plot it against the solar zenith angle. At one given angle, there is a variability of a factor of 4 between the fog cases. This variability is explained by the fog OD. Thinner fog, such as on 27 October 2014 and 14 December 2014, will interact less with the SW radiation and therefore absorb less than thicker fog, such as on 28 October 2014 and 2 November 2015. E_{SW} will also depend on fog temperature through $\frac{\mathrm{d}\rho_{\mathrm{s}}}{\mathrm{d}T}$, just like C_{LW}. All in all, E_{SW} is generally much smaller than C_{LW}, even for thick fog near (winter) midday, but it still represents a significant reduction in the net radiation-driven condensation rate in fog in daytime relative to night-time.

$R_{\mathrm{net,s}}$ varies from 0 to $140\,\mathrm{W\,m^{-2}}$ during the daytime in the six fog cases (Fig. 5c). Absorption of SW is the dominant term, and therefore we highlight the dependency on the solar zenith angle. However, net LW emission significantly reduces R_{net} below non-opaque fog (27 October and 14 December 2014) with up to $-60\,\mathrm{W\,m^{-2}}$ and also frequently reaches $-10\,\mathrm{W\,m^{-2}}$ in the opaque fog because the ground is warmer than the fog (not shown). Since thicker fog reflects more SW radiation, the absorbed SW is smaller below thick fog than thin fog at a given solar zenith angle, and this gives rise to the case-to-case variability in $R_{\mathrm{net,s}}$ of a factor of 3 seen in Fig. 5c, e.g. from $40\,\mathrm{W\,m^{-2}}$ to $120\,\mathrm{W\,m^{-2}}$ at a solar zenith angle of 70°. To study to what extent this absorbed heat is transferred to the fog, we compare the measurements of $R_{\mathrm{net,s}}$ (at 10 m) with the sensible heat flux measurements at 2 m during fog in daytime (Fig. 5d). The two parameters are clearly correlated ($R = 0.56$). The fraction of sensible heat flux to $R_{\mathrm{net,s}}$ in these data is found to have a 25 and 75 percentile of 0.20 and 0.40, respectively. Since $1\,\mathrm{W\,m^{-2}}$ heating of the fog corresponds to an evaporation rate of about $0.7\,\mathrm{g\,m^{-2}\,h^{-1}}$ (Sect. 2.4), the sensible heat flux will cause an evaporation rate of roughly 0.15–0.30 $\mathrm{g\,m^{-2}\,h^{-1}}$ per $\mathrm{W\,m^{-2}}$ of radiation absorbed at the surface. With a surface absorption of $100\,\mathrm{W\,m^{-2}}$ at midday below thin fog, this correspond to 15–30 $\mathrm{g\,m^{-2}\,h^{-1}}$ of evaporation, which is almost as large as C_{LW}. Considering that measurements using the eddy covariance method could underestimate the turbulent heat fluxes (Foken, 2008), the heating of the fog by $R_{\mathrm{net,s}}$ might in reality be even stronger than what we found here.

4.3 Radiation-driven condensation and evaporation in a fog with clouds above

Figure 7 presents the fog event occurring on 1 January 2016, during which the BASTA cloud radar detects cloud layers

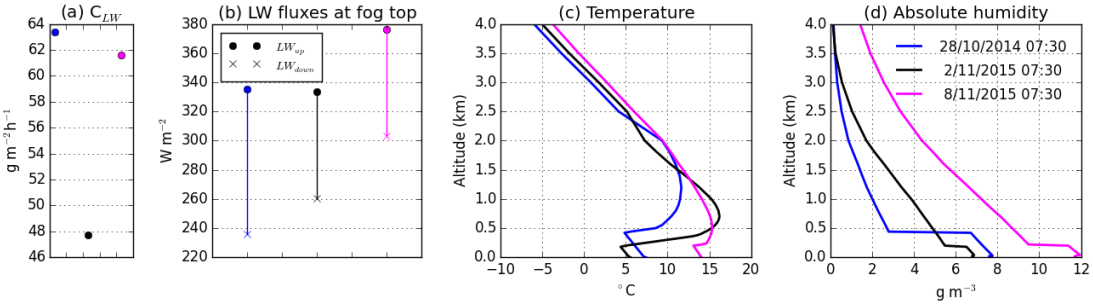

Figure 6. Comparison of three fog events at 07:30 UTC: **(a)** C_{LW} (defined in Sect. 2.1); **(b)** LW fluxes at fog top (cross is downwelling, circle is upwelling, thus length of vertical line indicates the (negative) LW budget at fog top). **(c)** Temperature and **(d)** humidity profiles estimated with the method described in Sect. 3.3. The fog top is located at the bottom of the sharp temperature inversion.

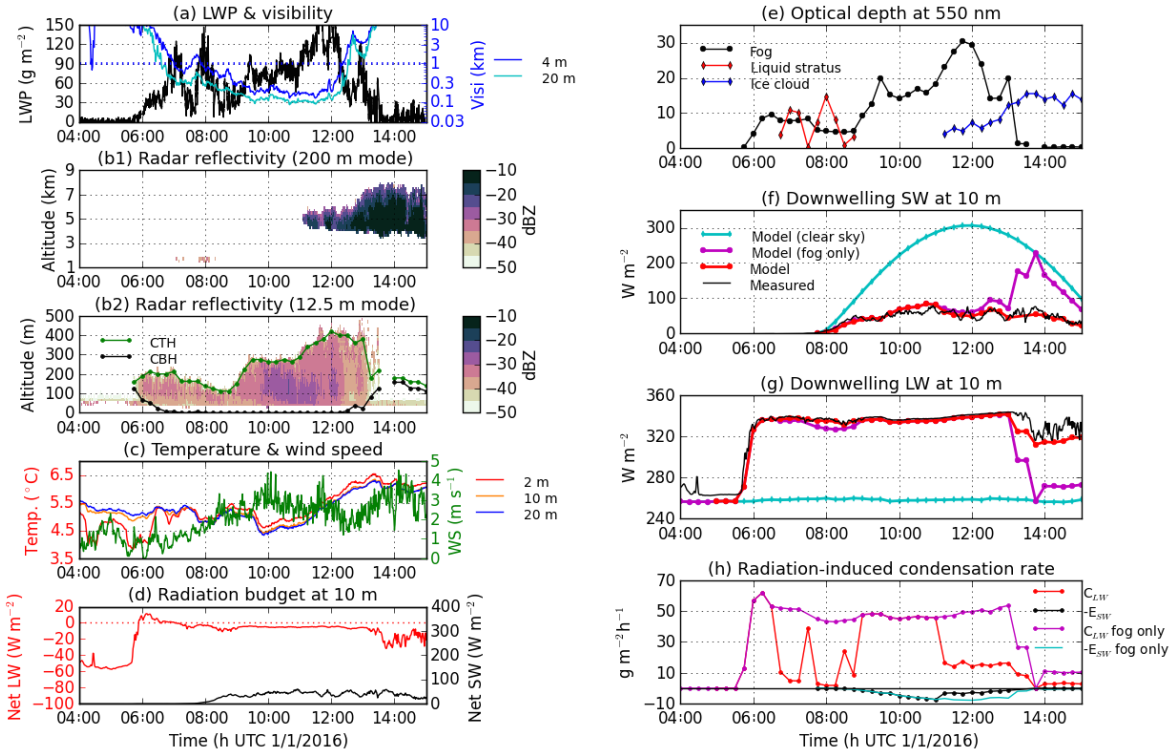

Figure 7. Case study of the fog event on 1 January 2016, when clouds appeared above the fog. Panels are the same as in Fig. 3, with a few additions. In **(b)**, there are two panels, the upper one showing the reflectivity from the 200 m mode of the radar and the lower one that of the 12.5 m mode. In **(e)**, the optical depths of the cloud layers above the fog are also indicated, and in **(f–h)** the results obtained when including only the fog (and not the higher clouds) have been added.

appearing above the fog: traces of a stratus at ≈ 1.6 km from 07:00 to 08:30 UTC, and a higher and thicker stratus after 11 UTC. During the presence of the second cloud, the fog evaporates rapidly around 12–13 UTC, leaving only traces of a cloud at ≈ 150 m (Fig. 7b).

The radar mode at 200 m resolution is just sensitive enough to detect the cloud at ≈ 1.6 km, so its geometrical thickness is uncertain. However, peaks in the LWP (Fig. 7a) appear at corresponding times when the cloud is observed by the radar. We therefore model the cloud as a liquid stratus and partition the LWP between the fog and overlying stratus cloud in the following way: in the period 06:45 to 07:30 (07:30 to 08:45) UTC, the first 30 (20) g m^{-2} is attributed to the fog layer, and the rest to the stratus. This results in an OD of the stratus of ≈ 10 when it is present (Fig. 7e). The stratus has a strong impact on C_{LW} (Fig. 7h), reducing it by 90–100 %, because it increases the downwelling LW radiation at the fog top (not shown). The presence of the stratus may therefore explain why the fog does not develop verti-

cally, but instead decreases its geometric thickness and LWP while the stratus is present (Fig. 7a–b).

A second higher cloud appears at 11 UTC between 4 and 6 km. The cloud persists and deepens while the fog dissipates. From the radiosounding at 11:35 UTC, we know that the temperature in the 4–6 km layer is −25 to −13 °C. Since the LWP drops to zero after the fog cloud disappears, we choose to model the overlying cloud as a pure ice cloud, even though it is possible that it also contains liquid water while overlying the fog, which could explain the peaks in LWP around 12 UTC (Fig. 7a). To get a rough estimate of the OD of this cloud, we use an ice water content of 0.05 g m^{-3}, which corresponds to the average ice water content found by Korolev et al. (2003) for glaciated frontal clouds at temperatures of around −20 °C. This results in an OD of ≈ 5 in the beginning, growing with the observed thickness of the cloud (Fig. 7e). This cloud reduces C_{LW} by ≈ 70 % (Fig. 7h), which is less than the effect of the first stratus. This is because the cloud is higher and colder, thus emitting less LW than the first cloud (Stephan Boltzmann's law). However, its effect is still more important than the variability in C_{LW} found between cases without a higher cloud (Sect. 4.2). The cloud at 4 km also causes a 50–80 % reduction in E_{SW} and a 15–30 % reduction in the SW that reaches the surface. These effects are due to reflection and absorption of SW radiation by the overlying cloud, and they increase with time as the cloud thickens. Thus, in the SW the cloud has the opposite effect on the fog LWP to that in the LW. However, the LW effect is more important than the SW effect for the fog LWP budget in this case: C_{LW} decreases by ≈ 35 g m^{-2} h^{-1} due to the cloud presence, which is much more than the decrease in E_{SW} of ≈ 4 g m^{-2} h^{-1} or the ≈ 10 W m^{-2} reduction in the SW absorbed at the surface (not shown) which should correspond to less than 5 g m^{-2} h^{-1} decrease in evaporation by sensible heat flux (see Sect. 4.2).

The modelled and observed downwelling SW at 10 m are compared in Fig. 7f. They agree well both when there is only the fog (e.g. at 10 UTC), when both the fog and the cloud at 4 km are present (e.g. at 12 UTC) and when only the cloud is present (e.g. at 14 UTC), which provides a validation of the estimated OD of the fog and the cloud.

5 Discussion

We link the variability in the radiative parameters found in Sect. 4 to various properties of the atmospheric conditions, such as fog LWP and the presence of clouds above the fog. In order to understand better how each factor impacts the radiation-driven condensation and evaporation, theoretical sensitivity studies are performed in which each input parameter is varied separately. Sensitivity to fog microphysical properties, temperature and humidity is analysed in Sect. 5.1, while impacts of higher clouds are explored in Sect. 5.2. Finally, a discussion of uncertainties is presented in Sect. 5.3.

5.1 Sensitivity of radiation-driven condensation and evaporation to fog properties, temperature and humidity

Figure 8 explores the sensitivity of our radiation parameters to the LWP and droplet sizes of the fog, which together determine its optical properties (see Sect. 3.2). The model runs use the input of the semi-transparent fog on 27 October 2014 at 08:30 UTC (Fig. 3), modifying only the fog LWP and/or the droplet effective radius.

Figure 8a shows that C_{LW} increases fast with fog LWP when LWP is less than ≈ 30 g m^{-2}. For higher LWP, the increase is much weaker, and beyond 50 g m^{-2} it approaches a constant value as the emissivity of the fog approaches 1. The dependency on r_{eff} for a given LWP is weak, which is due to a near cancellation between decreasing surface area and increasing absorption efficiency with r_{eff}, so that the LW optical depth of liquid clouds are almost entirely determined by LWP (Platt, 1976). The LW cooling process is thus sensitive to the fog LWP only if LWP $< \approx 40$ g m^{-2}, and it is not sensitive to droplet sizes within the range of effective radii studied here. Figure 8d shows that the downwelling LW flux at the surface increases with LWP in a very similar way to C_{LW}, which we use to evaluate the uncertainty in C_{LW} due LWP uncertainty (Appendix A).

Figure 8b shows that E_{SW} also increases with LWP. Compared to C_{LW}, E_{SW} depends less strongly on LWP for thin fog, but it keeps increasing with LWP also for opaque fog with LWP well above 50 g m^{-2}. This is due to the SW radiation being largely diffused in the forward direction, rather than being absorbed, so that much SW still remains to be absorbed even far down inside an optically thick cloud. Note also that some absorption occurs even in when LWP = 0, because of absorption by water vapour inside the cloud (Davies et al., 1984). E_{SW} is also sensitive to the sizes of the droplets: for a given LWP, the largest effective radius (10.7 µm) gives a ≈ 50 % larger evaporation rate than the smallest effective radius (4 µm), which can appear counterintuitive since the total surface area of the DSD decreases with r_{eff}. This occurs due to an increase in absorptivity in the near infrared with droplet size (Ackerman and Stephens, 1987).

The dependency of $R_{net,s}$ on fog properties (Fig. 8c) is the sum of LW and SW cloud effects. The fog reduces the SW reaching the surface by reflecting SW radiation, and this effect increases with LWP and decreases with r_{eff} (Twomey, 1977). In the LW, radiative cooling of the surface is reduced as LWP increases, thus increasing $R_{net,s}$ with LWP, because the cooling is transferred to the fog top. Beyond LWP ≈ 40 g m^{-2}, the sensitivity of $R_{net,s}$ to LWP is only due to SW. $R_{net,s}$ is about half as large when LWP is 100 g m^{-2} than for LWP of 20 g m^{-2}. In thick fog, the smallest droplets only let through half as much SW as the biggest droplets, while the dependency on droplet size is less pronounced for thin fog.

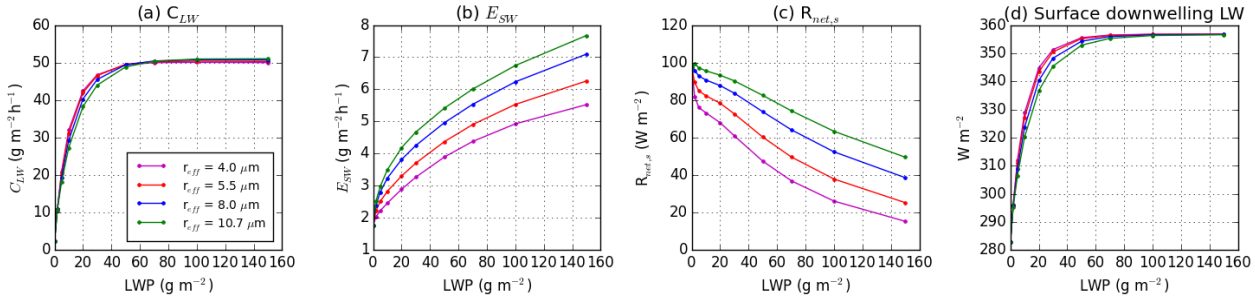

Figure 8. Dependency of C_{LW} **(a)**, E_{SW} **(b)**, $R_{\mathrm{net,s}}$ **(c)** (defined in Sect. 2.1), and the downwelling LW flux at the surface **(d)** on the fog LWP and effective radius. All other input data are fixed to the values of 27 October 2014 at 08:30 UTC: the fog is 100 m thick with no above clouds and there is a solar zenith angle of 73.9°.

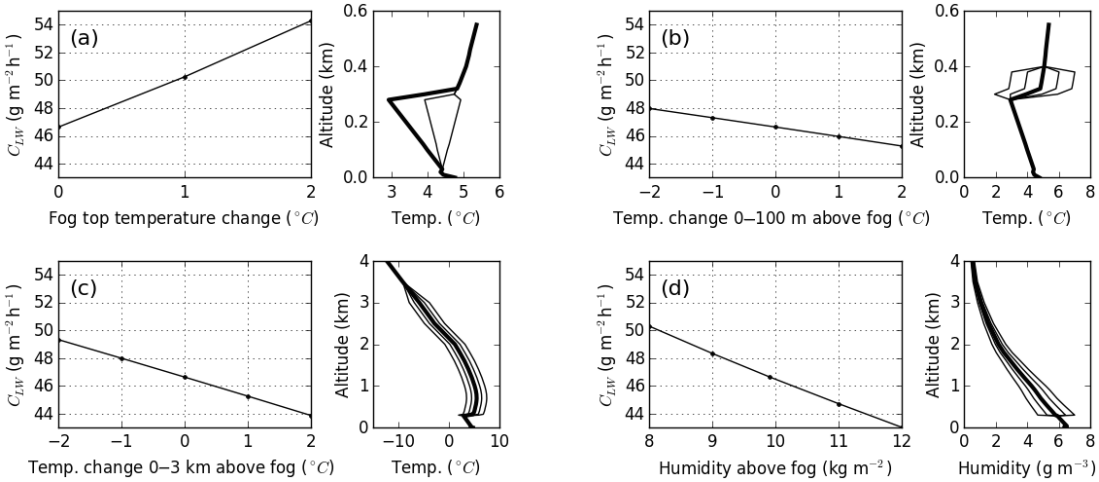

Figure 9. Sensitivity of C_{LW} (defined in Sect. 2.1) to changing the fog top temperature **(a)**, the temperature in the first 100 m above the fog **(b)**, the temperature in the first 3 km above the fog **(c)** and the humidity above the fog **(d)**. All other input data are kept constant at the values for 13 December 2015 at 10 UTC: the fog is 290 m thick with no clouds above and a visible optical depth of 16.4. To the right of each result is a plot showing how the profile of temperature or humidity is modified from the original profile (thick line).

In Fig. 9, we explore the sensitivity of C_{LW} to the vertical profiles of temperature and humidity. In these tests, we use the opaque fog on 13 December 2015 at 10 UTC. Figure 9a confirms that an increase in fog top temperature leads to a higher C_{LW}, by about 3 g m^{-2} h^{-1} per °C, caused both by higher emission of LW radiation by the fog (Stephan–Boltzmanns law) and the increase with temperature of the condensation rate per W m^{-2} (Sect. 2.4). A temperature change in the atmosphere above the fog has a weaker impact of about 1.4 g m^{-2} h^{-1} per °C (Fig. 9c). Figure 9b illustrates that the first 100 m above the fog is in fact responsible for half of this effect, which is because most of the downwelling LW radiation under a cloud-free sky comes from the first few tens of metres, as noted by Ohmura (2001). The sensitivity to temperature above the fog is thus mainly related to the strength of the inversion at the fog top. The sensitivity of C_{LW} to increased water vapour above the fog is about 2 g m^{-2} h^{-1} per added kg m^{-2} of IWV (Fig. 9d), which confirms the importance of the dryness of the atmosphere found in Sect. 4.2.

5.2 Impact of radiation-driven condensation and evaporation on fog dissipation

The evolution of a fog depends on the competition between processes that produce liquid water and processes that remove it. Radiative cooling from the emission of LW is found to be capable of producing 40–70 g m^{-2} of liquid water per hour in the absence of a higher cloud layer, which is a significant source for maintaining the fog LWP and capable of renewing the fog water in 0.5–2 h (see Sect. 4.2). If a fog layer does not increase its LWP in spite of the LW cooling, it is because the sink processes for liquid water amount to a similar magnitude. Sink processes can be heating which counteracts the cooling: either the radiative heating processes studied in this paper or other sources of heat, such as entrainment at fog top or adiabatic heating from subsidence. Another sink process is the deposition of fog droplets at the surface, which has been found to be important for limiting fog LWP (Mason, 1982; Price et al., 2015). If the LW cooling decreases while

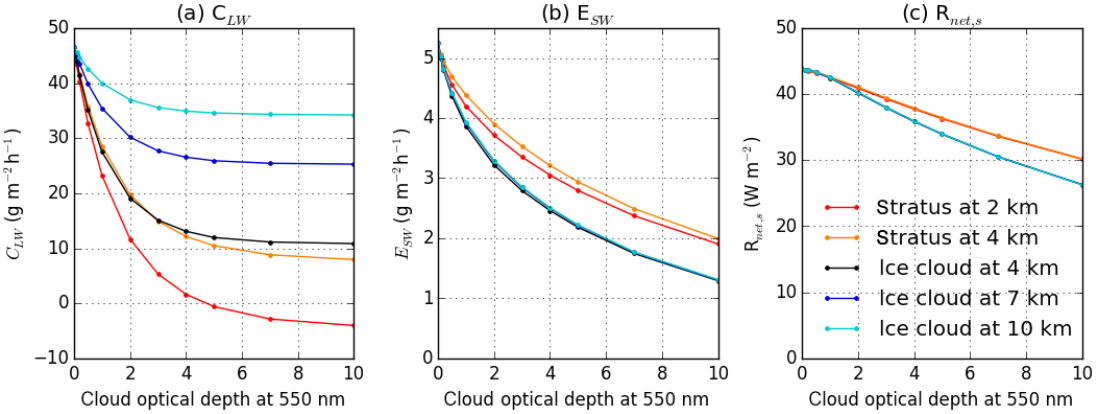

Figure 10. Sensitivity of C_{LW} **(a)**, E_{SW} **(b)** and $R_{\mathrm{net,s}}$ **(c)** (defined in Sect. 2.1) to the altitude, type and visible optical depth of a cloud appearing above the fog. All other input data are kept constant at the values for 13 December 2015 at 10 UTC (the same time as in Fig. 9). Solar zenith angle is 75.7°.

the sink processes do not, it will shift the LWP balance towards a reduction, eventually leading to fog dissipation. We found that C_{LW} increases with fog temperature and decreases with the humidity in the overlying atmosphere; thus, warm fog with a dry overlying atmosphere will be more resilient to dissipation than colder fog with a more humid overlying atmosphere. However, these factors cannot be expected to vary very fast, so they will probably not be an initiating factor for the dissipation of a fog layer. In contrast, the appearance of a second cloud layer above the fog can occur very fast by advection and instantly reduce C_{LW} by several tens of $\mathrm{g\,m^{-2}\,h^{-1}}$ (Sect. 4.3). This should be sufficient to shift the balance in LWP in the direction of a fast reduction, leading to the dissipation of the fog.

In Fig. 10, we explore how a higher cloud affects the radiation-driven condensation and evaporation in an opaque fog as a function of the OD and base altitude of the cloud. The impact on C_{LW} (Fig. 10a) increases with the cloud OD, but beyond an OD of 5 this dependency is no longer very strong. The effect of the cloud weakens with increasing altitude of the cloud base; an opaque cloud at 10 km reduces C_{LW} by only $\approx 30\,\%$, while a cloud at 2 km reduces it by $\approx 100\,\%$. This altitude dependency is due to the decrease of the temperature of the cloud with altitude due to the atmospheric lapse rate. At a given cloud OD and altitude, the effects of ice and liquid clouds are very similar. E_{SW} is also reduced by the presence of a higher cloud (Fig. 10b), since the cloud absorbs and reflects the SW radiation that would otherwise be absorbed in the fog. It also decreases with OD of the cloud, while the altitude matters little. The decrease with cloud OD continues even for opaque clouds. However, beyond an OD of 5 it has already been more than halved and it decreases less rapidly. Since the fog in this case is opaque to LW, the cloud affects $R_{\mathrm{net,s}}$ (Fig. 10c) mainly through its reflection of SW radiation, and the change is not dramatic since the fog is already reflecting most of the SW radiation. However, for thin fog, $R_{\mathrm{net,s}}$ is more strongly affected by the cloud, increasing due to the LW emission by the cloud and decreasing due to the SW reflection, similarly to how it is affected by fog LWP for thin fog in Fig. 8c (not shown).

The following conceptual comparison of the fog case on 13 December 2015 (Fig. 4) and the fog case on 1 January 2016 (Fig. 7) illustrates the possible role of radiation in determining the different evolutions of these two fog events. Both occur near midwinter at a temperature of about 5 °C, and both are optically thick with LWP $\approx 100\,\mathrm{g\,m^{-2}}$ around midday (a). While the fog cloud dissipates completely right after midday on 1 January 2016, the fog on 13 December 2015 only slightly reduces its LWP during the afternoon, from ≈ 70 to $\approx 50\,\mathrm{g\,m^{-2}}$. Based on the radiative transfer calculations, on 13 December 2015 C_{LW} is $\approx 50\,\mathrm{g\,m^{-2}\,h^{-1}}$ and varies little, while on 1 January 2016 C_{LW} is reduced from $50\,\mathrm{g\,m^{-2}\,h^{-1}}$ to $15\,\mathrm{g\,m^{-2}\,h^{-1}}$ when the higher cloud appears (h). The production of liquid water by LW cooling is thus $35\,\mathrm{g\,m^{-2}\,h^{-1}}$ higher in the fog on 13 December 2015 than in the fog on 1 January 2016, and the sink processes for liquid water must be stronger to dissipate the former. Conversely, the cloud also reduces the SW heating of the fog: at midday, E_{SW} is $\approx 5\,\mathrm{g\,m^{-2}\,h^{-1}}$ less on 1 January 2016 compared to 13 December 2015, and the SW reaching the surface is $\approx 40\,\mathrm{W\,m^{-2}}$ less (f) (which means that the evaporation rate from sensible heat is likely $\approx 10\,\mathrm{g\,m^{-2}\,h^{-1}}$ less, see Sect. 4.2). However, this is less important than the difference in C_{LW}. Differences in other processes probably also play a role in the very different developments of the two fog events. For instance, the higher wind speed on 1 January 2016 ($\approx 3\,\mathrm{m\,s^{-1}}$, against 1–1.5 $\mathrm{m\,s^{-1}}$ on 13 December 2015) could indicate that loss of liquid water by turbulent processes is more significant on 1 January 2016 and also contributes to its dissipation.

5.3 Uncertainty analysis

Table 3 provides rough estimates of the relative impact of the uncertainties in different measured and retrieved input data to the calculated values of C_{LW}, E_{SW} and $R_{\mathrm{net,s}}$. We assume that the uncertainties in these input data are more significant than the uncertainties related to the physics of the radiation model itself. The quantitative estimates are based on the results found in the sensitivity studies and on some further investigations that will be explained below.

Firstly, uncertainty arises from the estimates of fog optical properties. The uncertainty in fog LWP is found to be of the order of 5–10 $\mathrm{g\,m^{-2}}$ when LWP $< 40\,\mathrm{g\,m^{-2}}$ (Appendix A). This corresponds to an uncertainty in C_{LW} of 10–15 $\mathrm{g\,m^{-2}\,h^{-1}}$ (or 50 %) when LWP $< 20\,\mathrm{g\,m^{-2}}$ and 3–5 $\mathrm{g\,m^{-2}\,h^{-1}}$ (or 10 %) when LWP is 20–40 $\mathrm{g\,m^{-2}}$ (Fig. 8a). E_{SW} is affected both by the fog LWP and r_{eff} (Fig. 8b). The estimated uncertainty in r_{eff} of 30 % (Appendix B) indicates an uncertainty of ≈ 20 % in E_{SW}, while the LWP uncertainty of $\approx$ 5–10 $\mathrm{g\,m^{-2}}$ causes a similar uncertainty for small LWP, but lower for higher LWP (Fig. 8b). These uncertainties in LWP and r_{eff} will also cause uncertainties of the order of 20–30 % in $R_{\mathrm{net,s}}$, based on Fig. 8c. The uncertainties in $R_{\mathrm{net,s}}$ are also estimated using the observed and modelled downwelling fluxes at 10 m, finding an rms error of 0.046 in the SW transmissivity (translating to 20 $\mathrm{W\,m^{-2}}$ SW absorption at solar zenith angle of 70°), and an rms error in the LW absorption of 13.8 $\mathrm{W\,m^{-2}}$ when LWP $< 20\,\mathrm{g\,m^{-2}}$ and 4.8 $\mathrm{W\,m^{-2}}$ when LWP is in 20–40 $\mathrm{g\,m^{-2}}$ (Appendix A). Finally, it should be noted that in the presence of a higher cloud containing liquid, the partitioning of LWP between the fog and this cloud will increase the uncertainty in the fog LWP.

Neglecting aerosols in the calculations is another source of uncertainty. While the scattering by aerosols will be small compared to that of the fog, additional in-fog heating by aerosol absorption of solar radiation can significantly increase E_{SW}, since multiple scattering by droplets increases the probability of absorption (Jacobson, 2012) and since the fog droplets themselves only weakly absorb in the near infrared. Previous studies (Chýlek et al., 1996; Johnson et al., 2004) have found that this increase in absorption is limited to ≈ 15 % in stratocumulus clouds. However, this effect might be enhanced in fog, since the aerosol concentration can increase because the boundary layer is shallow and the fog is in direct contact with the surface. We test the impact of aerosols on E_{SW} by adding two standard aerosol populations described by Hess et al. (1998) to the fog layer on 13 December 2015, with relatively low (0.05) and relatively high (0.15) aerosol optical depth at 550 nm (AOD) (Table 4). The main difference between the two populations is that the urban aerosols include more black carbon particles than the continental average aerosols. Black carbon is responsible for most of the absorption, while its contribution to AOD is only 20 and 6 % in the two populations. The resulting increase in E_{SW} ranges from ≈ 10 % for continental average aerosols of AOD 0.05 to more than 100 % for urban aerosols with AOD 0.15 (Table 4). Retrievals of AOD at SIRTA from a sun photometer, which requires direct sunlight and therefore has sparse temporal coverage, indicate that AOD is closer to 0.05 than 0.15 most of the time in October–March. Considering this, and that some aerosols will be located above the fog, the runs where AOD is set to 0.05 are the most realistic and show that the increase in E_{SW} due to aerosols is probably not higher than 10–30 %. However, if black carbon optical depth increases due to a strong pollution event, E_{SW} could be more strongly enhanced. To investigate the aerosol effect on E_{SW} in more detail, measurements of the aerosol chemical composition should be used in addition to the AOD, since the most important parameter to be estimated is the fraction of AOD represented by absorbing aerosols. Due to the swelling of non-absorbing water soluble aerosols, this fraction is also impacted by the relative humidity at which AOD is measured. The interaction of the aerosols with the fog (e.g. immersion, wet deposition) can also modify their optical properties (Chýlek et al., 1996).

C_{LW} has uncertainty related to the temperature and humidity profiles. As the screen temperature is known, fog temperature is more uncertain in opaque fog than in thin fog through the temperature difference between screen level and fog top. Since there is observational evidence that fog temperature profile is near adiabatic (Sect. 3.3), we assume that the uncertainty of the fog top temperature is less than 1 °C even for very thick fog, which should impact C_{LW} less than 10 % (Fig. 9a). The MWR temperature profile has an uncertainty of less than 1 °C in the lower atmosphere (Löhnert and Maier, 2012) and even with significant uncertainty in the shape of the temperature inversion above the fog, the sensitivity studies indicate that the impact on C_{LW} is well below 10 % (Fig. 9b–c). The IWV of the MWR has an uncertainty of 0.2 $\mathrm{kg\,m^{-2}}$ (Sect. 2.2), which corresponds to a very small uncertainty in C_{LW} (Fig. 9d). However, as the vertical distribution of humidity is roughly estimated with only 2 degrees of freedom (Löhnert et al., 2009), sharp decreases in humidity, e.g. at the top of the boundary layer, will not be correctly represented. By analysing a case study in which the humidity profiles from the radiosonde and the MWR disagree strongly due to such a sharp decrease, we find an induced bias in C_{LW} of less than 10 % ($\approx 4\,\mathrm{g\,m^{-2}\,h^{-1}}$).

We finally turn to the uncertainties related to the properties of the higher clouds. Firstly, as shown in Sect. 4.3, higher clouds may be undetected by the radar due to their low reflectivity. This is confirmed from non-fog conditions, when the ceilometer often detects low stratiform clouds that significantly affect the downwelling LW at 10 m but that are invisible to the radar (not shown). For the method of this paper to be reliable in cases where such thin clouds may occur, a more sensitive radar is required. According to Stephens et al. (2002), low-level liquid clouds frequently have reflectivity down to −40 dBZ. The radar should therefore preferably

Table 3. Rough estimates of the relative uncertainty (in % of the estimated value) of each radiation parameter (defined in Sect. 2.1) due to various sources of uncertainty, for thin (LWP $< \approx 30\,\mathrm{g\,m^{-2}}$) and thick (LWP $> 30\,\mathrm{g\,m^{-2}}$) fog. The last two rows are relevant when an opaque or semi-transparent cloud overlies the fog. See text for details.

Uncertainty source	C_{LW}		E_{SW}		$R_{\mathrm{net,s}}$ (day)	
	Thin	Thick	Thin	Thick	Thin	Thick
Fog LWP	10–50[b]	< 10	20–40[b]	10	10	10
Droplet effective radius	< 5	< 5	20	20	20	30
Neglecting absorbing aerosols	–	–	10–30[a]	10–30[a]	< 5	< 5
Temperature profile	5	5–10	–	–	–	–
Humidity profile	5–10	5–10	–	–	–	–
OD of semi-transparent cloud above	20–80[c]	20–80[c]	50–80	50–80	30	20
OD of opaque cloud above	< 10	< 10	50	50	30	20

[a] Uncertainty towards higher values only. [b] Uncertainty is highest for the thinnest fog. [c] Uncertainty is bigger for low clouds than high clouds.

Table 4. Effect on E_{SW} (defined in Sect. 2.1) by adding aerosols to the fog layer on 13 December 2015 at 12 UTC. Urban and continental average aerosols are defined as in Hess et al. (1998). The aerosol optical depth (AOD) is spread evenly across the 275 m thick fog layer.

Type of aerosol aerosol	Aerosol single scattering albedo at at 550 nm, at 80 % relative humidity	AOD at 550 nm, at 80 % relative humidity	E_{SW} ($\mathrm{g\,m^{-2}\,h^{-1}}$)
No aerosols	–	0	7.9
Urban	0.817	0.05	11.0
		0.15	16.5
Continental average	0.925	0.05	8.8
		0.15	11.5

have a sensitivity of −40 dBZ for all altitudes at which liquid clouds occur (≈ 1–6 km), even though it is probably less critical for mid-level clouds, which often contain some ice, which enhances their reflectivity. At high altitudes, thin cirrus clouds may also have reflectivity down to −40 dBZ, but those with reflectivity below −25 dBZ rarely have OD > 1 (Stephens et al., 2002). Since high-level clouds with OD < 1 do not impact our results dramatically (Fig. 10), a sensitivity of −25 dBZ at high altitudes is acceptable.

Given that the higher cloud is detected, its altitude and thus temperature is readily estimated, so the uncertainty in its radiative impact is mainly related to its emissivity, which based solely on radar observations probably cannot be less uncertain than a factor of 2. If we are confident that the cloud is opaque (OD > ≈ 5), the uncertainty in its impact on C_{LW} is only a few $\mathrm{g\,m^{-2}\,h^{-1}}$, while a less opaque cloud will cause uncertainty of several tens of $\mathrm{g\,m^{-2}\,h^{-1}}$ (Fig. 10a). The relative uncertainty in E_{SW} and $R_{\mathrm{net,s}}$ caused by higher clouds are smaller than for C_{LW} when the cloud is semi-transparent, but on the other hand it is also important for thick clouds (Fig. 10b–c). Finally, it should be noted that cases of fractional cloud cover also will cause uncertainty, since the radar only sees what appears directly above, while clouds covering only parts of the sky also affect the radiation, in particular if they block the direct sunlight.

To conclude, the uncertainty in C_{LW} is small (≈ 10 %) when the fog is opaque (LWP > ≈ $30\,\mathrm{g\,m^{-2}}$) and there is either no higher cloud or the higher cloud is opaque and covers the entire sky, while a non-opaque fog and/or non-opaque overlying cloud will introduce higher uncertainty. A similar conclusion can be drawn for E_{SW}, although the uncertainty in the case of opaque fog/cloud remains higher than for C_{LW}, since the SW radiation penetrates deeper into the clouds than the LW cooling.

6 Conclusions

In this study, the magnitude and variability of the radiation-driven condensation and evaporation rates in continental fog during midlatitude winter have been quantified from observations of the atmospheric profile. We used a radiative transfer code to quantify the immediate tendencies in fog liquid water due to radiative cooling and heating, before they are modified by turbulent motions. Based on the results of this study, Table 5 summarises how different atmospheric conditions will impact the susceptibility of a fog to dissipation by affecting the radiative processes.

Firstly, the cooling of the fog by emission of LW radiation provides an important source of liquid water. In opaque fog (LWP > ≈ $30\,\mathrm{g\,m^{-2}}$) without an overlying cloud layer, this cooling seen in isolation will cause 40–70 $\mathrm{g\,m^{-2}\,h^{-1}}$ of

Table 5. Summary of how the susceptibility of fog to dissipation is affected by variability in atmospheric conditions through radiative processes. Positive (negative) means that the fog is more (less) likely to dissipate due to lower (higher) net production of liquid water by the indicated radiative process (defined in Sect. 2.1) due to the indicated atmospheric property. See text for details.

Atmospheric property	Less LW-driven condensation (C_{LW})	More SW-driven evaporation (E_{SW})	More surface heating ($R_{net,s}$)
Clouds above fog	strongly positive	negative	negative
Thin fog LWP ($< 30\,g\,m^{-2}$)	strongly positive	negative	positive
Absorbing aerosols in fog	–	positive	–
Higher fog temperature	negative	weakly positive	weakly positive
More humidity in atmosphere above fog	positive	–	–
Stronger temperature inversion above fog	weakly positive	–	–

condensation, which means that the fog typically can renew its liquid water in 0.5–2 h through this process. Its variability can mainly be explained by fog top temperature and the humidity above the fog, with warmer fog below a drier atmosphere producing more liquid water. In thin fog, the condensation is weaker, and the estimate is more uncertain due to the uncertainty in LWP of the fog.

The solar radiation absorbed by fog droplets causes a radiative heating of the fog layer during the daytime. This heating decreases with solar zenith angle and increases with droplet effective radius and fog LWP. At (winter) midday, the evaporation rate from this heating can reach $15\,g\,m^{-2}\,h^{-1}$ in thick fog, while it is weaker for thin fog ($0–5\,g\,m^{-2}\,h^{-1}$), based on absorption by pure liquid droplets only. The role of absorbing aerosols in fog is not extensively studied in this paper, but our results indicate that it increases the absorption of solar radiation by 10–30 % in a typical air mass at SIRTA. This aerosol absorption effect can be worth investigating in more detail using observations of aerosol chemical composition, as it could be stronger during pollution events. The important parameter is the optical depth of the absorbing aerosols, which might be only a small fraction of the total aerosol optical depth.

The radiative heating of the surface in daytime is more important in thin fog than thick fog, and it is found to vary from 40 to $140\,W\,m^{-2}$ at a solar zenith angle of 70° from the thickest to the thinnest fog studied here. In situ observations indicate that at least 20–40 % of this energy is transferred to the fog as sensible heat. Since $1\,W\,m^{-2}$ heating of the fog corresponds to an evaporation rate of $\approx 0.7\,g\,m^{-2}\,h^{-1}$, this process can cause an evaporation rate of up to $30\,g\,m^{-2}\,h^{-1}$ when the sun is high and thus is likely to be very important for reducing the LWP of the fog. A more detailed investigation of the surface energy budget during fog could lead to a more precise quantification of the evaporation of fog by sensible heat.

The appearance of a second cloud layer above the fog strongly reduces the LW cooling of the fog, especially a low cloud. The LW-induced condensation rate can be reduced by 100 % if the low cloud is optically thick, and even by more than 50 % for a semi-transparent cloud of optical depth 1. The presence of an overlying cloud can therefore be a determining factor for fog dissipation as the fog will then have much of its production of liquid water cut off. In cases in which no cloud appears above the fog it is unlikely that the LW cooling can change fast enough for it to be a determining factor for the dissipation. The detection of clouds above the fog with the cloud radar is therefore crucial for analysing the impact of radiative processes on fog dissipation. To detect all important clouds above the fog, the radar sensitivity must be sufficient to capture thin water clouds, requiring a sensitivity of −40 dBZ in the lower troposphere, and optically important high clouds, requiring a sensitivity of −25 dBZ in the upper troposphere. The current generation BASTA radars, which have a sensitivity of −40 dBZ up to 4 km and −30 dBZ at 10 km, should be able to detect most of the important clouds.

The results were obtained from seven observed fog events at the SIRTA observatory (Table 2) as well as sensitivity studies. Since our methodology treats radiative processes separately from dynamical processes, these results should be applicable to all fog occurring in the range of temperature and integrated water vapour (IWV) of the events in this study, which cover the range (−1)–14 °C and 6–28 $kg\,m^{-2}$. Thus it is a significant sample of midlatitude winter conditions. The same methodology should in principle be applicable to other climate zones as well, although ice crystals in fog occurring in very cold conditions would require a different retrieval method for fog optical properties due to the larger particle sizes (Gultepe et al., 2015). For pure liquid fog, the methodology should be generalisable to all fog types, as the radiative processes are not directly dependent on the fog formation mechanism.

The results of this paper have been obtained from the use of multiple instruments, in particular cloud radar, ceilometer and microwave radiometer. If these measurements can be rapidly transferred and processed, the methodology of this paper could be applied to quantify the radiation-driven condensation and evaporation rates in the fog in real time to be used to support short-term fog forecast. In order to be less instrumentally demanding and thus more applicable to other

sites, a simplified method using only the cloud radar and ceilometer could be envisaged, supplemented by screen temperature and visibility measurements and IWV from a GPS. Even though LWP will be less accurately estimated without the microwave radiometer, this method would still be able to capture the most important factors: higher cloud presence, fog vertical extent, fog temperature and IWV. For the efficient application of this methodology, a generalised retrieval algorithm of the (approximate) SW and LW emissivity of all clouds above the fog using cloud radar only would be very useful. Such a retrieval method could be developed by relating cloud altitude, thickness and reflectivity to satellite products of cloud optical depth.

The methodology of this paper could also be used to verify radiation schemes in numerical weather prediction models during fog and as a reference when studying how the presence of multilayer clouds affects the prediction of fog life cycle by these models.

Data availability. Radar, ceilometer and radiosonde data as well as the measurements of radiative fluxes at 10 m, surface meteorological parameters and visibility are available from the SIRTA public data repository, which is accessible online at http://www.sirta.fr. The data policy and a data download are available from the website. The data from the MWR and the data used for calculating the sensible heat fluxes are available on request on the SIRTA website: http://sirta.ipsl.fr/data_form.html. The data and code of ARTDECO are available on the AERIS/ICARE Data and Services Center website: http://www.icare.univ-lille1.fr/projects/artdeco.

Appendix A: Validation of surface radiative fluxes and LWP using radiation measurements at 10 m

Figure A1a evaluates the accuracy of the modelled downwelling SW fluxes at 10 m with the observed fluxes during the six fog events without higher cloud (Table 2). To eliminate the dependency on solar zenith angle, the fluxes are normalised with the incoming flux at the top of the atmosphere; we thus validate the atmospheric SW transmissivity. The disagreements between the observed and modelled transmissivity are mainly caused by uncertainty in the fog opacity. The rms error was found to be 0.046, and the spread is similar for different values of transmissivity (Fig. A1a). This corresponds to an uncertainty in the downwelling SW at the surface of about 20 $\mathrm{W\,m^{-2}}$ when the solar zenith angle is 70°.

We validate the downwelling LW flux at the surface when modelled fog LWP $< 20\,\mathrm{g\,m^{-2}}$ and when it is 20–40 $\mathrm{g\,m^{-2}}$ (Fig. A1b). In this LWP range, the fog is not yet completely opaque to LW radiation, so that the downwelling LW at the surface increases with fog LWP, typically by several tens of $\mathrm{W\,m^{-2}}$ in the range 0–40 $\mathrm{g\,m^{-2}}$ in the absence of higher clouds (Fig. 8d). Because the disagreement between modelled and observed surface clear-sky downwelling LW at the surface is typically no more than 5–15 $\mathrm{W\,m^{-2}}$ (based on 2 days of clear sky, not shown), the disagreement between modelled and observed downwelling LW flux below a non-opaque fog with no higher clouds will mainly be due to the error in fog LWP. Thus, the validation of the surface downwelling LW flux can be used to estimate the uncertainty in LWP. Since the LWP dependency of the downwelling LW flux at the surface is very similar to the LWP dependency of C_{LW} (Fig. 8a, d), we are also able to estimate the uncertainty in C_{LW} related to fog LWP. Based on the six fog events without higher clouds (Table 2), we find an rms of the difference between observed and modelled downwelling LW flux at the surface of 13.8 $\mathrm{W\,m^{-2}}$ when the (estimated) LWP $< 20\,\mathrm{g\,m^{-2}}$ and 4.8 $\mathrm{W\,m^{-2}}$ when LWP is 20–40 $\mathrm{g\,m^{-2}}$. This corresponds to about 5–10 $\mathrm{g\,m^{-2}}$ of uncertainty in LWP in both cases, considering Fig. 8d, which would cause roughly 10–15 $\mathrm{g\,m^{-2}\,h^{-1}}$ uncertainty in C_{LW} for LWP $< 20\,\mathrm{g\,m^{-2}}$ and 3–5 $\mathrm{g\,m^{-2}\,h^{-1}}$ for LWP 20–40 $\mathrm{g\,m^{-2}}$ (Fig. 8a), which are relative uncertainties of 50 and 10 %, respectively.

Appendix B: Estimation of vertical profiles of microphysical and radiative properties in fog

The method used in this study for relating the radar reflectivity Z to microphysical properties (Sect. 3.2) is only one of many possible approaches. The relationships can be derived by assuming a theoretical shape of the DSD (e.g. Maier et al., 2012), from a purely empirical fit to measurements from field campaigns (Fox and Illingworth, 1997; Sauvageot and Omar, 1987) and by modelling microphysical processes (Khain et al., 2008). However, accurate and general relationships cannot be found from Z alone, since Z is most sensitive to the largest droplets, which may only weakly impact LWC and r_{eff}. As the shape of the DSD varies significantly during and between fog events (Boers et al., 2012; Gultepe et al., 2007; Price, 2011), retrievals of LWC and r_{eff} using Z alone will only be rough estimates, even in the absence of drizzle. A synergy with the more reliable LWP from MWR is therefore used in several methods in the literature, with varying approaches for vertically distributing this liquid water inside the cloud. For example, the LWC can be assumed to increase linearly with height due to subadiabatic up- and downdraughts (e.g. Boers et al., 2000). More complex algorithms to retrieve LWC and r_{eff} have also been developed, which also utilise the ceilometer extinction (e.g. Martucci and O'Dowd, 2011) or the radar Doppler velocity (e.g. Kato et al., 2001).

Comparisons during 25 fog events observed at SIRTA reveal that the LWP estimated from Eq. (8) is often a factor 2–3 smaller than the MWR LWP (not shown). However, since we normalise the LWC with the MWR LWP, only the vertical distribution of LWC is impacted by the Z–LWC relationship, except when LWP $< 10\,\mathrm{g\,m^{-2}}$. This vertical distribution will not strongly impact our main results, since they are based on vertically integrating throughout the fog. On the other hand, the uncertainty in r_{eff} remains and will impact the calculated optical properties of the fog. The results of Fox and Illingworth (1997) indicate that the estimate of r_{eff} from Z comes with an rms error of about 20 %. Using the optical particle counter LOAC (Renard et al., 2016) lifted by a tether balloon during a few hours of a fog event at SIRTA when Z varied from −40 to −20 dBZ, we found a Z–r_{eff} relationship similar to Eq. (9), even though r_{eff} was ≈ 25 % smaller (not shown). Although only based on one case, this still indicates that Eq. (9) is an acceptable estimate for r_{eff} in fog, and that the uncertainty in r_{eff} is roughly of the order of 30 %. Finally, a calibration uncertainty of the radar of 1–2 dBZ also impacts the retrieval of LWC and r_{eff}, but it is apparent from Fig. 2 that the impact of this uncertainty is less important than the uncertainties in relating Z to LWC and r_{eff}.

Figure B1a–d shows some examples of the vertical profiles of microphysical properties in the fog calculated using the method of our study for one case of thin fog and two cases of thick fog. The observed profile of Z typically has a maximum somewhere in the middle of the fog and decreases towards the bottom and top, as seen in Fig. B1a. This therefore translates into profiles of LWC, r_{eff} and visible extinction with a similar shape (Fig. B1b–d). The visibility metres indicate that the extinction decreases strongly on approaching the surface (Fig. B1d). This vertical gradient in extinction is probably related to evaporation and deposition of fog droplets near the surface, which means that the LWC is probably in reality also decreasing strongly upon approaching the surface, in continuation of the decrease observed above the radar blind zone in the two cases of thick fog (Fig. B1b).

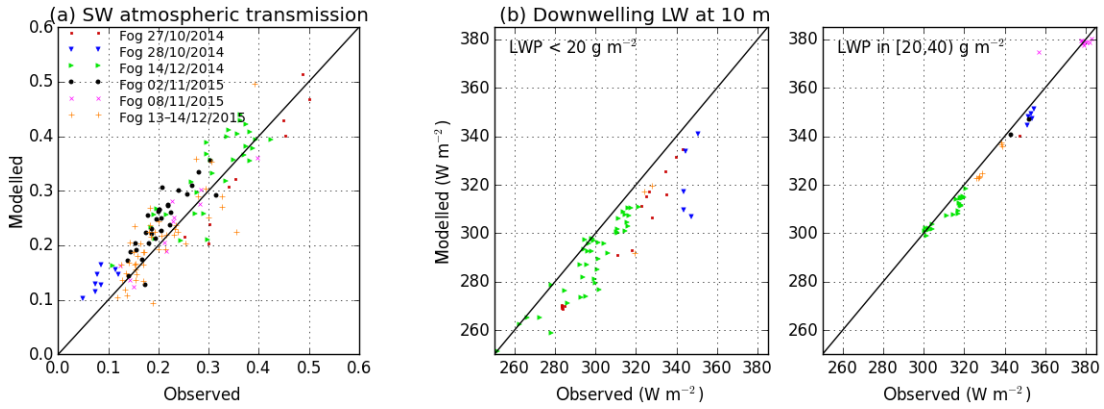

Figure A1. Comparison of modelled and measured SW and LW downwelling radiative flux at 10 m during the six fog cases without a higher cloud (Table 2): **(a)** atmospheric SW transmission (fraction of downwelling SW at 10 m and at the top of the atmosphere), including only times when observed flux exceeds 10 W m^{-2}; **(b)** downwelling LW flux at 10 m, in cases where fog LWP is estimated to less than 20 g m^{-2} and between 20 and 40 g m^{-2}.

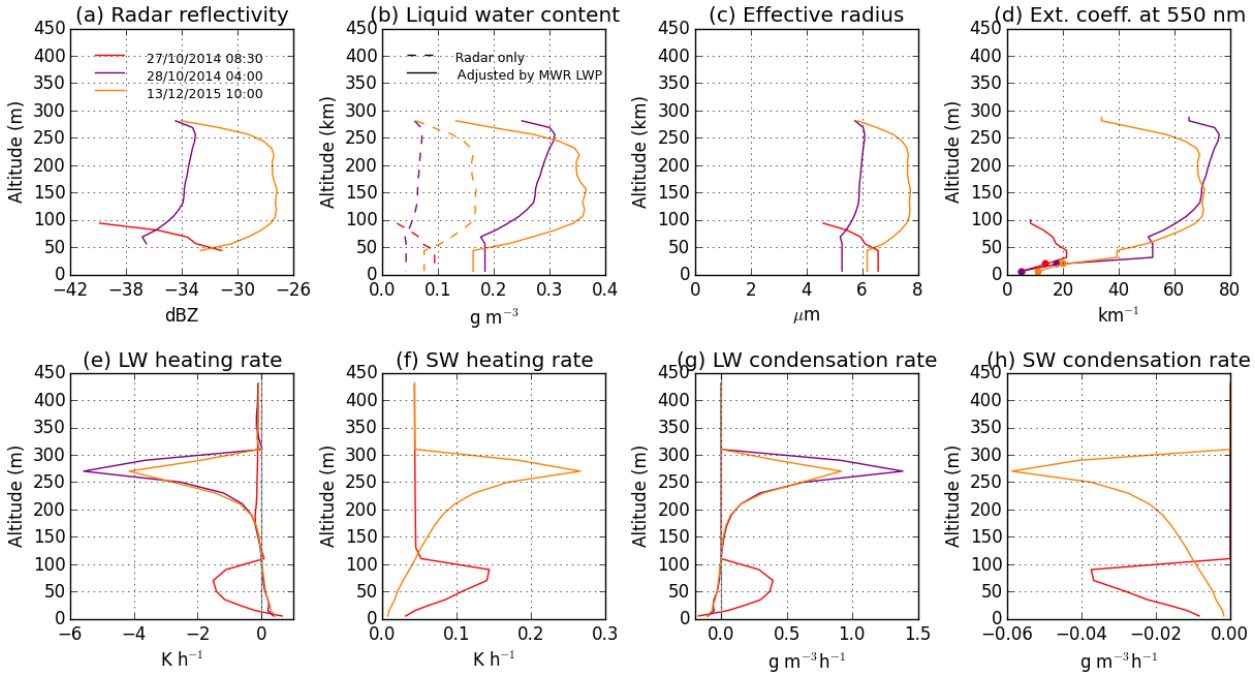

Figure B1. For three different observed fog profiles, vertical profile of **(a)** 10 min mean radar reflectivity; **(b)** LWC estimated with Eq. (8) before and after normalisation with the MWR LWP (normalisation not performed for red line, as LWP < 10 g m^{-2}); **(c)** r_{eff} estimated from Eq. (9); **(d)** visible extinction coefficient estimated from Eq. (6) (above 30 m) and from Eq. (10) (below 30 m; circles indicate estimates from the visibility metres); **(e–f)** radiative heating rate calculated from LW and SW radiation, and **(g–h)** the subsequently calculated condensation rates with Eq. (5). The solar zenith angle is similar in the two daytime conditions.

Compared to methods assuming a linear increase of LWC with height, our method usually produces a stronger vertical gradient in LWC in the lower fog and a lower LWC near the fog top, with the level of maximum LWC often significantly below the fog top.

The LW radiative cooling occurs predominantly in the first 50 m below fog top (Fig. B1e), as also found in modelling studies of fog (Nakanishi, 2000). The peak cooling rate is stronger and more vertically restricted in the case of thick fog than in the case of thin fog due to the extinction coefficient near the fog top being higher (Fig. B1d). The extinction coefficient in the thin fog may be underestimated though, since the MWR LWP is not used to scale the fog LWP in this case (as MWR LWP < 10 g m^{-2}). Near the sur-

face, there is radiative heating when the surface is warmer than the fog. This occurs in all the shown cases. In the absence of solar radiation on 28 October 2014 at 04:30 UTC, this warmer surface can be explained by the fog being cooled from above while the ground is sheltered by the fog. The SW heating rate (Fig. B1f) is also strongest near the fog top, but it penetrates further down into the fog than the LW cooling, which can be explained by the strong forward scattering by droplets and also agrees with the results of Nakanishi (2000). The SW heating rate is also significant above the fog due to molecular absorption (dominantly by water vapour), which indicates that water vapour absorption inside the fog can also be important for heating the fog, as discussed, e.g. by Davies et al. (1984). Finally, the calculated condensation rates (Fig. B1g–h) show the same patterns as the radiative heating rates with the opposite sign, as expected. Condensation occurs mainly near the fog top due to LW cooling, while a weaker evaporation is induced in the lower parts of the fog from SW and LW heating.

Author contributions. EW carried out the radiation simulations, supervised by MH and JCD. JCD calculated the surface sensible heat fluxes. PD is a developer of the ARTDECO code. He helped EW carry out the simulations. JD is a developer of the cloud radar BASTA. He deployed it at the SIRTA observatory and helped with the interpretation of the radar data. EW and MH prepared the manuscript, with contributions from all co-authors.

Competing interests. The authors declare that they have no conflict of interest.

Acknowledgements. This research is supported financially by the French ministry of defence – Direction Gérérale de l'Armement, and by the company Meteomodem. The authors would like to acknowledge SIRTA for providing the observational data used in this study, obtained in the framework of the ACTRIS-2 project (funded by the European Union's Horizon 2020 research and innovation programme under grant agreement No 654109). We thank the ICARE Data and Services Center for providing access to the ARTDECO model with associated data sets. ARTDECO has been developed with financial support (TOSCA programme) from the French space agency, "Centre National d'Etudes Spatiales" (CNES). We thank Jean-Baptiste Renard for his help with the instrument LOAC, enabling us to measure the droplet size distribution in fog.

Edited by: Hailong Wang
Reviewed by: two anonymous referees

References

Ackerman, S. A. and Stephens, G. L.: The Absorption of Solar Radiation by Cloud Droplets: An Application of Anomalous Diffraction Theory, J. Atmos. Sci., 44, 1574–1588, https://doi.org/10.1175/1520-0469(1987)044<1574:TAOSRB>2.0.CO;2, 1987.

American Meteorological Society: Fog, Glossary of Meteorology, available at: http://glossary.ametsoc.org/wiki/Fog (last access: 31 March 2017), 2017.

Anderson, G. P., Clough, S. A., Kneizys, F. X., Chetwynd, J. H., and Shettle, E. P.: AFGL Atmospheric Constituent Profiles (0.120 km), Air Force Geophysics Laboratory, Massachusetts, 1986.

Baum, B. A., Yang, P., Heymsfield, A. J., Bansemer, A., Cole, B. H., Merrelli, A., Schmitt, C., and Wang, C.: Ice cloud single-scattering property models with the full phase matrix at wavelengths from 0.2 to 100 µm, J. Quant. Spectrosc. Ra., 146, 123–139, https://doi.org/10.1016/j.jqsrt.2014.02.029, 2014.

Bergot, T.: Small-scale structure of radiation fog: a large-eddy simulation study, Q. J. Roy. Meteor. Soc., 139, 1099–1112, https://doi.org/10.1002/qj.2051, 2013.

Bergot, T., Terradellas, E., Cuxart, J., Mira, A., Liechti, O., Mueller, M., and Nielsen, N. W.: Intercomparison of Single-Column Numerical Models for the Prediction of Radiation Fog, J. Appl. Meteorol. Clim., 46, 504–521, https://doi.org/10.1175/JAM2475.1, 2007.

Boers, R., Russchenberg, H., Erkelens, J., Venema, V., Van Lammeren, A., Apituley, A., and Jongen, S.: Ground-based remote sensing of stratocumulus properties during CLARA, 1996, J. Appl. Meteorol., 39, 169–181, https://doi.org/10.1175/1520-0450(2000)039<0169:GBRSOS>2.0.CO;2, 2000.

Boers, R., Baltink, H. K., Hemink, H. J., Bosveld, F. C., and Moerman, M.: Ground-Based Observations and Modeling of the Visibility and Radar Reflectivity in a Radiation Fog Layer, J. Atmos. Ocean. Tech., 30, 288–300, https://doi.org/10.1175/JTECH-D-12-00081.1, 2012.

Bolton, D.: The computation of equivalent potential temperature, Mon. Weather Rev., 108, 1046–1053, https://doi.org/10.1175/1520-0493(1980)108<1046:TCOEPT>2.0.CO;2, 1980.

Brown, R. and Roach, W. T.: The physics of radiation fog: II–a numerical study, Q. J. Roy. Meteor. Soc., 102, 335–354, https://doi.org/10.1002/qj.49710243205, 1976.

Chýlek, P., Lesins, G. B., Videen, G., Wong, J. G. D., Pinnick, R. G., Ngo, D., and Klett, J. D.: Black carbon and absorption of solar radiation by clouds, J. Geophys. Res.-Atmos., 101, 23365–23371, https://doi.org/10.1029/96JD01901, 1996.

Cuxart, J. and Jiménez, M. A.: Deep radiation fog in a wide closed valley: study by numerical modeling and remote sensing, Pure Appl. Geophys., 169, 911–926, https://doi.org/10.1007/s00024-011-0365-4, 2012.

Davies, R., Ridgway, W. L., and Kim, K.-E.: Spectral Absorption of Solar Radiation in Cloudy Atmospheres: A 20 cm−1 Model, J. Atmos. Sci., 41, 2126–2137, https://doi.org/10.1175/1520-0469(1984)041<2126:SAOSRI>2.0.CO;2, 1984.

Delanoë, J., Protat, A., Vinson, J.-P., Brett, W., Caudoux, C., Bertrand, F., Parent du Chatelet, J., Hallali, R., Barthes, L., Haeffelin, M., and Dupont, J.-C.: BASTA: A 95-GHz FMCW Doppler Radar for Cloud and Fog Studies, J. Atmos. Ocean. Tech., 33, 1023–1038, 2016.

Dubuisson, P., Giraud, V., Chomette, O., Chepfer, H., and Pelon, J.: Fast radiative transfer modeling for infrared imaging radiometry, J. Quant. Spectrosc. Ra., 95, 201–220, https://doi.org/10.1016/j.jqsrt.2004.09.034, 2005.

Dubuisson, P., Roger, J. C., Mallet, M., and Dubovik, O.: A code to compute the direct solar radiative forcing: application to anthropogenic aerosols during the Escompte experiment, in: Proc. International Radiation Symposium (IRS 2004) on Current Problems in Atmospheric Radiation, edited by: Fischer, H., Sohn, B.-J., and Deepak, A., Hampton, Busan, Korea, 127–130, 2006.

Dupont, J.-C., Haeffelin, M., Protat, A., Bouniol, D., Boyouk, N., and Morille, Y.: Stratus–fog formation and dissipation: a 6-day case study, Bound.-Lay. Meteorol., 143, 207–225, https://doi.org/10.1007/s10546-012-9699-4, 2012.

Dupont, J.-C., Haeffelin, M., Stolaki, S., and Elias, T.: Analysis of dynamical and thermal processes driving fog and quasi-fog life cycles using the 2010–2013 ParisFog dataset, Pure Appl. Geophys., 173, 1337–1358, https://doi.org/10.1007/s00024-015-1159-x, 2016.

Foken, T.: The energy balance closure problem: an overview, Ecol. Appl., 18, 1351–1367, https://doi.org/10.1890/06-0922.1, 2008.

Fox, N. I. and Illingworth, A. J.: The retrieval of stratocumulus cloud properties by ground-based cloud radar, J. Appl. Meteorol., 36, 485–492, https://doi.org/10.1175/1520-0450(1997)036<0485:TROSCP>2.0.CO;2, 1997.

Gaussiat, N., Hogan, R. J., and Illingworth, A. J.: Accurate liquid water path retrieval from low-cost microwave radiometers using additional information from a lidar ceilometer and operational forecast models, J. Atmos. Ocean. Tech., 24, 1562–1575, https://doi.org/10.1175/JTECH2053.1, 2007.

Gultepe, I., Tardif, R., Michaelides, S. C., Cermak, J., Bott, A., Bendix, J., Müller, M. D., Pagowski, M., Hansen, B., Ellrod, G., Jacobs, W., Toth, G., and Cober, S. G.: Fog research: A review of past achievements and future perspectives, Pure Appl. Geophys., 164, 1121–1159, https://doi.org/10.1007/s00024-007-0211-x, 2007.

Gultepe, I., Pearson, G., Milbrandt, J. A., Hansen, B., Platnick, S., Taylor, P., Gordon, M., Oakley, J. P., and Cober, S. G.: The fog remote sensing and modeling field project, B. Am. Meteorol. Soc., 90, 341–359, https://doi.org/10.1175/2008BAMS2354.1, 2009.

Gultepe, I., Zhou, B., Milbrandt, J., Bott, A., Li, Y., Heymsfield, A. J., Ferrier, B., Ware, R., Pavolonis, M., Kuhn, T., Gurka, J., Liu, P., and Cermak, J.: A review on ice fog measurements and modeling, Atmos. Res., 151, 2–19, https://doi.org/10.1016/j.atmosres.2014.04.014, 2015.

Haeffelin, M., Barthès, L., Bock, O., Boitel, C., Bony, S., Bouniol, D., Chepfer, H., Chiriaco, M., Cuesta, J., Delanoë, J., Drobinski, P., Dufresne, J.-L., Flamant, C., Grall, M., Hodzic, A., Hourdin, F., Lapouge, F., Lemaître, Y., Mathieu, A., Morille, Y., Naud, C., Noël, V., O'Hirok, B., Pelon, J., Pietras, C., Protat, A., Romand, B., Scialom, G., and Vautard, R.: SIRTA, a ground-based atmospheric observatory for cloud and aerosol research, in: Annales Geophysicae, 23, 253–275, available at: https://hal-polytechnique.archives-ouvertes.fr/hal-00329353/ (last access: 16 February 2017), 2005.

Haeffelin, M., Bergot, T., Elias, T., Tardif, R., Carrer, D., Chazette, P., Colomb, M., Drobinski, P., Dupont, E., Dupont, J. C., Gomes, L., Musson-Genon, L., Pietras, C., Plana-Fattori, A., Protat, A., Rangognio, J., Raut, J.-C., Rémy, S., Richard, D., Sciare, J., and Zhang, X.: PARISFOG: shedding new light on fog physical processes, B. Am. Meteorol. Soc., 91, 767–783, https://doi.org/10.1175/2009BAMS2671.1, 2010.

Haeffelin, M., Dupont, J.-C., Boyouk, N., Baumgardner, D., Gomes, L., Roberts, G., and Elias, T.: A comparative study of radiation fog and quasi-fog formation processes during the Paris-Fog field experiment 2007, Pure Appl. Geophys., 170, 2283–2303, 2013.

Haeffelin, M., Laffineur, Q., Bravo-Aranda, J.-A., Drouin, M.-A., Casquero-Vera, J.-A., Dupont, J.-C., and De Backer, H.: Radiation fog formation alerts using attenuated backscatter power from automatic lidars and ceilometers, Atmos. Meas. Tech., 9, 5347–5365, https://doi.org/10.5194/amt-9-5347-2016, 2016.

Hautiére, N., Tarel, J.-P., Lavenant, J., and Aubert, D.: Automatic fog detection and estimation of visibility distance through use of an onboard camera, Mach. Vis. Appl., 17, 8–20, https://doi.org/10.1007/s00138-005-0011-1, 2006.

Hess, M., Koepke, P., and Schult, I.: Optical Properties of Aerosols and Clouds: The Software Package OPAC, B. Am. Meteorol. Soc., 79, 831–844, https://doi.org/10.1175/1520-0477(1998)079<0831:OPOAAC>2.0.CO;2, 1998.

Hu, Y. X. and Stamnes, K.: An Accurate Parameterization of the Radiative Properties of Water Clouds Suitable for Use in Climate Models, J. Climate, 6, 728–742, https://doi.org/10.1175/1520-0442(1993)006<0728:AAPOTR>2.0.CO;2, 1993.

Jacobson, M. Z.: Investigating cloud absorption effects: Global absorption properties of black carbon, tar balls, and soil dust in clouds and aerosols, J. Geophys. Res.-Atmos., 117, D06205, https://doi.org/10.1029/2011JD017218, 2012.

Johnson, B. T., Shine, K. P., and Forster, P. M.: The semi-direct aerosol effect: Impact of absorbing aerosols on marine stratocumulus, Q. J. Roy. Meteor. Soc., 130, 1407–1422, https://doi.org/10.1256/qj.03.61, 2004.

Katata, G.: Fogwater deposition modeling for terrestrial ecosystems: A review of developments and measurements, J. Geophys. Res.-Atmos., 119, 8137–8159, https://doi.org/10.1002/2014JD021669, 2014.

Kato, S., Mace, G. G., Clothiaux, E. E., Liljegren, J. C., and Austin, R. T.: Doppler cloud radar derived drop size distributions in liquid water stratus clouds, J. Atmos. Sci., 58, 2895–2911, https://doi.org/10.1175/1520-0469(2001)058<2895:DCRDDS>2.0.CO;2, 2001.

Khain, A., Pinsky, M., Magaritz, L., Krasnov, O., and Russchenberg, H. W. J.: Combined observational and model investigations of the Z-LWC relationship in stratocumulus clouds, J. Appl. Meteorol. Clim., 47, 591–606, 2008.

Korolev, A. V., Isaac, G. A., Cober, S. G., Strapp, J. W., and Hallett, J.: Microphysical characterization of mixed-phase clouds, Q. J. Roy. Meteor. Soc., 129, 39–65, https://doi.org/10.1256/qj.01.204, 2003.

Kotthaus, S., O'Connor, E., Münkel, C., Charlton-Perez, C., Haeffelin, M., Gabey, A. M., and Grimmond, C. S. B.: Recommendations for processing atmospheric attenuated backscatter profiles from Vaisala CL31 ceilometers, Atmos. Meas. Tech., 9, 3769–3791, https://doi.org/10.5194/amt-9-3769-2016, 2016.

Kratz, D. P.: The correlated k-distribution technique as applied to the AVHRR channels, J. Quant. Spectrosc. Rad., 53, 501–517, https://doi.org/10.1016/0022-4073(95)90050-0, 1995.

Löhnert, U. and Maier, O.: Operational profiling of temperature using ground-based microwave radiometry at Payerne: prospects and challenges, Atmos. Meas. Tech., 5, 1121–1134, https://doi.org/10.5194/amt-5-1121-2012, 2012.

Löhnert, U., Turner, D. D., and Crewell, S.: Ground-Based Temperature and Humidity Profiling Using Spectral Infrared and Microwave Observations. Part I: Simulated Retrieval Performance in Clear-Sky Conditions, J. Appl. Meteorol. Clim., 48, 1017–1032, https://doi.org/10.1175/2008JAMC2060.1, 2009.

Maier, F., Bendix, J., and Thies, B.: Simulating Z–LWC relations in natural fogs with radiative transfer calculations for future application to a cloud radar profiler, Pure Appl. Geophys., 169, 793–807, https://doi.org/10.1007/s00024-011-0332-0, 2012.

Marke, T., Ebell, K., Löhnert, U., and Turner, D. D.: Statistical retrieval of thin liquid cloud microphysical properties using ground-based infrared and microwave observations, J. Geophys. Res.-Atmos., 121, 14558–14573, https://doi.org/10.1002/2016JD025667, 2016.

Martucci, G. and O'Dowd, C. D.: Ground-based retrieval of continental and marine warm cloud microphysics, Atmos. Meas. Tech., 4, 2749–2765, https://doi.org/10.5194/amt-4-2749-2011, 2011.

Mason, J.: The physics of radiation fog, J. Meteorol. Soc. Jpn., 60, 486–499, https://doi.org/10.2151/jmsj1965.60.1_486, 1982.

Matrosov, S. Y., Uttal, T., and Hazen, D. A.: Evaluation of Radar Reflectivity–Based Estimates of Wa-

ter Content in Stratiform Marine Clouds, J. Appl. Meteorol., 43, 405–419, https://doi.org/10.1175/1520-0450(2004)043<0405:EORREO>2.0.CO;2, 2004.

Mlawer, E. J., Payne, V. H., Moncet, J.-L., Delamere, J. S., Alvarado, M. J., and Tobin, D. C.: Development and recent evaluation of the MT_ CKD model of continuum absorption, Philos. T. Roy. Soc. Lond. A, 370, 2520–2556, https://doi.org/10.1098/rsta.2011.0295, 2012.

Nakanishi, M.: Large-eddy simulation of radiation fog, Bound.-Lay. Meteorol., 94, 461–493, https://doi.org/10.1023/A:1002490423389, 2000.

Ohmura, A.: Physical Basis for the Temperature-Based Melt-Index Method, J. Appl. Meteorol., 40, 753–761, https://doi.org/10.1175/1520-0450(2001)040<0753:PBFTTB>2.0.CO;2, 2001.

Platt, C. M. R.: Infrared absorption and liquid water content in stratocumulus clouds, Q. J. Roy. Meteor. Soc., 102, 553–561, https://doi.org/10.1002/qj.49710243305, 1976.

Price, J.: Radiation fog. Part I: observations of stability and drop size distributions, Bound.-Lay. Meteorol., 139, 167–191, https://doi.org/10.1007/s10546-010-9580-2, 2011.

Price, J., Porson, A., and Lock, A.: An observational case study of persistent fog and comparison with an ensemble forecast model, Bound.-Lay. Meteorol., 155, 301–327, 2015.

Renard, J.-B., Dulac, F., Berthet, G., Lurton, T., Vignelles, D., Jégou, F., Tonnelier, T., Jeannot, M., Couté, B., Akiki, R., Verdier, N., Mallet, M., Gensdarmes, F., Charpentier, P., Mesmin, S., Duverger, V., Dupont, J.-C., Elias, T., Crenn, V., Sciare, J., Zieger, P., Salter, M., Roberts, T., Giacomoni, J., Gobbi, M., Hamonou, E., Olafsson, H., Dagsson-Waldhauserova, P., Camy-Peyret, C., Mazel, C., Décamps, T., Piringer, M., Surcin, J., and Daugeron, D.: LOAC: a small aerosol optical counter/sizer for ground-based and balloon measurements of the size distribution and nature of atmospheric particles – Part 1: Principle of measurements and instrument evaluation, Atmos. Meas. Tech., 9, 1721–1742, https://doi.org/10.5194/amt-9-1721-2016, 2016.

Rose, T., Crewell, S., Löhnert, U., and Simmer, C.: A network suitable microwave radiometer for operational monitoring of the cloudy atmosphere, Atmos. Res., 75, 183–200, https://doi.org/10.1016/j.atmosres.2004.12.005, 2005.

Rothman, L. S., Gordon, I. E., Babikov, Y., Barbe, A., Benner, D. C., Bernath, P. F., Birk, M., Bizzocchi, L., Boudon, V., Brown, L. R., Campargue, A., Chance, K., Coudert, L., Devi, V. M., Drouin, B. J., Fayt, A., Flaud, J.-M., Gamache, R. R., Harrison, J., Hartmann, J.-M., Hill, C., Hodges, J. T., Jacquemart, D., Jolly, A., Lamouroux, J., LeRoy, R. J., Li, G., Long, D., Mackie, C. J., Massie, S. T., Mikhailenko, S., Müller, H. S. P., Naumenko, O. V., Nikitin, A. V., Orphal, J., Perevalov, V., Perrin, A., Polovtseva, E. R., Richard, C., Smith, M. A. H., Starikova, E., Sung, K., Tashkun, S., Tennyson, J., Toon, G. C., Tyuterev, V. G., Vander Auwera, J. and Wagner, G.: The HITRAN2012 molecular spectroscopic database, J. Quant. Spectrosc. Ra., 130, 4–50, doi:org/10.1016/j.jqsrt.2013.07.002, 2013.

Sauvageot, H. and Omar, J.: Radar reflectivity of cumulus clouds, J. Atmos. Ocean. Tech., 4, 264–272, https://doi.org/10.1175/1520-0426(1987)004<0264:RROCC>2.0.CO;2, 1987.

Stamnes, K., Tsay, S.-C., Wiscombe, W., and Jayaweera, K.: Numerically stable algorithm for discrete-ordinate-method radiative transfer in multiple scattering and emitting layered media, Appl. Optics, 27, 2502–2509, https://doi.org/10.1364/AO.27.002502, 1988.

Steeneveld, G. J., Ronda, R. J., and Holtslag, A. A. M.: The Challenge of Forecasting the Onset and Development of Radiation Fog Using Mesoscale Atmospheric Models, Bound.-Lay. Meteorol., 154, 265–289, https://doi.org/10.1007/s10546-014-9973-8, 2015.

Stephens, G. L., Vane, D. G., Boain, R. J., Mace, G. G., Sassen, K., Wang, Z., Illingworth, A. J., O'Connor, E. J., Rossow, W. B., Durden, S. L., Miller, S. D., Austin, R. T., Benedetti, A., Mitrescu, C., and the CloudSat Science Team: The cloudsat mission and the a-train, B. Am. Meteorol. Soc., 83, 1771–1790, https://doi.org/10.1175/BAMS-83-12-1771, 2002.

Tardif, R. and Rasmussen, R. M.: Event-based climatology and typology of fog in the New York City region, J. Appl. Meteorol. Clim., 46, 1141–1168, https://doi.org/10.1175/JAM2516.1, 2007.

Teshiba, M., Hashiguchi, H., Uematsu, A., Tanaka, H., Ohmori, Y., and Fukao, S.: Fog observations with a millimeter-wave scanning radar at Miyoshi basin, Japan, Earth Planet. Space, 56, 259–268, https://doi.org/10.1186/BF03353408, 2004.

Twomey, S.: The Influence of Pollution on the Shortwave Albedo of Clouds, J. Atmos. Sci., 34, 1149–1152, https://doi.org/10.1175/1520-0469(1977)034<1149:TIOPOT>2.0.CO;2, 1977.

Wallace, J. M. and Hobbs, P. V.: Atmospheric science: an introductory survey, 2nd Edn., Elsevier Academic Press, Amsterdam, 2006.

Zhou, B. and Ferrier, B. S.: Asymptotic analysis of equilibrium in radiation fog, J. Appl. Meteorol. Climatol., 47, 1704–1722, https://doi.org/10.1175/2007JAMC1685.1, 2008.

3.2 Parametrising the radiative processes

By using the model ARTDECO, the radiative transfer is very precisely calculated. However, such comprehensive models rely on a large number of inputs to be precise, and these are often not available when the methodology is to be applied to a given site. Observations of the input profiles will only be roughly estimated when the radiation is to be calculated from a few ground-based remote sensing observations without radiosondes, and there will be substantial uncertainty in the optical properties of the observed clouds, as demonstrated in the paper above. It is therefore likely that the limiting factor for precision is the input data rather than the degree of sophistication of the model. Simpler calculation of the radiative processes could therefore give similarly accurate results as the comprehensive radiation transfer calculations with the ARTDECO code. A simpler parametrisation also has the advantages of being computationally faster and easier to understand. In this section, such parametrisations of SW and LW radiative transfer are presented, using the ARTDECO results to evaluate their accuracy. The parametrisations developed in this section are used in chapter 5 to estimate the impact of radiation on a larger number of fog events.

The first step is to rewrite Eq. (5) in W17 on integral form and using the same notation as introduced in chapter 4. We rewrite $\rho_s = \rho_a q_s \approx \rho_a \frac{\epsilon}{p} e_s$, where ϵ is the ratio of the gas constants of dry air and water vapour, p is pressure and q_s is the saturation mixing ratio of water vapour to dry air. We can then approximate $\frac{d\rho_s}{dT} \approx \rho_a \frac{\epsilon}{p} \frac{de_s}{dT}$, and by applying the flux divergence formulation for the radiative cooling of an infinitesimal layer

$$\left(\frac{dT}{dt}\right)_{rad} = -\frac{1}{\rho_a c_p} \frac{dF_{net}}{dz}, \tag{3.1}$$

where F_{net} is the net upward radiative flux, Eq. (5) in W17 becomes:

$$C_{rad} = \frac{s}{s+\gamma} \frac{1}{L_v} \frac{dF_{net}}{dz}, \tag{3.2}$$

where $s = \frac{de_s}{dT}$ and $\gamma = \frac{c_p p}{\epsilon L_v}$. Integrating this equation vertically through the fog from the surface ($z = 0$) to fog top ($z = z_t$), neglecting the vertical variability of ρ_a, s and γ, we obtain:

$$\begin{aligned} \left(\frac{dLWP}{dt}\right)_{rad} &= \int_0^{z_t} C_{rad} dz \\ &= \frac{s}{s+\gamma} \frac{1}{L_v} \int_0^{z_t} \frac{dF_{net}}{dz} dz \\ &= \frac{s}{s+\gamma} \frac{1}{L_v} (F^{\uparrow}{}_{top} - F_{\downarrow top} - F^{\uparrow}{}_{surf} + F_{\downarrow surf}) \end{aligned} \tag{3.3}$$

where subscripts $surf$ and top stand for the surface and fog top, respectively. Equation (3.3) can be applied for SW and LW radiation separately. In the following two subsections, the method for calculating the fluxes at the surface and fog top without ARTDECO are described. Although the fluxes at the surface are measured, it is worthwhile to be able to calculate them, both for validation and for the possibility to apply the methodology to sites without radiative flux measurements.

3.2.1 LW radiation

The fog interaction with LW radiation is simplified as a pure broad-band emission–absorption process, where the absorption coefficient is proportional to LWC:

$$\alpha_{abs} = k \cdot LWC \tag{3.4}$$

with $k = 130$ m^2 kg^{-1} (Larson et al., 2007). The emissivity of the fog is therefore:

$$\epsilon_f = 1 - e^{-k \cdot LWP} \tag{3.5}$$

As explained in section 2.5.1, the LWP retrieval of the MWR is relatively uncertain when LWP is weak. This is particularly critical for LW radiation, since it is very sensitive to the fog opacity when the latter is low. As in W17, we therefore don't use the MWR LWP when it is lower than 10 g m^{-2}. We instead use the parametrisation of the LWP from visibility and profile of radar reflectivity, as explained in section 2.5.2.

If we simplify the fog emission to occur only at fog top for upward emission and only at fog base for downward emission, then the upward LW flux at fog top and downward LW flux at the surface can be calculated as:

$$LW_{\downarrow surf} = (1 - \epsilon_f) LW_{\downarrow top} + \epsilon_f \sigma {T_{base}}^4 \tag{3.6}$$

$$LW^{\uparrow}{}_{top} = (1 - \epsilon_f) LW^{\uparrow}{}_{surf} + \epsilon_f \sigma {T_{top}}^4 \tag{3.7}$$

using Stefan-Boltzmann's law, where T_{base} and T_{top} are the temperatures at fog base and top, respectively, and $\sigma = 5.67 \cdot 10^{-8}$ W m^{-2} K^{-4} is the Stefan-Boltzmann's constant.

In non-opaque fog, radiation escapes from all levels of the fog, which makes this assumption imprecise. However, due to the assumption on adiabatic temperature profile, which is applied in any case, the fog-top and fog-base temperatures will be very close to one another for thin fog, so it should not cause much bias. Of course, in reality the thin fog may have a stable profile, which will cause a larger bias. However, this bias also occurs when we use ARTDECO, so it is not a bias introduced by the change of radiation scheme.

To solve the equations (3.6), (3.7), two boundary conditions are needed: the downward LW flux at fog top, and the upward LW flux from the surface. The latter is measured at SIRTA, so we can use it directly. For sites where this flux is not measured, it can be calculated from the surface skin temperature:

$$LW^{\uparrow}{}_{surf} = \epsilon_s \sigma {T_{surf}}^4 \tag{3.8}$$

where ϵ_s is the emissivity of the surface. However, in order to use this method, one must ensure that the skin temperature measurement technique actually captures the effective emission temperature of the surface.

In W17, we showed that the downwelling LW flux at the fog top in clear sky depends mainly on the temperature of the layer directly above and the IWV of the entire atmosphere above. This is similar to what has been found for the downwelling LW flux at the surface (Dupont et al., 2008). In fact, Prata (1996) developed a parametrisation of the clear-sky downwelling LW irradiance at the surface as function of the 2-m air temperature T_a and the IWV, using Stefan-Boltzmann's law and an effective

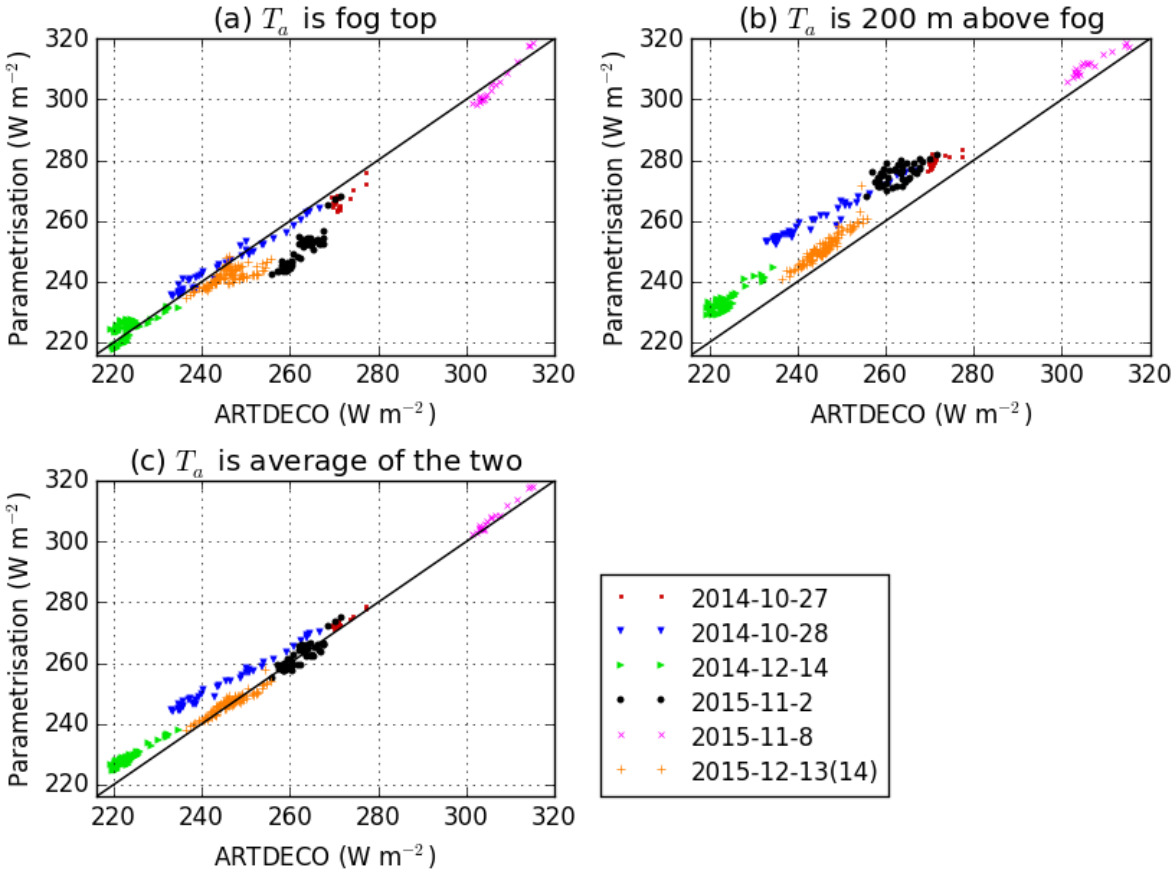

Figure 3.1: For each of the six fog events in W17 without clouds above, the downwelling LW flux at fog top calculated with Eq. (3.9) vs the flux calculated by ARTDECO. Three different estimates of T_a are used: (a) the fog-top temperature, (b) the temperature 200 m above fog top (found from the MWR), and (c) the average of these two temperatures.

emissivity of the atmosphere that increases with IWV:

$$LW_{\downarrow,clear} = \epsilon_A \sigma {T_a}^4 \tag{3.9}$$

$$\epsilon_A = 1 - (1 + c_1 IWV) e^{-\sqrt{c_2 + c_3 IWV}} \tag{3.10}$$

where $c_1 = 0.1$ m^2 kg^{-1}, $c_2 = 1.2$ and $c_3 = 0.3$ m^2 kg^{-1}. To parametrise the downwelling LW at fog top, we have applied this formula to the fog top instead of the surface, replacing IWV by the IWV above fog top. However, the coefficients of this formula were optimised using a standard atmospheric profile, which makes it underestimate the flux in cases of a strong and low inversion (Prata, 1996). Since the fog is typically immediately capped by an inversion, it is not ideal to apply the fog-top temperature in Eq. (3.9). Figure 3.1 shows how well the LW fluxes agree with ARTDECO when using as T_a the fog-top temperature, the temperature 200 m above fog top (from the MWR), and the average of the two. Since the average of the two temperatures gives the best overall agreement with ARTDECO in the six fog events, this is what is applied.

Finally, the effect of higher clouds on the LW radiation should also be parametrised, given its huge impact on the LW budget found in W17. To account for these clouds, we apply a simple parametrisation where the cloud is assumed to be a grey body, and assuming the cloud and clear-sky contributions to the downwelling LW radiation at fog top are spectrally decoupled. This is analogous

to assuming that the clear-sky atmosphere emits as a black body at temperature T_A at all wavelengths except in a 'window' band, and that the cloud emits like a grey body with emissivity ϵ_c, thus filling this window, but with the cloud temperature T_c, ignoring the spectral shift of the Planck curve with temperature. The complete formula for downwelling LW at fog top is then:

$$LW_{\downarrow top} = \epsilon_A \sigma {T_A}^4 + (1 - \epsilon_A)\epsilon_c \sigma {T_c}^4 \tag{3.11}$$

$$T_A = \frac{1}{2}(T_{top} + T_{top+200m}) \tag{3.12}$$

As no universal method for estimating the cloud OD from cloud radar alone is available, an all-or-nothing approach for the cloud emissivity is used: If the 100-m mode of the cloud radar detects a consistent cloud signal above the fog, $\epsilon_c = 1$ and T_c is set to the temperature (from the MWR) of the altitude of the lowest consistent cloud signal from the cloud radar (i.e. more than 50 % of the cloud radar measurements in a 10-min period retained by signal detection algorithm, see section 2.3). No distinction is made between rain and cloud, so in case of trailing precipitation from a cloud, the altitude of the cloud will be underestimated.

Figure 3.2a compares the condensation rate due to LW cooling (C_{LW}) using the method described in this section with the ARTDECO calculations. The variability is well captured, but the parametrisation overestimates systematically the C_{LW} by 5–10 g m^{-2} h^{-1}. The effect of the higher clouds on 1 Jan 2016 is also well reproduced, although the effect is slightly overestimated since the C_{LW} is slightly underestimated rather than overestimated in these situations (purple stars near (15,10) in Fig. 3.2a).

3.2.2 SW radiation

To parametrise the interaction of the fog with SW radiation, the δ-Eddington model, as described in Heus et al. (2010), is applied. This radiation scheme parametrises the profile of net downward SW flux (down minus up), given the profile of SW extinction coefficient, and two boundary conditions: (1) the surface albedo, and (2) the incoming direct SW flux at the top of the cloud. The net SW fluxes at cloud base and cloud top are thereby found, and can be inserted into Eq. (3.3).

The extinction coefficient is estimated using a log-normal size distribution with droplet concentration $N_c = 200$ cm^{-3} and geometric standard deviation $\sigma_g = 1.2$ (see section 3.3), and an average LWC determined from the fraction of LWP and fog geometric thickness. The effective radius is then:

$$r_e = \Big(\frac{3LWC}{4\pi\rho_l N_c}\Big)^{\frac{1}{3}} e^{\ln^2 \sigma_g}, \tag{3.13}$$

and the extinction coefficient is calculated as:

$$\alpha_{ext} = Q_{ext}\frac{3LWC}{4\rho_l r_e} + \alpha_{aer} \tag{3.14}$$

where $Q_{ext} = 2$ is the extinction efficiency of the droplets, and α_{aer} is an additional term for taking into account the extinction by non-activated aerosols with diameters of around 1 μm. Following the results of Elias et al. (2009), we apply $\alpha_{aer} = 10$ km^{-1}.

The surface albedo is set to 0.23, which is the default value in the implementation of the scheme in DALES, and also very close to what is typically observed at SIRTA (W17).

To estimate the incoming radiation at fog top, we have studied the downward SW flux predicted

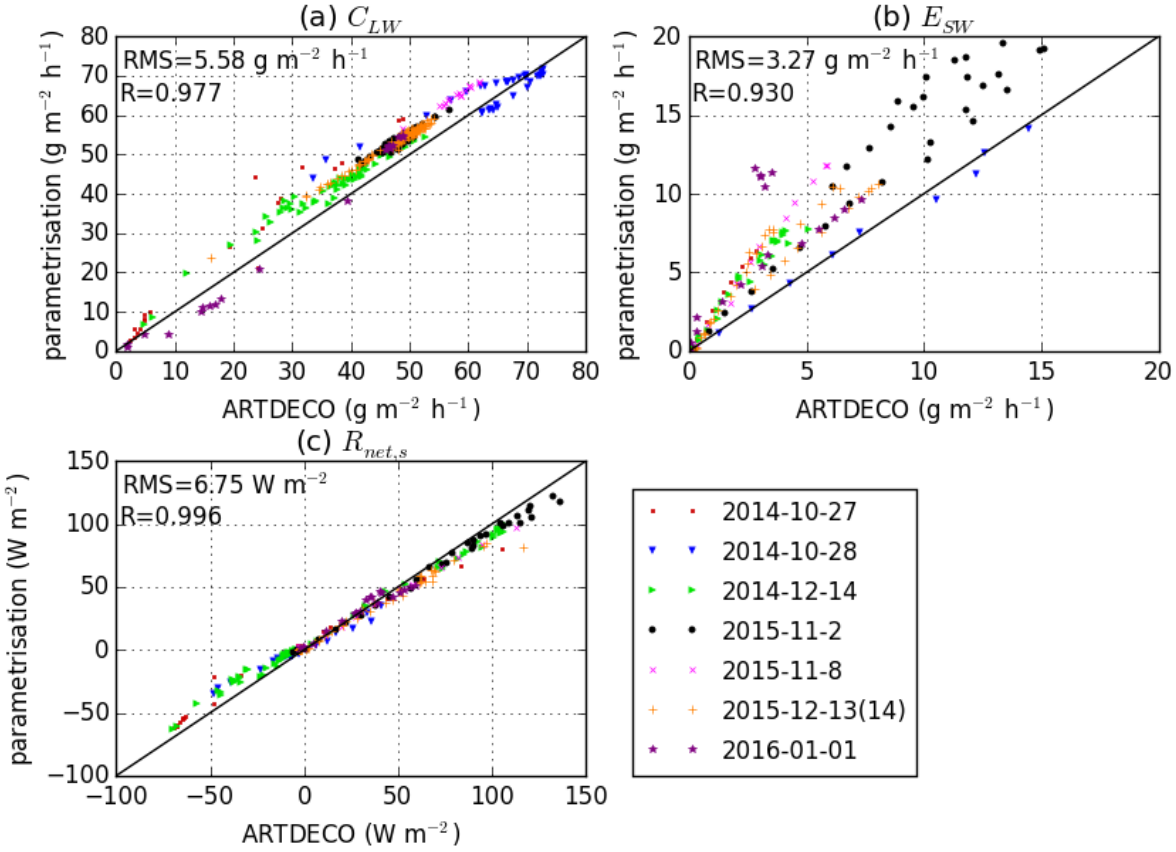

Figure 3.2: The three quantitative parameters defined in section 2.1 of W17, for each 15 min in the seven fog events studied in W17: comparison of their value when calculated using ARTDECO vs when using the simplified methods described in this section. The upward LW flux at the surface is nevertheless taken from ARTDECO in both cases, and we apply the same altitude and OD of the higher clouds as used in ARTDECO (section 4.3 in W17), in order to compare the methods rather than the different input. (a) LWP production from LW cooling (discussed at the end of section 3.2.1), (b) LWP loss due to absorption of SW radiation, and (c) net radiation absorbed at the surface (discussed at the end of section 3.2.2). Correlation coefficients (R) and RMS deviations are indicated.

by ARTDECO in the runs of W17. In fact, the δ-Eddington scheme assumes all the incoming SW radiation is direct. In clear-sky conditions, most of the downwelling SW radiation is indeed direct (Long and Ackerman, 2000). The upper boundary condition to the δ-Eddington scheme is therefore approximated by replacing the diffuse contribution with direct radiation:

$$SW_0 = \frac{SW_{\downarrow top}}{\mu_0} \tag{3.15}$$

where μ_0 is the cosine of the solar zenith angle, $SW_{\downarrow top}$ is the global downwelling SW flux at fog top given by ARTDECO, and SW_0 is the direct flux through a plane perpendicular to the solar beam.

In order to estimate SW_0 without using ARTDECO, we have derived a relationship between SW_0 from ARTDECO and the two principal parameters affecting it (in clear sky): (1) the solar zenith angle (affecting the atmospheric distance the solar beam must travel), and (2) the water vapour column (affecting the absorptivity of the atmosphere). SW_0 is in reality also affected by other factors, such as the AOD (Dupont and Haeffelin, 2008), but this is not taken into account (aerosols are not included in our ARTDECO simulations either). Using the six fog events without a cloud above in

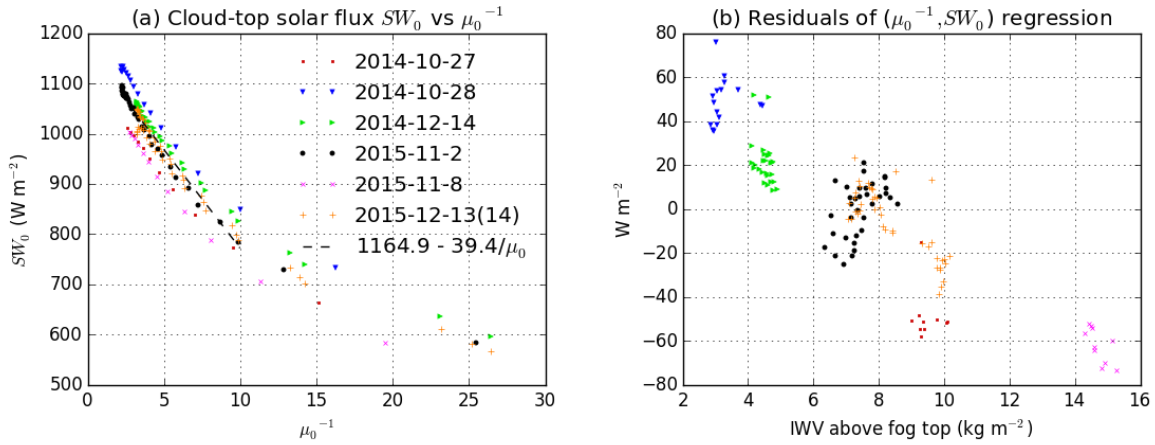

Figure 3.3: (a) SW_0 (global downwelling SW radiation at fog top normalised by μ_0) for the six fog events in W17 without a cloud above, plotted against ${\mu_0}^{-1}$, for times with a fog or low cloud-base and $\mu_0 > 0.035$. Also shown is the linear regression based on the data points with $\mu_0 > 0.1$. (b) The residuals of the regression shown in (a) as function of the IWV above fog top.

W17, a linear relationship between SW_0 and ${\mu_0}^{-1}$, for $\mu_0 > 0.1$, is found (Fig. 3.3a). Moreover, the residuals of this regression indicate a linear relationship with the IWV above the fog (Fig. 3.3b). We therefore apply a 2D linear regression to parametrise SW_0 as function of ${\mu_0}^{-1}$ and above-fog IWV:

$$SW_0 = a - \frac{b}{\mu_0} - c \cdot IWV_{ab} \tag{3.16}$$

where $a = 1234$ W m^{-2}, $b = 39.3$ W m^{-2}, and $c = 9.4$ W kg^{-1}. It can be seen that the fog event of 27/10/2014 fits less well to this linear model than the other events (Fig. 3.3b). This discrepancy could be related to the low cloud albedo of this fog, which is thinner than the others. A lower albedo means less diffusion of reflected radiation, which is a secondary contribution to $SW_{\downarrow top}$.

Note that we have not included any correction of the SW radiation in cases with a cloud above. Without knowledge of the cloud OD, it is harder to account for the SW effect of the cloud than its LW effect, since the SW cloud effects do not saturate as quickly with cloud OD as the LW cloud effect (see Fig. 10 in W17). However, in the case of a liquid cloud above, the fact that the MWR LWP also includes this cloud will compensate the lack of representation of the cloud in the SW scheme: the calculated SW radiation reaching the surface will be (correctly) reduced due to the higher LWP caused by the higher cloud. The fact that an important part of the SW radiation is absorbed in the cloud above rather than in the fog, will not be accounted for, though. It is therefore likely that the parametrisation will overestimate the LWP loss caused by the appearance of a higher cloud: Firstly, the cloud may not be completely opaque in the LW so that the fog LW cooling is underestimated. Secondly, the absorption of SW radiation in the cloud is not accounted for, so that the SW absorption in the fog is overestimated. A method for approximating the OD of the cloud above from cloud radar would be useful for improving both these caveats in the parametrisation. An alternative would be to use satellite data to estimate the cloud OD. The challenging aspect is that the cloud OD needs to be separated from that of the fog below.

In Fig. 3.4a, the net SW flux at the surface parametrised with the simplified method presented in this section is compared to observations, using a larger number of fog events. We see that in most

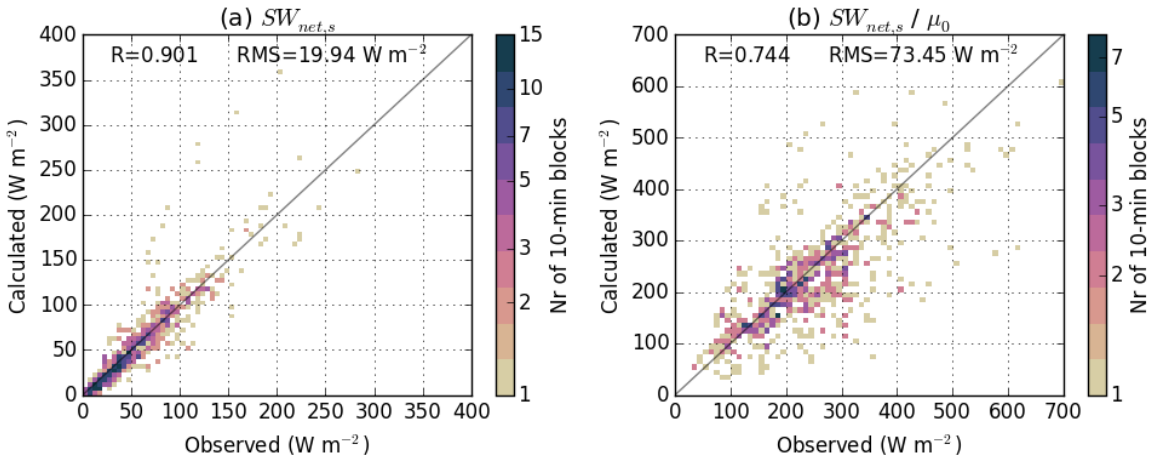

Figure 3.4: (a) Net SW radiation at the surface, and (b) normalised by μ_0, for each 10-min block during the 47 morning fog events (see section 5.1). The observed flux from pyranometers at 10 m is shown on the x-axis, while the flux calculated using the methodology of section 3.2.2 is shown on the y-axis. Correlation coefficient (R) and RMS deviation are indicated.

cases, the net SW flux is close to the observations, with no systematic offset, indicating that our constant value of 200 cm^{-3} for the number concentration is reasonable. The RMS deviation is 20 W m^{-2}, and correlation is 0.90. There are a few outliers which might be due to fractional cloud cover or ice clouds above the fog. Since a large part of the variability in the net SW radiation is due to the solar zenith angle, which is very well known, a clearer evaluation of the scheme can be obtained by comparing the net SW normalised by μ_0 (Fig. 3.4b), for which the correlation is reduced to 0.74. This is still a fairly good score and shows that with the LWP and IWV products of the MWR, the fraction of the SW radiation which is transmitted to the surface during fog can be reasonably well estimated. The main reason for the spread is most likely the variability of effective radius (through the number concentration), which is not accounted for.

In Fig. 3.2b, we compare the evaporation rate due to SW absorption inside the fog (E_{SW}) when calculating it with the methodology described above vs the full ARTDECO calculations. E_{SW} is often overestimated with 50–100 % by the simplified method. This might be due to the small droplet sizes used in the ARTDECO calculations. As found in Fig. 8b in W17, bigger droplets absorb the SW radiation more efficiently. In particular, the event 28/10/2014, where ARTDECO and the parametrisation agree well, is the only event where the ARTDECO calculations used an effective radius as large as 10.7 μm (because radar reflectivity is strong, see section 3.2 in W17). The overestimation of E_{SW} is not necessarily as big as it seems, though, since the ARTDECO calculations do not include the effect of absorbing aerosols, which is estimated to increase E_{SW} by up to 30 % in typical conditions (see Table 4 in W17). We also note 1 Jan 2016 as an example of the important overestimation of E_{SW} during presence of higher cloud layers, as discussed above.

Finally, Fig. 3.2c compares the net radiation at the surface calculated by ARTDECO and the simplified parametrisations. The variability is well reproduced by the simple scheme, and the RMS is 6.75 W m^{-2}. A slight underestimation occurs for positive values of $R_{net,s}$, and a relatively more important underestimation of (the absolute value of) negative $R_{net,s}$. The underestimation of LW cooling of the surface is probably related to the overestimated C_{LW} (Fig. 3.2a).

3.3 Estimation of droplet number concentration from SW radiation closure

The SW scheme introduced above requires knowledge of the droplet number concentration N_c in order to calculate the fog OD in the SW from the LWP. In situ measurements of N_c are only available from the FM-120, which measures only near the surface. There are obviously large vertical gradients in LWC near the surface, given the large difference in LWC measured by FM120 and the layer-average LWC (Figs. 2.10, 2.16). It could also be that N_c is significantly different in the layer as a whole than at 4 m. We can expect the layer-average N_c to be higher, as the droplets are expected to activate due to cooling in updrafts and from the radiative cooling near fog top, while evaporation in downdrafts as well as collection processes could reduce N_c near the ground.

The pyranometer measurements of net SW radiation at the surface allow us to perform a SW closure study, that is calculating the net SW radiation at the surface for different N_c, to find the N_c which gives the most consistent SW flux with observations. If LWC, N_c and σ_g are all constant with height, Eqs. (3.13), (3.14) imply that the fog OD is proportional to ${N_c}^{1/3}$ for a given LWP and fog thickness (before the contribution of α_{aer} is added), thus a relatively weak sensitivity to N_c compared to LWP. Figure 3.5a compares the surface SW net radiation calculated with N_c ranging 50–500 cm^{-3} with the observed radiation for the fog event 2/11/2015. We see that an N_c of 300 cm^{-3} seems most consistent with observations in the morning, growing to 500 cm^{-3} in the afternoon. Of course, N_c is not the only source of uncertainty of the SW scheme. There is notably uncertainty related to the retrieved LWP and the estimated SW flux at fog top, as well as simplifications in the scheme itself. Horizontal inhomogeneities, especially fractional cloud cover above the fog, could also introduce bias.

Figure 3.5b explores the sensitivity of the results to various parameters in the SW scheme. Using an LWC increasing from zero at the fog base to twice the vertical average value at fog top (red line), rather than using the average everywhere, did not alter significantly the net SW at the surface. If the parameter SW_0 is decreased by 50 W m^{-2} (about 5 %), the net SW decreases more significantly (cyan line). The reduction by 50 W m^{-2} is chosen because a comparison with observations on the clear-sky day of 1 Nov 2015, when the pyranometer measurements allow a direct evaluation of SW_0[1], indicates an overestimation of SW_0 of this magnitude (not shown). This overestimation may be due to the limitations of Eq. (3.16) and the ARTDECO calculations, which notably neglect the aerosol extinction. With the decreased SW_0, the SW budget can be closed with fewer droplets (250 cm^{-3} instead of 300–350 cm^{-3}). Uncertainty in the LWP corresponds to a similar sensitivity in the SW radiation (blue line, where the observed LWP of 47 g m^{-2} is increased by 10 g m^{-2}). However, we have no reason to expect a systematic overestimation of the LWP.

Uncertainty is also introduced by the Q_{ext} not being exactly 2, but rather a function of droplet size according to Mie theory (e.g. chapter 5.2 in Liou, 2002). However, since the fog droplets will typically have a size parameter of at least 10, the variability of Q_{ext} with size is not as large as for smaller droplet, and the uncertainty in Q_{ext} is probably less than 10 %. Increasing Q_{ext} from 2.0 to 2.2 (purple line) has an impact which is almost identical to the reduction of SW_0 by 50 W m^{-2}. If the extra extinction representing the non-activated aerosols is not included, the N_c needed to get agreement with observations increases from 300 cm^{-3} to 500 cm^{-3} (green line), which shows that the SW scheme is sensitive to the chosen value of this extra extinction.

Finally the orange line shows the calculated radiation when σ_g is increased from 1.2 to 1.7. This

[1] by using the measurement of downward global irradiance as $SW_{\downarrow top}$ in Eq. (3.15)

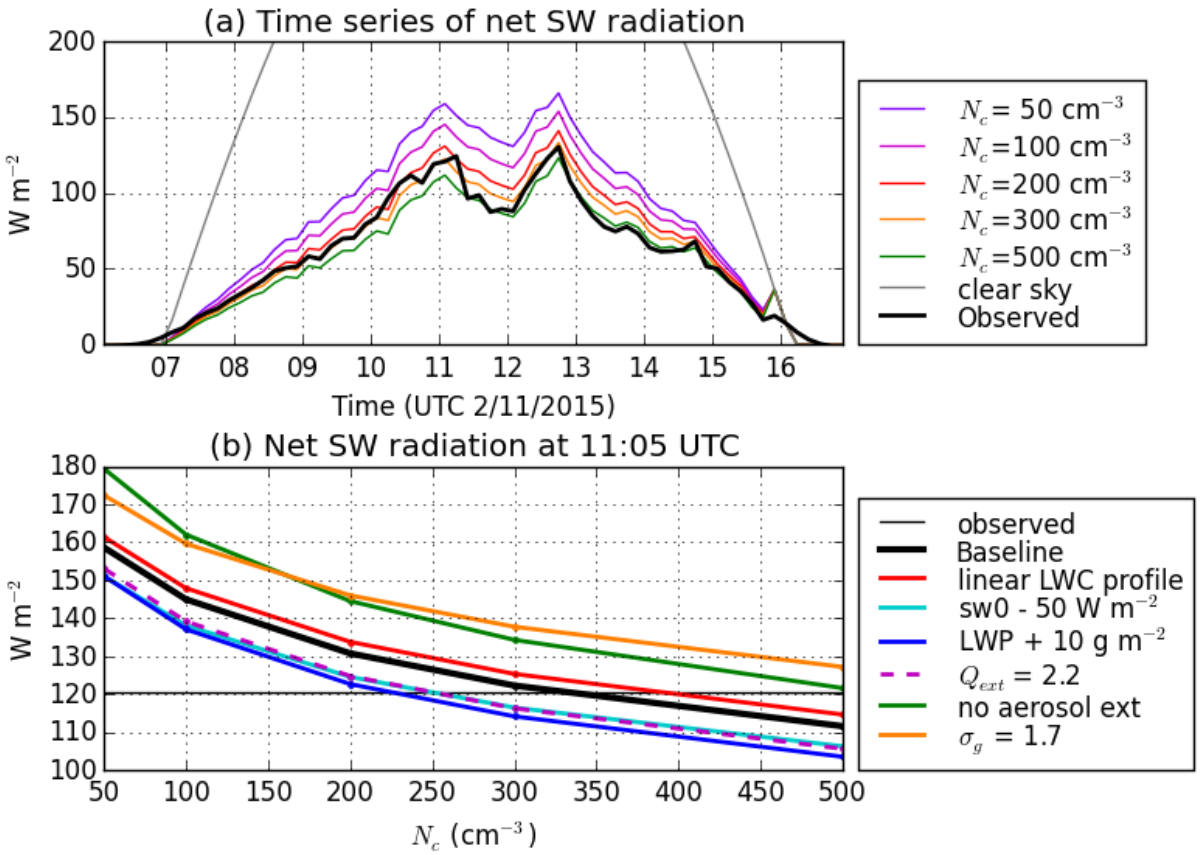

Figure 3.5: (a) Net SW radiation at the surface during the fog event on 2/11/2015, calculated with the scheme described in section 3.2.2, using different values of N_c, and with no cloud at all (clear sky). This is compared to the observations (thick line). (b) Net SW radiation at 11:05 UTC calculated with different values of N_c and imposing various modifications to the SW scheme: The black line is the baseline (same as is shown in (a) with coloured lines at 11:05), and the horizontal line marks the observed flux at this time. See text for explanation of the other lines.

is a much wider DSD, which therefore has a larger effective radius and transmits more SW radiation than in baseline. We show in section 5.3.5 that such a wide DSD corresponds better to the DSD observed at 4 m by the FM-120. However, given the very large number of droplets needed to close the SW budget with such a DSD (Fig. 3.5b), it seems unlikely that such a DSD shape occurs in the upper levels of the fog. The vertical profile of the DSD shape could be further studied in tethered balloon campaigns.

Figure 3.6 shows the same analysis as in Fig. 3.5a extended to all the fog events without cloud above studied in W17. Instead of time series, linear regression between observed and calculated net SW radiation is performed for each event. In this way, we can see which of the lines lies closest to the grey 1-1 line. Fig. 3.6a shows the event 2/11/2015, which we already considered in Fig. 3.5a, and as already noted N_c = 300 cm^{-3} gives the regression line slope closest to unity. A concentration of 300 cm^{-3} also works well for 28/10/2014 (Fig. 3.6f), but for some of the other events, a lower concentration fits better: 50 cm^{-3} for 8/11/2015 (Fig. 3.6b), 100 cm^{-3} for 13/12/2015 and 14/12/2014 (Fig. 3.6cg), and even less than 50 cm^{-3} for 27/10/2014 (Fig. 3.6e). However, for the latter, which is a very thin fog, the method is less reliable, due to the important relative uncertainty related to LWP. Judging from these examples, there seems to be a certain dependency of N_c on the fog LWP, with the thicker fog events with higher LWP (e.g. 2/11/2015, 28/10/2014) typically having a higher N_c than the thinner

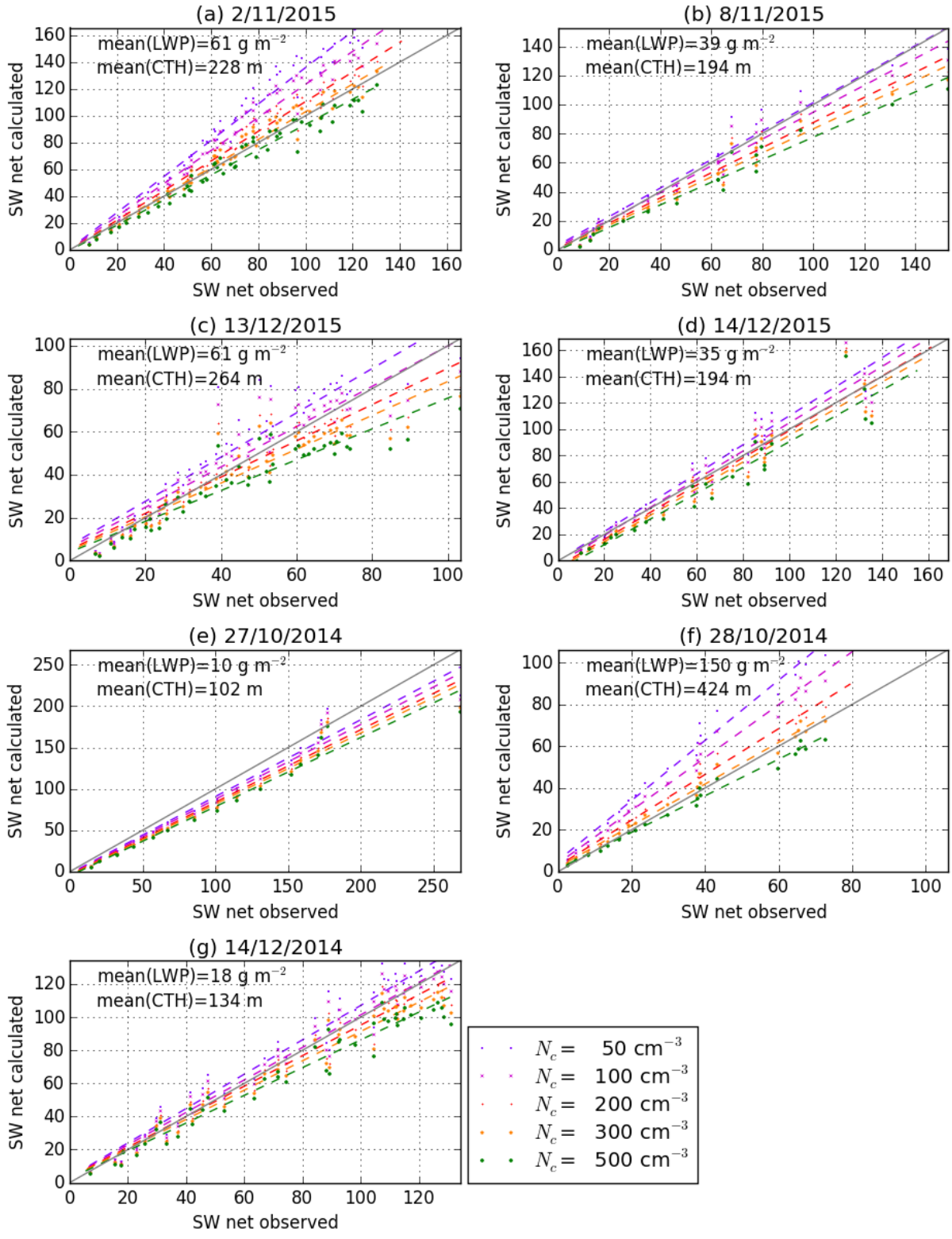

Figure 3.6: Net surface SW radiation calculated every 10 min during day in the fog events without a cloud above studied in W17. Calculated fluxes with the scheme described in section 3.2.2 is plotted against the observed flux. Each colour corresponds to a different value used for N_c in the SW scheme. Dashed lines result from linear regression. Also indicated are the mean values of LWP and CTH during the periods shown.

fog events with lower LWP (e.g. 27/10/2014, 14/12/2014).

As a compromise, 200 cm^{-3} is chosen as the constant value to use for N_c in the SW scheme. As seen in Fig. 3.4, this results in good agreement with the observed net SW at the surface in average. However, we should be careful about concluding that this means than the number concentration typically has this value in fog, since as already shown, uncertainties in other parameters in the scheme and the assumed extinction by unactivated particles impact strongly which value of N_c will fit best (Fig. 3.5).

3.4 Synthesis

This chapter studied the radiative processes in fog and their impacts on fog LWP budget using the comprehensive radiation code ARTDECO on seven fog events occurring at SIRTA in the winter. The main results to retain from this chapter are:

- LW cooling at fog top produces 40–70 g m^{-2} h^{-1} of liquid water when the sky is clear above and the fog is opaque to LW radiation. This is sufficient to renew the fog LWP in 0.5–2 h, making it an important process for maintaining the fog water against other processes which deplete it. The variability in the production is due to the IWV, fog temperature and inversion strength above. When $LWP <\approx 30$ g m^{-2}, the fog is semi-transparent to LW and the cooling is therefore weaker. The production of LWP increases importantly with LWP when LWP is less than 30 g m^{-2}.
- The LW radiative effect of clouds appearing above the fog is very important. Even semi-transparent clouds reduce drastically the production of LWP. The effect is much stronger for a low cloud than a high cloud, since it is warmer. In the sensitivity study, a cloud at 2 km reduces the LW cooling to zero when its OD is 4 or more, while an ice cloud at 10 km only reduces it by 20–30 %.
- A simplified parametrisation of the LW radiative transfer was formulated, taking into account the variability in IWV, LWP, fog top height and temperature, and inversion strength at fog top. It reproduces well the variability of production of LW radiation in clear sky calculated by ARTDECO, although it shows a systematic overestimation of 5–10 g m^{-2} h^{-1}.
- Heating by absorption of SW radiation inside the fog cloud by droplets and gases have a weaker and opposite impact than the LW cooling, causing typically evaporation of 5–15 g m^{-2} h^{-1} in winter daytime, with the impact increasing with fog LWP and with the sizes of the droplets. In addition, absorbing aerosols may increase the SW absorption by a factor 2 in polluted conditions (AOD=0.15) and by 30 % in more typical conditions (AOD=0.05).
- The SW radiation absorbed by the surface during fog at a solar zenith angle of 70° varies from 40 W m^{-2} for very thick fog to 140 W m^{-2} for thin fog. This makes it likely that the heating by solar radiation via the surface is at least as important a loss mechanisms as the direct absorption inside the fog, at least for thin fog, although its magnitude will depend on the Bowen ratio.
- The incoming SW radiation at fog top in clear sky calculated by ARTDECO could be well reproduced using linear regression with the variables solar zenith angle and IWV. The aerosols have been neglected, as in ARTDECO, but they probably only modify the incoming SW by a few percent.

- The delta-Eddington scheme was applied to model the interaction between the SW radiation and the fog. We find it is able to reproduce well (in average of many fog events) the observed SW radiation at the surface during fog by using a number concentration of 200 cm^{-3} in addition to 0.01 m^{-1} extinction from non-activated aerosols (RMS = 20 W m^{-2}). The SW closure method also indicates that the number concentration could be increasing with the LWP of the fog, although we should be careful to conclude since we only considered a few cases when this was investigated. The SW radiation absorbed in the fog calculated with the delta-Eddington scheme is 50–100 % higher than what was calculated by ARTDECO. It seems likely that this is partly explained by the droplet sizes being assumed bigger in the scheme than in ARTDECO. Moreover, the higher absorption is compensating the lack of aerosols in the ARTDECO calculations.
- The impact of clouds above on the LW radiation is well accounted for when the clouds are opaque, by using their altitude, for which the temperature is known from the MWR profile. However, the scheme currently does not distinguish opaque and semi-transparent clouds, and it also cannot take into account the effect of the cloud above on the SW radiation. The clouds above could be better taken into account in the future if an estimate of their emissivity could be retrieved from the cloud radar. This could be achieved by improved sensitivity of the cloud radar and the development of an algorithm to relate the cloud emissivity to the information available from the cloud radar (altitude, thickness, radar reflectivity, and possibly also Doppler velocity).
- To quantify the important variability in the radiative processes, we need to observe the fog LWP, the IWV, the fog top height, the stratification above fog top, the temperature and emissivity of clouds above, the 2-m temperature, the surface albedo and the surface emission temperature. Together, the cloud radar and MWR provide all the aloft variables, while surface in situ measurements can give the surface variables. Further development is needed for a sufficient retrieval of the emissivity of the clouds above, but a cloud radar with sufficient sensitivity should be able to provide a reasonable estimate, except during rain.

Chapter 4

Turbulent processes

The previous chapter quantified the impacts of radiative processes on fog and their variability. In this chapter, we extend the analysis to include also the dynamical and microphysical processes: mixing at fog top, turbulent heat fluxes at the surface and deposition of cloud droplets. These processes may change importantly from thin to thick fog and between day and night, due to different thermodynamic forcings. We have chosen to focus on the thick fog cases after sunrise.

In order to quantify the impacts of the dynamical processes, we perform large-eddy simulations (LES) on an observed fog event, thereby resolving the bigger turbulent eddies which transport heat, momentum and moisture in the vertical, and which are also responsible for mixing the foggy air with drier air above its top. Our large dataset of observed fog events, which includes nearby radiosondes from Trappes, allows us to study statistically the stratification and humidity in the layer above the fog top and how much they vary from case to case. We have therefore chosen in our LES to focus specifically on the impacts of these fog-top properties, which have not received much attention in the fog literature. The observed statistics allow us to perform sensitivity studies to the actual observed variability in stratification and humidity above fog top. Furthermore, we develop a method for separating the modelled LWP tendency into contributions from each of the local processes: LW radiation, SW radiation, surface turbulent heat fluxes, fog-top entrainment, droplet deposition and large-scale subsidence. This method allows us to quantify how much the impact of each process changes when performing sensitivity studies. It also allows a study of the impact of the surface energy balance and the large importance that the Bowen ratio plays for the fog LWP budget.

The investigations with the LES model are the object of a publication which was submitted to the Quarterly Journal of the Royal Meteorological Society in July 2018, and the paper manuscript corresponding to this submission is given in section 4.1[1]. The paper describes the statistics of properties above fog top (section 2.2), presents the case study that is modelled (2.3), describes the LES model (3.1), how the sensitivity studies are performed (3.2), and how the LWP budget is analysed from the model output (3.3). Thereafter, it presents the baseline simulation, comparing it with observations (4.1) and studying the impacts of each of the processes on the LWP budget (4.2). Then the results of the sensitivity studies to the variability in fog-top properties as well as water availability at the surface are presented (4.3), before conclusions are given (5). Finally, a sensitivity study to the impact of large-scale subsidence on fog dissipation is provided in section 4.2, after the paper manuscript. This study of subsidence is not integrated in the paper due to limitations on the length of the paper.

[1]The only difference from the submitted version, apart from page layout, is that Figure 9ab has been corrected for a couple of bugs which were discovered after the submission.

4.1 Submitted paper: Understanding the dissipation of continental fog by analysing the LWP budget using LES and in situ observations

Understanding the dissipation of continental fog by analysing the LWP budget using LES and in situ observations

Eivind G. Wærsted[a⋆], Martial Haeffelin[b], Gert-Jan Steeneveld[c], and Jean-Charles Dupont[d]

[a]*Laboratoire de Météorologie Dynamique, École Polytechnique, Université Paris-Saclay, Route de Saclay, 91128 Palaiseau, France*
[b]*Institut Pierre Simon Laplace, École Polytechnique, CNRS, Université Paris-Saclay, 91128 Palaiseau, France*
[c]*Meteorology and Air Quality section, Wageningen University, Droevendaalsesteeg 3, 6708 PB Wageningen, The Netherlands*
[d]*Institut Pierre Simon Laplace, École Polytechnique, UVSQ, Université Paris-Saclay, 91128 Palaiseau, France*

⋆Correspondence to: Eivind G. Wærsted. E-mail: ewaersted@lmd.polytechnique.fr

Abstract

Physical processes relevant for the dissipation of thick, continental fog after sunrise are studied through observations from the SIRTA observatory and sensitivity studies with the large-eddy simulation (LES) model DALES. Observations of 250 fog events during 7 years show that more than half of the fog dissipations after sunrise are transitions to stratus lasting 2 h or more. From the simulations, we quantify the contribution of each process to the liquid water path (LWP) budget of the fog. Radiative cooling is the source of LWP, while surface heat fluxes is the most important process contributing to loss of LWP, followed by the absorption of solar radiation, the mixing with unsaturated air at the fog top and the deposition of cloud droplets. The loss of LWP by surface heat fluxes is very sensitive to the Bowen ratio, which is importantly affected by the availability of liquid water on the surface (85 min earlier dissipation in a run without liquid on the surface relative to a Baseline simulation). The variability of stratification and humidity above fog top is documented by 47 radiosondes and cloud radar. Using DALES, we find that the variability in stratification has an important impact on the entrainment rate (a factor 3); the more rapid fog-top development in weak stratification enables the cloud base to lift from the ground 90 min earlier than in strong stratification. With relatively dry overlying air, the fog evaporates faster than if the air is near saturation, leading to 70 min earlier dissipation in our simulations. Continuous observations of the temperature and humidity profiles of the layer overlying the fog could therefore be useful for understanding and anticipating fog dissipation.

Key Words: fog; fog dissipation; LES; fog-top entrainment; Bowen ratio

1 Introduction

Fog is defined as the presence of suspended water droplets in vicinity of the surface, generally reducing the horizontal visibility to below 1 km (American Meteorological Society, 2018). Fog can form in most parts of the world, by a large number of different mechanisms depending on location and season (Gultepe et al., 2007). Fog may cause severe delays in traffic, in particular on airports, due to the necessary precautions in low visibility conditions (Gultepe et al., 2009). Predicting when and where fog will form, as well as the time of dissipation, is therefore an important objective for atmospheric sciences. Since fog formation depends on a subtle balance between many processes which may vary locally, fog has proven very challenging to forecast precisely with regional-scale numerical weather models (e.g. Steeneveld et al., 2015).

To improve fog forecasts for a specific site, e.g. an airport, nowcasting tools have been developed based on the statistical analysis of many years of surface meteorological observations at the site, to forecast visibility

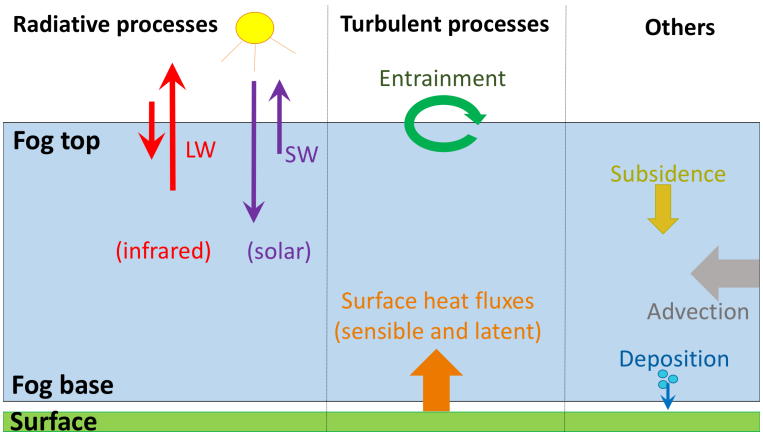

Figure 1: Schematic of the fog layer and the local processes that affect its liquid water content.

in the near future (e.g. Pasini et al., 2001; Román-Cascón et al., 2016). In order to extend such tools to more sophisticated observations such as vertical profilers (e.g. ceilometers, cloud radars), understanding of the physical processes responsible for the evolution of the fog is required to optimize the use of the profilers. These remote sensing instruments may detect phenomena that occur at a higher altitude than where the surface observations are taken; for example, ceilometers may detect the hygroscopic growth of aerosols at up to a few hundred meters altitude which often precedes fog formation (Haeffelin et al., 2016).

The dissipation of continental fog after sunrise is an interaction of many physical processes. Although fog often dissipates after sunrise due to heating caused by solar radiation, the time of dissipation can be very variable (see section 2.2). The persistence of fog depends on the presence of suspended liquid water near the surface. Fog dissipation may occur through a complete depletion of the liquid layer, but also through a transition of the fog into a low stratus cloud, since both these scenarios will increase the visibility at screen level. While the first scenario requires a complete depletion of the fog liquid water path (LWP), the second only requires a vertical displacement of the liquid water and may occur without a strong decrease in LWP. This paper explores the local processes which affect these two mechanisms.

The local processes affecting the fog layer are shown schematically in Figure 1. Radiative cooling at fog top is the main source of LWP (Brown and Roach, 1976; Wærsted et al., 2017), while many processes contribute to removal of LWP, notably the heating of the fog or underlying surface by solar radiation (Brown and Roach, 1976; Haeffelin et al., 2010; Wærsted et al., 2017), the mixing of the fog with warm, dry air above its top (Gultepe et al., 2007), or the deposition of droplets on the surface or canopy (Katata, 2014). Also indicated on the figure is "Advection", which represents all the processes that depend on horizontal heterogeneity, advection of synoptic phenomena and other non-local effects. These can impact fog importantly, but are not investigated in this paper.

Previous papers have applied large-eddy simulations (LES) to study the impacts of local processes in fog. They have focussed on the turbulent structures during phases of radiation fog (Nakanishi, 2000; Bergot, 2013, 2016), fog-layer deepening and transition from stable to adiabatic fog (Porson et al., 2011), the impact of cloud condensation nuclei concentrations on fog life cycle through radiative and microphysical processes (Maalick et al., 2016; Mazoyer et al., 2017), and the impact of the wind speed (Bergot, 2016; Maronga and Bosveld, 2017). However, certain other aspects have received less attention, especially the properties of the air overlying the fog.

In this paper, the following research questions are posed: (1) How much does each local process contribute to the LWP budget of the fog? (2) What is the impact of the presence of liquid water at the surface on fog dissipation? (3) What is the impact of the temperature and humidity profiles above the fog top on fog dissipation? To answer these questions, we perform LES sensitivity studies on an observed fog event. The aim is not primarily to reproduce this particular event, but rather to understand the contribution of various local processes and how sensitive they are to boundary conditions. The sensitivity studies to the temperature and humidity above fog top have high relevance because the applied values are based on the observed variability from 47 radiosondes. While the effect of the soil moisture was studied by Maronga and Bosveld (2017), the

impact of water present at the surface itself was not treated. We also study the relative importance of each process for the evolution of fog LWP using a novel approach of model output analysis (section 3.3).

The paper is structured as follows: In section 2, we describe the dataset of fog observations and some statistics which are used as basis for the sensitivity studies. In section 3, the LES model and the setup of each simulation are described, as well as the LWP budget analysis method. The results of the simulations are presented in section 4, together with a discussion of their implications. Conclusions and outlooks are presented in section 5.

2 Observations of fog at the SIRTA observatory

2.1 The observational dataset

The multi-instrumental atmospheric observatory SIRTA has continuously recorded a large number of atmospheric variables since 2002 (Haeffelin et al., 2005). This site is well suited for the study of fog due to the relatively high number of days with fog (about 30 per year), and fog has been a prioritised topic of study since 2006, when the ParisFog project started (Haeffelin et al., 2010). In this paper, several observations from the SIRTA main facility are used to study statistics of atmospheric state during many fog events, and to initialize and evaluate the LES model for a specific event (Table 1). The site is located 156 m above sea level in a suburban area about 20 km south of Paris city centre with patches of grass, forest and built-up areas. The closest surroundings are an open field, with a line of trees to the north and a small lake to the south. All the instruments are deployed in an area smaller than 200 m in diameter, apart from the radiosondes.

The visibility observed at 4 m is used to detect fog, while the visibility at 20 m is used to determine when the fog is thicker than 20 m. The environment of the fog is further characterised by the air temperature recorded at six levels on a 30-m mast, the skin temperature measured by an unshielded thermometer in the grass, the soil temperature and moisture measured at six depths, and the wind profile up to 200 m observed by sonic anemometers and a sodar. The different terms of the surface energy balance are also measured: short-wave (SW) and long-wave (LW) radiative fluxes at 10 m, turbulent sensible and latent heat fluxes at 2 m (eddy covariance method), and soil heat flux at 5 cm depth.

Full atmosphere profiles of temperature and humidity are available around 0000 and 1200 UTC from radiosondes launched from the Meteo-France station Trappes, which is located 15 km to the west of SIRTA and is 12 m higher above sea level.

The Vaisala CL31 ceilometer (Kotthaus et al., 2016) is used to detect the cloud-base height (CBH) of the fog cloud, when it is not touching the ground, using the threshold value of $2 \cdot 10^{-4}$ $m^{-1}sr^{-1}$ in the attenuated backscatter, following Haeffelin et al. (2016). Above the cloud base, the ceilometer signal is rapidly attenuated, preventing further information about the cloud beyond its base to be obtained. To observe the profile of the cloud and detect its top, the 95 GHz cloud radar BASTA is used (Delanoë et al., 2016). This cloud radar uses the frequency-modulated continuous wave (FMCW) technique, which requires much smaller emitted power than traditional pulsed radars, making its components less expensive. Its small blind-zone (40–60 m) and high vertical resolution (12.5 m) makes it well suited for fog studies. The average cloud top (e.g. in a 10-min period) is set to the highest cloud radar gate where at least half the measurements are retained after the automatic noise filtering algorithm of the cloud radar (Delanoë et al., 2016). Finally, the multi-wavelength microwave radiometer (MWR) HATPRO is used to retrieve the LWP of the atmospheric column and the temperature profile up to 10 km. The uncertainty of the LWP product is ± 20 g m^{-2} according to the manufacturer, but for relatively small LWP (<40 g m^{-2}), investigations indicate that the uncertainty is only $\pm$5–10 g m^{-2}, at least when the fog forms in clear sky so that a possible time-independent bias can be corrected for (Marke et al., 2016; Wærsted et al., 2017). The MWR temperature profile only has 4–5 degrees of freedom, limiting the details that can be retrieved from it, but with the best resolution in the lowest layer.

2.2 Atmospheric conditions during 7 years of fog events at SIRTA

We define fog using the visibility at 4 m. Each block of 10 min is considered to be fog if more than half the visibility measurements are less than 1 km. Fog events are defined based on positive and negative constructs, similar to the method of Tardif and Rasmussen (2007). We consider periods of 5 consecutive 10-min blocks

Instrument	Measured quantity	Used for	Vertical range and resolution	Temporal resolution
Remote sensing				
95 GHz Doppler FMCW cloud radar (LATMOS, BASTA)	Radar reflectivity (dBZ)	I,C,A	RA 0.05-6 km, RE 12.5 m	12 s
14-channel microwave radiometer (RPG HATPRO)	Liquid water path (g m^{-2})	I,C	Integrated	60 s
	Temperature profile (K)	I,A	RA 0–10 km, 4–5 deg. of freedom	≈5 min
905-nm Ceilometer (Vaisala CL31)	Attenuated backscatter (m^{-1} sr^{-1})	C,A	RA 0–7.6 km, RE 15 m	30 s
Sodar (Remtech SFAS)	Wind speed profile (m s^{-1})	I	RA 10–200 m, RE 5 m	10 min
Surface layer state				
550-nm scatterometer (Degreane DF320)	Visibility (m)	C,A	At 4 m	60 s
875-nm scatterometer (Vaisala PWD22)	Visibility (m)	A	At 20 m	60 s
Thermometers (Guilcor PT100)	Air temperature (K)	I,C	At 1,2,5,10,20,30 m	60 s
Barometer (Vaisala PTB110)	Surface pressure (Pa)	I	At 2 m	60 s
Sonic anemometers (METEK)	Mean wind speed (m s^{-1})	I	At 10,30 m	10 min
Ground and soil state				
Thermometer (unsheltered)	Skin temperature (K)	I,C	At ground level	60 s
Soil thermometer (Guilcor)	Soil temperature (K)	I	At 5,10,20,30,50,100 cm depth	60 s
Soil moisture sensor (ThetaProbe)	Soil moisture (m^3 m^{-3})	I	At 5,10,20,30,50,100 cm depth	60 s
Surface energy balance				
Pyranometers (Kipp & Zonen CMP22)	Down- and upwelling SW irradiance (W m^{-2})	C,A	At 10 m	60 s
Pyrgeometers (Kipp & Zonen CGR4)	Down- and upwelling LW irradiance (W m^{-2})	C,A	At 10 m	60 s
Heat flux sensor (Hukseflux HFP01SC)	Soil heat flux (W m^{-2})	C,A	At 5 cm depth	60 s
GILL sonic anemometer and LI-7200 infrared gas analyser	Sensible and latent heat flux (W m^{-2})	C,A	At 2 m	10 min
Radiosondes (Meteomodem M10, Météo France, Trappes)	Temperature (K) and relative humidity (%) profiles	I,A	RA 0–30 km, RE ≈ 5 m	12 h

Table 1: Overview of the observations used in this study. All observations are taken in the SIRTA observatory main facility, except the radiosondes which are launched at Trappes (15 km to the west of SIRTA). The column "Used for" indicates which observations are used for initialization of the model (I), for comparison with the model (C) and for the analysis on an extended dataset (presented in section 2 or section 4.3) (A).

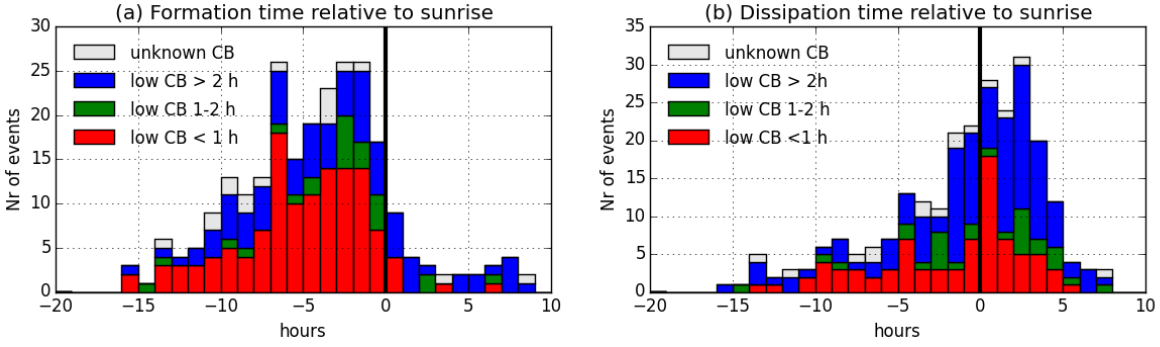

Figure 2: Time of formation (a) and dissipation (b) relative to sunrise of the 250 fog events at SIRTA in the period from 1 October 2010 to 30 September 2017. The different sections of the bars mark how long a cloud base (CB) is present below 400 m before formation (in a) and after dissipation (in b), ignoring cloud absence lasting less than 30 min.

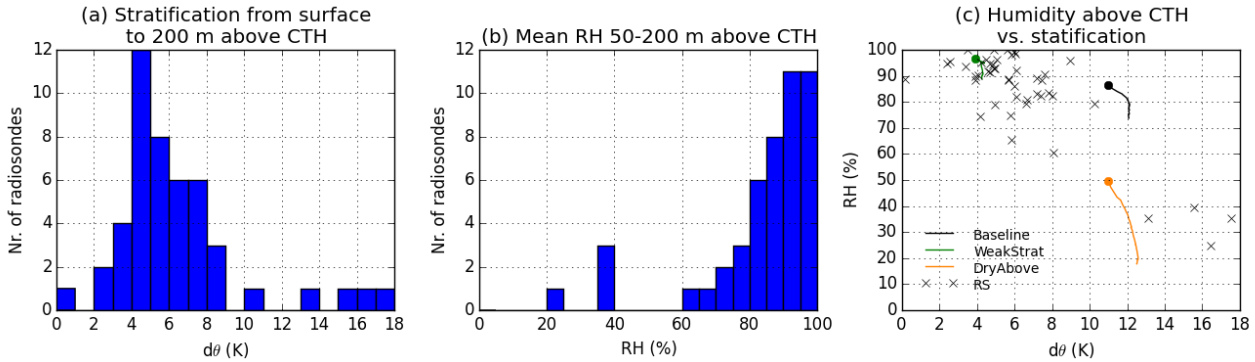

Figure 3: Statistics of observations of the layer above fog top: The data come from 47 radiosondes launched at Trappes near 0000 or 1200 UTC in the period from 1 October 2013 to 30 September 2017 when cloud base at SIRTA (from the ceilometer CBH product) was below 130 m and cloud top was below 600 m, and within 6 h of a fog event at SIRTA. (a) Stratification (difference in potential temperature from the 2-m station at Trappes to 200 m above CTH, $d\theta$); (b) average relative humidity in the layer from 50 m above CTH to 200 m above CTH. The CTH is determined using the cloud radar BASTA at SIRTA (except for three cases of very thin fog, where we use the visibility at 20 m). (c) The quantities shown in (a) and (b) plotted against each other (crosses). Also indicated are the initial states of three of the LES simulations performed in this paper (circles) and the evolutions in the first 3 h of the simulations (lines).

where the central block is a fog block: it is a positive construct if at least 2 other blocks also are fog blocks, and a negative construct otherwise. A fog event begins when a positive construct is encountered (the formation time is at the first fog block in that construct), and it ends with the last fog block in the last positive construct before either a negative construct or 3 consecutive non-fog blocks are encountered. Fog events separated by less than 1 h are merged, and finally all fog events lasting less than 1 h are discarded. This algorithm detects 250 fog events at SIRTA in the period 1 October 2010 to 30 September 2017, of which 218 occur in the winter half-year (October–March). In this section, some statistics of these fog events are presented, in order to put our simulations into context.

Figure 2 shows the formation and dissipation times of these fog events relative to the time of sunrise. The peak occurrence of fog formation is in the last few hours before sunrise, while fog dissipation most frequently occurs during the first 4 h after sunrise. This is consistent with previous studies on radiation fog and stratus-lowering fog (Tardif and Rasmussen, 2007; Dupont et al., 2016), which are the dominating fog types on this site (Dupont et al., 2016). There is also an important number of events that dissipate at night, but these are often short; more than half of the events dissipating at night last less than 3 h, while this is the case for only a quarter of the events with daytime dissipation (not shown). The classification of the histograms indicates how long time a cloud base below 400 m occurs before formation and after dissipation. For some events, the category is unknown due to missing ceilometer data. Figure 2a shows that the majority of the fog events that form at night are preceded by a cloud base for less than 1 h, which is typical for radiation fog, but it could also be fog appearing by advection. There are also many events which have a cloud base more than 2 h before formation, which would be expected for stratus-lowering fog. This type of formation can in particular explain the formation after sunrise. Figure 2b shows that the majority of the fog events that dissipate more than 1 h after sunrise is followed by a low cloud base for more than 2 h. Thus, these fog events will typically dissipate because their bases lift, without the LWP being reduced to zero. The preferred dissipation time after sunrise can be explained by the arrival of solar radiation which heats the fog and causes evaporation, an effect that will be quantified in our results.

To study the variability of temperature stratification and relative humidity above the fog, we use radiosonde measurements of these variables, and cloud radar to determine the cloud-top height (CTH) of the fog. Figure 3 is derived using 47 radiosondes at Trappes with simultaneous cloud radar measurements. The stratification $d\theta$ (Figure 3a) shows important variability from case to case. A value of 4–8 K is the most common, but there are also cases where $d\theta$ is as low as 2 K or >10 K. The humidity of the layer above (Figure 3b) is usually above 80 %, but there are also cases of humidity of 60–80 % and sometimes even below 40 %. The four cases of

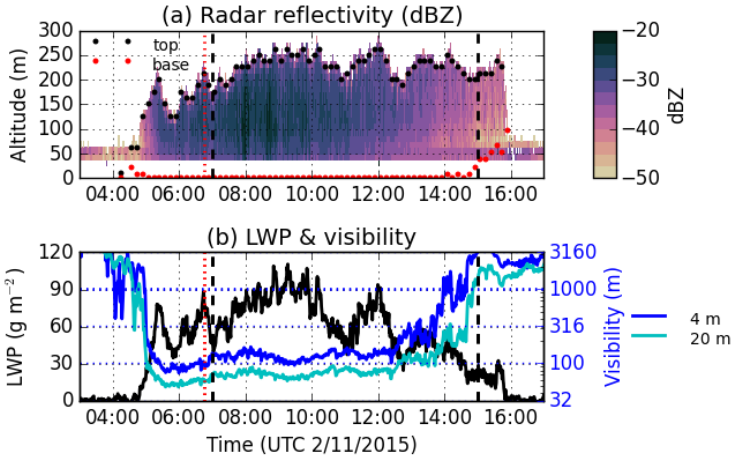

Figure 4: Observations from the SIRTA atmospheric observatory on 2 November 2015: (a) cloud radar reflectivity, (b) liquid water path and horizontal visibility at 4 m and 20 m. The vertical dotted line marks the time of sunrise. The vertical dashed lines mark the period that we simulate with the LES model (see section 3.2). In (a), only the data retained after applying noise filtering algorithm are shown, and retrievals of cloud base using ceilometer or visibility and of cloud top using the cloud radar (or visibility at 20 m) are indicated (see sections 2.1 and 2.2 for details).

very low humidity occurred during two very persistent periods of fog and low stratus near winter solstice when stratification was also very strong (Figure 3c).

2.3 The case study: A fog event on 2 November 2015

We chose a fog event which occurred at SIRTA on 2 November 2015 as basis for the simulations (Figure 4). Fog formed nearly 2 h before sunrise from clear sky and quickly reached a thickness of 200 m and an LWP of 60 g m^{-2}. It then persisted for most of the day with horizontal visibility of around 200 m at 4 m. The elevated values of LWP makes this event a thick fog, vertically well-mixed with a close-to adiabatic profile, which is confirmed by the 30-m mast measurements and the radiosonde at 1115 UTC (not shown). The visibility gradually improved after 1200 UTC until the fog base lifted at 1440 UTC, followed by complete dissipation of the cloud by 1600 UTC. Thus, this fog is one of the more persistent events, which makes it an appropriate case to answer our research questions.

This event occurred during a synoptic situation characterised by a rather weak low-pressure system right off the Atlantic coast of the Iberian Peninsula and a high-pressure system in Eastern Europe, with a southerly geostrophic wind at SIRTA. 10-m wind direction was easterly in the morning, turning south-easterly during the event. Integrated water vapour was around 10 kg m^{-2} (observed by MWR). Important cooling occurred in the surface layer, temperature at 30 m decreasing from 16 °C the previous evening to 5 °C at 0600 UTC, 1 h after fog formation. Measured radiative cooling of the surface was around 60 W m^{-2} during most of the night, with cloud-free sky. The fog was capped by a strong inversion, observed by the radiosonde launched at 1115 UTC (not shown).

3 Setup of the large-eddy simulations

3.1 Model description

We model the fog using the 3D large-eddy simulation (LES) model DALES (Heus et al., 2010), version 3.2.0. An overview of the model parameter values chosen for the Baseline simulation is shown in Table 2. Certain modifications to the code were applied; these are documented in Appendix A.

Due to the high resolution, the model domain must be restricted and have cyclic lateral boundary conditions to limit computational cost. A too small domain size should be avoided, though, since it causes an artificial

Parameter	Value (in Baseline)	Description
Model domain		
L_x (=L_y)	960 m	Horizontal model domain size
Δx (=Δy)	5 m	Horizontal resolution
Δz	2 m	Vertical resolution
Large-scale forcing		
V_g	5.39 m s^{-1}	Geostrophic wind speed
w_{ls}	$(-3.56 \cdot 10^{-6} s^{-1}) \cdot z$	Large-scale vertical velocity
Radiation model		
k	130 m^2 kg^{-1}	Extinction coefficient of liquid water for LW radiation
F_0	75 W m^{-2}	Cloud-top boundary condition for LW radiation
F_1	10 W m^{-2}	Cloud-base boundary condition for LW radiation
SW_0	(1187.1 - 45.9/μ_0) W m^{-2}	Incoming direct SW radiation at cloud top
α_s	0.23	Surface albedo for SW radiation
Surface model		
LAI	2	Leaf area index
c_{veg}	0.9	Fraction of the surface covered by vegetation
C_{skin}	20 kJ m^{-2} K^{-1}	Skin layer heat capacity
Λ	5 W m^{-2} K^{-1}	Skin layer conductivity
z_{0m}	0.2 m	Roughness length for momentum
z_{0h}	0.02 m	Roughness length for heat
W_l	0.2 mm	Initial surface liquid water reservoir
Microphysics		
N_c	200 cm^{-3}	Cloud droplet number concentration
σ_g	1.2	Geom. st. dev. of cloud droplet size distribution
σ_{gr}	1.5	Geom. st. dev. of rain drop size distribution

Table 2: Values of the relevant model parameters in the Baseline run. μ_0 is the cosine of the solar zenith angle. See text for details.

constraint on the sizes of the developing structures (De Roode et al., 2004). We tested domain sizes of 450 m, 900 m and 1.8 km, and found that the dominating scale for kinetic energy was 900 m in both the 900-m and 1.8-km testruns, with very small differences in the results of these two runs. We therefore decided on the compromise of a 960-m domain. The height of the domain is 1 km, with a vertical resolution which decreases gradually from 2 m at 300 m to 30 m at 1 km. Turbulence closure is ensured by the Deardorff 1.5 order scheme, which uses a prognostic subgrid-scale turbulent kinetic energy (TKE).

The interaction with the surface is parametrised using the Monin–Obukhov similarity theory coupled to a land-surface model with prognostic soil and surface skin temperature (Heus et al., 2010). We apply a constant value for the roughness length for momentum of 0.2 m, consistent with the friction velocity for a south-easterly wind direction at SIRTA (Fesquet et al., 2009), and a ten times smaller roughness length for heat (Garratt, 1992). A typical value from literature is also chosen for the skin heat conductivity (Van Ulden and Holtslag, 1985). Leaf area index (LAI) is set to 2 and vegetation fraction to 0.9, which are close to the values used for grass and croplands in the IFS model (ECMWF, 2016), on which the DALES land-surface model is based. The model also has a prognostic liquid water reservoir on top of the surface which can evaporate without surface resistance and is assumed to cover a fraction of the vegetation. This reservoir is fed by dew deposition, and we have also introduced that it is fed by droplet deposition (Appendix A). As this reservoir turns out to be of importance for fog dissipation, section 4.3.1 gives a further discussion.

The fog droplets are modelled with a simple one-moment scheme, using a constant prescribed number concentration N_c and a fixed log-normal shape of the size distribution with a geometric standard deviation $\sigma_g = 1.2$. Liquid water content (LWC) is diagnosed assuming all water vapour exceeding the saturation threshold is liquid. From N_c, σ_g and LWC, the droplet size distribution (DSD) is determined, which is consequently used to estimate the SW optical extinction coefficient (Appendix A) and the droplet sedimentation rate. The original

model did not include turbulent deposition of cloud droplets on the vegetation, but we have implemented this using the concept of a deposition velocity that provides the deposition flux when multiplied by the LWC of the first model level (Katata, 2014). We have chosen a constant deposition velocity of 2 cm s^{-1}, following e.g. Mazoyer et al. (2017). The two-moment scheme of Khairoutdinov and Kogan (2000) is used to parametrise bigger droplets (drizzle) forming from autocollection of fog droplets. This scheme includes autocollection, accretion, break-up, sedimentation and prognostic evaporation, and it is suitable for weakly precipitating stratocumulus clouds.

Radiative transfer is calculated with the simplified parametrizations for SW and LW radiation described in section 2.9 of Heus et al. (2010). These schemes only take into account the optical effect of the cloud droplets, and they therefore require boundary conditions and liquid water bulk coefficients (see Table 2). The boundary conditions F_0, F_1 and SW_0 are based on comprehensive radiative transfer calculations on the fog event 2 November 2015 using the ARTDECO code every 15 min (for details, see Wærsted et al. (2017)[1]). While the LW fluxes F_0 and F_1 are relatively constant during the fog, SW_0 depends almost linearly on the atmospheric pathway of the solar beam, which we have implemented into the model (see Table 2). Following Elias et al. (2009), we also add an extra extinction of 0.01 m^{-1} in the SW scheme inside the fog to represent the extinction by unactivated hydrated aerosols. We then find that the surface net SW radiation calculated from the DALES SW-scheme using LWP from the MWR and $N_c = 200$ cm^{-3} agrees well with the observations from the pyranometer, both for the fog on 2 November 2015 and for many other thick fog events at SIRTA (non shown).

3.2 Setup of the sensitivity studies

Since our objective is to investigate fog dissipation after sunrise, all simulations start at 0700 UTC, which is right after sunrise. By initialising the model with fog already present, we avoid expensive computation of the stable conditions before fog formation, and we also ensure that the fog has the same starting point at sunrise in all our simulations, which makes sensitivity studies more conclusive. The model is then run until 1500 UTC with output written every 5 min for horizontally averaged profiles and every 1 min for surface quantities and mean cloud base and top. The reference simulation, called Baseline, is initialised and forced according to observations (described later in this subsection), and sensitivity studies are thereafter performed by modifying certain model inputs (Table 3 and Figure 5). In particular, we modified the initial profiles of temperature and humidity to investigate the impact of the observed variability in stratification and humidity of the layer above fog top: the Baseline simulation corresponds to a case with stable but relatively humid air above, while the run WeakStrat corresponds to the many cases with high humidity and weak stratification, and the run DryAbove represents the less common cases of dry atmosphere above fog and strong stratification (Figure 3). The imposed radiative impacts of the temperature and humidity modifications in WeakStrat and DryAbove (Table 3) are based on sensitivity calculations with ARTDECO at 1100 UTC indicating that F_0 should be increased by 10 W m^{-2} in WeakStrat and by 20 W m^{-2} in DryAbove relative to Baseline, and SW_0 increased by 30 W m^{-2} in DryAbove, due to the different temperature and humidity profiles.

A simulation NoDew without any initial liquid at the surface is also carried out, to study the effect of this liquid reservoir. In all the other runs, the initial value for the reservoir is set to 0.2 mm, which is assumed to originate from dewfall during the night before fog forms, as no precipitation occurred. This seems a reasonable magnitude of dew based on the dew climatology from a grassland in the Netherlands, which found that average annual dewfall was 37 mm over 250 nights with dew (Jacobs et al., 2006).

The rest of this subsection describes how the observations are used to initialise and force the Baseline run. The initial profiles use 2-h averaged measurements (0600–0800 UTC) to get a more representative sample of the fog, as short-term variability is likely related to horizontal heterogeneity being advected past the observatory. The initial cloud top is set to the 2-h average value of 187.5 m. Averaged radar reflectivity (Z) is used to retrieve the LWC profile with the empirical formula of Fox and Illingworth (1997):

$$LWC = 9.27 \cdot 10^{0.0641 \cdot Z} \tag{1}$$

[1]We use the same method for quantifying radiative flux profiles as in Wærsted et al. (2017), except that specific humidity input above fog comes from the radiosonde and not the MWR.

Run name	Parameter changes			Other modifications
Baseline				
NoDew	W_l = 0 mm			
WeakStrat	F_0 = 85 W m^{-2}			Initial temp. & hum. profile (see Figure 5)
DryAbove	F_0 = 95 W m^{-2}	and	SW_0 = (1217.1 - 45.9/μ_0) W m^{-2}	Initial humidity profile (see Figure 5)

Table 3: List of the sensitivity runs performed with DALES, indicating which parameters and model input were changed relative to the Baseline run. The parameters are defined in Table 2.

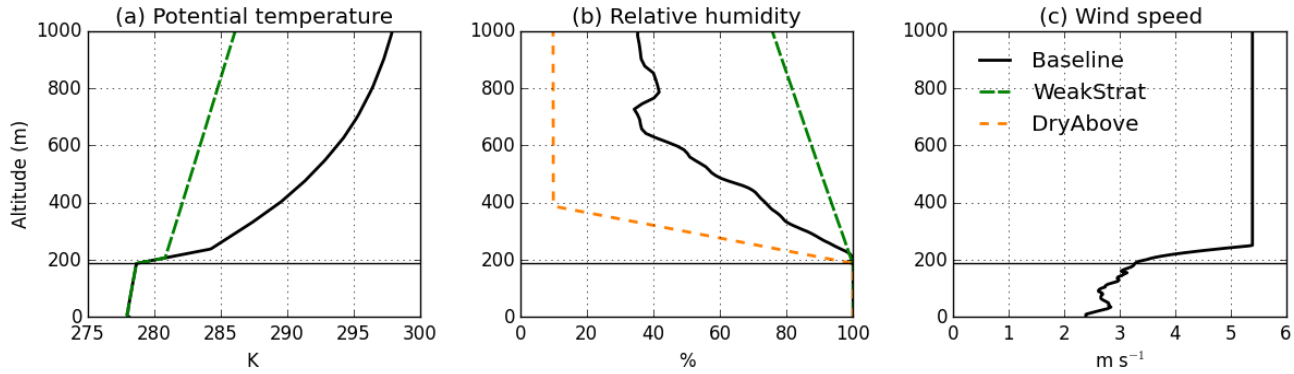

Figure 5: Initial profiles of DALES in the Baseline run (solid), and the modified profiles of the sensitivity runs. Altitude is given in metres above ground level, and the horizontal line indicates the fog top.

with LWC in g m^{-3} and Z in dBZ. In the cloud radar blind-zone (below ≈50 m) the LWC is assumed to increase linearly with height from 0 g m^{-3} at ground level. This profile of LWC is then normalised using the LWP of the MWR, since the latter is a more reliable measurement of the integrated liquid content than the reflectivity. Initial potential temperature, humidity and wind profiles are shown in Figure 5. The temperature profile above the fog is taken from the MWR retrieval. Inside the fog it is derived from in situ measurements at 30 m, assuming a saturated adiabatic profile inside the fog, capped by a 0.1 K m^{-1} inversion which is imposed until it encounters the temperature profile of the MWR. Relative humidity is set to 100 % inside the fog, and using the relative humidity measurements of the radiosonde launched at 1115 UTC above. The initial wind profile is taken from sonic anemometers at 10 m and 30 m, from the sodar in the range 30–200 m, then approaching linearly the geostrophic wind, which is used above 250 m. The geostrophic wind is constant with time and height and is taken from ERA5, the new global reanalysis of the ECMWF (Haiden et al., 2017), averaging over the levels 1000, 975, 950 and 925 hPa, the times 0600 and 1200 UTC and a 2° x 2° domain around SIRTA. A time-independent large-scale subsidence is also imposed, which increases linearly by 0.356 mm s^{-1} per 100 m, starting from 0 mm s^{-1} at the surface. This vertical gradient of subsidence is determined from the average subsidence of ERA5 at 950 hPa over the times 0600 and 1200 UTC in a 2° x 2° domain around SIRTA. No horizontal advection is imposed. Initial soil temperature and moisture are interpolated from SIRTA soil measurements, giving an upper soil temperature of 9 °C, and a soil moisture of 0.39 m^3 m^{-3}. This soil moisture exceeds the field capacity parameter of the model, which means that modelled transpiration is not restricted by soil moisture.

3.3 Analysis of the fog LWP budget

This section describes a method to separate the modelled LWP tendency into contributions from the various processes included in the model, that is radiation, entrainment, surface heat fluxes, droplet sedimentation and subsidence. This method is useful for comparing the importance of each process for the fog LWP budget, and for quantifying how much the impact from each process changes due to the modifications applied in the sensitivity tests. The approach is similar to the mixed-layer model for the LWP budget of stratocumulus clouds presented by Van der Dussen et al. (2014).

For simplicity, we neglect all horizontal variability and assume the fog layer has a thickness h and is saturated everywhere. We further assume that the temperature, air density and pressure inside the fog layer can

be approximated by their vertically averaged values. Thus, our simplified fog is a saturated layer of thickness h with temperature T_a, pressure p, density ρ_a and integrated liquid water content LWP. Since the air is assumed to be at saturation, the water vapour pressure e_a must equal its saturation value e_s at the fog temperature, i.e. $e_a = e_s(T_a)$. If the fog is heated, a certain amount of the liquid must evaporate so that the air remains saturated at the new, higher temperature. This fog droplet evaporation rate, which constitutes a sink of fog LWP, is denoted E_a, with SI units of kg m^{-2} s^{-1}, more conveniently given in g m^{-2} h^{-1} later in the paper. The fog layer is subjected to m processes which involve a flux of sensible heat, and n processes with a flux of latent heat (i.e. water vapour) apart from the fog droplet evaporation. We call these fluxes SH_i ($i = 1,2,3,...,m$) and LH_i ($i = 1,2,3,...,n$), with units of W m^{-2}, and they are defined positive when they tend to increase fog temperature/moisture. The processes of sensible heat are radiation (absorbed SW and LW flux by the liquid layer), upward turbulent sensible heat flux at cloud base, downward turbulent sensible heat flux at cloud top, and adiabatic heating from subsidence. The latent heat fluxes are the upward water vapour flux at cloud base and the downward water vapour flux at cloud top.

Since the fog must always remain at saturation,

$$\frac{de_a}{dt} = s\frac{dT_a}{dt}, \tag{2}$$

where $s = \frac{de_s}{dT}$. Since the specific humidity q_v relates to vapour pressure as $q_v = \frac{\varepsilon}{p}e_a$, we may rewrite Eq. (2) as

$$\gamma\frac{L_v}{c_p}\frac{dq_v}{dt} = s\frac{dT_a}{dt}, \tag{3}$$

where $\gamma = \frac{c_p p}{\varepsilon L_v}$ is the psychrometric constant, ε = 0.622 is the ratio of the gas constants of dry air and water vapour, c_p = 1004 J kg^{-1}K^{-1} is the specific heat capacity of air at constant pressure, and L_v = 2.5·10^6 J kg^{-1} is the specific latent heat of vaporisation. We have neglected the insignificant contribution from the rate of change of pressure to the tendency of q_v.

The fog temperature is increased by the sensible heat fluxes, while it is decreased by the latent heat of evaporation of the droplets:

$$\frac{dT_a}{dt} = \frac{1}{\rho_a c_p h}\Big(-L_v E_a + \sum_{i=1}^{m} SH_i\Big) \tag{4}$$

The specific humidity is increased by the evaporation of the droplets and by the latent heat fluxes:

$$\frac{dq_v}{dt} = \frac{1}{\rho_a h}\Big(E_a + \frac{1}{L_v}\sum_{i=1}^{n} LH_i\Big) \tag{5}$$

By inserting Eqs. (4, 5) into Eq. (3), we can eliminate $\frac{dT_a}{dt}$ and $\frac{dq_v}{dt}$:

$$\gamma\frac{L_v}{c_p}\frac{1}{\rho_a h}\Big(E_a + \frac{1}{L_v}\sum_{i=1}^{n} LH_i\Big) = \frac{s}{\rho_a c_p h}\Big(-L_v E_a + \sum_{i=1}^{m} SH_i\Big)$$

Some rearrangement of this equation results in the following expression for E_a:

$$E_a = \frac{s}{s+\gamma}\frac{1}{L_v}\sum_{i=1}^{m} SH_i - \frac{\gamma}{s+\gamma}\frac{1}{L_v}\sum_{i=1}^{n} LH_i \tag{6}$$

Since Eq. (6) is a linear sum over the fluxes from different processes, the contributions to E_a of each process are additive and can be analysed separately. While positive sensible heat fluxes cause loss of liquid water (positive contribution to E_a), positive latent heat fluxes provide a gain of liquid water (negative contribution to E_a). Because s increases with temperature, the effects of sensible heat fluxes become increasingly important with temperature, while the opposite is the case for latent heat fluxes (Figure 6).

To get the full fog LWP budget, we need to take into account also the vertical fluxes of liquid water across the fog base and top, caused by turbulent mixing and sedimentation of droplets. We call these liquid fluxes $F_{l,base}$ and $F_{l,top}$, defined positive when liquid is transported towards the fog. Finally, we account for

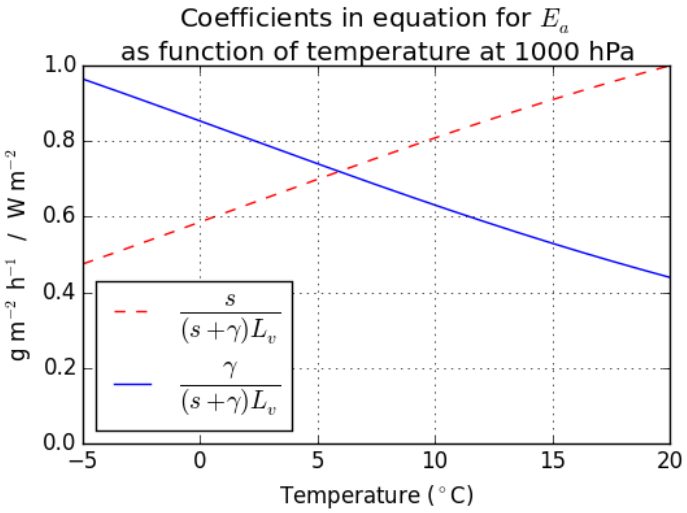

Figure 6: The fog evaporation rate (g m^{-2} h^{-1}) caused by a sensible heat flux of 1 W m^{-2} (dashed line), and the condensation rate caused by a latent heat flux of 1 W m^{-2} (solid line), as function of temperature at a pressure of 1000 hPa.

the reduction in LWP caused by the horizontal divergence due to the vertical gradient of subsidence ($\frac{dw_{ls}}{dz} = -3.56 \cdot 10^{-6}$ s^{-1}, see Table 2). The final expression for the fog LWP is then:

$$\frac{dLWP}{dt} = -E_a + F_{l,base} + F_{l,top} - (-\frac{dw_{ls}}{dz})LWP \quad (7)$$

Appendix B gives more details on the calculation of each term from the model output.

4 Results and discussions

4.1 Comparison of the Baseline simulation to observations

Figure 7 shows the evolution of the fog in the Baseline simulation compared to the observed fog. We note that the modelled fog base lifts several hours earlier than the observed fog base, dissipating at the surface at 1045 UTC, although the LWP is higher. The earlier lifting may be related to the vertical development of the mixed layer being stronger in the model than observed, thereby lifting the liquid layer up from the surface. The temperature, however, evolves similarly to observations. The relative similarity between model and observations indicates that the local processes likely played an important role in the evolution of the fog, although we cannot exclude that advection and other large-scale phenomena also played a role in the observed fog.

We now consider the energy budget of the surface (Figure 7d). The net radiation (R_{net}) is mainly driven by the SW and therefore evolves with the solar angle, reaching a maximum around noon. However, the dependence on LWP is also apparent, especially in the anti-correlated relationship between the observed R_{net} and the observed LWP (Figure 7b). The rather good agreement between observed and modelled R_{net} can thus be explained by the similar evolutions of LWP, which is the main parameter affecting how much radiation reaches the surface (Wærsted et al., 2017). The ground flux (G) is upward in this case, due to the soil being warmer than the air, and its contribution is in the order of 10–15 W m^{-2} in the morning both in model and observations.

We now turn to the surface sensible heat flux (SH) and latent heat flux (LE). Here the model and observations are no longer similar. The model predicts a Bowen ratio of around 2 after 10 UTC, and considerably higher in the early morning because of higher surface resistance due to low insolation (see section 4.3.1), but the LE contribution to surface energy balance is nevertheless significant. The observations show a considerably lower SH and an LE around zero. As a result, on average only 35 % of the available energy ($R_{net} - G$) is accounted for by the turbulent heat fluxes. The lack of closure in the surface energy balance indicate that

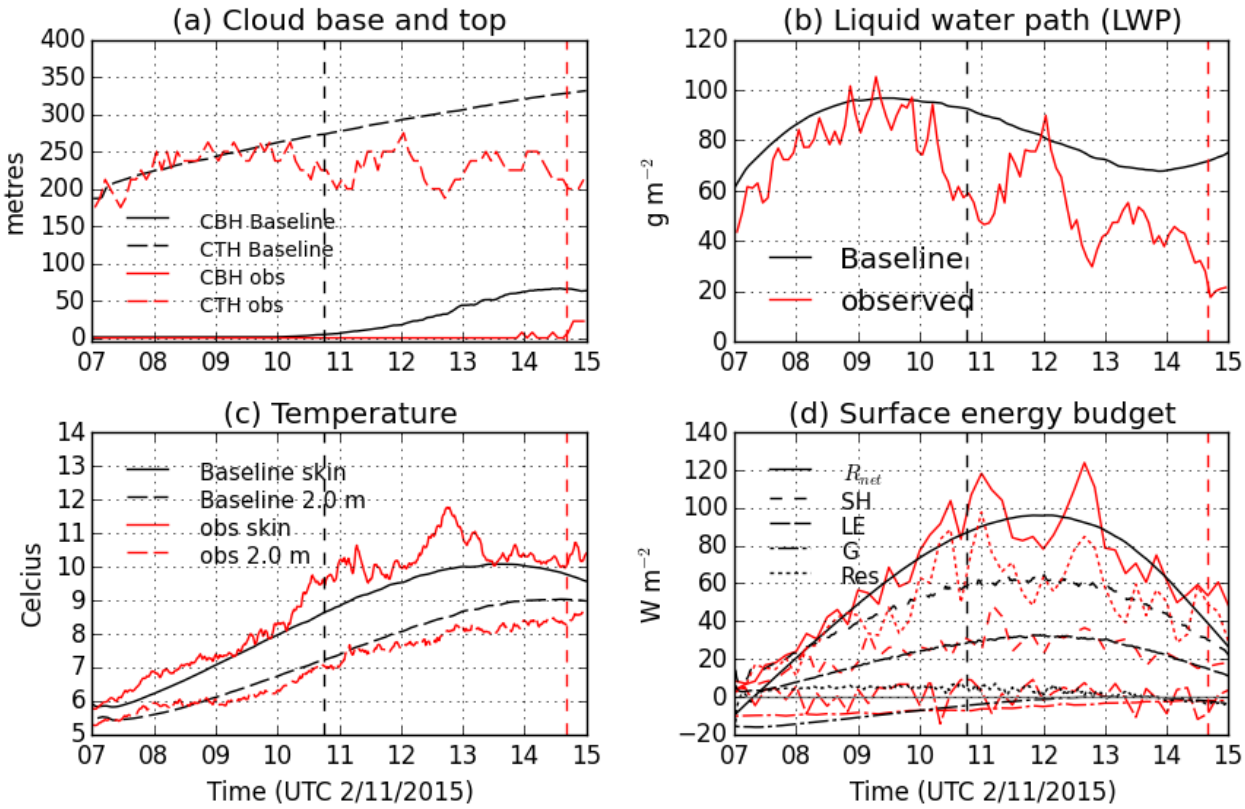

Figure 7: The evolution of the fog in the Baseline simulation (dark lines) and observations of the real fog on 2 November 2015 (light lines): (a) Cloud top and cloud base, (b) LWP, (c) screen temperature and surface skin temperature. (d) Terms in the surface energy balance: Net radiation absorbed (R_{net}), upward sensible (SH) and latent (LE) turbulent heat fluxes, and downward ground flux (G). The residual (Res) is calculated as $R_{net} - G - SH - LE$. The vertical lines indicate the time of dissipation. In the model, this is defined as the first time when average cloud base is above 4 m. The observations are averaged in 5-min blocks (CTH, CBH, LWP) and 10-min blocks (surface energy balance).

the turbulent flux observations must be better understood before they can be used to validate the predicted repartition of the available energy into SH and LE in the model. The challenge of the surface energy balance is discussed further in section 4.3.1.

4.2 Impacts of physical processes on fog LWP

Figure 8 separates the modelled tendency of fog LWP into contributions from each physical process, as explained in section 3.3. We first note that the LWP budget closes well: the residual is small compared to the important terms and it is centred at zero except for the first half hour. This indicates that the method of decomposition of the LWP budget in the model works well in spite of the simplifications applied. We further note that the residual is strikingly anti-correlated with the entrainment term, indicating that the residual mainly can be attributed to this term, as discussed in Appendix B. We have therefore chosen in the later figures to derive the entrainment term from the residual of the other terms of the LWP budget.

The LWP increases until 0930 UTC, after which it decreases, but only by 5–10 g m^{-2} h^{-1}. The increase in the early morning is due to the LW radiative cooling. In comparison, heating and divergence by subsidence play a negligible role due to the weak large-scale velocity. As the sun rises, the absorption of solar radiation inside the fog layer becomes an increasingly important loss term of LWP; its magnitude is in agreement with what we calculated in Wærsted et al. (2017) if the absorption by unactivated aerosols of optical depth 0.05 is accounted for.

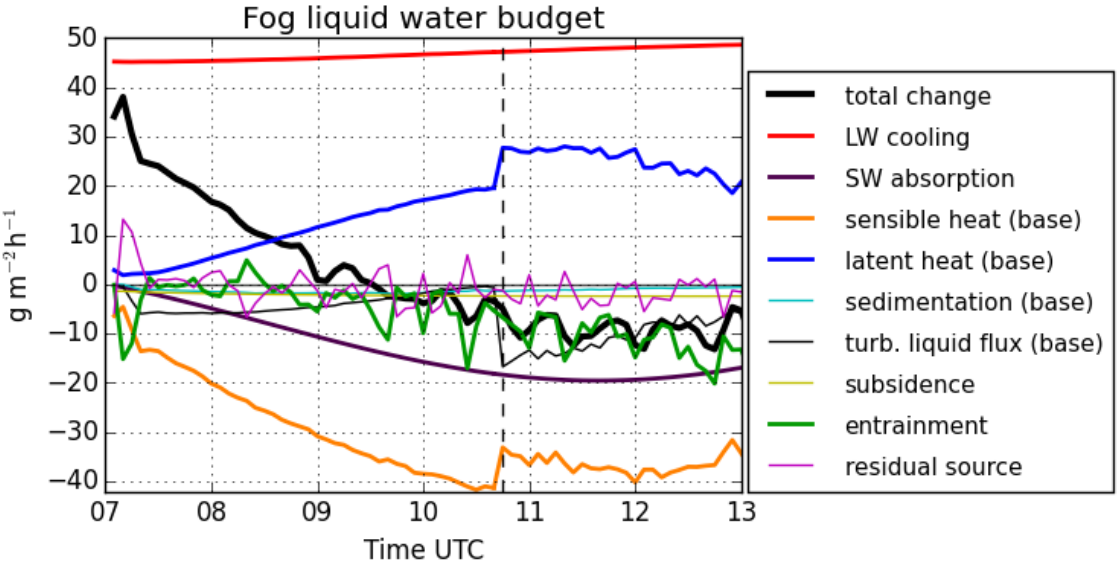

Figure 8: The terms of the fog LWP budget in the Baseline simulation, calculated from the model output (see Eqs. (6, 7) and Appendix B). The thick black line is the change with time of fog LWP in the model, while the other lines are the contributions from each process (NB: the lines for sedimentation and subsidence are almost on top of each other near -2). The pink line is the residual, i.e. the total change in LWP minus the sum of all contributions. The vertical dashed line marks the time of dissipation.

The most significant negative term in the LWP budget is the sensible heat flux from the surface, which increases rapidly as the sun rises. However, the contribution from surface latent heat flux is also important and has the opposite sign. At our fog temperature of 5–8 °C, each 1 W m^{-2} of latent heat gives approximately the same LWP to the fog as is lost by 1 W m^{-2} of sensible heat (Figure 6), making their combined effect roughly proportional to $SH - LE$. The Bowen ratio is therefore very important for the combined effect of the surface heat fluxes on the fog LWP.

The droplet sedimentation rate at the surface is very weak, because the LWC is low near the surface, while sedimentation contributes importantly to vertical transport of water within the fog (Figure 9ab). The low LWC near the ground also limits the amount of turbulent deposition, which is still a stronger contributor than sedimentation (Figure 8). Our results are not very sensitive to this added deposition; in a testrun where the turbulent liquid deposition was not included, the fog LWP was 5 % higher than in Baseline at 1000 UTC[2] and dissipation was 15 min later (not shown). The weak deposition can be explained by the heating from below: the modelled cloud water evaporates when approaching the surface, rather than depositing, giving large flux gradients at the first model level, as liquid water moves down and water vapour up (Figure 9b); this is a consequence of the immediate adjustment to saturation in the model. This is also why a fraction of the LWP loss by surface heat fluxes suddenly changes to a loss by turbulent liquid flux once the fog base lifts from the surface (Figure 8). The drizzle parametrisation generates little rainwater (it is highest around 0930 UTC), but contrary to the cloud water the raindrops do not evaporate as efficiently near the surface, and they produce a sedimentation flux at the surface which is twice as large as that of cloud droplets, although both are in the order of 1 g m^{-2} h^{-1} only (Figure 9b). However, the cloud droplet sedimentation is sensitive to the chosen parameters for the DSD. We therefore performed a testrun (not shown) with σ_g increased to 1.7, which gives a wider DSD with more big droplets; this agrees better with typical observed DSD at 4 m with a fog monitor (not shown), than when $\sigma_g = 1.2$. In this run, loss by deposition is about 50 % higher (mainly through increased sedimentation) and the fog dissipates 25 min sooner than in Baseline. However, setting σ_g to the observed values at the surface may not yield the best results in DALES, since such a wide DSD shape may be less realistic close to the fog top, where LWC is much higher (Figure 9a), and the wider DSD causes a reduction of

[2]This is a weaker impact than we would expect from removing the term "turb. liquid flux" in Figure 8. There is actually a compensating effect through an higher Bowen ratio caused by a smaller surface liquid reservoir, due to less feeding by deposition.

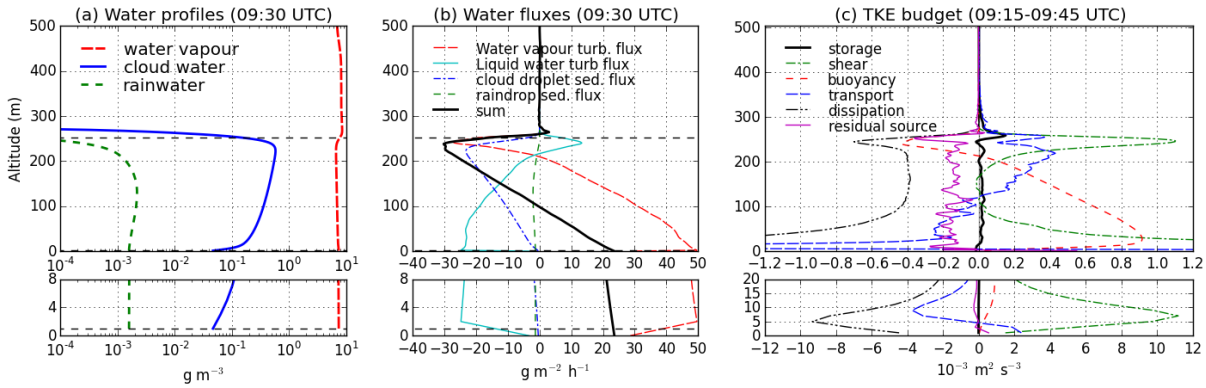

Figure 9: Horizontally averaged profiles at 0930 UTC in the Baseline simulation: (a) Water vapour, cloud water and rainwater content, and (b) upward fluxes of water at 0930 UTC. The horizontal lines indicate the cloud base and cloud top. (c) The resolved TKE budget (averaged in 0915–0945 UTC) (discussed in section 4.3.2). The term "storage" is the increase in TKE, while the "residual" is the storage minus the sum of the other terms (i.e. the source of TKE which is not accounted for). The lower panels are just enlargements of the lowest parts of the profiles.

fog opacity of about 25 %.

Entrainment at fog top is only a weak sink of LWP in the Baseline run. It amounts to less than 10 g m^{-2} h^{-1} in the first hours of the simulation (Figure 8). This is because the relative humidity directly above the fog is set very high in the initial conditions (see Figure 5). As the fog develops vertically, it comes into contact with layers of lower relative humidity, thus increasing the loss from entrainment with time. However, entrainment has a different role, too. The thickening of the mixed layer with time, which is the result of entrainment and opposed by subsidence, enables the fog base to lift from the surface even when the LWP is not decreasing dramatically. The fact that the modelled fog becomes thicker than the observed fog can therefore be a main reason why it lifts sooner. This important role of entrainment is further explored in a sensitivity study in section 4.3.2.

All in all, the LWP budget of the Baseline simulation suggests that, once the sun has risen importantly, the radiative heating of the surface is the main loss process for fog LWP, with a strong importance of the Bowen ratio, followed by the SW absorption inside the fog.

4.3 Sensitivity studies

4.3.1 A wet surface and the surface energy balance

In the NoDew run, the LWP is depleted sooner and more rapidly, leading to an 85 min earlier dissipation by lifting of the cloud base, while the cloud top develops very similarly to Baseline (Figure 10a). Consequently, the cloud base lifts sooner. Clearly it is the larger loss by surface fluxes (10 g m^{-2} h^{-1} more over 0800–0915 UTC, Figure 10d) that is responsible for the faster decrease in LWP in NoDew than Baseline. The impacts on LWP by radiation and entrainment are the same as Baseline (Figure 10df), while the microphysics loss is smaller before dissipation (Figure 10e), due to the earlier reduction in liquid near the ground. After dissipation, the microphysics term becomes very big, but this is actually representing the mixing of the droplets with the dry air from the sub-cloud layer, compensating the decrease in the "surface fluxes" term at dissipation (i.e. it is a consequence of our definition of the terms, see section 4.2). The increased loss from surface fluxes relative to Baseline is due to a higher Bowen ratio, caused by the extra surface resistance involved when evaporation cannot occur directly from the surface.

Thus, this sensitivity test indicates that the presence of a liquid layer on top of the surface can importantly affect the dissipation of fog. Although the soil is very moist, the relatively low temperature and small amount of solar radiation makes the canopy resistance (which in DALES is calculated from the Jarvis (1976) parametrisation) very high compared to the aerodynamic resistance, especially in the first hours after sunrise (Figure 11a). This means that the evaporation through transpiration will be low, in spite of the high soil moisture. For the

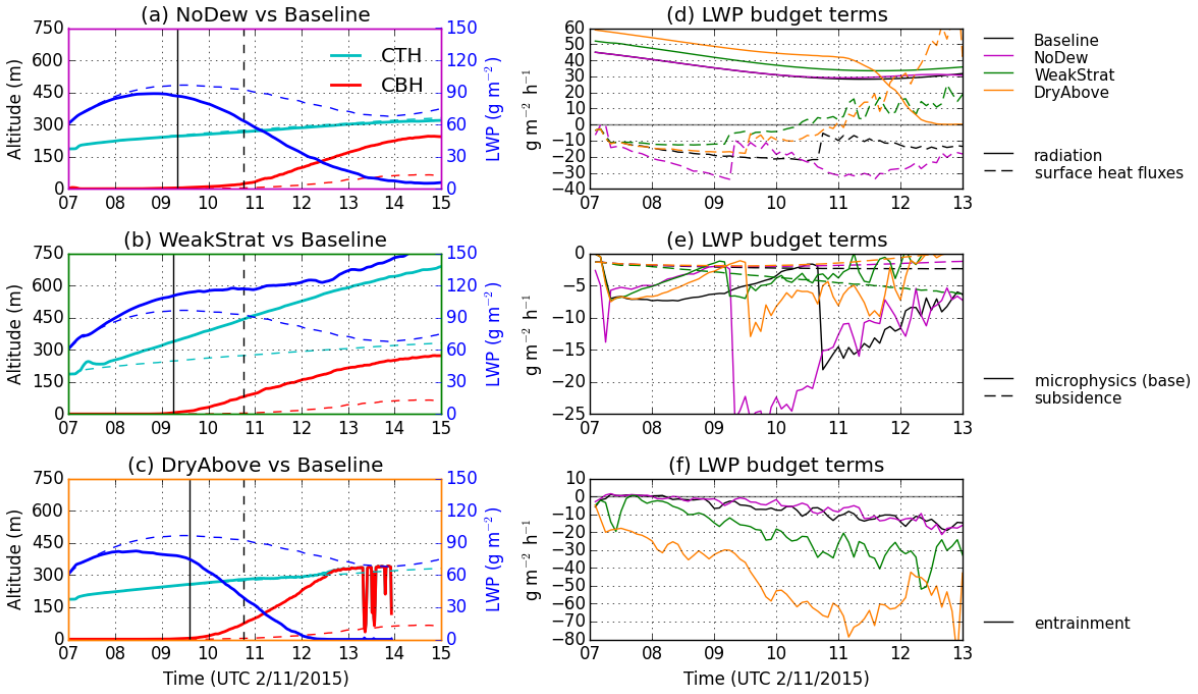

Figure 10: (a-c) Comparison of the modelled evolution of the fog base (red), fog top (cyan) and LWP (blue), and dissipation time (vertical line), between Baseline (dashed) and each of the sensitivity runs (solid). (d-f) Comparison of the terms in the LWP budget equation between the four runs. The term "radiation" includes both SW and LW, "surface heat fluxes" is total effect of sensible and latent heat, and "microphysics" combines sedimentation and turbulent liquid flux at fog base (i.e. all liquid transport across fog base). There is no residual because the entrainment term has been derived from LWP closure rather than calculated. NB: In (d), the lines "radiation" of Baseline and NoDew are on top of each other.

fraction of vegetation covered by liquid, however, there is no surface resistance, and we can therefore expect a Bowen ratio of $\frac{\gamma}{s}$ from the Penman equation (Penman, 1948), so that the surface fluxes cause no evaporation of the fog (to see this, insert $SH = \frac{\gamma}{s} LH$ in Eq. (6) to get $E_a = 0$). It is the difference in the fraction of vegetation covered by liquid (c_{liq}) that causes a higher overall Bowen ratio in NoDew relative to Baseline (Figure 11d). This fraction is very low in NoDew, while in Baseline it starts at 0.5 and then decreases (Figure 11c). In DALES, this fraction is parametrised rather crudely as being proportional to the surface liquid water reservoir W_l:

$$c_{liq} = \frac{W_l}{0.2\text{mm} \cdot LAI} \tag{8}$$

Since $LAI = 2$ (Table 2), the initial 0.2 mm reservoir imposed in Baseline causes the fraction to be 0.5 initially, and then it decreases due to evaporation. Although Eq. (8) is probably too simple for real situations, the sensitivity test has shown the importance of a wet surface for maintaining fog after sunrise. Since the evaporation occurs at microscale, it is to be expected that the fraction of the surface covered by liquid is more important for the Bowen ratio than the total liquid reservoir. In reality, the vegetation type can be expected to strongly impact how much of the surface stays wet as the water is redistributed by wind, throughfall, and infiltration to the soil. The fog itself could help maintaining a high liquid coverage due to deposition of cloud droplets on the vegetation. Price (1991) studied the evaporation over a bog and found it to be close to equilibrium evaporation during fog, arguing that this was enabled by fog drip which wetted the surface. Wetting of the surface could also be caused by rainfall before or during the fog.

Given the importance of the Bowen ratio for the fog LWP budget, validation of model predictions is important. Unfortunately, since the closure in the observed energy balance is only 35 % (Figure 7d), it leaves too much uncertainty to perform such a validation. The low closure percentage is not only occurring in fog, though. We considered the whole month of November 2015, and found that during day (for solar zenith angle less than 85°), the average closure is 43 %. The non-closure of the surface energy balance is a well-known issue

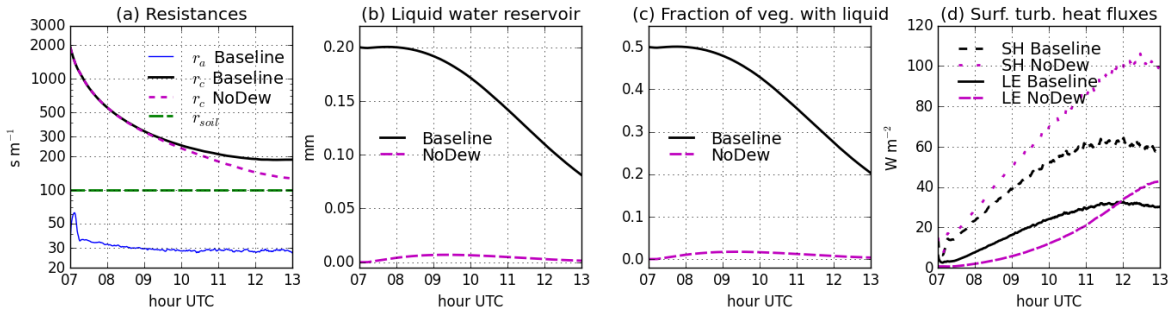

Figure 11: Simulated variables in the surface parametrisation in DALES for the runs Baseline and NoDew, as function of time: (a) aerodynamic resistance (r_a), canopy resistance (r_c, applied to the fraction of vegetation not covered by liquid) and soil resistance (r_{soil}, a prescribed value applied to the 10 % of the surface assumed not to have vegetation); (b) surface liquid water reservoir (W_l); (c) fraction of vegetation covered by the liquid (c_{liq}); (d) surface sensible and latent heat fluxes. In (a), r_a in NoDew is not shown because it is always very close to that of Baseline.

in micrometeorology, and it is common that the available energy ($R_{net} - G$) is larger than the measured turbulent heat fluxes ($SH + LE$) (Foken, 2008). This positive residual is likely explained either by a non-negligible storage term in the uppermost soil and vegetation or an underestimation of the turbulent fluxes, since R_{net} is rather precisely measured (Leuning et al., 2012). In our case the residual is too large to be mainly explained by storage, and it seems more likely that an underestimation of the turbulent heat fluxes is the main reason for the non-closure. Foken (2008) argues that this underestimation occurs not merely due to measurement errors, but also because of coherent mesoscale circulations, generated by surface heterogeneities, whose flux contributions cannot be detected by covariances at a single location. Evidence for this theory has been found from the improved closure obtained from scintillometers (which are able to measure averaged fluxes over a larger area), and from the good closure obtained in very homogeneous landscapes such as deserts (Foken, 2008). SIRTA lies in a heterogeneous landscape, which may contribute to the poor closure. However, we found a similarly low closure (46 %) for the observatory Cabauw in the Netherlands (Beljaars and Bosveld, 1997) for daytime in November 2011, which was a similar period as November 2015 at SIRTA (including several fog events and with R_{net} rarely higher than 200 W m^{-2}).

Although surface energy balance measurements are a topic of much research, to our knowledge no publication studies it specifically for fog. Our results show that it is worth investigating. Alternative measurement techniques such as scintillometers could be studied to see if they measure the turbulent fluxes in fog better than the eddy covariance method.

4.3.2 The stratification and humidity above the fog

In WeakStrat, the cloud top develops much faster than in Baseline (Figure 10b). Due to the weaker stratification, less potential energy needs to be overcome to mix the fog with the air above, and the entrainment therefore can happen much faster. The entrainment velocity in the period 0800–1000 UTC amounts to 72.7 m h^{-1} in WeakStrat, compared to 22.2 m h^{-1} in Baseline. This vertical displacement of the fog top enables a dissipation of the fog at ground level 90 min earlier than in Baseline. The earlier dissipation occurs in spite of a higher LWP. This sensitivity test therefore shows that the dissipation of fog at ground level (i.e. lifting of the cloud base) can depend as much on the evolution of the CTH as the LWP. The LWP increases more in WeakStrat than in Baseline in spite of the larger loss by entrainment (Figure 10f). This can be explained by the stronger radiative cooling, and by the weaker loss by sensible heating from the surface (eventually even becoming a gain) once there is a sub-cloud layer (Figure 10d). There is also less loss by microphysics (Figure 10e).

In the DryAbove run, the fog more rapidly loses liquid water and lifts 70 min earlier than in Baseline, and the whole cloud dissipates around noon (Figure 10c). Even though there is not more entrainment than in Baseline (cloud top develops at the same rate), the introduced air is much drier and therefore causes much more liquid water loss (Figure 10f). However, the dry air above the fog also has an opposite effect: the radiative cooling is stronger than in Baseline due to the drier atmosphere (Figure 10d). This second effect is considerable,

but smaller than the effect of more drying from the entrainment. All in all, the LWP budget is more negative than in Baseline, leading to stronger LWP decrease. Thus, similarly to in NoDew, in the DryAbove run the fog dissipates earlier than in Baseline because the LWP is smaller with the same fog thickness.

An overall interpretation of the three sensitivity tests is that the fog dissipation at the surface occurs when the fog LWP is no longer sufficient to fill the entire mixed layer, so that the fog base lifts. Dissipation can be triggered from a decrease in LWP or an increase in the CTH. In NoDew and DryAbove, it is the decrease in LWP that explains the earlier dissipation, while for WeakStrat it is the increase in CTH.

Based on the runs Baseline and WeakStrat (Figure 10b), the observed variability in stratification above fog top has a strong impact on the entrainment velocity. In situations when the fog top is capped by a weaker inversion and a weak stability in the following hundreds of meters, it will more easily thicken and transition into stratus than in situations when the fog is capped by a stronger inversion. Thus, the stratification at fog top should be considered a major factor for the fog dissipation, and observations of this parameter might be useful for anticipating fog dissipation. As radiosondes only give snapshots of the situation, the observation by MWR is more practical. We find that the MWR reproduces the parameter $d\theta$ observed by radiosondes (Figure 3a) with a correlation coefficient of 0.92, although it systematically underestimates $d\theta$ for strong stratification (not shown).

The entrainment rate at the fog top not only depends on the stratification, but also on the amount of TKE available to overcome the potential energy of the stratification. Several entrainment parametrisations have been developed for the clear or stratocumulus-topped convective boundary layer. These essentially compute the entrainment rate as a ratio of the produced TKE in the mixed layer to the stability of the capping inversion (Stevens, 2002; Conzemius and Fedorovich, 2006). TKE can be produced both by buoyancy and wind shear. In our case, the fog layer is efficiently destabilised by cooling at the top and heating from the surface, while the wind is relatively weak. Nevertheless, the profile of TKE budget (Figure 9c) shows that both wind shear and buoyancy give important contributions to the production of TKE in the model. The wind shear produces TKE near the surface and in the entrainment zone. However, most of the TKE produced by shear near the surface is dissipated locally (Figure 9c), and previous studies have shown that surface shear gives a negligible contribution to entrainment (Conzemius and Fedorovich, 2006). In a testrun where wind forcing and initial wind were both set to zero, entrainment velocity (averaged over 0800–1000 UTC) was only 6 % lower than in the Baseline setup (not shown). Thus, the wind shear is of secondary importance for entrainment relative to buoyancy in our case study. It is therefore likely that fog thickening by entrainment is enhanced by heating of the surface, thus likely being more efficient in spring/autumn than near winter solstice. The entrainment could also be stronger for thick (opaque) fog than for thin fog, due to the stronger radiative cooling at fog top (Wærsted et al., 2017).

As shown in the run DryAbove, the humidity above the fog also has an impact on fog dissipation and could be an interesting parameter to observe. However, its effect is less straightforward due to the opposing impacts on LWP of radiation and entrainment, which both increase when the air above is dry (Figure 10df). These two processes are not sensitive to the humidity at the same altitudes. While the drying effect from entrainment is only affected by the humidity in the first few tens of meters above the fog top, with which the fog mixes, the radiative impact is also sensitive to the atmosphere higher up. This means that in special cases where there is a humid layer directly above the fog top while the rest of the atmosphere above is very dry, the radiative effect would dominate and the fog could be more resistant to dissipation than when the atmosphere is moister. Indeed, this is likely what happened during the periods of persistent fog which correspond to the four radiosondes in Figure 3 with lowest humidity. The combination of a strong stratification and little insolation near winter solstice limits the entrainment, so that the radiative effect of the dry atmosphere can dominate over the entrainment effect. If the humidity in the layer directly above fog top is to be observed by remote sensing (without confusing it with the fog or the humidity higher up), an instrument with both high vertical resolution and the ability to penetrate the fog is needed. The MWR humidity profile lacks the resolution, while differential absorption lidars, which would have sufficient resolution (Spuler et al., 2015), cannot penetrate clouds. An alternative would be to measure the layer in situ, for example using a drone.

5 Summary and conclusions

Fog dissipation depends on processes occurring both at the surface and fog top, and the increasing possibilities for measuring properties aloft, in situ or by remote sensing, makes it important to understand the impacts of the fog-top properties. Using observations of 250 fog events during 7 years, we showed that more than half the fog events dissipating after sunrise transition to a stratus which lasts at least 2 h, indicating that the vertical displacement of the liquid layer is the most frequent dissipation scenario. We further quantified the contribution of different local processes to the liquid water path (LWP) budget of a thick fog after sunrise, and investigated how the fog dissipation is affected by the temperature and humidity at the fog top, and by the liquid water at the surface. This was achieved using idealised sensitivity simulations carried out with the large-eddy model DALES, where we tested the impact of the variability of fog-top properties observed by 47 radiosondes and cloud radar.

The quantifications of the terms of the fog LWP budget in the simulations indicate that the most important loss process of LWP is the turbulent heat fluxes from the surface, responsible for 20–30 g m^{-2} h^{-1} in the late morning. The loss by absorption of SW radiation in the fog layer reaches 15 g m^{-2} h^{-1} in the late morning. The loss by cloud-top entrainment can be very weak if the air overlying the fog is nearly saturated, while it can be as strong as the surface flux term if the air is dry. All these processes counteract the production of LWP by radiative cooling at fog top.

Our sensitivity study indicates that the presence of liquid water on top of the surface is important for the fog LWP budget. Even with saturated soil, in the simulation without initial liquid on the surface the fog dissipates 85 min earlier than in the simulation where the initial fraction of surface covered by liquid is 50 %. This is because the loss of LWP by surface fluxes is very sensitive to the Bowen ratio. A dry surface therefore causes a lower fog LWP, while not affecting the cloud-top height, thereby triggering an earlier fog dissipation.

The profiles of humidity and temperature in the layer right above the fog top have a significant impact on fog dissipation time. If the humidity in this layer is low, it can incite fog dissipation through its evaporative effect when mixing with the fog: dissipation is 70 min earlier in the run with dry air above than in the run where the air above is close to saturation. However, as the humidity also affects radiative cooling, the effect of a dry atmosphere aloft will depend on the details of the humidity profile. The simulated fog develops vertically much faster when the layer above is weakly stratified, thereby causing a dissipation by lifting of the fog base 90 min earlier in the run with weak stratification than in the Baseline run which has stronger stratification. Thus, in this case it is the faster increase in the cloud-top height which allows an earlier dissipation, while the LWP is actually higher than in Baseline. This shows that the evolutions of both the cloud-top height and the LWP are important for fog dissipation at the surface.

The deposition of droplets appears as a weak sink process (5–10 g m^{-2} h^{-1}). However, the sedimentation is sensitive to the microphysics parametrisation, notably the width of the droplet size distribution, while the contribution of turbulent deposition may be very dependent on the vegetation type (Katata, 2014). Nevertheless, our results suggest that in day the deposition has a secondary role to the turbulent heat fluxes, because the droplets evaporate when approaching the surface rather than deposit.

Given the large importance of the Bowen ratio, future efforts should be made to better estimate it in fog conditions from measurements, as we found that the eddy covariance method does not give sufficiently accurate measurements to determine the Bowen ratio. In the meantime, the net radiation at the surface, which can be measured with high accuracy, could be used to estimate the turbulent heat fluxes with some assumption on the Bowen ratio or surface resistance and the ground flux fraction. The important impacts of the variability in the stratification and relative humidity directly above fog top found by radiosondes suggest that a more detailed and continuous observations of this layer could be interesting for understanding and prediction fog. When studying the performance of fog forecasts by numerical weather prediction (NWP) models, attention should be given to how well the model reproduces these above-fog properties, since the quality of fog forecasts likely is sensitive to it. Assimilation of new observations (e.g. microwave radiometer, water vapour lidar) might improve the forecasts by improving the initial temperature and humidity profiles. The analysis method used to study the LWP budget in this paper, which to our knowledge is a novel approach to study model output, could also be applied to other model studies of fog. It could also be applied to columns in 3D NWP models, if all necessary outputs are available, including the advection through the lateral boundaries.

Appendix A Modifications to the DALES code

Here follows a list of the modification we did to the DALES code:

- The calculation of the solar zenith angle is performed more accurately, with the algorithm used in the 5S solar radiation code (Tanré et al., 1990).
- The parameter SW_0 (sw0) varies with solar zenith angle (see Table 2).
- The DSD is made consistent between the SW radiation scheme and the bulk microphysics scheme by calculating in each grid cell the effective radius r_e (used in the SW scheme) from the parameters N_c and σ_g (Table 2) and current LWC, rather than using a constant value (ρ_l is liquid water density):

$$r_e{}^3 = \frac{3LWC}{4\pi\rho_l N_c} e^{3\ln^2\sigma_g} \tag{9}$$

- In the SW scheme, the extinction coefficient is increased by 0.01 m^{-1} in grid cells with cloud water to account for hydrated unactivated aerosols.
- At the first model level, a turbulent deposition flux, proportional to the LWC at this model level, is added: $F_{dep} = V_d \cdot LWC$, where V_d = 0.02 m s^{-1}. The water is moved from the first model level to the surface liquid reservoir.
- Sedimentation fluxes at first model level feed the surface liquid reservoir (this was not included in the original code).
- Sedimentation fluxes are written as model output.
- Adjustments of the interface between the surface module and radiation module to make it work correctly when using the parametrised radiation scheme (which has different conventions for the model fields than the full radiation scheme)
- Correction of a bug that prevented the broadcasting of the variables N_c (Nc_0) and σ_g (sig_g) to all computation cores

Appendix B LWP budget terms from model output

This appendix explains how we apply Eqs. (6, 7) on the model output to produce the terms shown in Figure 8. All terms are calculated from the horizontal and temporal mean profiles of state variables and fluxes provided as model output every 5 min. We consider the fog to be contained between the current mean CBH and mean CTH in the model, which are also given in the output.

Since only the cloud interacts with radiation in the simplified parametrisation used in the model (section 3.1), the sensible heat fluxes from LW and SW radiation is calculated as the difference between the net downward irradiance at the bottom and top of the domain. The sensible heat from adiabatic compression by subsidence is calculated using the adiabatic lapse rate ($\frac{g}{c_p}$) and the constant vertical gradient in large-scale vertical velocity ($\frac{dw_{ls}}{dz}$):

$$SH_{sub} = \int_{CBH}^{CTH} \rho_a c_p \frac{g}{c_p}(-w_{ls})dz = \frac{1}{2}\rho_a g(-\frac{dw_{ls}}{dz})(CTH^2 - CBH^2), \tag{10}$$

where $g = 9.81$ m s^{-2} is the acceleration of gravity. The "subsidence" term in Figure 8 is the sum of SH_{sub} and the divergence effect (the last term in Eq. (7)).

The interactions between the fog and the layers below and above have contributions from sensible heat, latent heat and liquid fluxes. These are taken directly from the model profile output at the model interface closest to the current mean CBH and CTH. At the upper boundary, we combine all the fluxes to the term named "entrainment". This entrainment term is more challenging to quantify from the model output than the other terms, due to the horizontal heterogeneity of CTH and the increase of CTH with time. The inclusion a new level means that the liquid already present at this level and its degree of non-saturation needs to be taken

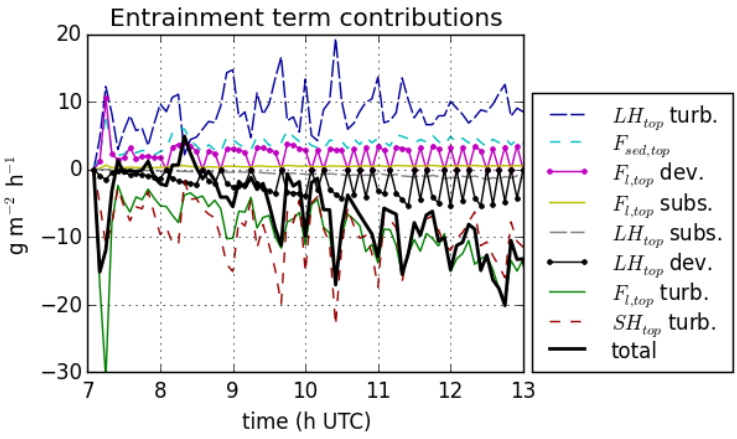

Figure 12: The magnitudes of the terms in Eqs. (11, 12, 13) when they are put into the the LWP budget equation (Eq. 7), for the Baseline simulation.

into account. The latter is considered as a negative latent heat flux. In addition, the large-scale subsidence will transport some of the air from the layer above cloud top into the cloud. To account for all of these effects, the total expressions for the entrainment fluxes are:

$$SH_{top} = -\rho_{a,top} c_p \overline{w'\theta'}_{top} \tag{11}$$

$$LH_{top} = -\rho_{a,top} L_v \overline{w'q'_v}_{top} - (-w_{ls,ab})\rho_{a,ab} L_v (q_s(T_{ab}) - q_{v,ab}) - \sum_j \rho_{a,j} L_v (q_s(T_j) - q_{v,j}) \frac{\Delta h_j}{\Delta t} \tag{12}$$

$$F_{l,top} = -\rho_{a,top} \overline{w'q'_l}_{top} + (-w_{ls,ab}) LWC_{ab} + \sum_j LWC_j \frac{\Delta h_j}{\Delta t} + F_{sed,top} \tag{13}$$

The over-barred expressions are the turbulent kinematic vertical fluxes of sensible heat, specific humidity and specific liquid water content at the current CTH. The sums go over the model levels above CTH which are added to the fog layer between the current and the next output time. Δt is the time between two output times (5 min), and Δh_j and T_j are the thickness and temperature, respectively, of the model level being added. F_{sed} is the downward flux of LWC due to sedimentation. q_s is the saturation specific humidity. Subscript *top* indicates the first model level above CTH, and *ab* the next level above this (from which the subsidence velocity is transporting the properties across CTH, assuming $w_{ls} < 0$). The first term in SH_{top} (LH_{top}) represents the turbulent sensible (latent) heat flux across the current CTH. The second term in LH_{top} accounts for the subsaturation introduced by subsidence transport, and the third term is the subsaturation in the added model levels due to vertical development of CTH. The terms of $F_{l,top}$ represent, respectively, the turbulent liquid transport across the current CTH, the transport by large-scale subsidence across current CTH, the liquid already present in layers being added to the fog as it develops vertically, and the sedimentation flux (of cloud water and rainwater) across the current CTH.

Figure 12 shows the relative importance of all these contributions to the entrainment term in the LWP budget equation in Figure 8. The total entrainment term is a difference between positive and negative contributions that are similar in magnitude (apart from the subsidence terms, which are weak), the most important terms being the (Eulerian) turbulent fluxes of heat, water vapour and liquid. Due to the large gradients in temperature and humidity at the non-flat cloud top, the precision of these flux estimates is limited. Recognising that the entrainment term is most likely the main source of the residual in the LWP budget, at least until fog dissipation, we have chosen to deduce the entrainment term from the closure of the LWP budget rather than calculating it in Figure 10.

At the lower boundary, the terms SH_{base}, LH_{base} and $F_{l,base}$ are calculated in a similar way as for the top, except that the effect of subsidence is neglected and that levels are being removed instead of added. The expressions for the terms "sensible heat (base)", "latent heat (base)", "sedimentation (base)" and "turb. liquid flux (base)" in Figure 8 are then, respectively:

$$SH_{base} = \rho_{a,base} c_p \overline{w'\theta'}_{base} \tag{14}$$

$$LH_{base} = \rho_{a,base} L_v \overline{w'q'_{vbase}} \quad (15)$$

$$F_{l,base,Sed} = -F_{sed,base} \quad (16)$$

$$F_{l,base,Turb} = \rho_{a,top} \overline{w'q'_{lbase}} - \sum_j LWC_j \frac{\Delta h_j}{\Delta t} \quad (17)$$

In Eq. (17), the sum goes over the layers being removed from the fog as CBH rises. However, until the mean CBH lifts to 4 m, we let the lower boundary ("base") be at the surface, so that the fluxes from below correspond to the surface-atmosphere interaction, which is parametrised with Monin–Obukhov similarity theory (for SH_{base}, LE_{base}) and the parametrised turbulent deposition (for $F_{base,Turb}$). Once the CBH has lifted to above 4 m (our definition of fog dissipation), the fluxes correspond to the interaction between two atmosphere layers, which is governed by the model interior dynamics. This is the reason for the discontinuity seen in the terms in Figure 8 at fog dissipation.

Acknowledgements

This research is supported financially by the French ministry of defence – Direction Générale de l'Armement, and by the company Meteomodem. GJS acknowledges financial support from NWO contract 863.10.010 (VENI study – Lifting the fog). The authors would like to acknowledge SIRTA for providing the observational data used in this study, obtained in the framework of the ACTRIS-2 project (funded by the European Union's Horizon 2020 research and innovation programme under grant agreement No 654109). The authors would like to thank the technical and computer staff of the SIRTA Observatory and Trappes Meteo-France station for taking the observations and making the data set easily accessible. We thank KNMI for providing the Cabauw tower data via `http://www.cesar-database.nl/`. ERA5 data are provided through ECMWF, COPERNICUS Climate Change Service data, available from the ESPRI/IPSL data center. The numerical simulations were performed with the supercomputer facilities at SURFsara and financially sponsored by the Netherlands Organisation for Scientific Research (NWO) Physical Science Division (project number SH-312-15). The authors benefited from mobility grants from the Wageningen Institute for Environment and Climate Research and the ACTRIS Trans-National Access. We would like to thank Stephan de Roode, Arnold Moene and Fred Bosveld for their help with interpreting our results, and Chiel van Heerwaarden for his help with setting up the DALES model.

References

American Meteorological Society (2018). "Fog", Glossary of Meteorology. [Available online at http://glossary.ametsoc.org/wiki/Fog]. Accessed: 2018-07-09.

Beljaars, A. C. and Bosveld, F. C. (1997). Cabauw data for the validation of land surface parameterization schemes. *Journal of climate*, 10(6):1172–1193. `https://doi.org/10.1175/1520-0442(1997)010%3C1172:CDFTVO%3E2.0.CO;2`.

Bergot, T. (2013). Small-scale structure of radiation fog: a large-eddy simulation study. *Quarterly Journal of the Royal Meteorological Society*, 139(673):1099–1112. `https://doi.org/10.1002/qj.2051`.

Bergot, T. (2016). Large-eddy simulation study of the dissipation of radiation fog. *Quarterly Journal of the Royal Meteorological Society*, 142(695):1029–1040. `https://doi.org/10.1002/qj.2706`.

Brown, R. and Roach, W. T. (1976). The physics of radiation fog: II–a numerical study. *Quarterly Journal of the Royal Meteorological Society*, 102(432):335–354. `https://doi.org/10.1002/qj.49710243205`.

Conzemius, R. J. and Fedorovich, E. (2006). Dynamics of sheared convective boundary layer entrainment. Part II: Evaluation of bulk model predictions of entrainment flux. *Journal of the atmospheric sciences*, 63(4):1179–1199. `https://doi.org/10.1175/JAS3696.1`.

De Roode, S. R., Duynkerke, P. G., and Jonker, H. J. (2004). Large-eddy simulation: How large is large enough? *Journal of the atmospheric sciences*, 61(4):403–421. https://doi.org/10.1175/1520-0469(2004)061<0403:LSHLIL>2.0.CO;2.

Delanoë, J., Protat, A., Vinson, J.-P., Brett, W., Caudoux, C., Bertrand, F., Parent du Chatelet, J., Hallali, R., Barthes, L., Haeffelin, M., and Dupont, J.-C. (2016). BASTA: A 95-GHz FMCW Doppler Radar for Cloud and Fog Studies. *Journal of Atmospheric and Oceanic Technology*, 33(5):1023–1038. https://doi.org/10.1175/JTECH-D-15-0104.1.

Dupont, J., Haeffelin, M., Stolaki, S., and Elias, T. (2016). Analysis of dynamical and thermal processes driving fog and quasi-fog life cycles using the 2010–2013 parisfog dataset. *Pure and Applied Geophysics*, 173(4):1337–1358. https://doi.org/10.1007/s00024-015-1159-x.

ECMWF (2016). *IFS Documentation Cy43r1*, chapter "Part IV: Physical processes". ECMWF.

Elias, T., Haeffelin, M., Drobinski, P., Gomes, L., Rangognio, J., Bergot, T., Chazette, P., Raut, J.-C., and Colomb, M. (2009). Particulate contribution to extinction of visible radiation: pollution, haze, and fog. *Atmospheric Research*, 92(4):443–454. https://doi.org/doi:10.1016/j.atmosres.2009.01.006.

Fesquet, C., Drobinski, P., Barthlott, C., and Dubos, T. (2009). Impact of terrain heterogeneity on near-surface turbulence structure. *Atmospheric Research*, 94(2):254–269. https://doi.org/10.1016/j.atmosres.2009.06.003.

Foken, T. (2008). The energy balance closure problem: an overview. *Ecological Applications*, 18(6):1351–1367. https://doi.org/10.1890/06-0922.1.

Fox, N. I. and Illingworth, A. J. (1997). The retrieval of stratocumulus cloud properties by ground-based cloud radar. *Journal of Applied Meteorology*, 36(5):485–492. https://doi.org/10.1175/1520-0450(1997)036<0485:TROSCP>2.0.CO;2.

Garratt, J. R. (1992). *The Atmospheric Boundary Layer*. Cambridge University Press, 316 pp.

Gultepe, I., Pearson, G., Milbrandt, J. A., Hansen, B., Platnick, S., Taylor, P., Gordon, M., Oakley, J. P., and Cober, S. G. (2009). The fog remote sensing and modeling field project. *Bulletin of the American Meteorological Society*, 90(3):341–359. https://doi.org/10.1175/2008BAMS2354.1.

Gultepe, I., Tardif, R., Michaelides, S. C., Cermak, J., Bott, A., Bendix, J., Müller, M. D., Pagowski, M., Hansen, B., Ellrod, G., Jacobs, W., Toth, G., and Cober, S. G. (2007). Fog research: A review of past achievements and future perspectives. *Pure and Applied Geophysics*, 164(6-7):1121–1159. https://doi.org/10.1007/s00024-007-0211-x.

Haeffelin, M., Barthès, L., Bock, O., Boitel, C., Bony, S., Bouniol, D., Chepfer, H., Chiriaco, M., Cuesta, J., Delanoë, J., Drobinski, P., Dufresne, J.-L., Flamant, C., Grall, M., Hodzic, A., Hourdin, F., Lapouge, F., Lemaître, Y., Mathieu, A., Morille, Y., Naud, C., Noël, V., O'Hirok, B., Pelon, J., Pietras, C., Protat, A., Romand, B., Scialom, G., and Vautard, R. (2005). SIRTA, a ground-based atmospheric observatory for cloud and aerosol research. In *Annales Geophysicae*, volume 23, pages 253–275. hal-00329353.

Haeffelin, M., Bergot, T., Elias, T., Tardif, R., Carrer, D., Chazette, P., Colomb, M., Drobinski, P., Dupont, E., Dupont, J. C., Gomes, L., Musson-Genon, L., Pietras, C., Plana-Fattori, A., Protat, A., Rangognio, J., Raut, J.-C., Rémy, S., Richard, D., Sciare, J., and Zhang, X. (2010). PARISFOG: shedding new light on fog physical processes. *Bulletin of the American Meteorological Society*, 91(6):767–783. https://doi.org/10.1175/2009BAMS2671.1.

Haeffelin, M., Laffineur, Q., Bravo-Aranda, J.-A., Drouin, M.-A., Casquero-Vera, J.-A., Dupont, J.-C., and De Backer, H. (2016). Radiation fog formation alerts using attenuated backscatter power from automatic lidars and ceilometers. *Atmospheric Measurement Techniques*, 9(11):5347–5365. https://doi.org/10.5194/amt-9-5347-2016.

Haiden, T., Janousek, M., and Hersbach, H. (2017). ERA5 aids in forecast performance monitoring. *ECMWF Newsletter*, 150 (Winter 2016/17), [Available online at https://www.ecmwf.int/en/newsletter/150/news/era5-aids-forecast-performance-monitoring].

Heus, T., Van Heerwaarden, C. C., Jonker, H. J., Siebesma, A. P., Axelsen, S., Van Den Dries, K., Geoffroy, O., Moene, A. F., Pino, D., De Roode, S. R., and Vilà-Guerau de Arellano, J. (2010). Formulation of the Dutch Atmospheric Large-Eddy Simulation (DALES) and overview of its applications. *Geoscientific Model Development*, 3(2):415. https://doi.org/10.5194/gmd-3-415-2010.

Jacobs, A. F., Heusinkveld, B. G., Wichink Kruit, R. J., and Berkowicz, S. M. (2006). Contribution of dew to the water budget of a grassland area in the Netherlands. *Water Resources Research*, 42(3). https://doi.org/10.1029/2005WR004055.

Jarvis, P. (1976). The interpretation of the variations in leaf water potential and stomatal conductance found in canopies in the field. *Philosophical Transactions of the Royal Society of London. Series B, Biological Sciences*, 273(927):593–610.

Katata, G. (2014). Fogwater deposition modeling for terrestrial ecosystems: A review of developments and measurements. *Journal of Geophysical Research: Atmospheres*, 119(13):8137–8159. https://doi.org/10.1002/2014JD021669.

Khairoutdinov, M. and Kogan, Y. (2000). A new cloud physics parameterization in a large-eddy simulation model of marine stratocumulus. *Monthly weather review*, 128(1):229–243. https://doi.org/10.1175/1520-0493(2000)128<0229:ANCPPI>2.0.CO;2.

Kotthaus, S., O'Connor, E., Münkel, C., Charlton-Perez, C., Haeffelin, M., Gabey, A. M., and Grimmond, C. S. B. (2016). Recommendations for processing atmospheric attenuated backscatter profiles from Vaisala CL31 ceilometers. *Atmospheric Measurement Techniques*, 9(8):3769–3791. https://doi.org/10.5194/amt-9-3769-2016.

Leuning, R., Van Gorsel, E., Massman, W. J., and Isaac, P. R. (2012). Reflections on the surface energy imbalance problem. *Agricultural and Forest Meteorology*, 156:65–74. https://doi.org/10.1016/j.agrformet.2011.12.002.

Maalick, Z., Kühn, T., Korhonen, H., Kokkola, H., Laaksonen, A., and Romakkaniemi, S. (2016). Effect of aerosol concentration and absorbing aerosol on the radiation fog life cycle. *Atmospheric Environment*, 133:26–33. https://doi.org/10.1016/j.atmosenv.2016.03.018.

Marke, T., Ebell, K., Löhnert, U., and Turner, D. D. (2016). Statistical retrieval of thin liquid cloud microphysical properties using ground-based infrared and microwave observations. *Journal of Geophysical Research: Atmospheres*, 121(24). https://doi.org/10.1002/2016JD025667.

Maronga, B. and Bosveld, F. (2017). Key parameters for the life cycle of nocturnal radiation fog: a comprehensive large-eddy simulation study. *Quarterly Journal of the Royal Meteorological Society*, 143:2463–2480. https://doi.org/10.1002/qj.3100.

Mazoyer, M., Lac, C., Thouron, O., Bergot, T., Masson, V., and Musson-Genon, L. (2017). Large eddy simulation of radiation fog: impact of dynamics on the fog life cycle. *Atmospheric Chemistry and Physics*, 17(21):13017. https://doi.org/10.5194/acp-17-13017-2017.

Nakanishi, M. (2000). Large-eddy simulation of radiation fog. *Boundary-layer meteorology*, 94(3):461–493. https://doi.org/10.1023/A:1002490423389.

Pasini, A., Pelino, V., and Potestà, S. (2001). A neural network model for visibility nowcasting from surface observations: Results and sensitivity to physical input variables. *Journal of Geophysical Research: Atmospheres*, 106(D14):14951–14959. https://doi.org/10.1029/2001JD900134.

Penman, H. L. (1948). Natural evaporation from open water, bare soil and grass. *Proceedings of the Royal Society of London. Series A, Mathematical and Physical Sciences*, 193(1032):120–145.

Porson, A., Price, J., Lock, A., and Clark, P. (2011). Radiation fog. Part II: Large-eddy simulations in very stable conditions. *Boundary-layer meteorology*, 139(2):193–224. https://doi.org/10.1007/s10546-010-9579-8.

Price, J. S. (1991). Evaporation from a blanket bog in a foggy coastal environment. *Boundary-Layer Meteorology*, 57(4):391–406. https://doi.org/10.1007/BF00120056.

Román-Cascón, C., Steeneveld, G., Yagüe, C., Sastre, M., Arrillaga, J., and Maqueda, G. (2016). Forecasting radiation fog at climatologically contrasting sites: evaluation of statistical methods and WRF. *Quarterly Journal of the Royal Meteorological Society*, 142(695):1048–1063. https://doi.org/10.1002/qj.2708.

Spuler, S., Repasky, K., Morley, B., Moen, D., Hayman, M., and Nehrir, A. (2015). Field-deployable diode-laser-based differential absorption lidar (DIAL) for profiling water vapor. *Atmospheric Measurement Techniques*, 8(3):1073–1087. https://doi.org/10.5194/amt-8-1073-2015.

Steeneveld, G. J., Ronda, R. J., and Holtslag, A. a. M. (2015). The Challenge of Forecasting the Onset and Development of Radiation Fog Using Mesoscale Atmospheric Models. *Boundary-Layer Meteorology*, 154(2):265–289. https://doi.org/10.1007/s10546-014-9973-8.

Stevens, B. (2002). Entrainment in stratocumulus-topped mixed layers. *Quarterly Journal of the Royal Meteorological Society*, 128(586):2663–2690. https://doi.org/10.1256/qj.01.202.

Tanré, D., Deroo, C., Duhaut, P., Herman, M., Morcrette, J., Perbos, J., and Deschamps, P. (1990). Technical note description of a computer code to simulate the satellite signal in the solar spectrum: the 5S code. *International Journal of Remote Sensing*, 11(4):659–668. https://doi.org/10.1080/01431169008955048.

Tardif, R. and Rasmussen, R. M. (2007). Event-based climatology and typology of fog in the New York City region. *Journal of applied meteorology and climatology*, 46(8):1141–1168. https://doi.org/10.1175/JAM2516.1.

Van der Dussen, J., De Roode, S., and Siebesma, A. (2014). Factors controlling rapid stratocumulus cloud thinning. *Journal of the Atmospheric Sciences*, 71(2):655–664. https://doi.org/10.1175/JAS-D-13-0114.1.

Van Ulden, A. and Holtslag, A. (1985). Estimation of atmospheric boundary layer parameters for diffusion applications. *Journal of Climate and Applied Meteorology*, 24(11):1196–1207. https://doi.org/10.1175/1520-0450(1985)024<1196:EOABLP>2.0.CO;2.

Wærsted, E. G., Haeffelin, M., Dupont, J.-C., Delanoë, J., and Dubuisson, P. (2017). Radiation in fog: quantification of the impact on fog liquid water based on ground-based remote sensing. *Atmospheric Chemistry and Physics*, 17(17):10811–10835. https://doi.org/10.5194/acp-17-10811-2017.

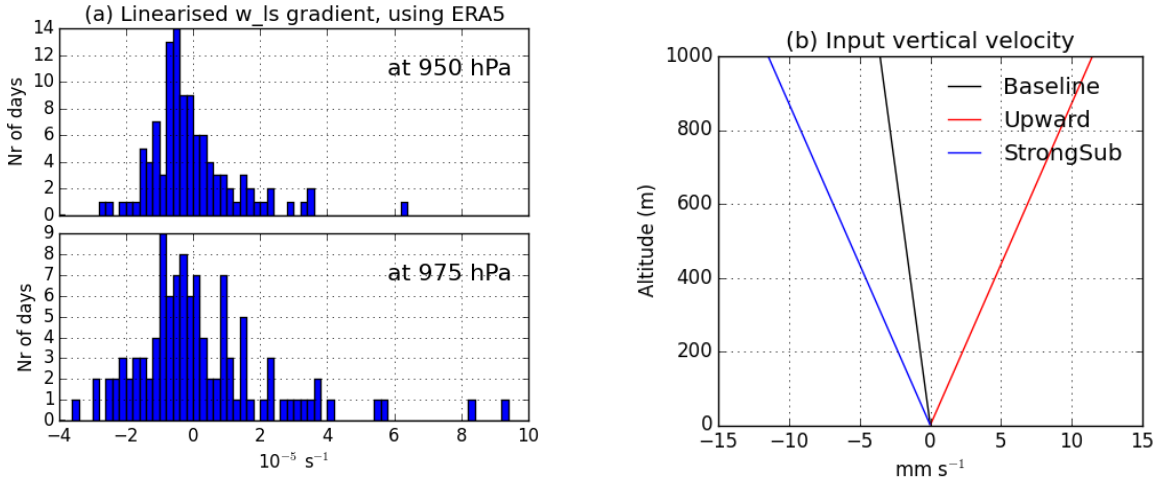

Figure 4.1: (a) Vertical gradient in the large-scale vertical velocity, calculated using the vertical velocity at 950 hPa or 975 hPa in ERA5, averaged in a domain of size 1° x 1° around SIRTA, and averaged from sunrise to fog dissipation, for 108 days with fog at sunrise in 2010–2017. (b) Large-scale vertical velocity profiles used in three runs with DALES to test the impact of this velocity on the fog.

4.2 Impact of subsidence

The findings in the paper above suggest that the CTH is a critical parameter for the dissipation of fog, since the fog will lift if the cloud top develops sufficiently, even if LWP is increasing. A topic that is not investigated in the paper is the role of subsidence. An upward large-scale velocity will make the fog thicker, which could lead to lifting, while a negative vertical velocity (subsidence) will contribute to keeping the fog layer thin.

To investigate the variability of subsidence, 108 days with fog present at sunrise in 2010–2017 are considered. Similarly to what is done in the paper, the vertical gradient in large-scale vertical velocity is calculated using the values of large-scale velocity and altitude at 950 hPa or 975 hPa[2] from ERA5, and assuming a linear increase with height from zero at the surface. The gradient is calculated for each time from sunrise to fog dissipation, and then averaged in time. This results in the distribution shown in Fig. 4.1a. Using 950 hPa and 975 hPa results in similar distributions, and the distributions show a peak occurrence of subsidence between $-1 \cdot 10^{-5}$ s^{-1} and 0 s^{-1}. Considering the statistics at 975 hPa, 76 % of the days have a gradient between $\pm 2 \cdot 10^{-5}$ s^{-1}, and upward motion is almost as common as downward (48 days vs 60 days). The runs in the paper used a gradient $\frac{dw_{ls}}{dz}$ of $-3.56 \cdot 10^{-6}$ s^{-1}, which is close to the most common value according to the statistics.

To test the impact of subsidence, two sensitivity runs with DALES are performed, one run in which the subsidence gradient is increased (in absolute terms) to $-1.1 \cdot 10^{-5}$ s^{-1}, representing a situation of stronger subsidence than Baseline, and one run where an upward large-scale velocity of the same magnitude is imposed (Fig. 4.1b). We call these runs StrongSub and Upward, respectively. To save computational time, these runs are carried out on a lower resolution than the main runs, using horizontal resolution of 10 m and vertical resolution of 5 m. To remove all variability due to different resolution, we carried out a new Baseline simulation at this reduced resolution as well. However, we verified that the results of the baseline simulation changes very little due to the coarser resolution; the

[2]975 hPa corresponds to 100–350 m above SIRTA ground, and 950 hPa is about 220 m higher.

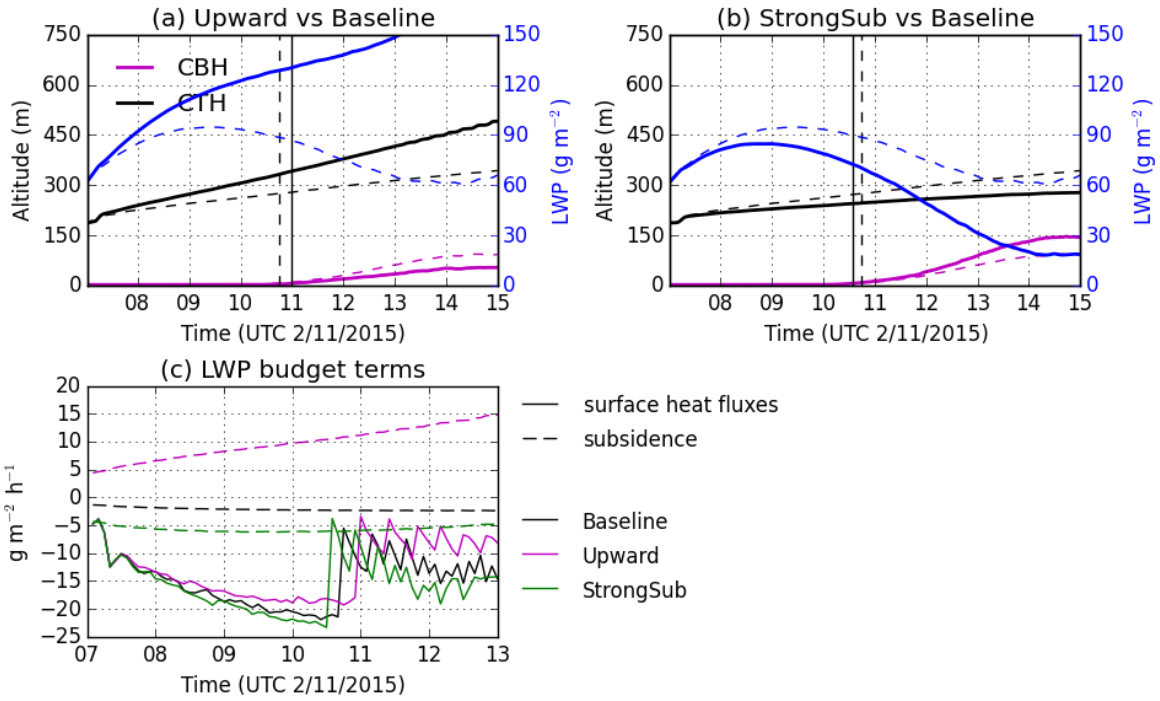

Figure 4.2: Comparison between the runs with different large-scale vertical velocity (see text for details): (a-b) The evolution of cloud base, cloud top and LWP in the run "Upward" (a) and in the run "StrongSub" (b), compared to Baseline (dashed). Also shown is the dissipation times (vertical lines). (c) Comparison of the subsidence (dashed) and surface fluxes (solid) terms in the LWP budget between the three runs (see W18 for an explanation of these terms).

biggest impact is a weak increase in the LWP loss by deposition of 1 g m^{-2} h^{-1}, while the fog top develops very similarly until dissipation, and dissipation time is still at 10:45 (not shown). The lower resolution should therefore be sufficient to study the effect of subsidence.

Figure 4.2ab compares the evolution of the fog layer in the three simulations. The differences in LWP are striking: the LWP reaches 130 g m^{-2} at 11 UTC in Upward, while StrongSub only has about 70 g m^{-2} at the same time. The cloud-top height also increases considerably more in Upward than in StrongSub. In comparison, the effect on the cloud base is rather small; it lifts 10 min earlier in StrongSub and 15 min later in Upward, relative to Baseline. The only terms in the LWP budget that change significantly between the runs are the subsidence and the surface heat fluxes, which are shown in Fig. 4.2c. The subsidence term becomes positive in Upward, since the fog in this runs converges (instead of diverging) and cools through adiabatic effect of upward motion (instead of heating from subsidence). These effects increase as the fog becomes thicker, so that the subsidence term in the LWP equation becomes very significant towards the end of the Upward simulation. This effect on the LWP production appears to almost exactly compensate for the increased need for LWP to fill a thicker fog layer, an effect which is studied further in section 5.3.4. The result that the fog base lifts earlier in StrongSub than in Upward might indicate that the effect on LWP is more important than the effect on the CTH. The reduction in LWP by subsidence also has an indirect contribution through the surface heat fluxes: a fog which remains thinner due to subsidence will reflect less SW radiation and thereby lose more LWP from surface heat fluxes, as we can see in Fig. 4.2c.

Based on these results, we would not expect that stronger subsidence in itself should favour fog

persistence, but rather that it should weakly favour an earlier dissipation. Of course, it could be that as the fog becomes thicker, microphysical processes will trigger loss through sedimentation of bigger droplets; however, this cannot be studied using the simple cloud microphysics scheme of DALES. Another thing to keep in mind is that subsidence is not an isolated phenomenon. Strong subsidence normally occurs during anticyclonic situations, which can be beneficial for fog persistence due to the dry atmosphere, absence of higher clouds and weak winds. It is therefore possible that subsidence could be correlated with fog persistence, even if it is not beneficial for fog persistence in itself.

4.3 Synthesis

The impacts of dynamical processes on thick fog after sunrise, and their variability due to the variability in fog boundary conditions, have been studied using the large-eddy model DALES. The main points to retain are:

- A method for separating the impacts of each local process on LWP from model output has been developed, by assuming a saturated, well-mixed fog layer and considering each process as a heat, moisture, and/or liquid flux. This method closes the modelled LWP budget in the LES well, although the entrainment term is challenging to quantify correctly due to the undulating fog top and strong vertical gradients. Using this method, we can analyse which processes are affected by the sensitivity studies we perform, and how much.
- The surface sensible heat fluxes are the dominating loss process of LWP after sunrise, with 20–30 g m^{-2} h^{-1} of loss in the late morning. The impact is sensitive to the Bowen ratio, which in turn seems to be sensitive to the presence of liquid water at the surface, due to the high surface resistance in the low-insolation conditions below the fog layer. The fog dissipates 85 min earlier in the simulation without initial liquid water at the surface than in the baseline simulation with 50 % of the surface covered by liquid.
- Upward and downward large-scale motion both occur frequently during fog at SIRTA, with subsidence being only slightly more common than upward large-scale motion (56 % of the morning fog events). According to the LES simulations, the impact of subsidence is a slightly earlier dissipation, but the effect is weak due to the compensating effects of the reduction in LWP and the inhibition of cloud-top increase. When strong large-scale upward motion is present, the fog increases both its LWP and its thickness, resulting in a much thicker fog than in the case of subsidence, but which nevertheless does not dissipate very much later.
- Entrainment at fog top has two effects which can importantly impact fog dissipation time: Firstly, the mixing of the fog with unsaturated air can be an important loss process for LWP if the air in the layer directly above the fog is dry (a relative humidity far below saturation). Secondly, the vertical development of the cloud top enables the fog base to lift due to the thickening of the mixed layer, in which the fog will stick to the upper boundary.
- The drying effect will have significant variability according to the humidity of the layer above. We used radiosondes to quantify the variability of the humidity above fog top, and carried out sensitivity studies based on this observed variability. The sensitivity run where the air above fog top was dry gave a fog dissipation 70 min earlier than in the baseline simulation with humidity near saturation, due to the loss of LWP by entrainment being around -30 g m^{-2} h^{-1} or more,

instead of 5–10 g m^{-2} h^{-1}. However, as a dry atmosphere above fog also enhances the radiative cooling of the fog, the impact of humidity above fog top depends on the details of the humidity profile in the lower atmosphere, and it is necessary to distinguish the humidity directly above the fog from the humidity in the rest of the atmospheric column.

- The radiosondes were also used to quantify the variability in the thermal stratification above fog top. Based on this observed variability, the sensitivity studies show that the entrainment rate is importantly impacted by the stratification: the entrainment velocity is 3 times higher in a run with weak stratification than in the baseline run with strong stratification. This enables the fog to lift 90 min earlier in the run with weaker stratification.
- The droplet deposition appears to be a weak sink process compared to the surface heat fluxes during the day. This might be due to the droplets rather evaporating than depositing when they approach the surface. However, the microphysics scheme is simple in DALES, which limits our investigations of this process.
- The important parameters to observe for quantifying the impact of the dynamical processes found in this chapter are the surface turbulent heat fluxes and their ratio, and the stratification and humidity in the layer right above fog top. The radiation absorbed at the surface can be quantified rather well by the radiation schemes, using the cloud radar and MWR (section 3.2), but the partitioning of this radiation into sensible and latent heat fluxes is not sufficiently measured at SIRTA: we showed that the measurements of eddy covariance are not precise enough to determine the Bowen ratio. Future work should therefore focus on how best to quantify the Bowen ratio during fog, for example using alternative measurement techniques. The variability of stratification above fog top can be captured rather well using the MWR and the observed cloud top (correlation 0.89, section 2.6). In contrast, we do not currently have a measurement available of the humidity above fog top with sufficient vertical and temporal resolution. Such a measurement would greatly improve the capability of quantifying the impact of entrainment on fog LWP.

Chapter 5

Dissipation scenarios

The motivation for this thesis is to understand which conditions are favourable for fog dissipation vs persistence and the key processes involved, and how these physical processes can be observed locally to understand and possibly anticipate the fog evolution in the near future. The previous two chapters explored these processes and quantified how much the LWP of the fog is impacted by them under different conditions. The goal of this chapter is to investigate to what extent ground-based observations can explain the evolution of a fog situation by diagnosing the processes. We will apply what has been learned in the previous chapters to analyse a larger number of fog events, focussing on the case-to-case variability in the processes and to what extent it can explain the different observed evolutions of the fog layers.

By using the LES model, we found that fog dissipation can be sensitive both to the development of the fog top and to the depletion of LWP (chapter 4). In fact, as is shown in this chapter (section 5.2), there is a critical LWP, which increases with CTH; if the fog LWP is smaller than the critical LWP, the fog base is likely to lift from the surface. Therefore, in order to understand when the fog will dissipate, the evolutions of both LWP and CTH are important. The MWR and cloud radar at SIRTA can track the evolutions of these two variables. Furthermore, by using what is learned from the previous two chapters, we create a conceptual model which estimates the impacts on LWP and CTH by local processes using observed parameters. It is likely that an important part of the evolution of LWP and CTH is related to the local processes which we can observe, even though non-local processes also can play a role. We apply the conceptual model to 45 daytime fog events, with the goal of using the model to understand these fog events and their differences, as well as to evaluate to what extent the model is able to explain the observed evolutions in LWP and CTH.

A rapid presentation of the 45 fog events is given in section 5.1. Thereafter, the model relating fog thickness and LWP is introduced and applied to the fog events in section 5.2. The conceptual model is described in detail in section 5.3. Statistical results for all 45 events are presented in section 5.4, before six of the events are analysed in detail (section 5.5). Finally, an uncertainty discussion of the conceptual model is provided in section 5.6, where we also suggest how it could be developed further.

5.1 45 days with fog at sunrise: Dissipation scenarios and seasonality

The investigations of this chapter is limited to the fog events which are present at sunrise, which we name "morning fog events". Most of the analysis that is introduced could also be applied to fog events that dissipate in the night, but it is convenient to have sunrise as a common reference for all

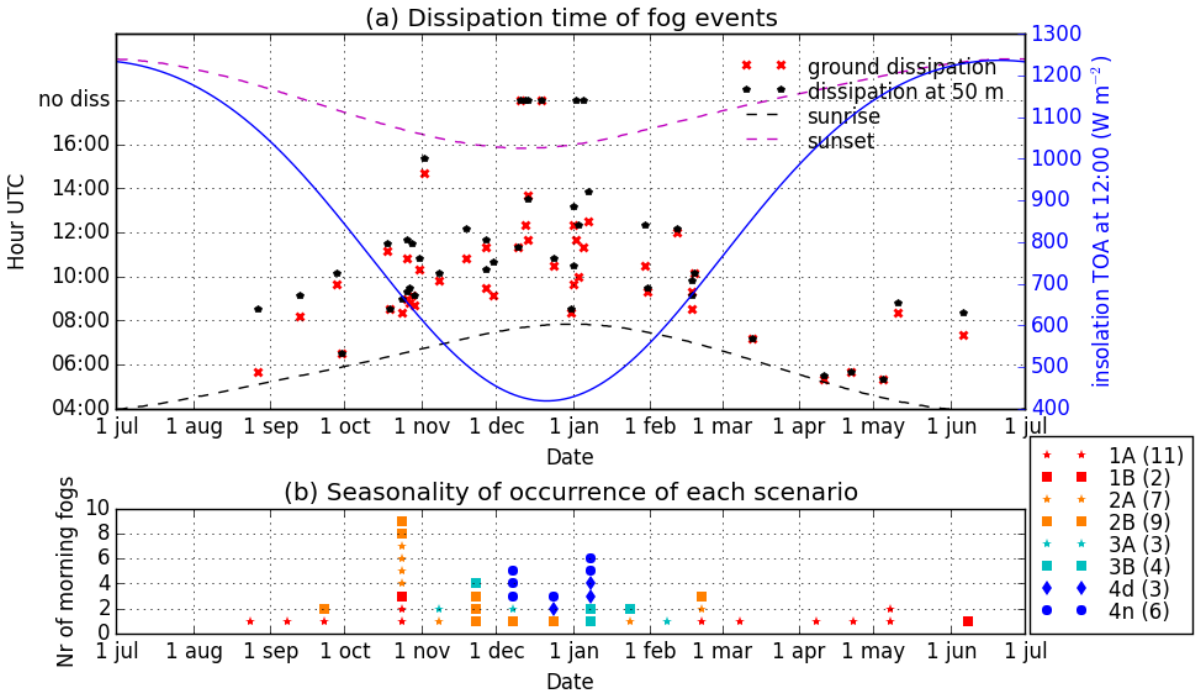

Figure 5.1: Seasonal occurrence of the 45 morning fog events in the period Oct 2013 – Sept 2017 which are studied in this chapter. (a) Time of dissipation of cloud at the ground and at 50 m vs date of occurrence of each fog (red crosses and black bullets). "no diss" means that the cloud base did not dissipate before sunset. Seasonal variations in the time of sunrise and sunset are indicated as dashed lines, and the amount of solar flux at the top of the atmosphere at 12:00 UTC is indicated with the solid line (using the year 2015–2016). (b) The number of fog events of each scenario (see Fig. 5.2) occurring in each half-month period (all 4 years together).

the different observed scenarios. Moreover, the analysis performed with the LES model (chapter 4) focuses on the fog evolution after sunrise. Among the 250 fog events observed in the period Oct 2010 – Sept 2017, there are 108 morning fog events. 51 of them occur after 1 Oct 2013, of which 45 have the necessary observations for performing the analysis of this chapter (except that 4 of them miss ground flux measurements).

These fog events show a large variability in their time of dissipation (Fig. 5.1a). Because some fog events lift their base by only a few tens of metres before lowering again, we have decided to define also the time of dissipation at 50 m, $t_{d,50m}$, which is the time when the cloud base becomes higher than 50 m and remains so for at least 30 minutes. We have defined eight dissipation scenarios, which are schematically explained in Fig. 5.2. Figure 5.1a shows the dissipation time at the surface and at 50 m for each of the 45 events, plotted against the date of the fog. Two of the fog events do not dissipate at any point during the day, and in four additional cases a cloud base remains below 50 m for the whole day. In all these four events, the fog reforms on the surface before sunset. There are also three more events where fog reforms on the surface before sunset, but where the cloud base rises to above 50 m during a period of 1–2 h during the day. All these nine events, where the cloud remains below 50 m for all or almost all the day, correspond to scenario 4 (see Fig. 5.2). Scenarios 1–3 are defined by the time of dissipation at 50 m, and they are further classified into A and B according to how long a low stratus (below 400 m) remains after dissipation at 50 m (Fig. 5.2).

Figure 5.1b shows the number of fog events of each scenario and the seasonal distribution. There is a clear seasonal cycle in the time of dissipation, with later dissipation near mid-winter than closer

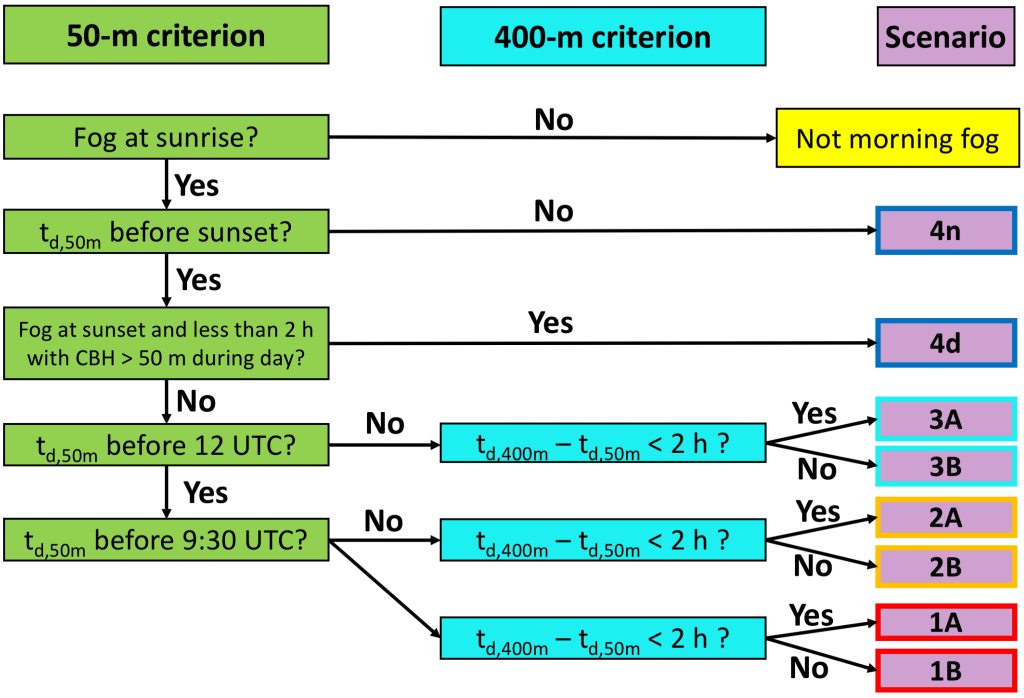

Figure 5.2: Schematic explanation of the definition of the dissipation scenarios of morning fog. $t_{d,50m}$ is the first time after sunrise that the cloud base becomes higher than 50 m (or dissipates completely) and remains so for 30 minutes, and $t_{d,400m}$ is the same for a cloud base higher than 400 m. First the events lasting all day are identified as scenario 4, then the other events are classified according to $t_{d,50m}$, and then according to how much longer a cloud base below 400 m remains.

to the summer. The seasonal cycle in insolation and time of sunrise is a likely explanation for this pattern. The fog events which do not dissipate at 50 m during the whole day are all very close to the winter solstice, which is likely related to low insolation and late sunrise. All events that occur in the summer half-year are of scenario 1 (50-m dissipation before 9:30 UTC). It is not surprising since the sun rises much earlier in summer than in winter (actually, several events in the summer persist for several hours after sunrise, but still dissipate before 09:30 UTC). In the transition season (October to early November, and late January to early March), the fog events are mostly of scenario 1 and 2, thus dissipating before 12 UTC. The mid-winter period (late November to early January) has many days with scenario 4, and also several of scenario 2 and 3. In this season there are also a much higher fraction of B events, especially for scenario 2, where the cloud base remains below 400 m for at least 2 h after it lifts to above 50 m. The more persistent low stratocumulus clouds near winter solstice can be related to the weaker solar heating, as solar heating is one of the important factors for dissipation of stratocumulus over land (Wood, 2012).

Even though the seasonality can explain a large part of when each scenario occurs, there is also important case-to-case variability of dissipation time within the same season. This variability might be explained by differences such as fog thickness, stratification or clouds appearing above the fog, which we found to be important factors in the previous chapters. The tools which are introduced in the following sections will enable us to analyse this.

5.2 Model of critical fog LWP

It was found previously in this thesis (section 2.2) that the fog at SIRTA usually dissipates through the lifting of the cloud base. If a cloud is present in a well-mixed layer, the cloud will always be adjacent to the top of the layer since the temperature is lowest there, due to the adiabatic cooling. Thus, when a well-mixed fog layer lifts, it is most likely because its LWP is no longer sufficient to fill the layer between the surface and fog top. To estimate a critical value of LWP needed to fill a fog of a given thickness, a model of the LWC profile is needed.

Cermak and Bendix (2011) developed such a model for the vertical profile of LWC in very low stratus clouds. Their motivation was to distinguish fog from low stratus when observing with passive remote sensing instruments from a satellite. These instruments retrieve CTH, cloud temperature and LWP, but not CBH, which is the critical parameter to distinguish fog from a low cloud. The LWC profile is modelled in order to estimate the cloud thickness, which together with the CTH gives an estimate of the CBH.

We have implemented the Cermak and Bendix (2011) model (hereafter called the CB2011 model) using as input the CTH from the cloud radar (see section 2.3), the LWP from the MWR or from visibility and cloud radar (see section 2.5), and surface in situ observations of temperature and pressure. Our cloud radar has a significantly higher precision of the CTH than what can be obtained by passive satellite instruments thanks to the high resolution (12.5 m). As in Cermak and Bendix (2011), the LWC profile is parametrised from a subadiabatic model of the cloud microphysics. The LWC at altitude z in the cloud is estimated as

$$LWC_{(z)} = (1 - \beta) LWC^{ad}{}_{(z)}, \tag{5.1}$$

where $LWC^{ad}{}_{(z)}$ is the adiabatic LWC at the same level, and β is a measure of the subadiabaticity (also known as the in-cloud mixing parameter). As in Cermak and Bendix (2011), we divide the cloud in three layers and let β be constant with height ($\beta = \beta_1$) in the middle layer (see Fig. 5.3). Cermak and Bendix (2011) let β_1 be proportional to the cloud-top altitude z_t ($\beta_1 = 0.3$ km$^{-1} z_t$) because the coupling with the surface is generally more efficient the closer to the ground the cloud is. However, this leads to a systematic underestimation of the cloud thickness compared to observations in our fog events (the ceilometer shows that the cloud reaches further down than the CB2011 model would indicate). We have therefore instead applied $\beta_1 = 0.3$ for all situations, which is a common value in literature for boundary layer stratocumulus clouds according to Cermak and Bendix (2011).

In the lowest 75 m of the cloud, β increases linearly with height from 0 to β_1 (due to higher coupling near cloud base), and in the uppermost 50 m the LWC decreases linearly to reach zero at z_t (due to mixing with unsaturated air aloft), following Cermak and Bendix (2011). The paper does not indicate what to do if the cloud is thinner than 125 m. We have chosen in these cases to let the interior layer disappear and keep the ratio 3/2 between the thicknesses of the two other layers. We name the intersections between the three layers z_1 and z_2 (see Fig. 5.3).

LWC^{ad} is calculated from the difference in saturation vapour density ρ_s (kg m^{-3}) from the cloud base (z_b) to the current altitude:

$$LWC^{ad}{}_{(z)} = \rho_{s(z_b)} - \rho_{s(z)} \tag{5.2}$$

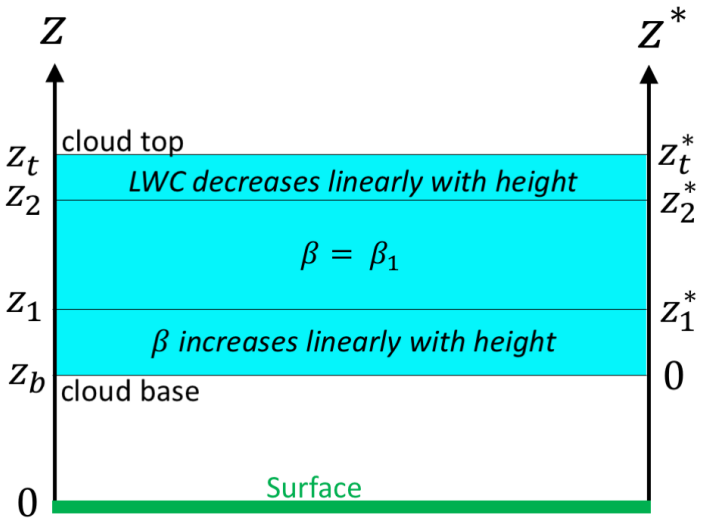

Figure 5.3: The three layers of a fog or low stratus cloud assumed in the CB2011 model, and the intersection altitudes between them. They are given in two height coordinates, one with the surface as reference (z) and one with the cloud base as reference (z^*). If the cloud is thicker than 125 m, then $z_1 - z_b = 75$ m and $z_t - z_2 = 50$ m. See text for details.

Using the ideal gas approximation for water vapour

$$\rho_s = \frac{e_s}{R_v T}, \tag{5.3}$$

the vertical gradient in ρ_s is found from the saturated adiabatic lapse rate Γ_s and the temperature dependency of ρ_s:

$$\frac{d\rho_s}{dz} = \frac{d\rho_s}{dT}(-\Gamma_s) \tag{5.4}$$

$$= -\frac{\Gamma_s(sT - e_s)}{R_v T^2} \tag{5.5}$$

where $s = \frac{de_s}{dT}$. Since we work with relatively thin layers, we neglect vertical variability in Eq. (5.5) and apply the layer-averaged temperature ($\overline{T}$). Inserting this into Eq. (5.2) results in a linear increase of LWC^{ad} with altitude above cloud base:

$$LWC^{ad}{}_{(z^*)} = \kappa z^* \tag{5.6}$$

where

$$\kappa = \frac{\Gamma_s(s\overline{T} - e_{s(\overline{T})})}{R_v \overline{T}^2} \tag{5.7}$$

and $z^* = z - z_b$ is the altitude above the cloud base (see Fig. 5.3). Inserting Eq. (5.6) into Eq. (5.1) results in:

$$LWC = \kappa(1 - \beta)z^* \tag{5.8}$$

Applying the hypothesis of the CB2011 model for the profile of subadiabaticity, the total modelled

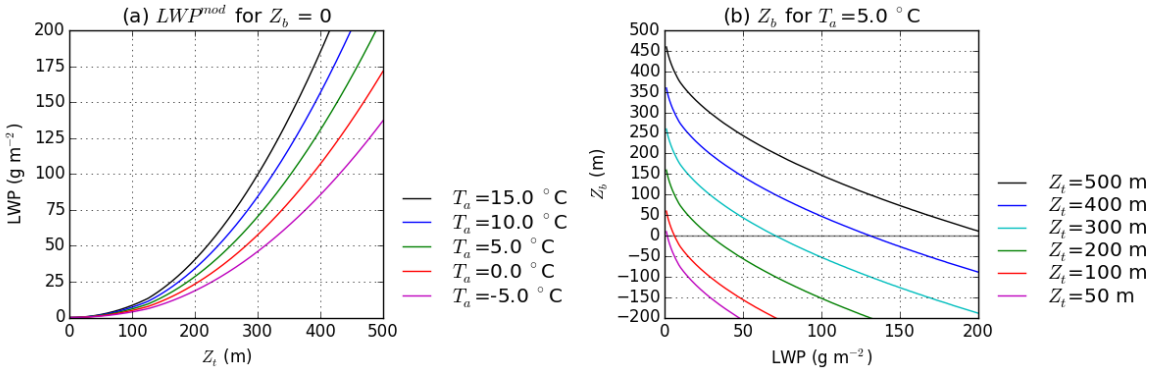

Figure 5.4: Sensitivity study of the model of Cermak and Bendix (2011) as implemented by us: (a) The dependency of the critical LWP (LWP^{crit}) on fog thickness and screen temperature; (b) the dependency of the predicted CBH on LWP and CTH at a screen temperature of 5 °C. Surface pressure is set to 1000 hPa in all cases.

LWP of the cloud can be obtained by integrating Eq. (5.8) throughout the cloud:

$$\begin{aligned}
LWP^{mod} &= \int_0^{z_1^*} LWC_{(z^*)}dz^* + \int_{z_1^*}^{z_2^*} LWC_{(z^*)}dz^* + \int_{z_2^*}^{z_t^*} LWC_{(z^*)}dz^* \\
&= \int_0^{z_1^*} \kappa(1-\beta)z^*dz^* + \int_{z_1^*}^{z_2^*} \kappa(1-\beta)z^*dz^* + \int_{z_2^*}^{z_t^*} LWC_{(z_2^*)}\frac{z_t^*-z^*}{z_t^*-z_2^*}dz^* \\
&= \int_0^{z_1^*} \kappa(1-\beta_1\frac{z^*}{z_1^*})z^*dz^* + \int_{z_1^*}^{z_2^*} \kappa(1-\beta_1)z^*dz^* + \int_{z_2^*}^{z_t^*} \kappa(1-\beta_1)z_2^*\frac{z_t^*-z^*}{z_t^*-z_2^*}dz^* \\
&= \kappa\left[(\frac{1}{2}-\frac{\beta_1}{3})z_1^{*2} + \frac{1}{2}(1-\beta_1)(z_2^{*2}-z_1^{*2}) + \frac{1}{2}(1-\beta_1)z_2^*(z_t^*-z_2^*)\right] \\
&= \kappa\left[\frac{1}{2}(1-\beta_1)z_2^*z_t^* + \frac{1}{6}\beta_1 z_1^{*2}\right] \qquad (5.9)
\end{aligned}$$

where z_1^* and z_2^* are the altitudes, relative to cloud base, of the bottom and top, respectively, of the middle layer where $\beta = \beta_1$, and z_t^* is the cloud thickness (see Fig. 5.3).

Equation (5.9) can be used to calculate LWP^{crit}, the critical LWP necessary for maintaining the fog at the surface, by setting $z_b = 0$:

$$LWP^{crit} = LWP^{mod}{}_{(z_b=0)} \qquad (5.10)$$

The dependency of LWP^{crit} on CTH and temperature is shown in Fig. 5.4a. Due to the increase in LWC with height, LWP^{crit} increases more than linearly with CTH. At 5 °C, a 100-m thick fog needs only 6 g m^{-2} to reach the surface according to the model, while a 200-m thick fog needs 29 g m^{-2}, a 300-m cloud 70 g m^{-2} and a 400-m cloud 131 g m^{-2}. The temperature dependency is also important, with a 300-m thick fog requiring 58 g m^{-2} to reach the surface at 0 °C and 100 g m^{-2} at 15 °C. While the temperature dependency can explain differences in LWP between fog events, changes in temperature with time are not likely to be a major factor for the cloud-base lifting through its effect on LWP^{crit}, since the temperature changes rather slowly compared to the CTH.

Equation (5.9) can also be used as in Cermak and Bendix (2011), to estimate the predicted cloud base for an observed cloud top and LWP. This is done by calculating LWP^{mod} iteratively, modifying z_b up or down while keeping z_t constant, until LWP^{mod} converges to the observed LWP. This product

is shown as function of LWP and cloud top in Fig. 5.4b. The interpretation of this CBH is that a positive value indicates that the fog base should lift to this altitude, while a negative value means that the fog currently has more LWP than what is needed to sustain liquid near the surface.

Figure 5.5 shows the diagnosed CBH with the CB2011 model in each 10-min block for each of the 45 morning fog events, comparing to the observed CBH. We can first observe that the CBH CB2011 mainly has negative values when the fog touches the ground in reality. When the cloud base lifts, the CBH CB2011 follows the observed cloud base closely in several of the events, such as 24 Oct 2013 (ag), 2 Nov 2015 (an), 19 Nov 2014 (ap) and 30 Nov 2014 (as). Even in some of the mid-winter events where the persistent fog layer lifts a few metres from the surface, this happens when the CBH CB2011 is close to zero, such as on 14 Dec 2014 (ax), 5 Jan 2015 (bf) and 13 Dec 2015 (av)[1]. In other fog events, the CBH CB2011 is slightly biased, predicting a few tens of metres too low or too high CBH when the base lifts, thereby crossing zero too early or too late, such as on 26 Oct 2015 (ai), 29 Jan 2017 (bh) and 11 May 2016 (br).

There are also events where the CB2011 model does not perform well at all, such as on 29 Oct 2014 (al), 7 Jan 2015 (bg) and 27 Nov 2015 (ar). The most critical issue is perturbations in the input data, especially in the MWR LWP, which will not represent the LWP of the fog layer only if there are liquid clouds above the fog. We have therefore indicated in Fig. 5.5 the periods when the cloud radar detects a higher cloud or rain, which could cause a negative bias in CBH CB2011 due to the overestimation of LWP. However, there are still many cases remaining when the cloud radar does not detect a cloud above even when its effect on the CBH CB2011 is apparent, for example the downward peaks in CBH CB2011 that occur around 8 UTC on 19 Oct 2013 (af), or the negative value at 10 UTC on 29 Oct 2014 (al) when the fog cloud is almost completely evaporated but the MWR still indicates an LWP of more than 50 g m^{-2}. Improvements in the sensitivity of the cloud radar might allow these clouds to be detected. There are also some cases where the fog is able to stay on the ground in spite of the CBH CB2011 indicating it should lift (e.g. 18 Oct 2013 (ae), 30 Dec 2016 (ba), 2 Jan 2017 (be)). This usually occurs when the reflectivity is strong, so one hypothesis could be that the sedimentation of bigger droplets in these cases permits the fog to stay on the ground with less LWP than what would normally be required.

Overall, in the majority of the fog events, the CB2011 model is able to reproduce the cloud base evolution at dissipation rather well while staying negative before dissipation. For these cases, the CB2011 model provides an interesting diagnostic for the sufficiency of the current LWP to fill the current fog thickness. This could potentially be useful for the nowcasting of fog base evolution. The remaining challenge is to predict the LWP and CTH, which usually do not have very steady tendencies. There are some exceptions, though, where the CBH CB2011 increases gradually during the day, thereby providing and indication of when the fog might dissipate. Rather subjectively, we have marked in Fig. 5.5 seven events where the CBH CB2011 increases rather steadily in an important period of time after sunrise (and before dissipation) (green frames) and ten other events where a tendency can also be discerned, but not as clearly (cyan frames). In these events, the time of dissipation could be anticipated by extrapolating the observed tendency, although the fog does not in all these cases dissipate (e.g. 10 Dec 2016 (au), 18 Dec 2016 (ay)). In most cases, however, the CBH CB2011 changes drastically its tendency at least once between sunrise and dissipation: in some cases it increases to

[1]It is hard to perceive it due to the small figures, but in these three events, the green line lifts marginally up from the 0-line in periods, due to an increase in visibility.

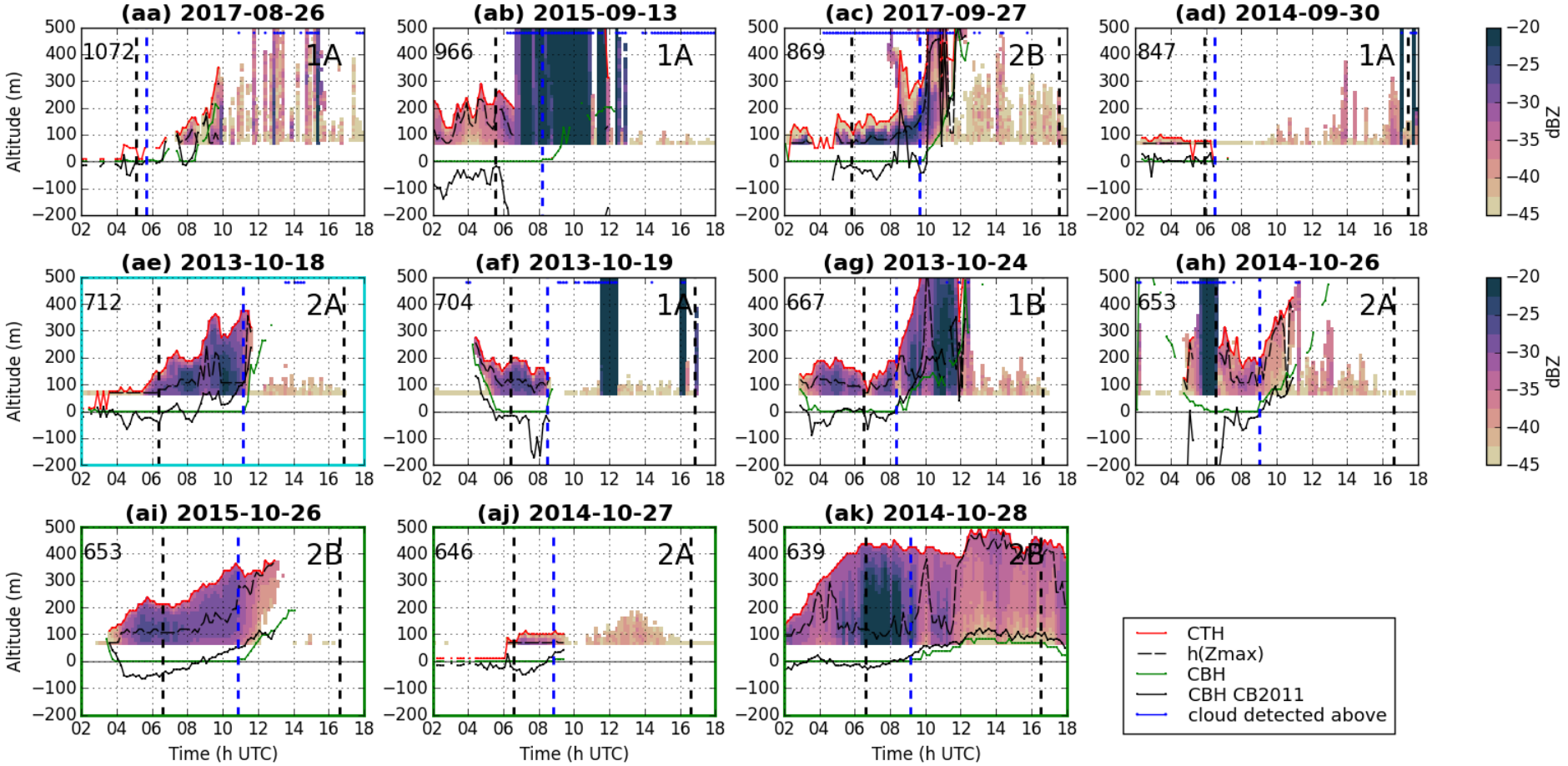

Figure 5.5: Observed time series of radar reflectivity during the 45 fog events present at sunrise in 2013–2017. Observed cloud base (green line) and cloud top (red line) are indicated, as well as the altitude of max reflectivity (dashed black line) and the cloud base calculated with the CB2011 model (solid black line). Vertical lines mark sunrise and sunset (black) and surface dissipation time (blue). The scenario of each fog (defined in section 5.1) is indicated in upper right corner, and the calculated solar radiation at top of the atmosphere at 12 UTC is indicated in the upper-left corner (in W m^{-2}). The blue lines at the top of the figures mark periods when a signal is detected between the fog and 7 km by the cloud radar. Green (cyan) frames mark events which show a gradual (relatively gradual) tendency in CBH CB2011 after sunrise (subjectively selected). NB: The figure continues on the next two pages.

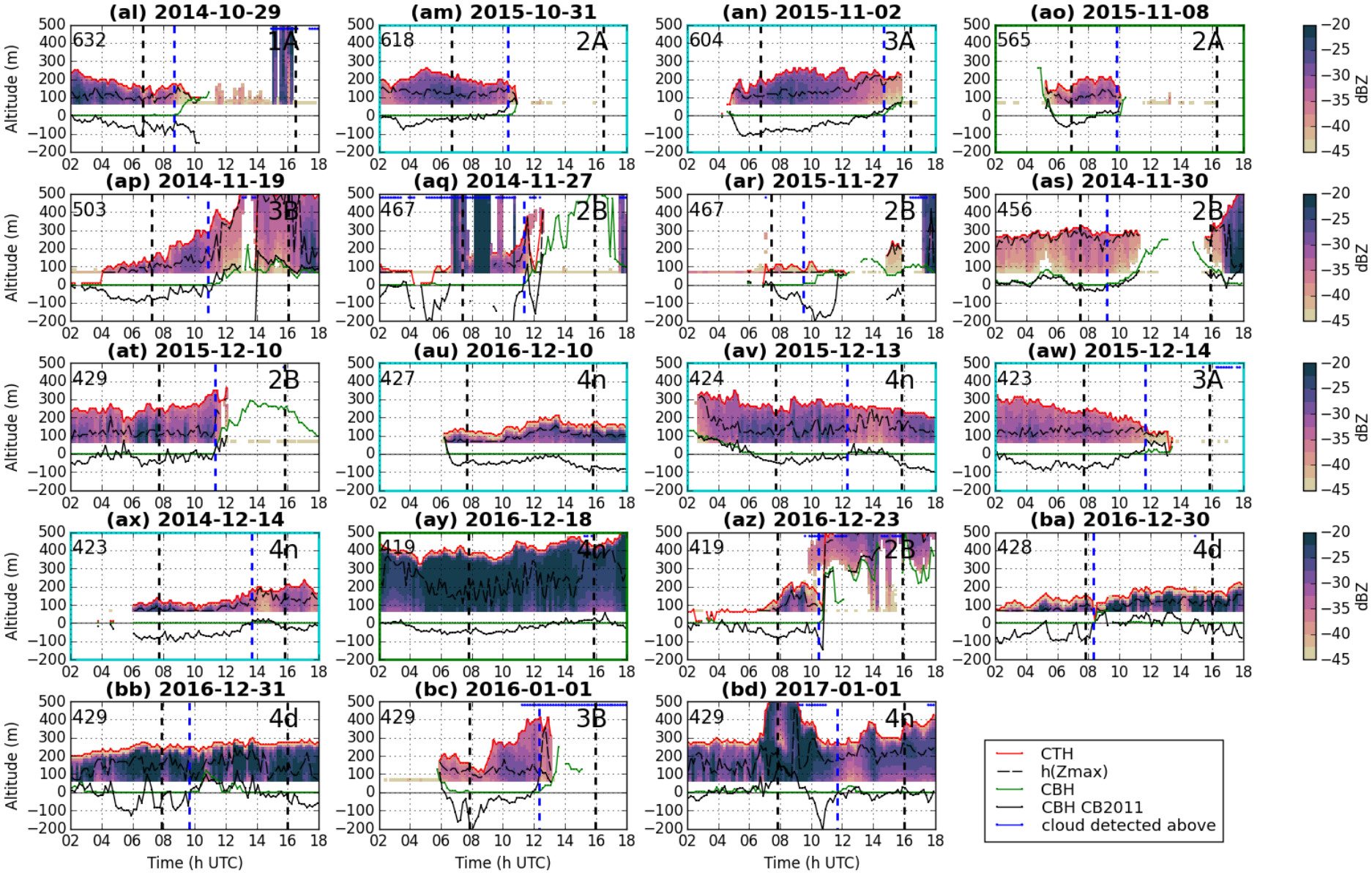

Figure 5.5: (continued)

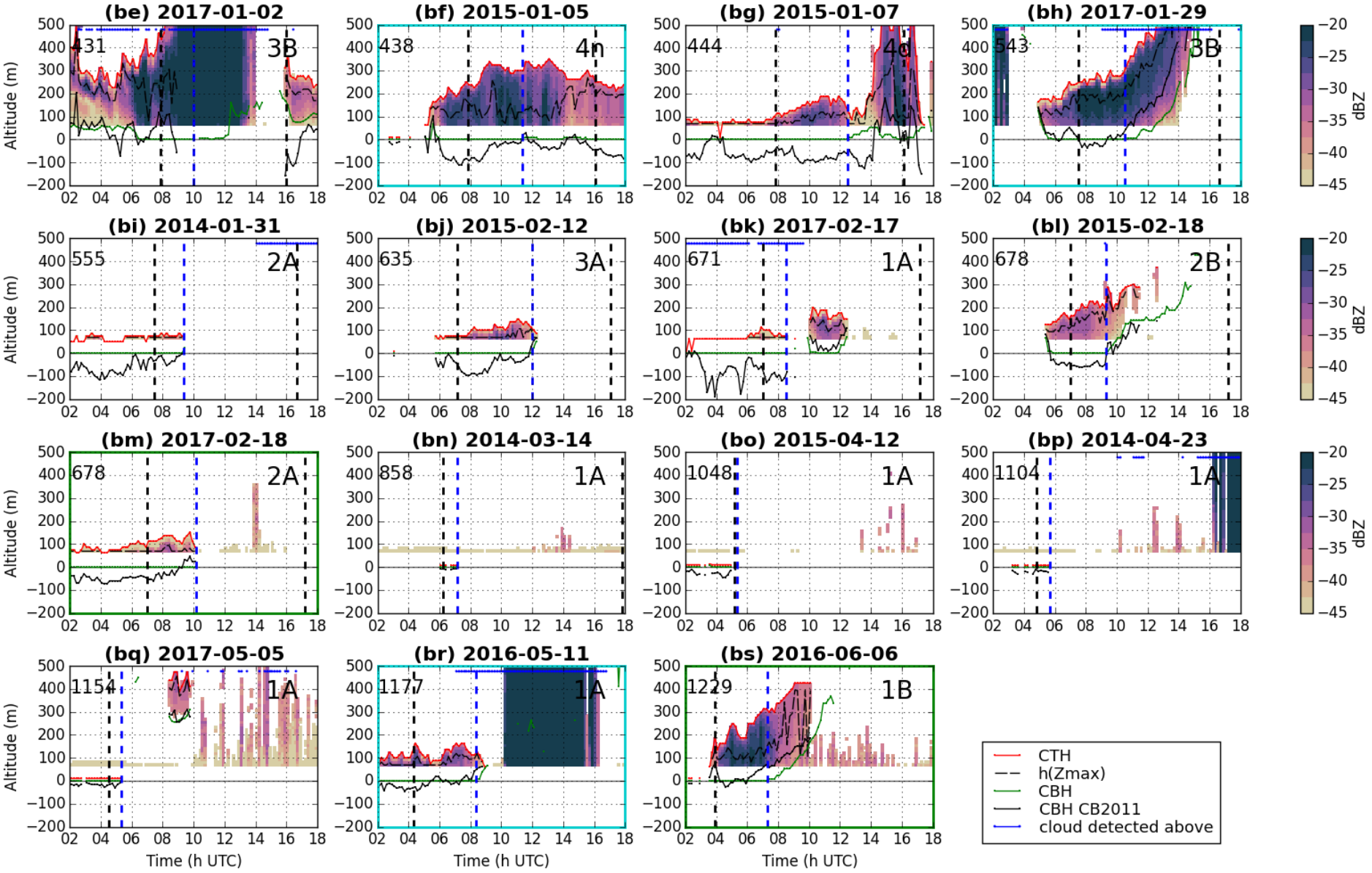

Figure 5.5: (continued)

zero more than once before the fog base actually lifts, and in other cases it stays close to zero for a long time before the fog suddenly lifts. It is therefore important to understand how different processes will impact the evolutions of LWP and CTH.

Figure 5.6 summarises some of the patterns found using the CB2011 model. There is a link between the tendencies of CTH and LWP in the last 45 min before dissipation (Fig. 5.6a): in most cases when LWP increases, the CTH increases too, while cases when the CTH decreases are also associated with a decrease in LWP. The result we found earlier that the LWP often increases at dissipation (Fig. 2.15d) can therefore be explained by the CTH also increasing. The two outliers in Fig. 5.6a where CTH decreases when LWP increases are probably due to cases of clouds above the fog (in one of them, a cloud is indeed detected). This pattern between the tendencies in LWP and CTH results in a CBH CB2011 which is nearly always increasing at dissipation when no detected clouds above perturb the tendency (Fig. 5.6b). Figure 5.6c shows the time difference between the lifting of the CBH in the CB2011 model and the observed lifting. The two times are mostly within 40 min of each other. In 16 events the two times are even closer than 20 min; however, this includes six cases when the cloud completely dissipates before the CBH CB2011 has become positive.

In Fig. 5.5, we also show the profile of reflectivity, and the altitude of the highest reflectivity (dashed line). For the events that are thick enough to have a significant observed reflectivity profile, we can note that the altitude of max reflectivity is sometimes near the fog top, and at other times lower down close to the centre of the fog layer. For example, the max is close to the fog top on 30 Nov 2014 (as), on 18 Feb 2015 (bl) and on 10 Dec 2016 (au). In some cases, the lifting of the fog base from the surface is associated with a decrease in reflectivity and a shift of the max-value towards the fog top, such as on 2 Nov 2015 (an), 13 Dec 2015 (av) (although the base only lifts very slightly), 26 Oct 2015 (ai) and 28 Oct 2014 (ak). We know that the reflectivity represents the sizes (and number) of the droplets, so the interpretation of the shift of the max towards the top is that the droplets sizes are decreasing in the lower layers of the fog, associated with the lifting. In contrast, the reflectivity is often stronger and with a max towards the centre earlier in its life cycle. However, we see that the shift of the altitude of max reflectivity can occur both before (e.g. 2 Nov 2015 (an)) and after (e.g. 28 Oct 2014 (ak)) the CBH lifts from the surface, and in some cases it occurs without the fog lifting from the surface (e.g. 18 Dec 2016 (ay)).

5.3 Conceptual model of fog LWP budget and CTH development

5.3.1 The LWP equation and general assumptions

The previous section has confirmed that the main parameters determining the CBH, and thereby fog dissipation vs persistence, are the LWP and CTH. To understand why the LWP and CTH tendencies evolve as they do, the effects of both local and non-local processes must probably be taken into account. In this section, we develop a conceptual model to quantify the contributions from the local processes to the tendencies in these two parameters, based on observations.

Following the idea of W18, the LWP budget of the fog is formulated by estimating the current impacts of each of the processes on LWP. This time around, the terms are estimated directly from observations, using various parametrisations (Fig. 5.7). The assumptions are the same here as in the method used for the model output analysis in W18: the fog layer is assumed to be well-mixed, saturated everywhere, have a saturated adiabatic temperature profile, and to extend between the

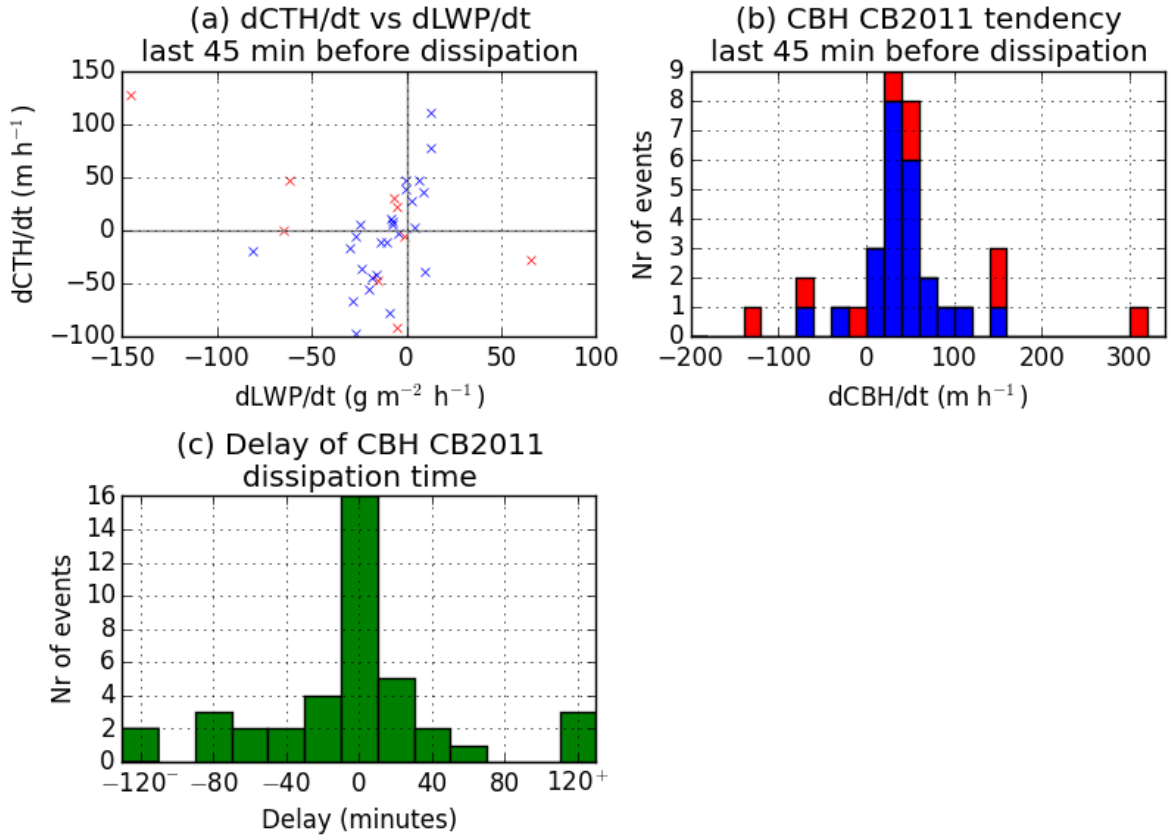

Figure 5.6: Statistics of the LWP and CTH tendencies and the predicted CBH by the CB2011 model around dissipation time of the 45 morning fog events: (a) Tendency of CTH vs tendency of LWP in the last 45 min before dissipation, estimated from the difference between the mean value in 60–30 min before dissipation and the mean value from 10 min before to 10 min after dissipation. It is only calculated when a CTH is detected for all the relevant blocks (35 events), and the events where the cloud radar detects a signal between the fog and 7 km are marked in red (9 events). (b) The resulting tendency in CBH CB2011 from the data in (a). (c) Distribution of the time when CBH CB2011 becomes positive (or the cloud dissipates) relative to the time of dissipation (based on 2-block averages). 5 of 45 events are missing due to insufficient cloud radar sensitivity, rain or no dissipation before midnight.

surface and the observed fog top. The well-mixed assumption is reasonable for thick fog after sunrise, due to destabilisation (section 2.6).

The vertical development of the cloud top is estimated by assuming it is affected by entrainment and subsidence only, i.e.:

$$\frac{dh}{dt} = w_{ls(z=h)} + w_e \tag{5.11}$$

where h is the CTH, w_{ls} is the large-scale vertical velocity (positive for upward motion, negative for subsidence), and w_e is the entrainment velocity (see section 5.3.3). Thus, we neglect other impacts on the CTH, such as decoupling of rising plumes or saturation of the overlying layer by radiative cooling.

The conceptual model estimates the impacts on fog LWP from the processes of LW radiative cooling, absorption of SW radiation, surface turbulent heat fluxes, entrainment at fog top, subsidence and droplet deposition. Several parametrisations documented in the scientific literature have been combined to estimate these terms using observations from 8 different instruments at SIRTA as input.

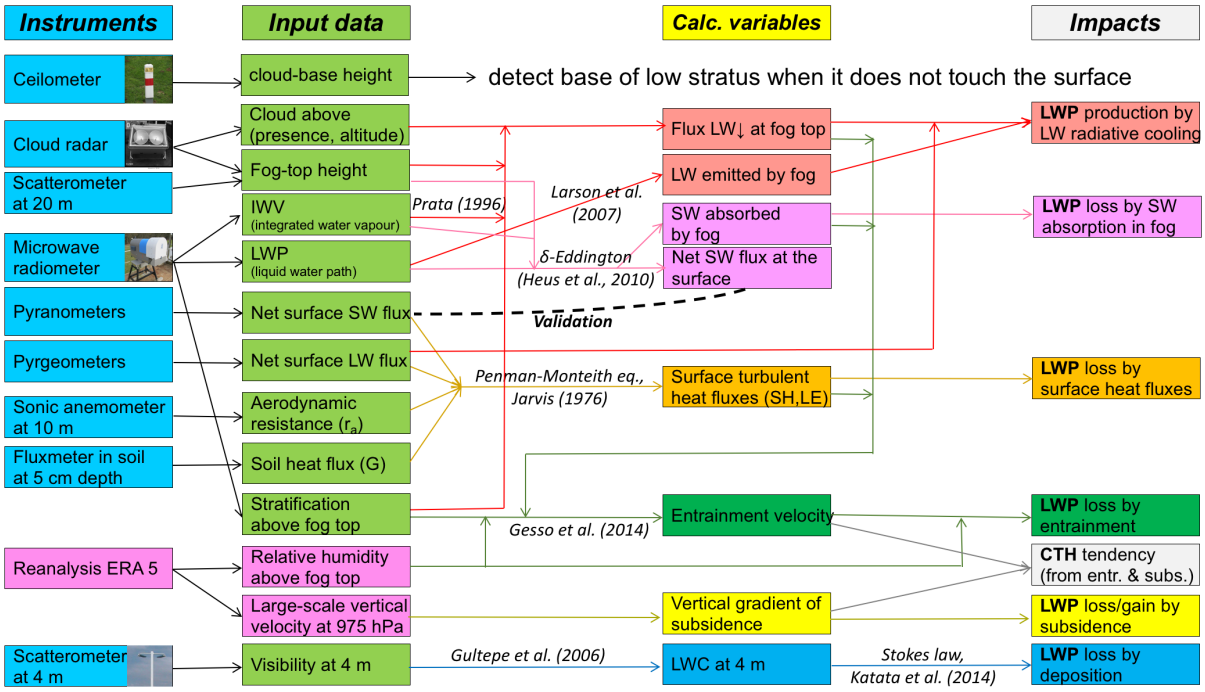

Figure 5.7: Schematic overview of the conceptual model which estimates 6 terms in the fog LWP budget as well as the CTH tendency, using 8 instruments and the reanalysis ERA5. In addition to the observations indicated on this chart, temperature and pressure observations at screen level are utilised by the model. The calculation of the radiative terms (red and pink sector in the schematic) is detailed in section 3.2, the surface energy budget calculations (orange) are presented in section 5.3.2, the entrainment parametrisation (dark green)in section 5.3.3, the subsidence term (yellow) in section 5.3.4 and the deposition calculations (blue) in section 5.3.5.

Some input data that are not observed locally are taken from the reanalysis ERA5: the large-scale subsidence, which we cannot observe locally, and the relative humidity in the layer above fog top, which we do not have the means to observe accurately except for radiosondes, as explained in section 2.6. The reanalysis is not available in real time. However, in an operational application of the conceptual model, the reanalysis could be replaced by a 6-h forecast from a forecast centre, which could also allow a higher temporal resolution; the reanalysis data are only given every 6 hours.

The conceptual model is applied to 10-min blocks. The observations from SIRTA are averaged within these blocks to create input data to the conceptual models, while reanalysis data are interpolated in time.

Under the assumptions given above, and assuming no impact from horizontal advection, the LWP equation for the fog layer is (see section 3.3 in W18 for details):

$$\frac{dLWP}{dt} = -\frac{s}{s+\gamma}\frac{1}{L_v}\sum_{i=1}^{5} SH_i + \frac{\gamma}{s+\gamma}\frac{1}{L_v}\sum_{i=1}^{2} LH_i - F_{dep} + \frac{dw_{ls}}{dz}LWP \tag{5.12}$$

where SH_i are the 5 sensible heat flux contributions in W m^{-2} (LW radiation, SW radiation, subsidence, entrainment and surface sensible heat flux), LH_i are the 2 latent heat flux contributions in W m^{-2} (entrainment and surface latent heat flux), F_{dep} is the deposition flux in kg m^{-2} s^{-1}, and the last term is the divergence due to subsidence. Fog average values of s and γ are calculated at the geometric midpoint of the fog layer. Air temperature and pressure at this level are estimated by extrapolating

the measurements at 2 m using the saturated adiabatic lapse rate and the hydrostatic equation (just as in the CB2011 model, see section 5.2).

This equation is applied during fog, and also when the cloud base is in the range 0–50 m. Although the layer may not be completely saturated down to the surface when the base is not at 0 m, it is still interesting to include the periods right after dissipation in the analysis. The following subsections explain how the different terms in Eq. (5.12) are calculated, apart from the radiation terms, which are explained in section 3.2. Note that the conceptual model is purely diagnostic. We use neither Eq. (5.12) nor Eq. (5.11) to prescribe future values for LWP or CTH. We only analyse the diagnosed tendencies.

5.3.2 Surface turbulent heat fluxes

As shown in W18, the turbulent heat fluxes at the surface are the main loss mechanism for fog in daytime, and the Bowen ratio is a critical parameter because of the opposing impacts of sensible and latent heat fluxes on the fog LWP. It was also found that we unfortunately do not dispose of reliable measurements of the turbulent heat fluxes from the surface at SIRTA. To get an estimate of the turbulent heat fluxes, the Penman-Monteith equation (Monteith, 1965) is applied. When the air is saturated, this equation predicts the following latent heat flux:

$$L_v E = \frac{s(R_{net} - G)}{s + \gamma(1 + \frac{r_s}{r_a})}, \tag{5.13}$$

The surface net radiation (R_{net}) and ground flux (G) are available from observations[2]. r_a is determined from the observations of the sonic anemometer at 10 m:

$$r_a = \frac{\overline{V}}{\sqrt{\overline{u'w'}^2 + \overline{v'w'}^2}} \tag{5.14}$$

where $\overline{V}$ is the mean horizontal wind speed and $\overline{u'w'}$ and $\overline{v'w'}$ the momentum fluxes in the x- and y-direction, respectively.

The surface resistance r_s relates to the transpiration activity of the vegetation. If the available energy $R_{net} - G < 0$, then $L_v E < 0$, corresponding to dew deposition, for which $r_s = 0$. For positive available energy, we apply the method of Jarvis (1976), which assumes that r_s can be found by multiplying the contributions from SW radiation, soil moisture, temperature, relative humidity and CO_2 concentration. Only the contributions from SW radiation and temperature are taken into account, since the air is saturated and the soil is generally moist during the fog season at SIRTA[3]. The parametrisation is then:

$$r_s = \frac{r_{s,min}}{LAI} \cdot f_1(SW_\downarrow) \cdot f_2(T), \tag{5.15}$$

where the functions of downwelling SW radiation at the surface ($SW_\downarrow$) and temperature (T) are:

$$f_1(SW_\downarrow) \quad = \quad \max[1, \frac{0.81(0.004SW_\downarrow + 1)}{0.004SW_\downarrow + 0.05}] \tag{5.16}$$

[2]Ground flux observations are missing for four of the fog events (the three in October 2013 and 30 Sept 2014). For these events, G is set to zero.

[3]The high soil moisture is affected by the nearby lake, and it could therefore be that the soil is less moist in other areas in the Paris region covered by the same fog bank.

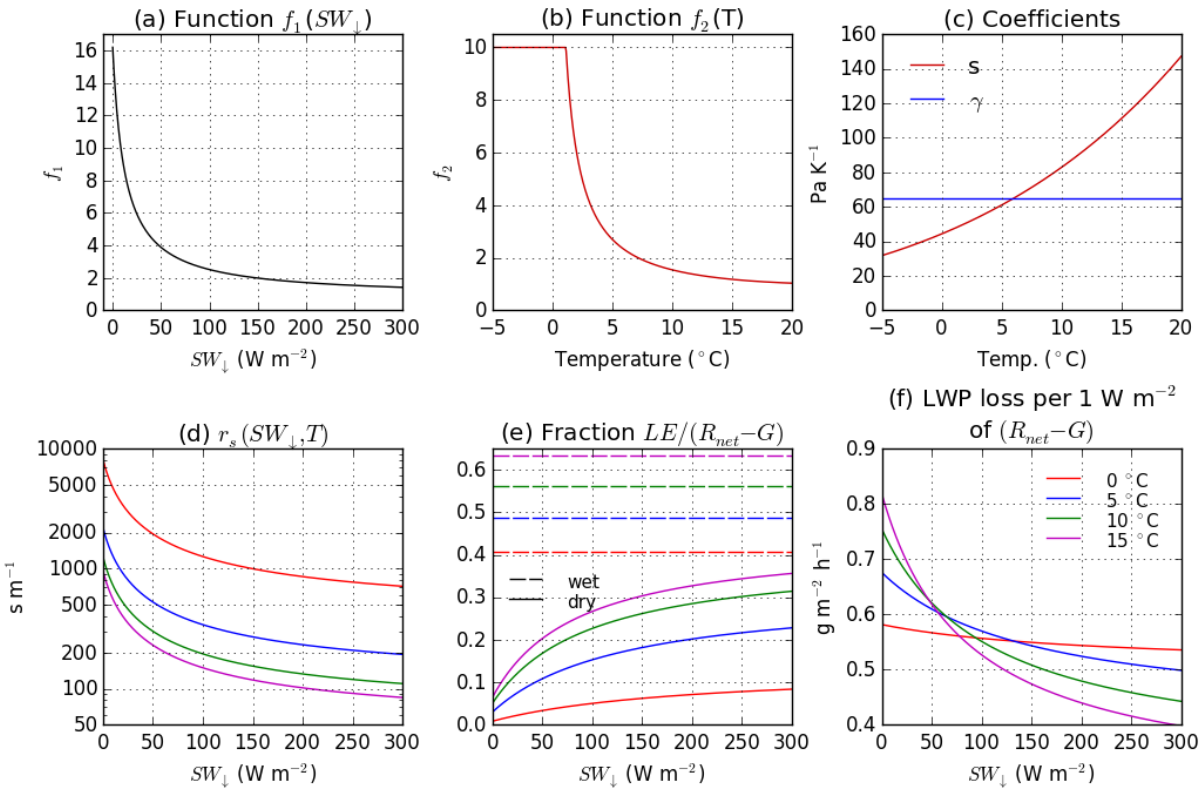

Figure 5.8: Analysis of the sensitivity of Eq. (5.20) to downwelling SW radiation ($SW_\downarrow$) and temperature T. Pressure has been set to 1000 hPa, and aerodynamic resistance to 40 s m^{-1}. (a) The function f_1 describing the dependency of r_s on $SW_\downarrow$, and (b) its dependency f_2 on T, (c) the coefficients s and γ, (d) the total r_s, (e) the fraction of available energy which goes to latent heat for a wet (dashed) and dry (solid) surface, and (f) the loss of LWP per 1 W m^{-2} available energy from a dry surface. The temperature legend in (f) is also valid for (d) and (e).

$$f_2(T) \quad = \quad \min[10, 1 - (\frac{298 - T}{25})^2] \tag{5.17}$$

We apply $r_{s,min} = 100$ s m^{-1} and LAI $= 2$, corresponding to the values used for grass and cropland in the IFS model (ECMWF, 2016). The coefficients in the formulas for f_1 and f_2 are as in the LES model DALES. Figure 5.8abd shows this dependency of r_s on $SW_\downarrow$ and T.

Building on the findings of W18, we introduce the concept of liquid present on a fraction of the surface c_{liq}, from which evaporation can occur without any surface resistance, and the remaining fraction $c_{dry} = 1 - c_{liq}$ which has the surface resistance calculated by (5.15). Then the latent heat flux can be calculated as:

$$L_v E = s(R_{net} - G)\Big[\frac{c_{dry}}{s + \gamma(1 + \frac{r_s}{r_a})} + \frac{c_{liq}}{s + \gamma}\Big] \tag{5.18}$$

From Eq. (5.12), the effect of the surface fluxes on fog LWP can be calculated as

$$\frac{dLWP}{dt}_{surf} = -\frac{s}{s + \gamma}\frac{1}{L_v}(SH - \frac{\gamma}{s}L_v E) \tag{5.19}$$

Inserting (5.18) into (5.19), and computing the sensible heat flux from energy closure ($SH = R_{net} -$

$G - L_v E$), results in:

$$\frac{dLWP}{dt}_{surf} = -\frac{s}{s+\gamma}\frac{1}{L_v}(R_{net} - G) \cdot \frac{\gamma \frac{r_s}{r_a}}{s + \gamma(1 + \frac{r_s}{r_a})} \cdot c_{dry} \tag{5.20}$$

When interpreting this expression, we can first note that the LWP loss is proportional to c_{dry}. This is because according to the Penman equation, the air coming from a wet surface will be saturated with vapour, so that the fraction of surface covered by liquid does not give any LWP loss. Therefore, the loss of liquid water from surface fluxes will be the loss from a dry surface, scaled with the fraction of surface that is dry.

The first half of the expression in Eq. (5.20) (before the big fraction) represents the loss of LWP we would get if there was only sensible heat and no evaporation. The big fraction represents the reduction of this loss due to some of the heat flux from the dry surface being latent.

Figure 5.8ef explores the sensitivity of Eq. (5.20) to temperature and humidity for $r_a = 40$ s m^{-1}, normalised by $(R_{net} - G)c_{dry}$. Each 1 W m^{-2} of $R_{net} - G$ from the dry surface corresponds to 0.4–0.8 g m^{-2} h^{-1} of LWP loss. Higher temperatures give a stronger dependency on insolation, with the loss per W m^{-2} decreasing with $SW_{\downarrow}$. For warmer fog, we therefore get a slightly weaker diurnal cycle in the loss of LWP from surface fluxes than in colder fog: when the sun is low, $R_{net} - G$ is smaller than when the sun is high, but each W m^{-2} causes more LWP loss. For weak $SW_{\downarrow}$, the loss is stronger for higher temperature, while for higher $SW_{\downarrow}$ the loss is stronger for lower temperature.

Since c_{cry} is not observed, we have chosen to apply the constant value of 0.5, which means that the estimated loss of LWP from surface fluxes is half as large as shown in Fig. 5.8f.

5.3.3 Entrainment

A common way to parametrise the mixing between the well-mixed atmospheric boundary layer (BL) and the layer above is through an entrainment velocity w_e, describing how fast the mixed layer grows vertically into the overlying atmosphere. This approach assumes that all air with which the layer mixes subsequently becomes part of the well-mixed layer.

Consider a fog layer of thickness h, average potential temperature θ, density ρ_a and specific humidity q_v, which mixes with a much thinner overlying layer of thickness δh, potential temperature θ^+, density ρ_a^+ and humidity q_v^+. If the two layers mix adiabatically and there is no phase change, the new fog average potential temperature and humidity will be the mass-weighted average of the two layers, i.e.:

$$\theta + \delta\theta = \frac{\rho_a h\theta + \rho_a^+ \delta h \theta^+}{\rho_a h + \rho_a^+ \delta h} \tag{5.21}$$

$$q_v + \delta q_v = \frac{\rho_a h q_v + \rho_a^+ \delta h q_v^+}{\rho_a h + \rho_a^+ \delta h} \tag{5.22}$$

Eq. (5.21) can be rewritten as:

$$\rho_a h\delta\theta + \rho_a^+ \delta h\theta + \rho_a^+ \delta h\delta\theta = \rho_a^+ \delta h\theta^+ \tag{5.23}$$

If we let $\delta h \to 0$, we may neglect the contribution from the third term. We then get:

$$\rho_a h\delta\theta = \rho_a^+ \delta h(\theta^+ - \theta) \tag{5.24}$$

Assuming the layer δh is being entrained during a time δt, the increase in fog average temperature due to mixing can be expressed as a sensible heat flux:

$$\begin{aligned} SH_{entr} &= \rho_a c_p h \frac{\delta\theta}{\delta t} - \rho_a c_p h \frac{\delta h}{2\delta t}\frac{g}{c_p} \\ &= \rho_a^+ c_p w_e(\theta^+ - \theta) - \frac{1}{2}\rho_a g h w_e \end{aligned} \tag{5.25}$$

where we have defined the entrainment velocity $w_e = \frac{\delta h}{\delta t}$. The first term is the increase in potential temperature of the fog layer. The second term is the "adiabatic" effect, i.e. the decrease in fog mean temperature due to the decrease in fog mean pressure related to the upward displacement of the fog centre of mass. Equivalently, we can express the increase of humidity of the fog layer due to entrainment as a latent heat flux:

$$\begin{aligned} LH_{entr} &= \rho_a L_v h \frac{\delta q_v}{\delta t} \\ &= \rho_a^+ L_v w_e(q_v^+ - q_v) \end{aligned} \tag{5.26}$$

Of course, Eqs. (5.21, 5.22) are only valid if θ and q_v are adiabatically conserved qualities. If the fog mixes with unsaturated air, evaporation will take place, so that neither are conserved. However, it is still correct to use Eqs. (5.25, 5.26) in Eq. (5.12) since the latter equation requires the sensible and latent heat fluxes *before* any evaporation inside the fog occurs. Although the mixing and evaporation in reality will happen simultaneously, and not one after the other, the final result will be the same.

With Eqs. (5.25, 5.26), the effect of entrainment on fog LWP can be calculated if the difference in temperature and humidity between the fog and the air above and the entrainment velocity are known. For the latter, there is a large body of literature on the subject. The phenomenon of entrainment at the top of a well-mixed boundary layer has been much studied in atmospheric science, due to its important role for the thickness of the boundary layer and the dispersion of stratocumuls clouds (e.g. Stevens, 2002; Conzemius and Fedorovich, 2006). The case of fog in daytime is particular because the BL is completely saturated and much thinner than a typical well-mixed BL. Assuming the fog layer is adiabatic and well-mixed, entrainment parametrisations meant for stratocumulus-capped BL's could in principle be applicable to fog as a special case. For our conceptual model, we apply the scheme presented by Gesso et al. (2014), which is based on the work of Stevens (2002), for the special case of cloud base at the surface. The expression for the entrainment velocity is:

$$w_e = \frac{5\eta\Theta_{NE}}{2\Delta_I\theta_v + 2.5\eta\Delta_I\theta_{v,s}}, \tag{5.27}$$

where η is an entrainment efficiency set to 0.2, Θ_{NE} has units of K m s^{-1} and represents the buoyancy production through kinetic heat fluxes other than entrainment occurring inside the BL, and the denominator is a measure of the stratification at fog top, which is simplified to an infinitely sharp inversion where the state variables change abruptly.

Θ_{NE} is parametrised as

$$\Theta_{NE} = \frac{1}{2}(A_s\overline{w'\theta'}_s + B_s T_0 \overline{w'q'_{vs}} + A_s\Delta F) \tag{5.28}$$

where $\overline{w'\theta'}_s$ and $\overline{w'q'_{vs}}$ are the kinematic sensible and latent heat fluxes at the surface, respectively,

which we get from the surface flux parametrisation (section 5.3.2). Note that in the entrainment parametrisation, the sensible and latent heat fluxes have a similar impact (Fig. 5.9a), so that the entrainment parametrisation is much less sensitive to the Bowen ratio than the LWP impact of the surface fluxes. ΔF is the radiative contribution to heating at fog base and cooling at fog top (i.e. to destabilising the fog layer). Since absorption of SW radiation mainly occurs near the fog top, it is considered a negative contribution (heating above). We further simplify the LW radiation as a cooling flux at fog top $-SH_{LW,top}$ and a heating flux at fog base $SH_{LW,base}$. The expression for ΔF is then:

$$\Delta F = \frac{1}{\rho_a c_p}(-SH_{LW,top} + SH_{LW,base} - SW_{abs}) \tag{5.29}$$

where SW_{abs} is the SW radiation absorbed inside the fog (in W m^{-2}), calculated by the SW parametrisation (see section 3.2.2), and

$$SH_{LW,top} = \epsilon_f(LW_{\downarrow,top} - \sigma T_{top}^4) \tag{5.30}$$

$$SH_{LW,base} = \epsilon_f(LW_{base}^{\uparrow} - \sigma T_{base}^4) \tag{5.31}$$

(see section 3.2.1 for details). The coefficients A_s and B_s are defined as:

$$A_s = \frac{\gamma}{s+\gamma}(1 + \epsilon_I q_v - q_l + s\frac{T_0}{p}) \tag{5.32}$$

$$B_s = \frac{L_v A_s}{c_p T_0} - 1 \tag{5.33}$$

where $\epsilon_I = \epsilon^{-1} - 1$. T_0 is a reference temperature, which is set to the fog average temperature, p is fog average pressure, and q_l is the average liquid water mixing ratio of the fog, which is found from

$$q_l = \frac{LWP}{\rho_a h} \tag{5.34}$$

Since the fog is saturated, q_v is known from the fog temperature. Due to the immediate warming, radiative and surface sensible heat fluxes are weighed slightly higher in the calculation of Θ_{NE} than surface latent heat flux (Fig. 5.9a). We see that each 1 W m^{-2} corresponds to 0.5–1 K m h^{-1} of generated "buoyancy" (i.e. Θ_{NE}).

$\Delta_I\theta_v$ is the jump in virtual potential temperature at the fog top inversion. It is calculated as

$$\Delta_I\theta_v = \theta_v^+ - \theta_{v,top} \tag{5.35}$$

where the fog-top value of virtual potential temperature $\theta_{v,top}$ is found using the assumed adiabatic temperature profile. θ_v^+ is the virtual potential temperature right above the inversion. To have an updated value for the potential temperature at this level, the MWR temperature profile is applied (using hydrostatic equation to get pressure). Since the MWR cannot resolve the sudden inversion at fog top, a level 200 m above fog top is used to estimate the stratification at fog top. This level is named h_{ab}. We already showed in Fig. 2.20a that the MWR reproduces reasonably well the variability in stratification between the surface and h_{ab} observed by radiosondes. The relative humidity at h_{ab} is interpolated in time and altitude from the reanalysis ERA5, averaging over a 1° x 1° domain. Having estimates for relative humidity and potential temperature at h_{ab}, these same values are applied to the

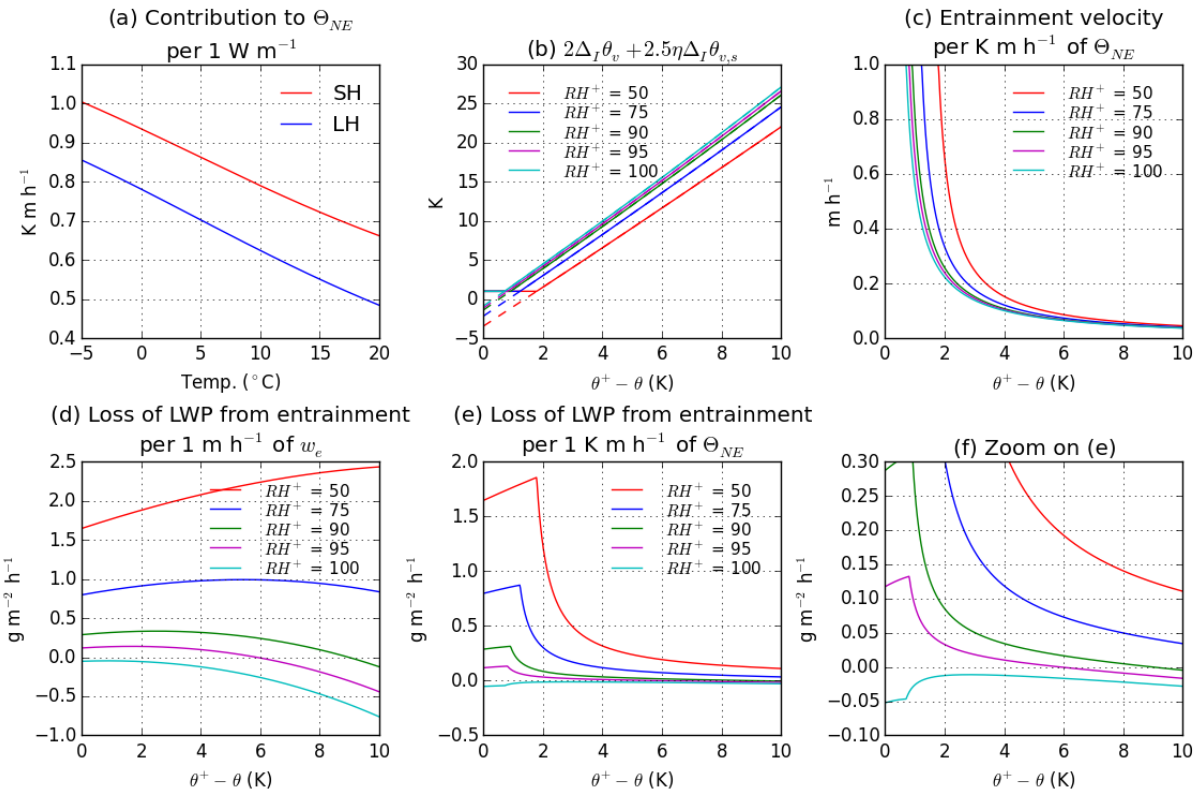

Figure 5.9: Quantities predicted by the entrainment parametrisation for a fog layer of thickness 200 m, LWP 50 g m^{-2}, at pressure 1000 hPa and (for b-f) a fog temperature of 6 °C: (a) The contribution to Θ_{NE} of 1 W m^{-2} of surface sensible heat or radiative cooling at fog top or radiative heating at fog base (i.e. $\frac{A_s}{2\rho_a c_p}$, red) and the contribution of 1 W m^{-2} of surface latent heat (i.e. $\frac{B_s T_0}{2\rho_a L_v}$, blue), as function of fog temperature. At the fog temperature 6 °C, (b) the denominator of Eq. (5.27), (c) w_e (Eq. 5.27) per unit of Θ_{NE}, (d) LWP loss per w_e and (e) LWP loss per Θ_{NE} (f is a zoom on the small values in e), as function of the potential temperature difference $(\theta^+ - \theta)$ from the fog average to the air above, for different values of relative humidity above fog (RH^+).

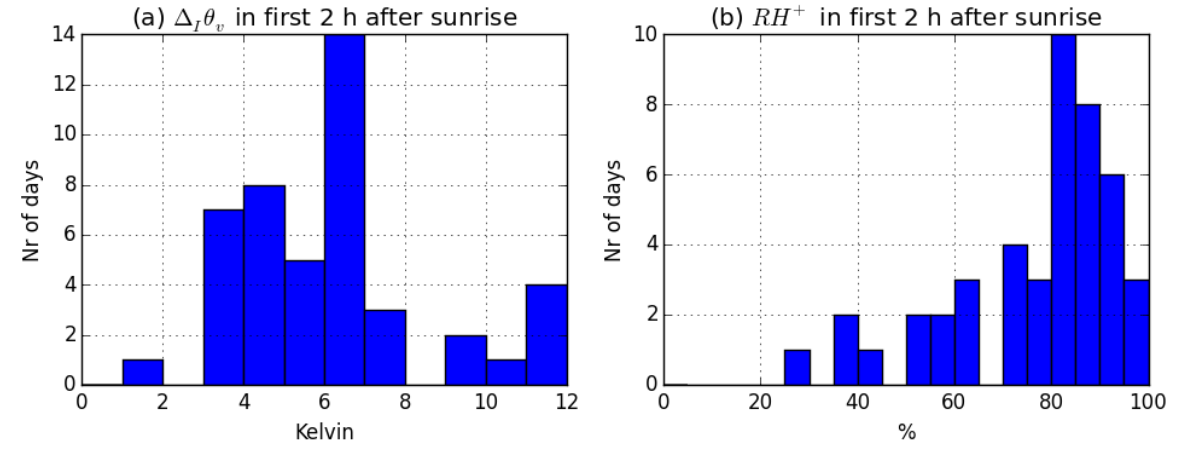

Figure 5.10: (a) The mean value of $\Delta_I\theta_v$ and RH^+ in the first 2 hours after sunrise in each of the 45 morning fog events, calculated from the MWR and ERA5 (see text for details).

air directly above fog top, θ^+ and RH^+ (we basically assume that RH and θ are constant with height from the fog-top inversion to 200 m above). From these values, ρ_a^+, q_v^+ and θ_v^+ can be calculated. Fig. 5.10 shows the distribution of $\Delta_I\theta_v$ and RH^+ in the first 2 hours after sunrise among the morning fog events. There is important variability in both of these parameters. The two parameters have a similar distribution to what we found using the radiosondes in W18, but with less occurrence of RH close to saturation, which can be explained by using 200 m above fog top rather than the layer 50–200 m above. Since it is likely that the potential temperature increases and the relative humidity decreases between the fog-top inversion and 200 m above fog top, θ^+ might be overestimated and RH^+ underestimated, which will be discussed in section 5.6.3.

Having the estimates for θ^+ and RH^+, we can also calculate $\Delta_I\theta_{v,s}$, which is defined as:

$$\Delta_I\theta_{v,s} = A_s\Delta_I\theta_l + B_sT_0\Delta_I q_t \tag{5.36}$$

where

$$\Delta_I\theta_l = \theta^+ - \left(\theta - \frac{L_v}{c_p}\left(\frac{p_0}{p}\right)^{\frac{R_d}{c_p}} q_l\right) \tag{5.37}$$

$$\Delta_I q_t = q_v^+ - (q_v + q_l) \tag{5.38}$$

where $p_0 = 1000$ hPa. However, the denominator in Eq. (5.27) is dominated by its first term.

We are now finally able to obtain values for w_e, $\theta^+ - \theta$ and $q_v^+ - q_v$, which allows the calculation of SH_{entr} and LH_{entr} and thereby the loss of LWP by entrainment.

Figure 5.9b-f explores the behaviour of this entrainment parametrisation for a fog temperature of 6 °C, LWP 50 g m^{-2} and thickness 200 m. The denominator in Eq. (5.27) increases strongly with $\theta^+ - \theta$ and slightly with RH^+ (Fig. 5.9b). For small values of $\theta^+ - \theta$, it becomes negative, which is unphysical. A lower limit of 1 K has therefore been imposed, to prevent w_e from growing to infinity or becoming negative. Figure 5.9c shows the resulting entrainment velocity per 1 K m h^{-1} of Θ_{NE}, which is actually the inverse of (b) since $\eta = 0.2$.

Figure 5.9d shows the loss of LWP from a unit of entrainment velocity. We see that this loss depends mainly on the relative humidity of the entrained air (RH^+), as we would expect. However, there is also a dependency on the stability $\theta^+ - \theta$. For weak $\theta^+ - \theta$ or low RH^+, the loss increases with $\theta^+ - \theta$, due to the warmer entrained air having a larger vapour pressure deficit for the same RH^+. However, for strong $\theta^+ - \theta$ or high RH^+, the loss decreases with $\theta^+ - \theta$ and can even become negative. This is due to the non-linearity of the Clausius-Clapeyron equation: when two air parcels of different temperature mix, the resulting air will have a higher relative humidity than the mass-weighted average of the relative humidities of the parcels. Finally, Fig. 5.9e shows the LWP loss due to entrainment per unit of Θ_{NE}. The magnitudes of the quantities shown in Fig. 5.9 will change slightly if the fog temperature, fog thickness or fog LWP changes, but the main patterns are the same (not shown). Finally, note that w_e is set to zero if $\Theta_{NE} < 0$ (a stabilising layer).

As an example, let's say the fog is subjected to a surface sensible heat flux of 50 W m^{-2}, a surface latent heat flux of 20 W m^{-2}, a cloud-top radiative cooling of 60 W m^{-2} and a cloud base radiative heating of 10 W m^{-2}. We then get:

$$\Theta_{NE} = 0.85 \cdot (50 + 60 + 10) \text{ K m h}^{-1} + 0.69 \cdot 20 \text{ K m h}^{-1} = 116 \text{ K m h}^{-1}$$

where the coefficients at 6 °C has been read off from Fig. 5.9a. Having obtained the value for Θ_{NE}, we can read off the entrainment velocity in Fig. 5.9c and the LWP loss in Fig. 5.9ef. If for example $RH^+ = 90$ % and $\theta^+ - \theta = 5$ K, then $w_e \approx 0.1 \cdot 116$ m h^{-1} = 12 m h^{-1} and the LWP loss from entrainment $\approx 0.025 \cdot 116$ g m^{-2} h^{-1} = 2.9 g m^{-2} h^{-1}. If we instead have $RH^+ = 75$ % and $\theta^+ - \theta$ = 2 K, we get $w_e \approx 0.3 \cdot 116$ m h^{-1} = 35 m h^{-1} and the LWP loss becomes $\approx 0.30 \cdot 116$ g m^{-2} h^{-1} = 35 g m^{-2} h^{-1}.

5.3.4 Subsidence

The large-scale vertical velocity at 975 hPa (w_{975}) is taken from ERA5, using a 1° x 1° horizontal average, and then interpolated in time to each time block. As in W18, w_{ls} is assumed to vary linearly with height from zero at the surface, so that we can calculate its vertical gradient:

$$\frac{dw_{ls}}{dz} = \frac{w_{975}}{z_{975}} \tag{5.39}$$

where z_{975} is the altitude of the 975 hPa level above the SIRTA surface, which is interpolated from ERA5 the same way as w_{975}. Having this vertical gradient, the divergence term (last term in Eq. 5.12) can be calculated using the current LWP of the fog. The heat flux due to subsidence can be found from the adiabatic lapse rate integrated in the vertical, which gives:

$$SH_{subs} = -\frac{1}{2}\rho_a g \frac{dw_{ls}}{dz} h^2, \tag{5.40}$$

while the CTH tendency due to subsidence is:

$$w_{ls}(h) = \frac{dw_{ls}}{dz} h. \tag{5.41}$$

We note that the impact of the subsidence increases importantly with fog thickness (h), in both the heating and cloud-top tendency, and also in the divergence term (due to the increase of LWP with thickness). Thus, subsidence can be expected to be more important for thicker than thinner fog layers.

Given the parametrisation for the critical LWP introduced in section 5.2 and the effect of subsidence on LWP and CTH shown here, we can now return to the issue discussed in section 4.2 on the impact of subsidence (or conversely upward large-scale motion) on the fog dissipation. The investigations carried out with the LES model indicated that subsidence favours dissipation, while large-scale upward motion favours persistence. The effect was rather subtle, though, since the subsidence both affects CTH and LWP. Using the parametrisations, we can now compare the impacts of a given large-scale velocity on LWP and on LWP^{crit} (through CTH).

The effect of increased CTH on LWP^{crit} is found from differentiating the expression for LWP^{mod} (Eq. 5.9) with respect to z_t, setting $z_b = 0$ and assuming $z_t > 125$ m so that $z_1 = 75$ m and $z_2 = z_t - 50$ m. The LWP^{crit} then has an explicit dependency on z_t, but it also has an implicit dependency through the factor κ, which changes due to the layer-averaged pressure and temperature, which both change slightly with z_t (if surface values are kept constant). However, it turns out that the implicit dependency through κ is at least 1 order of magnitude smaller than the explicit dependency, and it is therefore

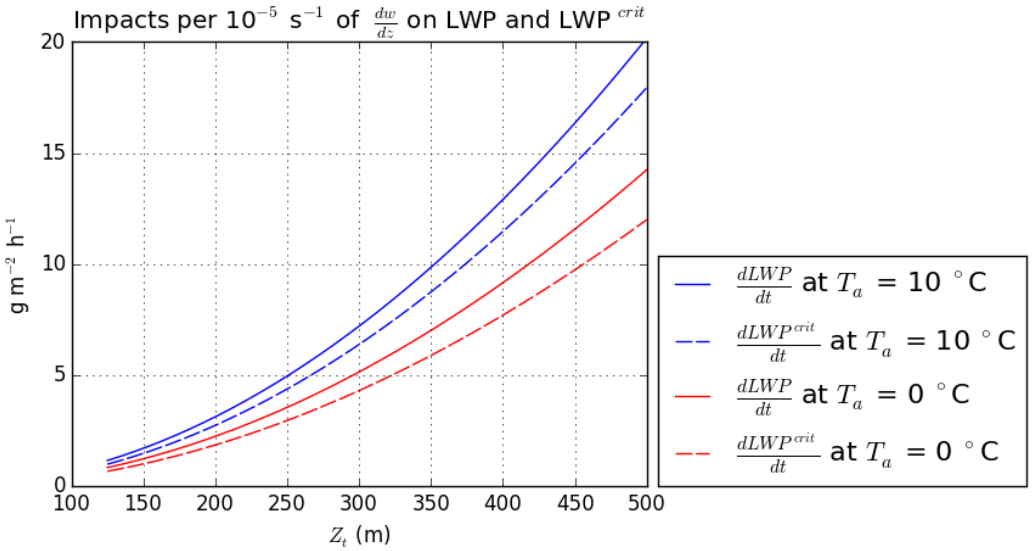

Figure 5.11: The impact of large-scale vertical velocity on fog LWP (solid) and on the LWP^{crit} (through cloud-top development, dashed), at two different temperatures, when LWP=LWP^{crit}, as function of fog thickness. The impacts are proportional to $\frac{dw_{ls}}{dz}$; the value given here is for $\frac{dw_{ls}}{dz} = +1 \cdot 10^{-5}$ s^{-1}.

neglected. The derivative is then:

$$\frac{dLWP^{crit}}{dz_t} \approx \kappa(1-\beta_1)(z_t - 25\text{m}) \tag{5.42}$$

This expression can then be multiplied by the vertical velocity at cloud top (Eq. 5.41) to give the tendency of LWP^{crit} due to subsidence:

$$(\frac{dLWP^{crit}}{dt})_{subs} = \kappa(1-\beta_1)(h - 25\text{m})h\frac{dw_{ls}}{dz}, \tag{5.43}$$

which we can compare with the tendency of LWP due to subsidence (which we get from combining Eqs. (5.12),(5.40)):

$$(\frac{dLWP}{dt})_{subs} = \Big[\frac{s}{s+\gamma}\frac{1}{L_v}\frac{1}{2}\rho_a g h^2 + LWP\Big]\frac{dw_{ls}}{dz} \tag{5.44}$$

Figure 5.11 shows these two tendencies as function of CTH for two different temperatures, assuming LWP = LWP^{crit}. We see that the two tendencies are of similar magnitude, but that the effect on LWP is slightly larger than the effect on LWP^{crit}. Note that the second term in Eq. (5.44) contributes about 35–45 % when $LWP = LWP^{crit}$, so that the LWP must be significantly smaller than LWP^{crit} to get $|(\frac{dLWP}{dt})_{subs}| < |(\frac{dLWP^{crit}}{dt})_{subs}|$. So the conclusion is in agreement with what was found in section 4.2: subsidence in itself weakly favours fog dissipation, while upward motion favours fog persistence, at least before feedbacks through other processes are considered.

5.3.5 Deposition

The loss term by deposition of fog droplets is probably the most difficult of all the processes to measure. This is due to the weak water fluxes, typically below 0.1 mm h^{-1}, too weak for most rain measuring

techniques to detect them, and to the very heterogeneous nature of the deposition (Katata, 2014). The deposition is also the combined effect of several different interactions between the fog and the surface below. Some of the water is intercepted by the canopy of tall vegetation, while another part deposits on the ground or low vegetation such as grass, and different plants may collect water at very different efficiencies (Tav et al., 2018). The downward motion of the droplets is in part due to their terminal fall speed, but the fall velocity is so much smaller than for rain droplet that turbulent vertical transport is also important. The wind has a catalysing effect on deposition since it enhances the contact between droplets and the canopy, leading to impaction as the droplets are drawn through fine-masked foliage with the air flow (Katata, 2014). Depending on the wind direction and structure of the canopy, the deposition can be very much higher in certain areas than others, for example at the edge between a forest and an open area. Due to all these subtle processes and their variability, fog deposition is hard to measure in order to validate parametrisations, and the uncertainties can be as large as 2 orders of magnitude (Katata, 2014).

The sedimentation contribution is the most straightforward to quantify. The terminal fall speed of a droplet smaller than 30 μm in radius can be predicted by Stokes' law (Rogers and Yau, 1989):

$$V_t = k_{St} r^2 \tag{5.45}$$

where r is the droplet radius and $k_{St} = 1.2 \cdot 10^8$ m^{-1} s^{-1}. If the number concentration of droplets of each size is known, the sedimentation flux F_{sed} can readily be calculated:

$$\begin{aligned} F_{sed} &= \int_0^\infty n(r) \cdot \frac{4}{3}\pi\rho_l r^3 \cdot V_t(r) dr \\ &= \frac{4}{3}\pi\rho_l k_{St} \int_0^\infty n(r) r^5 dr \end{aligned} \tag{5.46}$$

Thus, we may calculate the sedimentation flux using the measurements by the FM-120, which indicate a power law between LWC and F_{sed} (Figure 5.12a), i.e.

$$F_{sed} = aLWC^b \tag{5.47}$$

Linear log-log regression indicates $a = 99.6$ (for LWC in g m^{-3} and F_{sed} in g m^{-2} h^{-1}) and $b = 1.209$. In the absence of FM-120 data, this empirical relationship can be used to approximate F_{sed} from the LWC, which can be estimated approximately from the measurement of visibility at 4 m using Eq. (2.4) (see Fig. 2.11).

In the LES simulations, a lognormal DSD was applied (W18). The sedimentation rate for such a distribution is:

$$F_{sed} = k_{St} \cdot \left(\frac{4}{3}\pi\rho_l\right)^{-2/3} \cdot LWC^{5/3} \cdot e^{5\ln^2\sigma_g} \tag{5.48}$$

For constant N_c and σ_g, this gives a steeper increase of F_{sed} with LWC than found by FM-120 ($b = 5/3$ instead of 1.22). This may be partly due to the N_c increasing with LWC in average (not shown). We also see that the baselines values of $N_c = 200$ cm^{-3} and $\sigma_g = 1.2$ used in the LES give a much too small sedimentation rate (Fig. 5.12a).

To understand better the discrepancies, individual fog events were studied, comparing the DSD observed by FM-120 to the lognormal DSD, given the same N_c and LWC as observed by FM-120. One example is shown in Fig. 5.13. Firstly, $N_c < 200$ cm^{-3} near the surface most of the time (Fig. 2.10b,

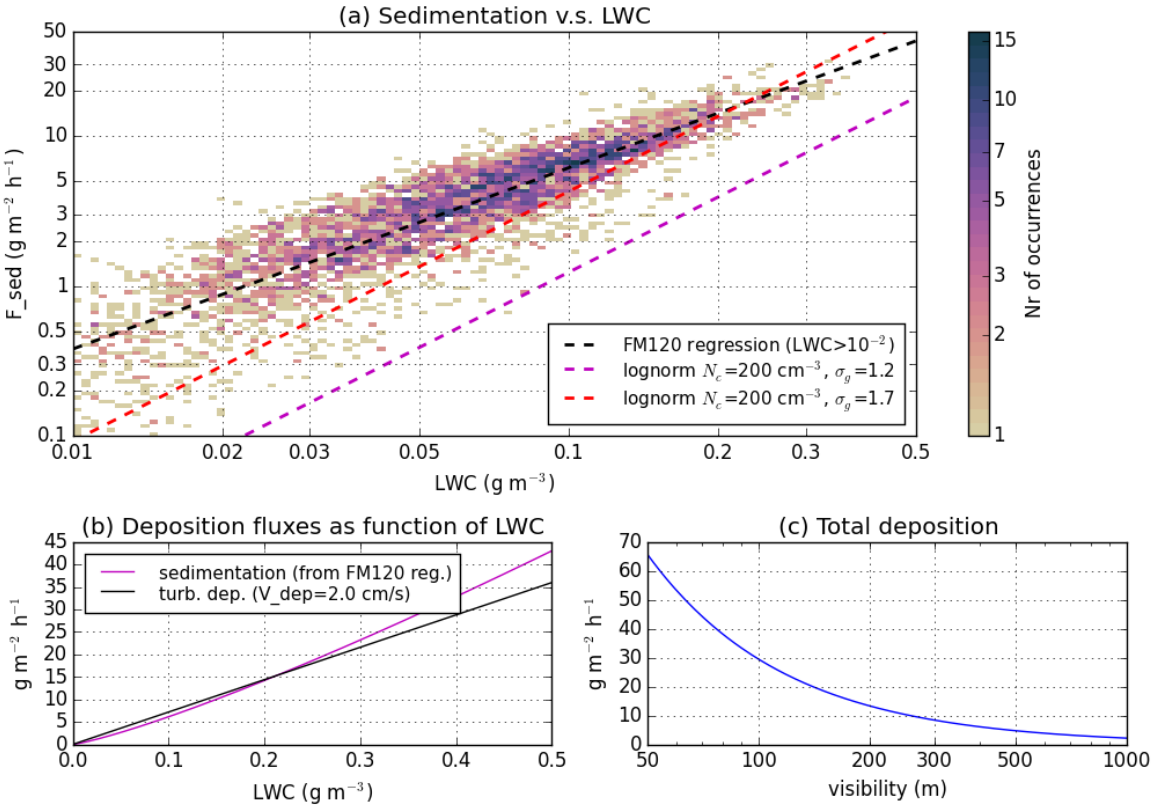

Figure 5.12: (a) Calculated sedimentation rate F_{sed} (using Eq. (5.46)) vs LWC from 5-min averages of FM-120 measurements (see section 2.4.1) during 64 fog events (dots) and regression line for these data (dashed line). Blocks of LWC < 0.01 g m^{-2} occur, but they are not included in the regression. Also shown are the relationship between LWC and F_{sed} when assuming a lognormal DSD with a droplet concentration of 200 cm^{-3} for two different geometric standard deviations. (b) Fog water deposition as function of LWC in our conceptual model: Contribution from deposition (black), and from sedimentation (blue). (c) The total deposition in the conceptual model, as function of visibility.

Fig. 5.13a). Secondly, except for very thin fog layers, we systematically find, as in the example in Fig. 5.13, a DSD that is much wider than in the lognormal DSD with $\sigma_g = 1.2$. The wider DSD has more droplets with diameters 20–30 μm, which dominate the sedimentation (Fig. 5.13h), even though they are few in number (Fig. 5.13b). A lognormal DSD with $\sigma_g = 1.7$ represents much better the observed decrease of droplet concentration with size (Fig. 5.13b). However, the lognormal DSD still has limited skill in reproducing the observed DSD because the latter usually has a bimodal shape in our measurements, which has also been found in previous studies for mature phase of radiation fog (e.g. Price, 2011; Degefie et al., 2015). The first mode, at 10 μm or less, contains most of the droplets, and the second mode, centred between 20–30 μm, dominates the sedimentation, while both modes may give significant contributions to the extinction and LWC (which of them dominates the extinction and LWC varies from case to case). Although the second mode is not always as pronounced as in the shown example, there is nearly always a levelling-off in the curve in Fig. 5.13b around 20 μm, giving bimodal shapes in the extinction and LWC distributions (Fig. 5.13df). So even though increasing σ_g from 1.2 to 1.7 significantly improves the representation of sedimentation, it is not the correct sizes of droplets that produce the sedimentation.

To estimate the turbulent contribution to deposition flux (impaction), a deposition velocity of

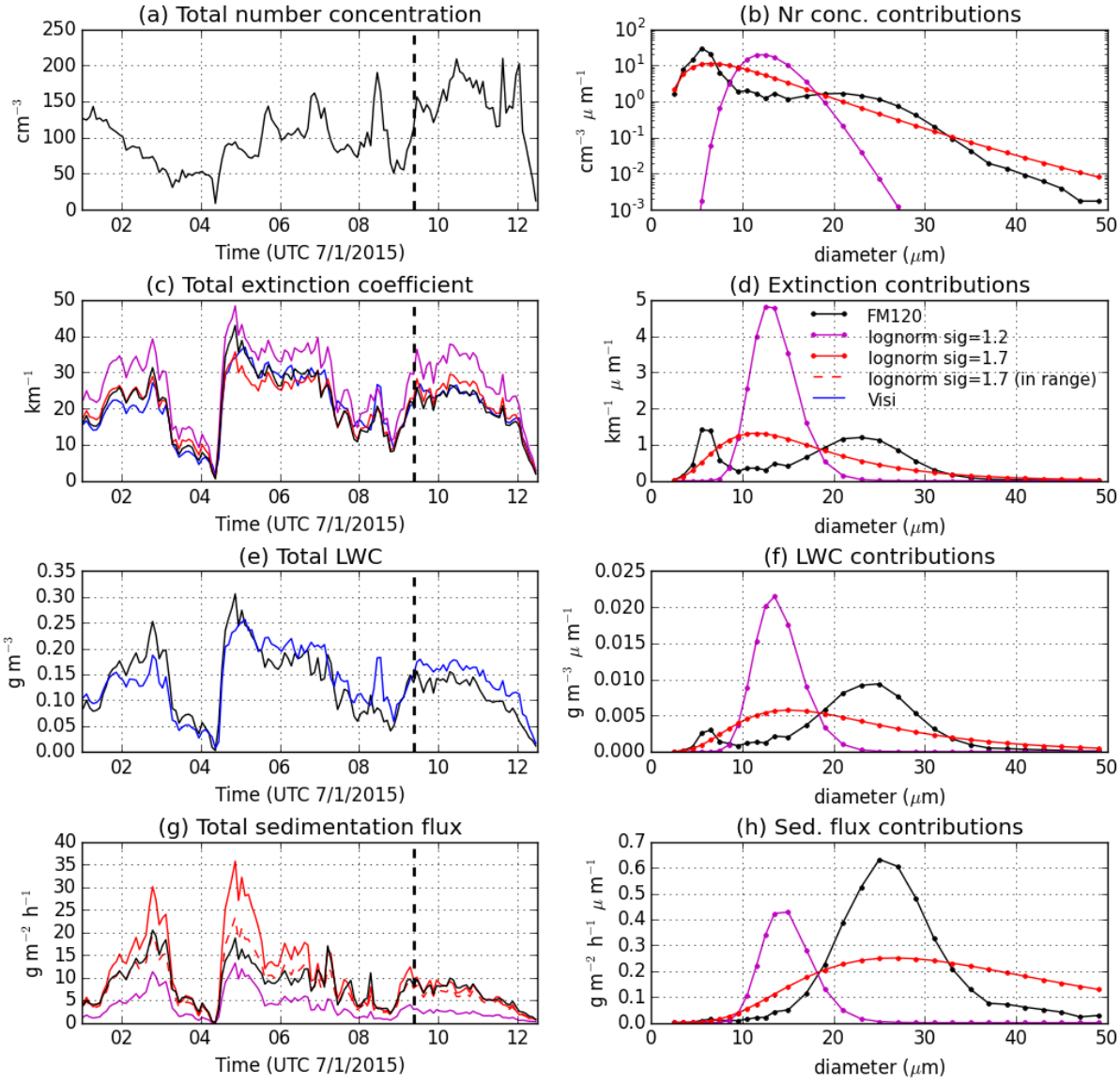

Figure 5.13: Observations by FM-120 (see section 2.4.1) during the fog event on 7/1/2015 (black lines). In the left-hand panels, time series, in the right-hand panels, contributions from different droplet sizes at the time marked by vertical dashed line in the left panels: (a-b) droplet number concentration (N_c), (c-d) extinction coefficient (assuming extinction efficiency of 2), (e-f) LWC and (g-h) sedimentation flux (Stokes' law). The blue line shows the extinction coefficient from visibility in (c), and in (e) the LWC calculated from visibility using Eq. (2.4). The red and purple lines result from using a lognormal distribution with the same N_c and LWC as FM-120, using two different values for the geometric standard deviation σ_g. The dashed red line in (g) is the calculated sedimentation flux from the lognormal DSD with σ_g=1.7 when only droplets smaller than 50 μm are included. All data are based on 5-min averages.

$V_d = 2$ cm s^{-1} is applied:

$$F_{dep,turb} = V_d \cdot LWC \tag{5.49}$$

Katata (2014) presents a range of values for V_d found in field experiments using various measurement techniques. For grassland, the range is 2–8 cm s^{-1}. We chose to apply the lower limit of 2 cm s^{-1}, which gives a turbulent deposition contribution close to the sedimentation contribution (Fig. 5.12b). Sedimentation has been found to dominate over impaction for wind speed below 2 m s^{-1} typical for radiation fog, while impaction dominates for higher wind speed (Katata, 2014). Given the distribution of wind speed in the fog (Fig. 2.4d), which shows mostly values of 0.5–3 m s^{-1}, it seems plausible that the two contributions could be similar in magnitude. V_d may also be parametrised as function of the wind speed (Katata, 2014); however, this is not done in our study.

To sum up, the term F_{dep} in the conceptual model (Eq. 5.12) is calculated by first approximating screen-level LWC from visibility using Eq. (2.4) and then calculating and adding the contributions from sedimentation (Eq. (5.46) with coefficients from FM-120 regression) and impaction (Eq. (5.49) with $V_d = 2$ cm s^{-1}). This results in a deposition flux that depends on visibility as shown in Fig. 5.12c. The predicted deposition varies in the range 5–30 g m^{-2} h^{-1} in the common range of visibility 100–500 m (Fig. 2.4a).

5.4 Statistics of all the morning fog events

5.4.1 Distribution of values in the conceptual model

Figure 5.14 shows the range of values for the impact of each process on LWP and CTH, as predicted by the conceptual model presented in section 5.3. All the terms exhibit important variability. For some of the terms, the variability is strongly related to the solar zenith angle, which is given on the x-axis. This is especially pronounced for the SW absorption (Fig. 5.14b) which is an important loss term in cases where fog persists to important solar zenith angles. The loss from surface fluxes (Fig. 5.14c) also increases with the solar angle, and this loss term is about twice as strong than the SW absorption term in average. For a given value of μ_0, both these terms have important variability, which can be related to the fog thickness (a thicker fog increases in-fog absorption and reduces the surface absorption, W18) and the temperature (through s). Note that in mid-winter μ_0 reaches only about 0.3 at midday, and the large clustering of data around this value is explained by the many persistent fog events in mid-winter. Seeing how much more LWP is lost from this term in the fog events which reach higher solar angles, it is a likely explanation for why so few fog events can last all day apart from mid-winter.

The LW cooling term (Fig. 5.14a) is unrelated to solar zenith angle and is usually in the range 30–60 g m^{-2} h^{-1} (68 % of the data), sometimes >70 g m^{-2} h^{-1} and occasionally zero or less. These magnitudes are very similar to what was found in W17. The low values are cases where clouds appear above or where the fog is so thin that it is semi-transparent to the LW radiation. The low values are likely occur more often that what is calculated, due to the clouds above which are not detected. Thus, the variability in the LW term is very significant and likely has important impact on the fog LWP budget.

The deposition (Fig. 5.14d) has an important spread and can be stronger than 20 g m^{-2} h^{-1} although it more commonly is at 15 g m^{-2} h^{-1} or less (79 % of the data). This term shows a tendency to be stronger at lower solar angles. This is due to the higher visibility in day, which is to be expected as

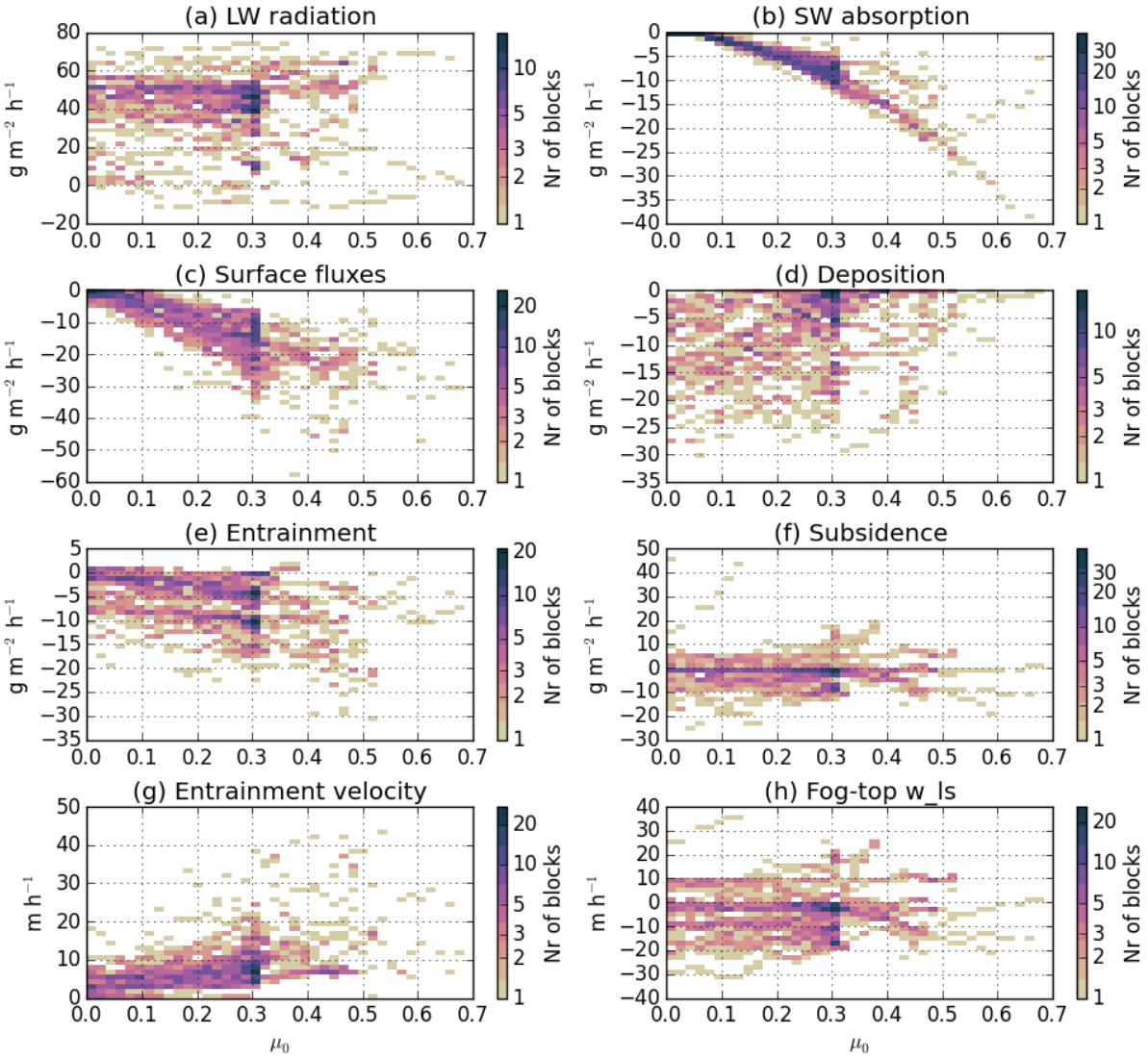

Figure 5.14: Calculated impact of each process on LWP (a-f) and the impact of entrainment and subsidence on CTH (g-h), for all daytime 10-min blocks during the 45 days with morning fog when CBH < 50 m, plotted against the cosine of the solar zenith angle (μ_0). The colour indicates how often the quantity takes each value (on y-axis) for each value of μ_0. Nearly all the data are inside the plotted range: only 1 block is out of range in (e) and (g), and 7 in (f) and (h), and none in (a–d).

most of the fog events dissipate during the day associated with an increase in visibility. The statistics also include the periods with fog base between 0 and 50 m, when visibility is very high and therefore deposition very weak.

The predicted entrainment loss of LWP (Fig. 5.14e) is mainly in the range 0–20 g m^{-2} h^{-1} (95 % of the data). It has a weak dependency on solar zenith angle, with stronger negative values when the sun is higher. This can be explained by the extra buoyancy produced by the surface fluxes. The subsidence term (Fig. 5.14f) is usually close to zero, and it is mostly within $\pm$10 g m^{-2} h^{-1} (88 % of the data).

Fig. 5.14g-h shows the impact that entrainment and subsidence has on the CTH according to the parametrisation. The entrainment velocity is most of the time less than 10 m h^{-1} (72 % of the data) and occasionally reaches 20 m h^{-1} in the day (Fig. 5.14g). This is similar to the magnitude predicted for the subsidence velocity (Fig. 5.14h), and it is a weaker entrainment rate than we would expect

from the results of the LES modelling in chapter 4, which we will come back to in section 5.6.3.

5.4.2 Diurnal cycle in the conceptual model

Figure 5.15 shows the diurnal cycle of the LWP budget and the differences between the four scenarios defined in section 5.1 (which basically distinguish the time of dissipation at 50 m). Figure 5.16 shows similarly the diurnal cycle of the terms impacting the CTH. The diurnal cycle of the terms follows the same features as we already saw by plotting the terms against the solar zenith angle (Fig. 5.14), with pronounced maxima in the SW absorption and surface fluxes loss around midday(Fig. 5.15bc), and also an entrainment rate and entrainment LWP loss which increase during the morning (Fig. 5.15e, Fig. 5.16a). The consecutively earlier and stronger increase in the SW absorption and surface flux terms in scenario 1 than 2 than 3 than 4 (Fig. 5.15bc) is due to the fog events of scenario 1 occurring further from mid-winter than those in scenario 2, and so on (Fig. 5.1b). In particular, scenario 1 loses much more LWP in the morning than the other scenarios due to these processes, leading to its earlier negative total LWP budget (Fig. 5.15g), which can explain why these fog events dissipate early, although the observed decrease in LWP is not as strong (Fig. 5.15h). Scenario 1 also has the strongest predicted entrainment velocity in the morning (Fig. 5.16a), which may help these fog events to lift.

Scenarios 2–4 are rather close when it comes to the total calculated LWP budget in the morning (Fig. 5.15g), which means that the difference in the SW absorption and surface flux terms are compensated by other terms. The LW cooling produces in average less LWP in scenario 4 than in scenarios 2–3 (Fig. 5.15a), which can be due to the higher temperature in the transition seasons compared to winter solstice (the term $\frac{s}{s+\gamma}$ in Eq. 5.12 increases with temperature, see Fig. 5.8c). The deposition loss is also calculated higher in scenarios 3–4 than in scenario 2 (Fig. 5.15d).

The subsidence term is significantly different in the events of scenario 4 from the others, and especially in the afternoon the vertical velocity is consistently negative (Fig. 5.16b), quite different from scenario 3, for which positive large-scale velocity often occurs. However, as we found in 4.2 and section 5.3.4, the subsidence in itself is not favourable for fog persistence. The fact that we find subsidence systematically more often for persistent fog than for fog which dissipates is therefore likely due to indirect effects: subsidence is related to anticyclonic situations, when other conditions favourable for fog occur. We see for example that the LW cooling term in scenario 4 increases in the afternoon (Fig. 5.15a) as subsidence increases (Fig. 5.16b).

If we compare the medians of the total calculated LWP budget (Fig. 5.15g) and the observed tendency in LWP (Fig. 5.15h), we can note that the diurnal cycle is much more pronounced in the model than in observations. In the night, the calculated production of LWP is typically around 20 g m^{-2} h^{-1}, then becoming negative after about 9 UTC with values frequently reaching -10 g m^{-2} h^{-1} in the late morning for scenarios 2 and 4, and below -20 g m^{-2} h^{-1} for scenario 3. In the observations, the night production is smaller, usually 10 g m^{-2} h^{-1} or less, and the loss around midday is less pronounced for scenarios 3 and 4. In the evening, we do not observe such a rapid increase of the LWP of the events of scenario 4 as predicted by the conceptual model, either. NB: In Figs. 5.15, 5.16, the number of fog events included decreases with time for scenarios 1–3, while it is fairly constant in scenario 4 (Fig. 5.15i). It is therefore easier to analyse the diurnal cycle for scenario 4 than for the others.

A too strong diurnal cycle in the model could be due to an overestimation of the loss from the terms related to solar radiation (SW absorption and surface fluxes). However, the overestimation of

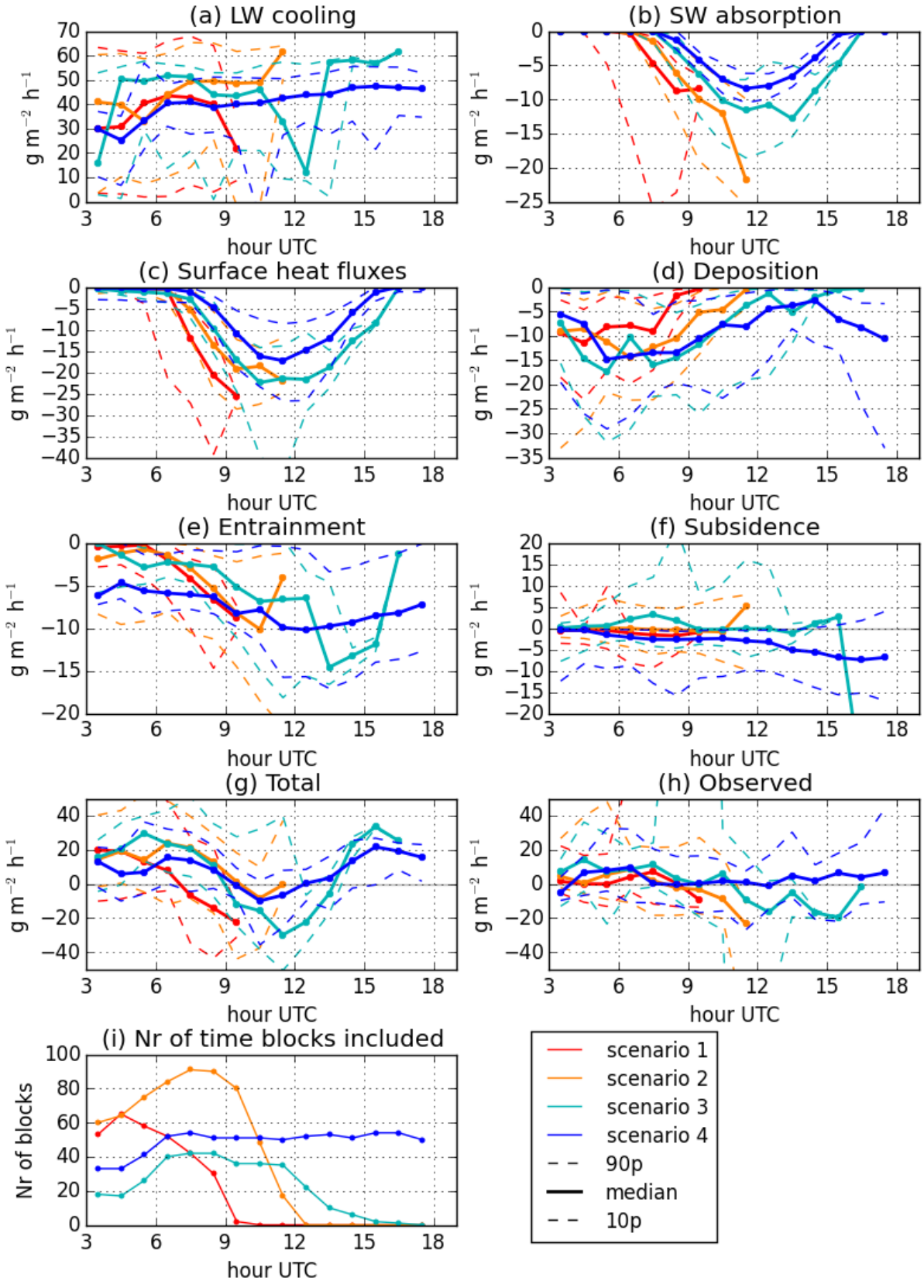

Figure 5.15: (a-f) For each 1-h period of the day, the values taken by each of the terms in the LWP budget in the fog events of each of the 4 scenarios (defined in section 5.1). The lines indicate the median (solid) and 10 % and 90 % percentiles (dashed) among all time blocks with CBH < 50 m in the fog events that occur in each hour. The sum of all the six terms is shown in (g), while the observed tendency in LWP (based on 90-min running average of MWR retrieval) is shown in (h). The number of blocks included for each hour is indicated in (i) (i.e. the number of events included is roughly 1/6 of this).

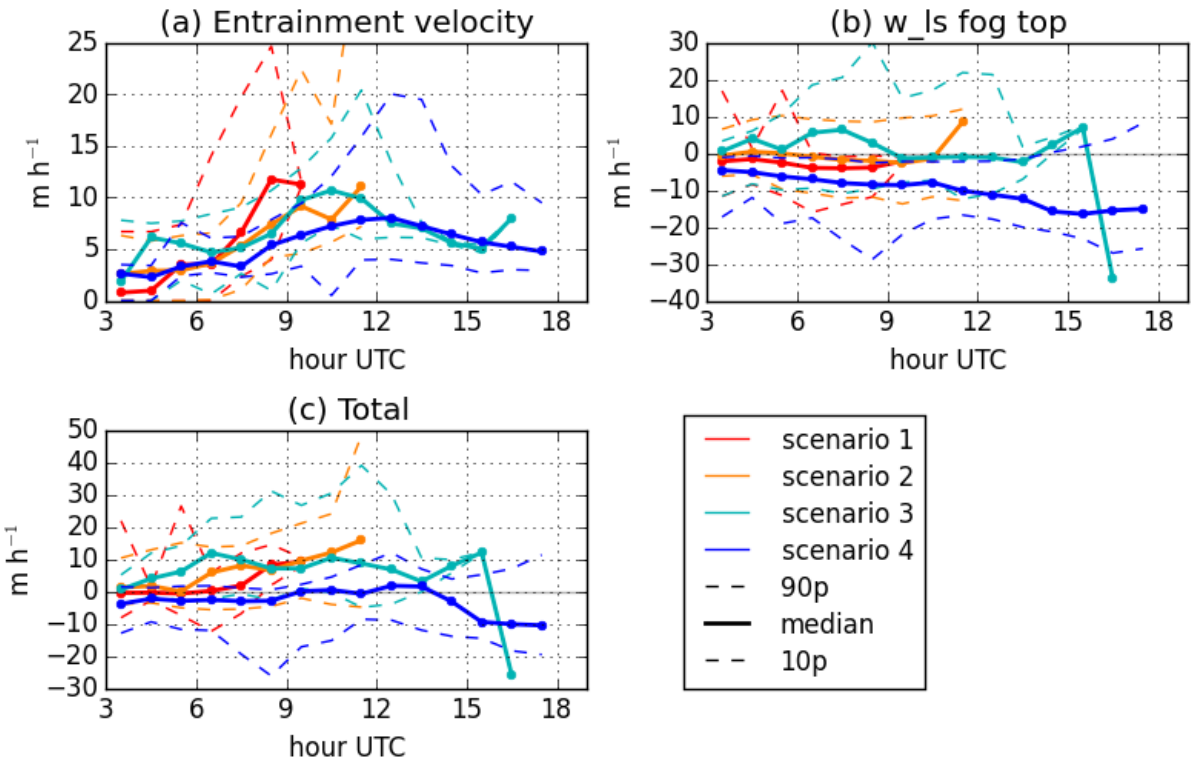

Figure 5.16: Same as Fig. 5.15, but for the impacts on the CTH of entrainment (a) and subsidence (b), and their sum (c). The sample in each scenario at each hour is the same as in Fig. 5.15.

production in the night must have another explanation. One possibility is that the turbulent deposition during night is underestimated. The deposition could act as a negative feedback, balancing the LWP produced by LW cooling and preventing the LWP from becoming too large. The visibility, which we use to estimate deposition rate, may not be sufficient to capture this increased deposition. If important deposition occurs in the night, which feeds the surface with water that can evaporate again in the day, it could also allow a lower Bowen ratio and therefore less loss by surface heat fluxes in the day (corresponding to a $c_{dry} < 0.5$ in our surface scheme). When the surface is warm in the day, it could also be that the droplets which normally would settle on the ground by deposition instead are evaporated as they approach the surface or vegetation. If so, they contribute to cool the air and should therefore be part of the "surface heat fluxes" term and not the deposition term, thereby reducing the overall LWP loss in the day.

5.4.3 Fog thickness and development

Figure 5.17a shows the time of dissipation vs the fog thickness at sunrise. All the 5 fog events which are very thin (<50 m) around sunrise dissipate within 1 h. This can be explained by the heating from the surface evaporating rapidly the small amounts of LWP in the fog. Most of the fog events thinner than 100 m dissipate rather early, too (within 2.5 h). However, there is one exception: the fog event on 12/2/2015, which persists for several hours in spite of being thin with only 10–20 g m^{-2}; this event has a large negative calculated LWP budget with loss from surface fluxes (not shown), so we cannot explain why this fog does not dissipate sooner from the mechanisms captured by our conceptual model. For fog thicker than 100 m at sunrise, no clear relationship between thickness and dissipation time can be seen. For these fog events, the dissipation time must be explained by other factors, for example

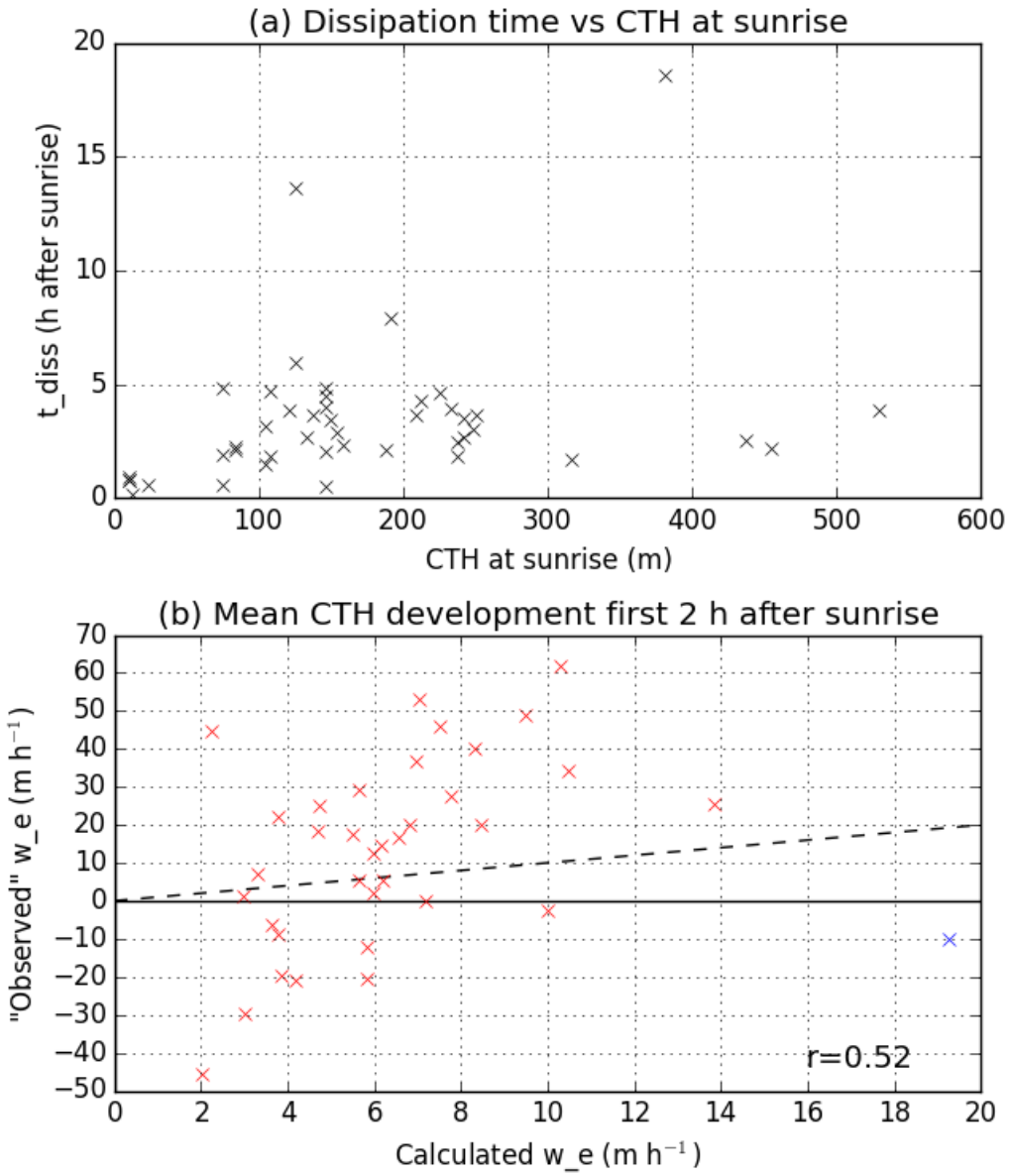

Figure 5.17: (a) Time of dissipation relative to sunrise, plotted vs the fog thickness at sunrise (30-min average). (b) For each event where the cloud remains at least 2h20 after sunrise: On the x-axis: the mean calculated entrainment velocity (see section 5.3.3) in the first 2 h after sunrise. On the y-axis: The observed CTH tendency during the first 2 h after sunrise, minus the mean large-scale vertical velocity at fog top (from ERA5, see section 5.3.4) in this period. The observed CTH tendency is calculated by subtracting the 30-min mean CTH at sunrise from the 30-min mean CTH 2h after sunrise. The correlation r is given, excluding the blue outlier (when the outlier is included, the correlation is 0.30).

the season or the layer above fog top.

A main result from chapter 4 is the importance of a weak stratification for the vertical development of fog top, which in turn triggers dissipation. We already saw in Fig. 5.16a that the entrainment velocity is in average smaller for the persistent fog events than for those dissipating early. To investigate if the entrainment parametrisation can to some extent explain the observed vertical development of fog top, we have plotted the predicted entrainment velocity against the observed fog-top development (after subtracting the effect of subsidence) in the first 2 hours after sunrise (Fig. 5.17b). If the upward motion of the cloud top was only affected by entrainment and subsidence, and the entrainment

parametrisation was very accurate, we would expect the points to lie along the 1-1 line. However, there are many other factors playing a role: the observed tendency of CTH can be dominated by variability due to advection, so that a tendency due to entrainment is "hidden", and both the subsidence and entrainment terms have important uncertainties (see section 5.6). Nevertheless, a correlation between entrainment velocity and cloud-top development can be seen, although it is weak. The outlier, which is 26 Oct 2014, actually develops rapidly upwards shortly after 2 h after sunrise (Fig. 5.5(ah)), showing that the correlation in Fig. 5.17b can be sensitive to the time period chosen. Our interpretation of Fig. 5.17b is that the stratification (which is the main source of variability in the calculated w_e) has an impact on the CTH tendency, but that advection, which occurs on shorter timescales, makes it non-trivial to observe the effect of stratification.

Considering the values in Fig. 5.17b, the observed development has much larger magnitudes than the calculated entrainment velocity. This would indicate that the entrainment velocity could systematically be underestimated, as was already noted in section 5.4, which we will come back to in section 5.6.3. Of course, the negative values in the observed development cannot be explained by entrainment velocity, which is always positive. The negative values might be caused by advection, or by evaporation of the cloud top leading to downward displacement of the CTH.

5.5 Case studies

In this section, we will take a closer look at some case studies. The fog events were selected to represent contrasted cases both near mid-winter and in the autumn/spring season.

5.5.1 Two fog events in November and February

We first consider two morning fog events which both occur closer to the equinox than to winter solstice, but which develop very differently. Figure 5.18 presents the fog event on 2 November 2015. This is the same event as that modelled with the LES in W18. It forms at 5 UTC, 2 h before sunrise, and dissipates first in the afternoon, around 14:30 UTC. The cloud top height increases gradually until 9 UTC, after which it stays rather constant or even decreases a little (Fig. 5.18a). The LWP varies in a similar pattern to the cloud top, but it decreases gradually after 09 UTC (Fig. 5.18b). This decrease in LWP without a similar decrease in the cloud top makes the cloud base predicted by the CB2011 model increase from around -100 m to above -10 m at 13 UTC (Fig. 5.18a). As the fog lifts, the observed CBH and the one calculated by the CB2011 model are very similar. This is therefore one of the cases where the time of dissipation can be very well explained by the CB2011 model: the fog base lifts from the surface when LWP reaches below a critical value relative to the CTH.

The relatively modest development of the fog top can be explained by the strong stratification above the fog. Fig. 5.18h shows a stability of 9–10 K, which is in the upper end of the observed scale (Fig. 5.10a). Fig. 5.18g shows that the calculated entrainment velocity is only around 2–6 m h^{-1} in the morning, reaching 9 m h^{-1} at most around midday (green line), which is relatively low compared to the statistics of all the events (Fig. 5.14g). This panel also shows the total calculated velocity of the cloud top (entrainment + subsidence) (black) and the observed tendency in the CTH (pink). The observed tendency is a lot more variable than the calculated one, even though is has undergone a 90-min running mean. The variability on scales of 1 h can likely be attributed to advection of horizontal inhomogeneities. In the calculated cloud-top development, the subsidence is the dominating term in

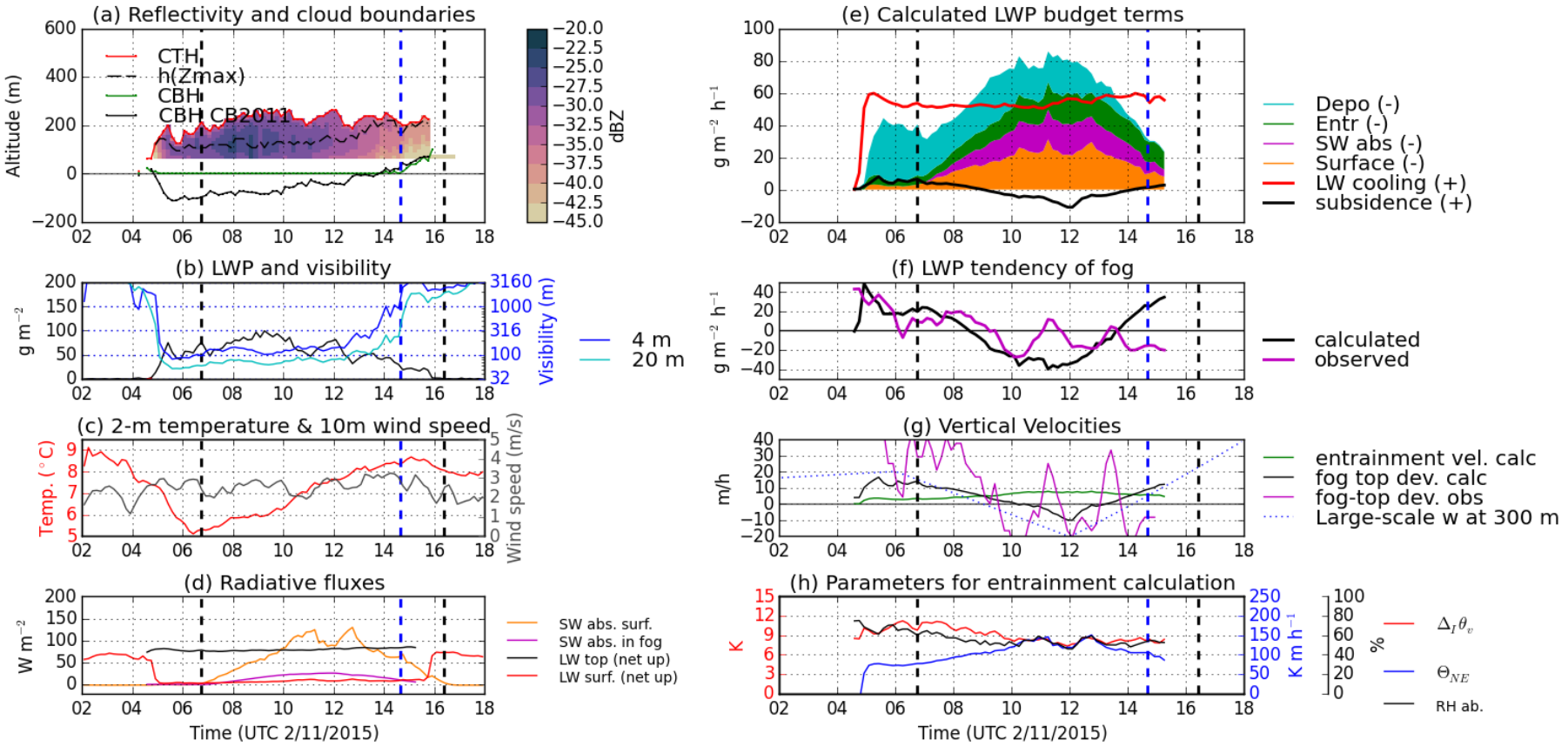

Figure 5.18: Time series of observed and calculated quantities for the fog event on 2 November 2015: (a) Reflectivity profile from the cloud radar BASTA, indicating detected CTH (red), observed CBH (green) and the CBH calculated using the CB2011 model (section 5.2) (black). Also indicated is the altitude of highest reflectivity (black, dashed). (b) Observed visibility (blue), and LWP retrieved from MWR (black) or by visibility and radar reflectivity (red, shown only when MWR LWP < 10 g m^{-2}). (c) Observed temperature and wind speed. (d) Observed net SW flux absorbed at the surface (orange), the calculated SW flux absorbed in the fog (pink), observed net upward LW flux at the surface (red), and calculated net upward LW flux at fog top (black). (e) Fog LWP budget terms calculated as described in sections 5.3, 3.2: subsidence and LW cooling terms are shown separately and are positive when they produce LWP, while the other four terms are stacked on top of each other so that the top of the graphic indicates the loss of LWP of all four combined. (f) Comparison of the total tendency in LWP from the six calculated terms in (e) (black) with the observed change in MWR LWP (pink, calculated from a 90-min running mean of LWP). (g) Vertical velocities at cloud top: calculated entrainment velocity (section 5.3.3, green) and large-scale vertical velocity at 300 m (blue, dotted), the total calculated vertical development of cloud top (entrainment + large scale velocity, black), and the observed tendency of the cloud top (pink, calculated from a 90-min running mean of CTH). (h) Three of the main parameters used in the calculation of the entrainment (section 5.3.3). In all panels, the vertical dashed lines indicate sunrise and sunset (black) and time of dissipation (blue).

this case, creating a positive tendency in the morning and a negative tendency at midday. This shift from positive to negative tendency is in agreement with the observations, although the observed values are larger, at least in the morning.

Figure 5.18e shows the terms in the calculated LWP budget. In the early morning, the increase in LWP is driven by radiative cooling, while loss of LWP is dominated by deposition, with a small contribution from entrainment. Once the sun rises, loss by surface heat fluxes and absorption of SW radiation inside the fog become important, while deposition loss is reduced (reflecting an increase in the visibility, which is used to calculate deposition (section 5.3.5)). The loss by entrainment increases as well, which we see is mainly due to an increase in the calculated entrainment velocity (Fig 5.18g), related to increased buoyancy production and reduced stratification (Fig. 5.18h), but also a reduction in the relative humidity above fog top (Fig. 5.18h). The latter effect is due to the cloud top development, which causes a lower relative humidity 200 m above fog top because the relative humidity of ERA5 is decreasing with height. The loss by entrainment reaches almost 20 g m^{-2} h^{-1}, which is high relative to the range of values occurring for the events (Fig. 5.14e).

Figure 5.18f compares the total calculated LWP tendency to the observed change in LWP from the MWR. Both show an increase in the night and morning and then a decrease after 09 UTC. However, the increase in the morning is overestimated by the model, and the loss later on is overestimated (i.e. an overestimation of the diurnal cycle in the LWP budget, as discussed in section 5.4.2). The observed tendency in LWP around 11 UTC breaks the diurnal pattern and cannot be explained by our conceptual model. This increase in LWP might be caused by some non-local process, and it allows the fog to persist longer. After 14 UTC the calculated and observed LWP tendencies are also very different, with an increase predicted by the model, due to sinking sun and therefore less loss by heating, while the observations actually show a rapid decrease. There are several possible explanations: The loss by entrainment might increase if the fog top reaches a layer of lower humidity, the Bowen ratio may increase due to an exhaustion of the liquid on the surface, so that loss by surface fluxes increases, or a non-local process, such as advection of drier air, could cause the loss of LWP. This points to three areas where the conceptual model could be improved: (1) more precise information on the relative humidity profile (see also section 5.6.3), (2) a better estimate of the Bowen ratio, and (3) introducing the LWP impact of non-local processes, such as the advection of drier air.

The fog event on 2 Nov 2015 is also an example of a transition in the profile of reflectivity (Z). After 12 UTC, the altitude of the highest value of Z, marked as a dashed line in Fig. 5.18a, approaches the fog top. Earlier in the fog event, Z is stronger and has its highest value closer to the middle of the fog layer. As discussed in section 5.2, the transition from a strong reflectivity with max-value in the centre of the fog layer to a weaker reflectivity with max value near the fog top likely represents the disappearance of bigger droplets which sediment towards the fog base. This is shown more clearly in Fig. 5.19 with the profile of Z plotted every hour. In this figure, we can see the change of the shape of the profile, first with a max value at 100–150 m, and then a decrease of Z here and a less strong decrease at the higher levels, giving a max near 200 m. After 12 UTC, the visibility is also improving gradually, both at 4 m and 20 m (Fig. 5.18b), which can be related to a decrease in the LWC which also explains the decreased reflectivity.

Figure 5.20 shows the observations and analysis of the fog event on 18 February 2015. This fog event forms from clear sky in the presence of important surface radiative cooling (60–70 W m^{-2}) (Fig. 5.20d), similarly to the event on 2 Nov 2015 (Fig. 5.18d). It also forms at a very similar time

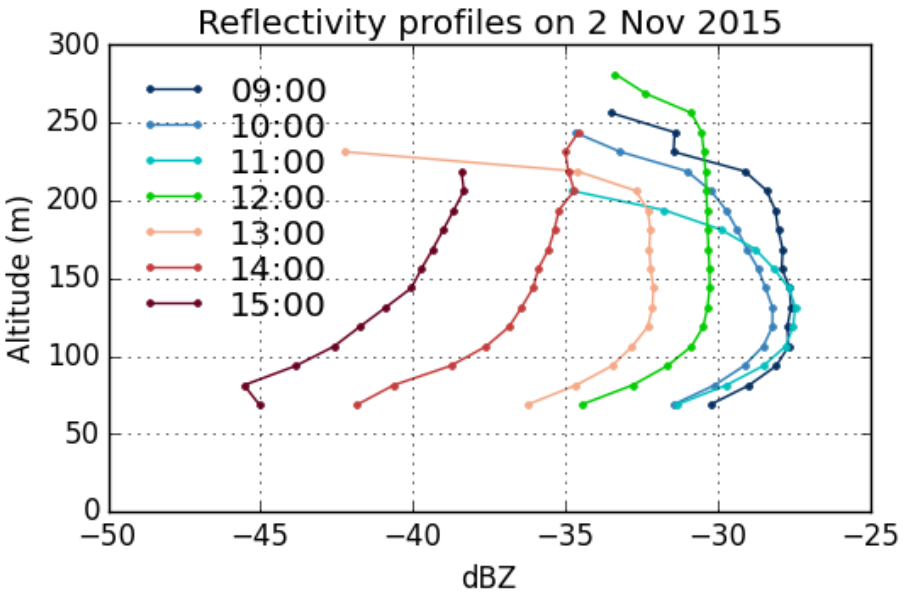

Figure 5.19: The observed 10-min median profiles of radar reflectivity by the cloud radar at several times during the fog event on 2 Nov 2015.

and has a similar thickness at sunrise. However, this fog event is capped by a considerably weaker stratification than the event on 2 Nov (only 5 K around sunrise), and it decreases to 3 K within 2 h (Fig. 5.20h). This likely impacts the increase in the CTH, which reaches 300 m at 10:30 UTC and might contribute to the loss of LWP. The observed cloud-top development is stronger than the one predicted from the entrainment parametrisation (20–30 m h^{-1} rather than 10–15 m h^{-1}). Since the relative humidity above is very high (Fig. 5.20h), the predicted loss by entrainment is still small (Fig. 5.20e). The loss by surface heat fluxes is strong, particularly after 9 UTC, but the conceptual model still underestimates the total loss of LWP at this time (Fig. 5.20f). The LWP budget predicts a positive tendency throughout the fog event, which is most of the time much stronger than the observed LWP evolution (Fig. 5.20f). One reason could be the entrainment rate, which is stronger in reality than calculated, judging by the increase in CTH. Another reason that the calculated LWP budget for this event is more positive than for 2 Nov 2015 is the smaller calculated loss by deposition, especially around sunrise (Fig. 5.20e, Fig. 5.18e).

The observed LWP decreases around 9 UTC (Fig. 5.20b), causing an increase in the CBH predicted by the CB2011 model (Fig. 5.20a), which enables the fog to lift. The reflectivity profile in this fog has the max value close to the fog top during the whole event (dashed in line Fig. 5.20a), and a lower absolute value of the reflectivity than in the first hours of the event on 2 Nov 2015 (Fig. 5.18a), which could indicate a lack of bigger droplets that can sediment towards the lower levels. The profile of reflectivity before dissipation on 18 Feb 2015 is similar to what is seen close to dissipation time in the fog on 2 Nov 2015, with the very low values of reflectivity near the surface before the fog base lifts.

After lifting from the surface, the cloud base is present and keeps rising, reaching 300 m at 14:30 UTC (Fig. 5.20a), with an LWP of 20–30 g m^{-2} (Fig. 5.20b), but the cloud radar does not detect it after 10:30 UTC (Fig. 5.20a), which again shows the importance of cloud radar sensitivity, as discussed in section 2.3.

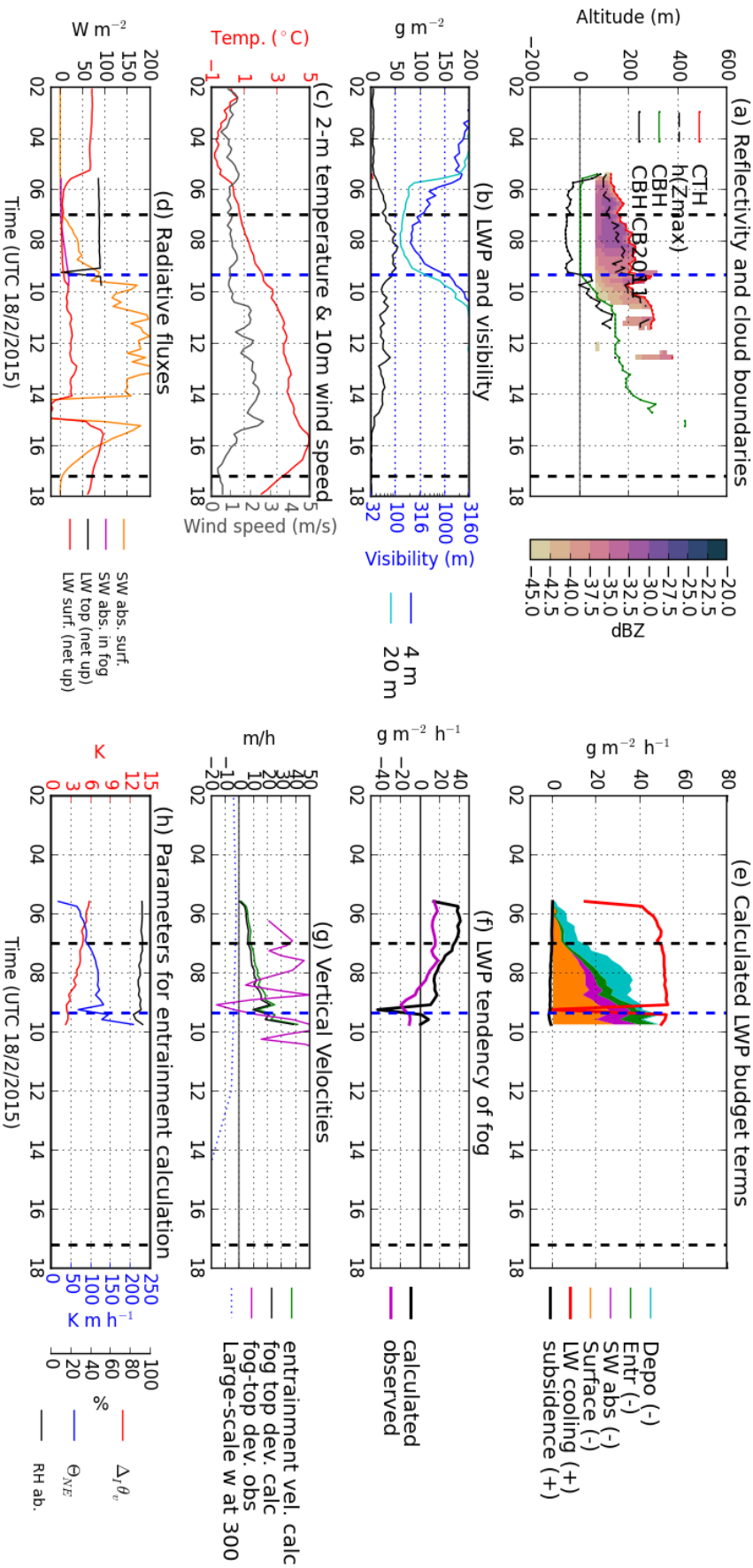

Figure 5.20: Process analysis of the fog event on 18 February 2015. See Fig. 5.18 for explanation.

5.5.2 Two fog events near winter solstice

The fog event on 5 Jan 2015, shown in Fig. 5.21, is a persistent fog which lasts all the day, apart from lifting by a few metres during two short periods (around 12 and 15 UTC). The CB2011 model can very well explain these periods of lifted cloud base by a deficit of LWP relative to the fog thickness (Fig. 5.21a). Being near mid-winter, the terms in the LWP budget (Fig. 5.21e) relating to solar radiation (SW absorption and surface fluxes) are significantly weaker than on 2 Nov 2015 when the fog had a similar thickness and LWP (Fig. 5.18e), reaching 25–30 g m^{-2} h^{-1} instead of 40 g m^{-2} h^{-1} near midday. The entrainment term is predicted to be the main loss term of LWP in the afternoon, stronger than on 2 Nov 2015 (Fig. 5.18e), due to the lower stratification the lower value of relative humidity above fog top (Fig. 5.21h, Fig. 5.18h). However, in this particular case, the humidity above fog top appears to be largely underestimated by ERA5, judging by the radiosonde launched at 11:13 UTC (see Fig. 5.26 (as)). Even with this (too) important loss predicted from entrainment, the fog event on 5 Jan 2015 has generally a more positive LWP budget than on 2 Nov 2015 around midday, which can be attributed to the weaker loss by the solar-related processes, but also to the calculated deposition being so much weaker (Fig. 5.21e, Fig. 5.18e). The observed and calculated LWP tendencies are closer to each other in this fog event than in the previous ones, with a similar positive tendency before 9 UTC and then a weakly negative average tendency later in the day. However, the observed tendency becomes positive around midday, and then strongly negative around 14 UTC; there is no signal in the parametrisations of the LWP budget terms that can explain this, so it might be a non-local effect such as advection.

In this fog event, subsidence is strong, so that the total vertical velocity of cloud top is calculated to be negative. This decrease in fog thickness is also observed in the afternoon, but until 9 UTC the CTH increases importantly (Fig. 5.21a). With our local observations, we do not know if this thickening is due to entrainment or advection, but if it is entrainment our parametrisation underestimates it strongly.

At 14 UTC, the reflectivity is decreasing and its max value moves towards the top. This could be interpreted as a sign that the fog will lift (Fig. 5.21a), but in this case the fog does not lift more than a few metres, and lowers to the surface soon after. However, as opposed to the event on 2 Nov 2015 (Fig. 5.18), on 5 Jan 2018 the impact of surface heat fluxes is weak at the time when the fog base starts lifting (Fig. 5.21e), which could be limiting the efficiency of this dissipation mechanism. As the LWP tendency becomes positive, the cloud base can lower again.

Figure 5.22 shows the fog event occurring on 1 Jan 2016. This fog event was also presented in the radiation analysis in W17 and is characterised by the clouds appearing above the fog. The thin liquid clouds appearing around 7 and 8 UTC could barely be seen in the 200-m BASTA signal (see discussion in W17), and in fact their signal is not clear enough to be detected by the automatic algorithm for detecting the higher clouds (section 3.2.1), so their effect on the LW radiation term in the LWP budget has not been captured (Fig. 5.22e), which is likely the main cause of the strong overestimating in the LWP budget. The overestimation of the LWP tendency before the arrival of these clouds (before 7 UTC) could be because the sub-cloud layer is still present and that water is used to saturate it; this is not taken into account in the conceptual model, which assumes the layer is completely saturated down to the surface. The clouds appearing above the fog around sunrise also perturb the CBH from the CB2011 model (Fig. 5.22a) because of their perturbation of LWP (peaks in Fig. 5.22b), making the CBH CB2011 unreliable for indicating the likelihood of fog lifting while the clouds are present (see

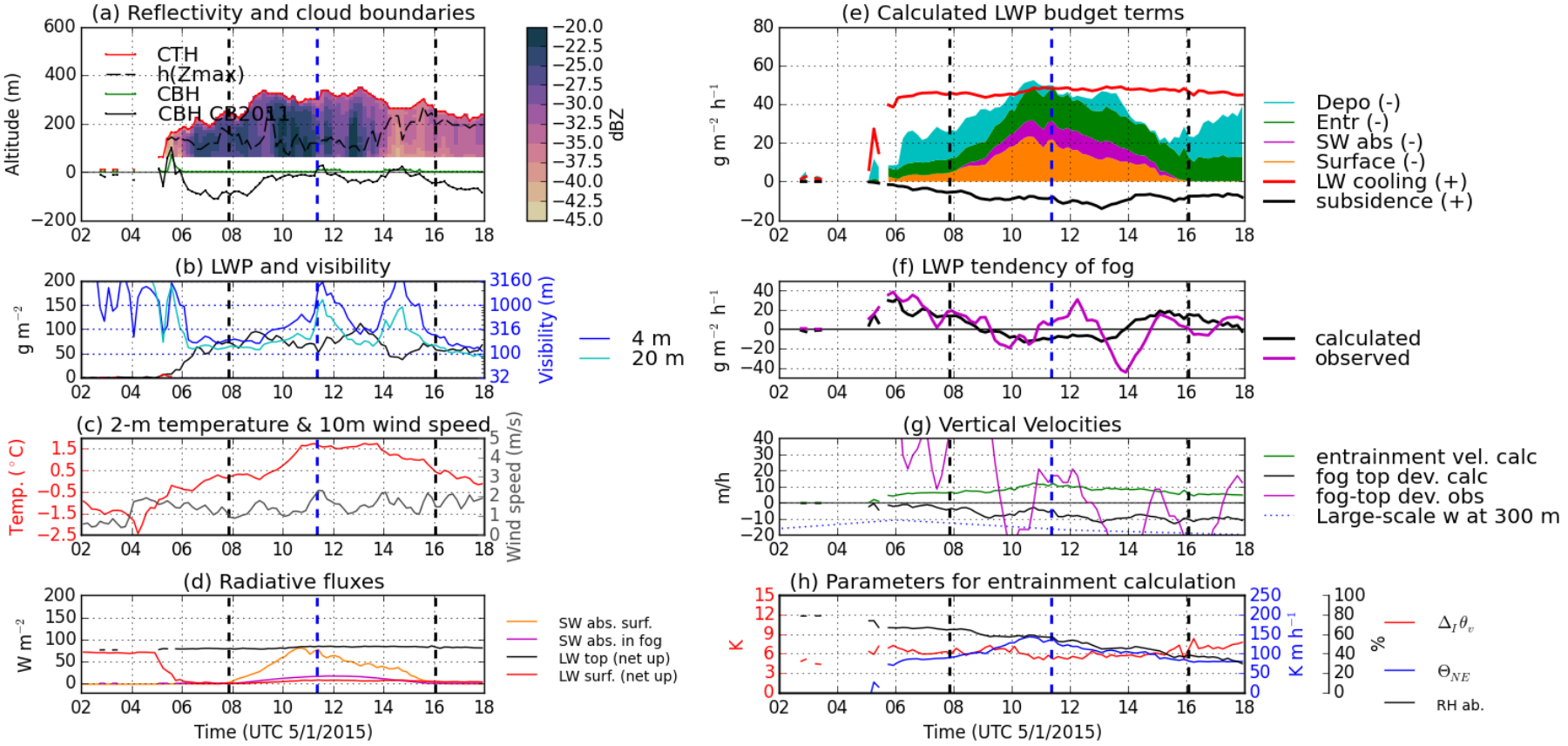

Figure 5.21: Process analysis of the fog event on 5 January 2015. See Fig. 5.18 for explanation.

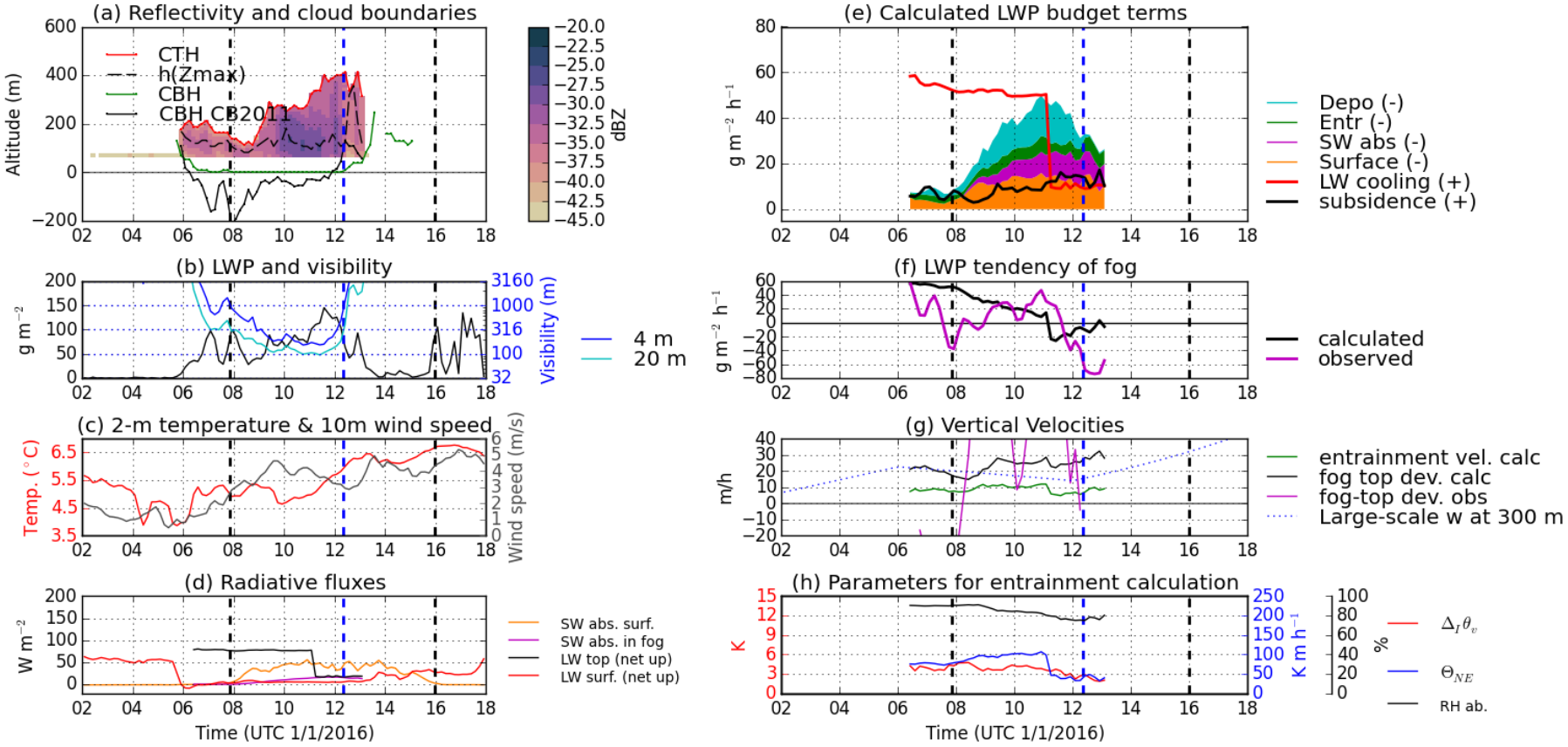

Figure 5.22: Process analysis of the fog event on 1 January 2016. See Fig. 5.18 for explanation.

section 5.2).

The cloud appearing at 11 UTC (which is detected by the cloud radar), is likely composed mainly of ice, so the MWR measurement of fog LWP and the CBH CB2011 is not perturbed by it (as argued in W17). The cloud lifts when the LWP drops at 12 UTC so that the CBH CB2011 becomes positive. The main cause for the drop in LWP is likely the appearance of the cloud above, as is captured by the conceptual model (Fig. 5.22ef).

The strong increase in LWP between 9 and 11 UTC is well correlated with the increase in CTH. These increases occur so suddenly that they are likely explained by advection. However, the overall increase can be attributed in part to the upward large-scale velocity (Fig. 5.22g). 20 m h^{-1} at 300 m corresponds to a gradient of $1.9 \cdot 10^{-5}$ s^{-1}, which is even more than in the sensitivity study with the LES model shown in section 4.2. Both LWP and CTH are increased importantly when the large-scale velocity is upward (section 5.3.4). The predicted total upward motion of the cloud top of 20–30 m h^{-1} (Fig. 5.22g) falls nevertheless far short of explaining the 300 m increase in CTH observed over 3 hours (Fig. 5.22a). This might indicate that a thicker fog layer is advected from elsewhere (the wind (Fig. 5.22c) is strong in this event relative to typical values in fog (Fig. 2.4), increasing the probability of advection), or that the calculated entrainment velocity is underestimated (section 5.6.3).

5.5.3 Two contrasted events in October 2014

Figure 5.23 presents the fog event occurring on 27 Oct 2014. This fog differs from the other case studies by being thin, only around 100 m at its thickest, with LWP not exceeding 20 g m^{-2}. As seen in Fig. 5.5, there are several of these thin fog events, most of them dissipating soon after sunrise. The LWP budget on 27 Oct 2014 (Fig. 5.23e) shows that this can be explained, as we would expect, by the surface heat fluxes. Once the sun has risen, the thin fog lets most of the radiation through and is evaporated by the heating.

Although the conceptual model is not really applicable for stable fog, it is interesting to note the balance predicted between radiative cooling and deposition in the period of intermittent fog before sunrise (Fig. 5.23e); this is also seen in the other thin fog events (not shown). The correlation between the two terms is of course due to them being calculated from the same data: when the fog is only 10 m thick, the visibility at 4 m is used both for fog opacity in the radiation scheme (section 3.2.1) (because the LWP comes from visibility, see section 2.5.2) and for deposition calculation (section 5.3.5). The transition from a thin radiation fog to a more opaque fog, as seen here around 6 UTC, is associated with an increase in the LWP, so that significant radiative cooling starts to occur, which enables further production of LWP (Fig. 5.23e). The reason that the observed increase in LWP in the period 6–8 UTC is weaker than what we calculate (Fig. 5.23f) might be that the layer is not yet completely well-mixed and saturated, so that liquid water is being consumed to saturate the thicker fog layer that has been created.

Again we see that the CB2011 model gives a good indication of the required water for the fog to stay at the ground, even when this fog is much thinner than most of the other events. The fog lifts at 8:50 UTC, 20 min after the CBH CB2011 becomes positive. Afterwards, the two CBHs deviate a bit, but this must be expected since the LWP is so low at this time that its relative uncertainty is high.

A very different fog event, occurring the day after, is shown in Fig. 5.24. This fog grows very thick during the night, with its LWP increasing simultaneously, and it reaches a thickness of more than 400 m and LWP of 200 g m^{-2} right after 6 UTC. The LWP then decreases during the morning while

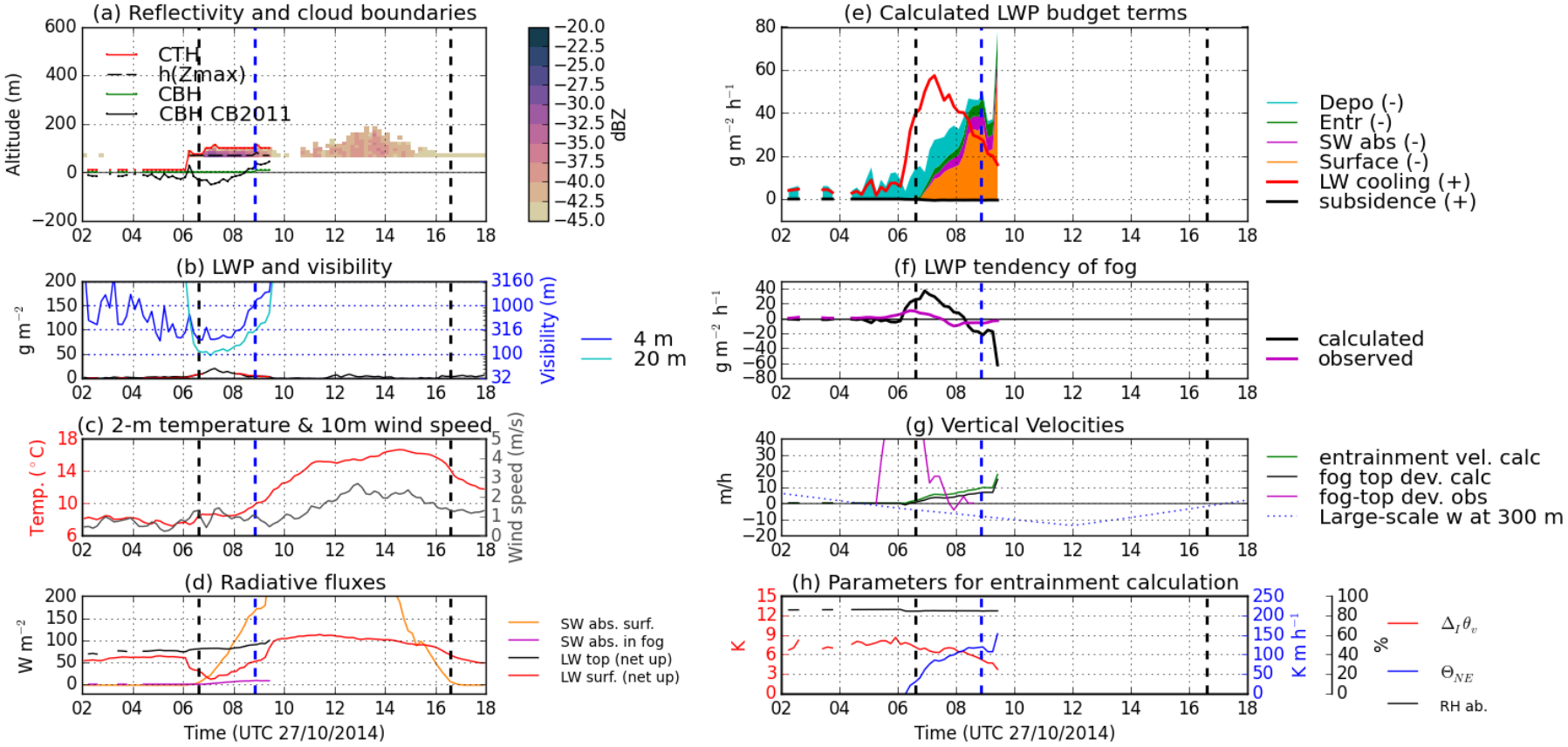

Figure 5.23: Process analysis of the fog event on 27 October 2014. See Fig. 5.18 for explanation.

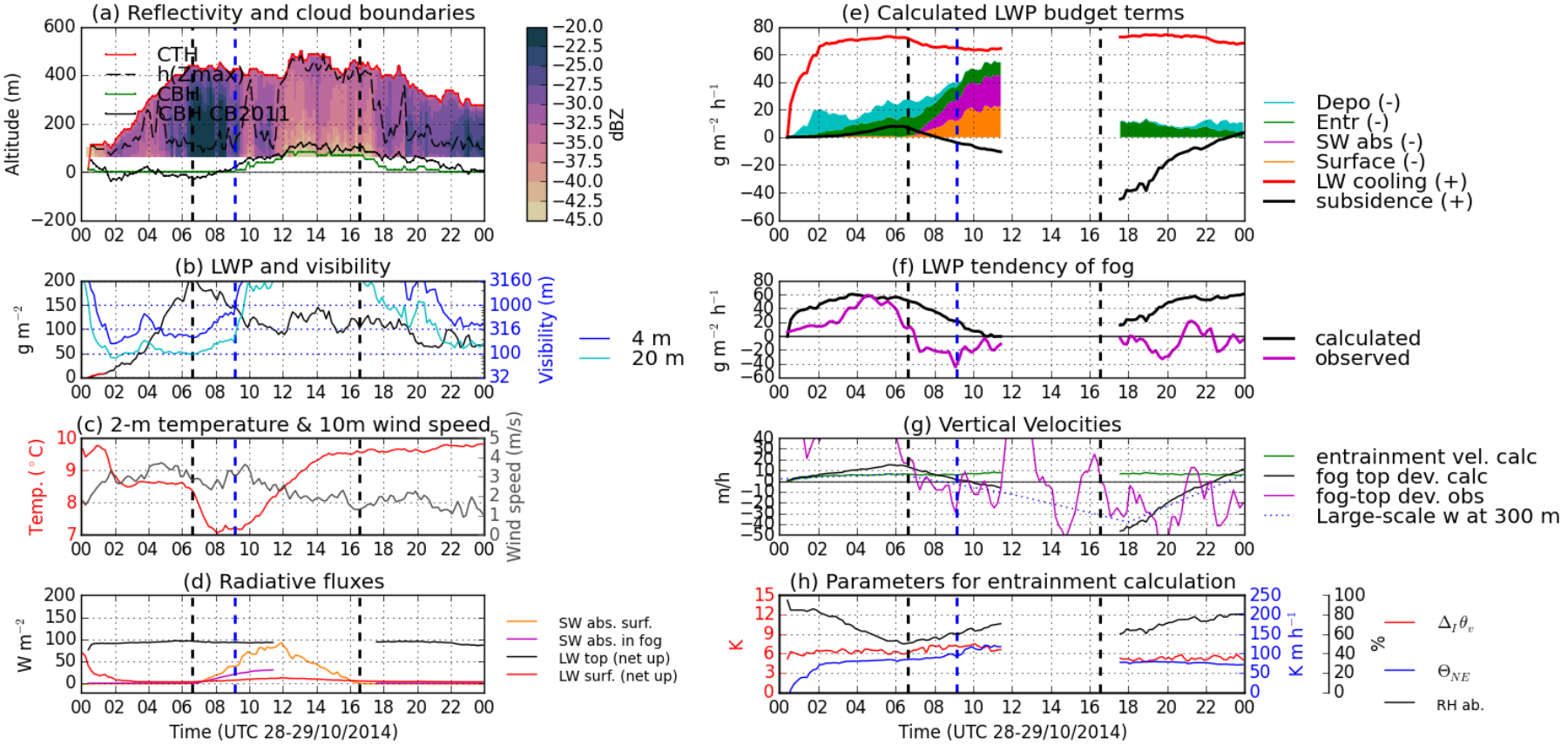

Figure 5.24: Process analysis of the fog event on 28 October 2014. See Fig. 5.18 for explanation.

the CTH remains constant. When the fog base lifts at 9:10 UTC, there is a rather good agreement between the observed CBH and the one calculated by the CB2011 model. The CB2011 model can also explain that the fog forms again around 21 UTC, although the CBH CB2011 is slightly too high. Thus, Figs. 5.23a and 5.24a show that the CB2011 model can work well both for thin (100 m) and very thick (>400 m) fog.

The production of LWP from radiative cooling is particularly strong in this event (Fig. 5.24e, compare to range in 5.14a), which was already noted in W17. This is probably an important reason that this cloud could remain all day even when it occurs quite far from the winter solstice. Its high LWP also helps reducing the SW radiation reaching the surface (Fig. 5.24d), so that there is less loss of LWP from surface fluxes (Fig. 5.24e). The thicker fog will absorb more SW radiation, though; the conceptual model actually indicates that the SW absorption term is as important as the surface fluxes term.

The rapid growth of the fog top before sunrise is not explained by the conceptual model. In this case, no strong upward large-scale velocity is diagnosed, and the entrainment velocity is rather weak, pointing to a contribution from advection. However, the calculated LWP production is even stronger than the observed increase (Fig. 5.24), which would be even more so if the increase is attributed to advection. It is therefore likely that entrainment also gave an important contribution, in order to provide a stronger sink for the LWP, which indicates again that the entrainment velocity is importantly underestimated (see section 5.6.3)

In the evening, the observed decrease in CTH is similar to the applied subsidence velocity in the conceptual model (Fig. 5.24g). Indeed, the subsidence is very strong in the evening, and it is a likely explanation for why the fog top is descending so much. Radiative cooling is still very strong in the evening, and the calculated LWP budget much larger than the observed tendency. Perhaps this could again be attributed to an underestimation of the mixing with the rather dry air above.

Prior to the lifting of the fog base at 9:10 UTC, the fog loses more than 50 g m^{-2} of LWP over a period of 2 hours. During this time, the reflectivity is strong, and the Doppler velocity becomes negative, with a mean value of -0.47 m s^{-1} in the range 70–300 m for 6:30–8:30 UTC (not shown). This is an indication of the presence of large droplets. We may therefore suggest that the deposition of these droplets can explain the reduction in LWP. As the big droplets do not impact visibility very much, it is not surprising that the deposition scheme (based on visibility) cannot detect this phenomenon. FM-120 data are available for this fog event, but the FM-120 does not detect an important sedimentation rate, only 2–4 g m^{-2} h^{-1} (not shown). The FM-120 does not measure droplets that are bigger than 50 μm, though, and the fall speed of -0.5 m s^{-1} may indicate that there are droplets present which are bigger than this (theoretically, the droplets need a diameter of 0.1–0.2 mm to have this fall speed (Rogers and Yau, 1989)). However, a spectropluviometer deployed at SIRTA does not detect any precipitation particles in this period (not shown). It is possible that there are droplets that contribute to deposition which are too small to be detected by the spectropluviometer and too large to be detected by FM-120.

5.6 Uncertainty sources in the conceptual model

The conceptual model described in section 5.3 quantifies the impacts of the different local processes on the fog LWP and CTH. However, the parametrisations are built on multiple assumptions and often uses indirectly observed quantities. They therefore have important uncertainty. Some terms are more precise than others. A summary of the uncertainty sources of each term is given in Table 5.1. Also

indicated is the overall confidence that the parametrisation gives an accurate estimate of the term. A discussion of the uncertainties in each term is given in the following.

5.6.1 Radiative processes

The production by LW cooling is probably the most precisely quantified term. The main uncertainty source is the clouds above, as they may not be detected, or they may be semi-transparent (while the parametrisation assumes that they are opaque). When there are no clouds above, the uncertainty is likely in the order of 20–30 %, considering the uncertainty analysis of W17 and the agreement between ARTDECO and the LW parametrisation (Fig. 3.2a). If the systematic overestimation of C_{LW} relative to ARTDECO could be improved, the uncertainty would be less. The uncertainty related to the adiabatic profile of the fog may be the most significant in absence of higher clouds, as the fog top temperature can be importantly underestimated in cases when the fog is stable. The IWV is well estimated, giving confidence in the downwelling LW flux arriving at fog top, and the LW flux at the surface is directly measured.

The relatively good agreement between surface net radiation observed and calculated (Fig. 3.4) indicates that the fog opacity is rather well represented. The main uncertainty source for the amount of SW radiation absorbed by the fog is the absorptivity of the fog. This is discussed in section 5.3 of W17: notably, the presence of absorbing aerosols can impact the absorptivity, and also the droplet sizes. The SW absorption term is likely to be overestimated in case of clouds above, since the absorption of SW radiation by these clouds is not accounted for; this effect can easily reduce the SW absorbed in the fog by 50 % (Fig. 10b in W17).

In spite of these caveats, both radiation terms have been put to "high confidence" in Table 5.1, because their variability due to the main parameters determining them (LWP, IWV, μ_0) are calculated with high confidence, which is not so for several other terms. To reduce the uncertainty when higher clouds are present, it is firstly necessary to detect them, requiring a sensitive cloud radar which preferably scans the sky in all directions to detect fractional cloud cover, and secondly a parametrisation of the cloud opacity from cloud radar only is needed.

5.6.2 Surface fluxes

The net radiation absorbed at the surface is observed directly and therefore has very low uncertainty. Since the ground heat flux is measured at 5 cm depth, the heat flux going into the soil may be underestimated, thereby overestimating the turbulent heat fluxes. Some heat may also be stored in the vegetation or other objects on the ground, such as trees. However, the main uncertainty in the impact of surface fluxes is the Bowen ratio. As we showed in W18, the loss by surface fluxes is very sensitive to the Bowen ratio. If we trust the Penman-Monteith equation applied in section 5.3.2 to calculate the Bowen ratio, there is still a large uncertainty related to the arbitrary parameter c_{dry} which the loss from surface fluxes is proportional to. If the surface is completely dry, the loss is twice as big as what we have calculated (since we use $c_{dry} = 0.5$). If reliable measurements of the Bowen ratio in fog were to be obtained, it could be interesting to investigate whether the parametrisation can reproduce the Bowen ratio with a specific value of c_{dry}, and if not, whether the value of c_{dry} can be related to some observable parameters of the surface wetness (e.g. recent rainfall or dew measurements/calculations). Another point is that the soil may not always be moist, as assumed in our model, and a drier soil could increase the Bowen ratio.

Term	Main uncertainty sources	Confidence
LW cooling	clouds above, adiabaticity, DSD	High
SW absorption	absorbing aerosols, clouds above, DSD	High
Surface fluxes	Bowen ratio, ground flux/storage	Medium
Subsidence	vertical velocity in ERA5	Medium
Entrainment	parametrisation validity, humidity in ERA5†, stratification	Low
Deposition	turbulent deposition velocity, Vis–F_{sed} relationship	Low

Table 5.1: Uncertainty sources (sorted according to importance) and overall confidence of the parametrisations of each of the terms in the LWP (and CTH) budgets. †The humidity only causes important uncertainty in the LWP loss by entrainment, not the impact by entrainment on CTH.

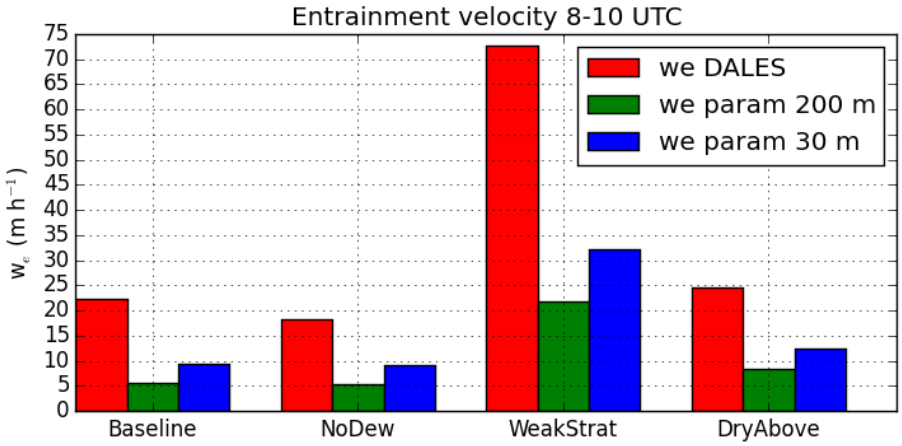

Figure 5.25: Average entrainment velocity 8–10 UTC in the LES sensitivity tests (W18), as produced by the LES model itself (red) and calculated with the parametrisation in section 5.3.3 using the model output fields as input, with $h_{ab} = 200$ m (green) and $h_{ab} = 30$ m (blue).

All in all, since the available energy is rather precisely known, but the Bowen ratio is not, the precision of the surface fluxes term has been set to medium in Table 5.1. We can readily study the variability of the hypothetical impact of the surface fluxes for a given a value for c_{dry}, but the fact that c_{dry} may be different in different situations limits the precision with which we can quantify the actual impact of surface fluxes.

5.6.3 Entrainment velocity and entrainment loss

The entrainment parametrisation used in the conceptual model (section 5.3.3) is not developed specifically for fog, but for thicker layers capped by stratocumulus. It is therefore not given that it correctly quantifies the entrainment rate in fog. Indeed, we have several times in this chapter (sections 5.4, 5.5) found indications that the entrainment rate is underestimated. As the observed entrainment velocity appears to be masked by advection (section 5.4.3), an evaluation of the calculated entrainment velocity from observations is not trivial. However, the model output from the LES simulations that were performed in W18 allows a comparison of entrainment predicted by the LES model vs the parametrisation of section 5.3.3 (Fig. 5.25). When applying the model output, we may also calculate the entrainment velocity with θ_v^+ and RH^+ taken from an altitude much closer to the fog top, which is more appropriate to represent the air with which the fog is currently mixing. We therefore compare the parametrised entrainment velocity when using the fields 200 m above fog top and when using the

fields 30 m above fog top.

The results show that the entrainment parametrisation largely underestimates the entrainment velocity calculated by the LES. The impact of taking the above-cloud values 30 m above fog top rather than 200 m above improves the estimate significantly, but it still underestimates the LES entrainment by a factor 2–3. So the main uncertainty seems to lie in the formulation of the entrainment parametrisation, rather than the input data. Nevertheless, the relative difference in entrainment velocity in the LES between Baseline and WeakStrat (and even the more subtle difference between Baseline and DryAbove) is captured rather well by the parametrisation. The entrainment rate is larger in WeakStrat than Baseline by a factor 3.3 in the LES, by a factor 3.9 in the parametrisation using 200 m above, and by a factor 3.4 when using 200 m above. So it seems like the relative increase of entrainment with decreasing stratification is correctly represented, while the overall entrainment efficiency is underestimated. This would indicate that the entrainment velocities in Fig. 5.9c and the loss rates in Fig. 5.9ef should be 2–3 times bigger. However, it could be that the shapes of the curves need to be adjusted too, in particular the very steep dependency of w_e on stratification for $\theta^+ - \theta < 4$ K, which is far below the range of stratification considered by Gesso et al. (2014), but which nevertheless occur in our dataset. To conclude on an improved entrainment parametrisation for fog, a more detailed study with LES would be needed, varying systematically all the parameters that are used in the entrainment parametrisation.

Of course, the entrainment calculations also strongly depend on the validity of the adiabatic temperature profile, so that if the fog is stable the entrainment parametrisation is not likely to provide a correct representation of the entrainment rate.

The input parameters to the entrainment parametrisation are also associated with uncertainty. The buoyancy production in the fog (Eq. 5.28) is relatively precisely quantified, since the radiative fluxes have rather low uncertainty (section 5.6.1) and the Bowen ratio only has a weak impact on the buoyancy production. More important uncertainty is related to the characterisation of the layer above. The values of temperature and humidity applied to the air above the fog should preferably be close to those directly above the fog-top inversion. Figure 5.26 shows the profiles of temperature and humidity observed by the 47 radiosondes launched during or near a fog event and compares them to the MWR temperature retrieval and the humidity from ERA5. As these radiosondes likely have been used to assimilate ERA5, they are not strictly independent for evaluation, and we should keep in mind that the humidity agreement might be less good at other times. Nevertheless, the humidity comparison can still give an idea of the difference between the humidity applied in the entrainment parametrisation (the large blue square 200 m above fog top) and the actual humidity directly above fog top (seen from the radiosonde profile). Note that the cloud top may not be exactly at the same height at Trappes and SIRTA; the cloud top in the radiosonde profiles is more likely to be around the altitude where an inversion starts. For example, on 2 Jan 2017 23:01 (bt), the inversion is at 200 m while the CTH at SIRTA is observed at 300 m.

To evaluate the input stratification above fog top, we compare the MWR estimate of the potential temperature above fog top (red square in Fig. 5.26) with the potential temperature at the top of the temperature inversion in the radiosonde (the inversion is not always so marked in the radiosonde profile, which makes it hard to evaluate in these cases). We see that in most cases, the two potential temperatures correspond well (e.g. (ac),(ae),(ai),(al),(bf),(bt),(bu)). In contrast, we see the naive approach of applying the value from the MWR directly above the inversion would not give a good

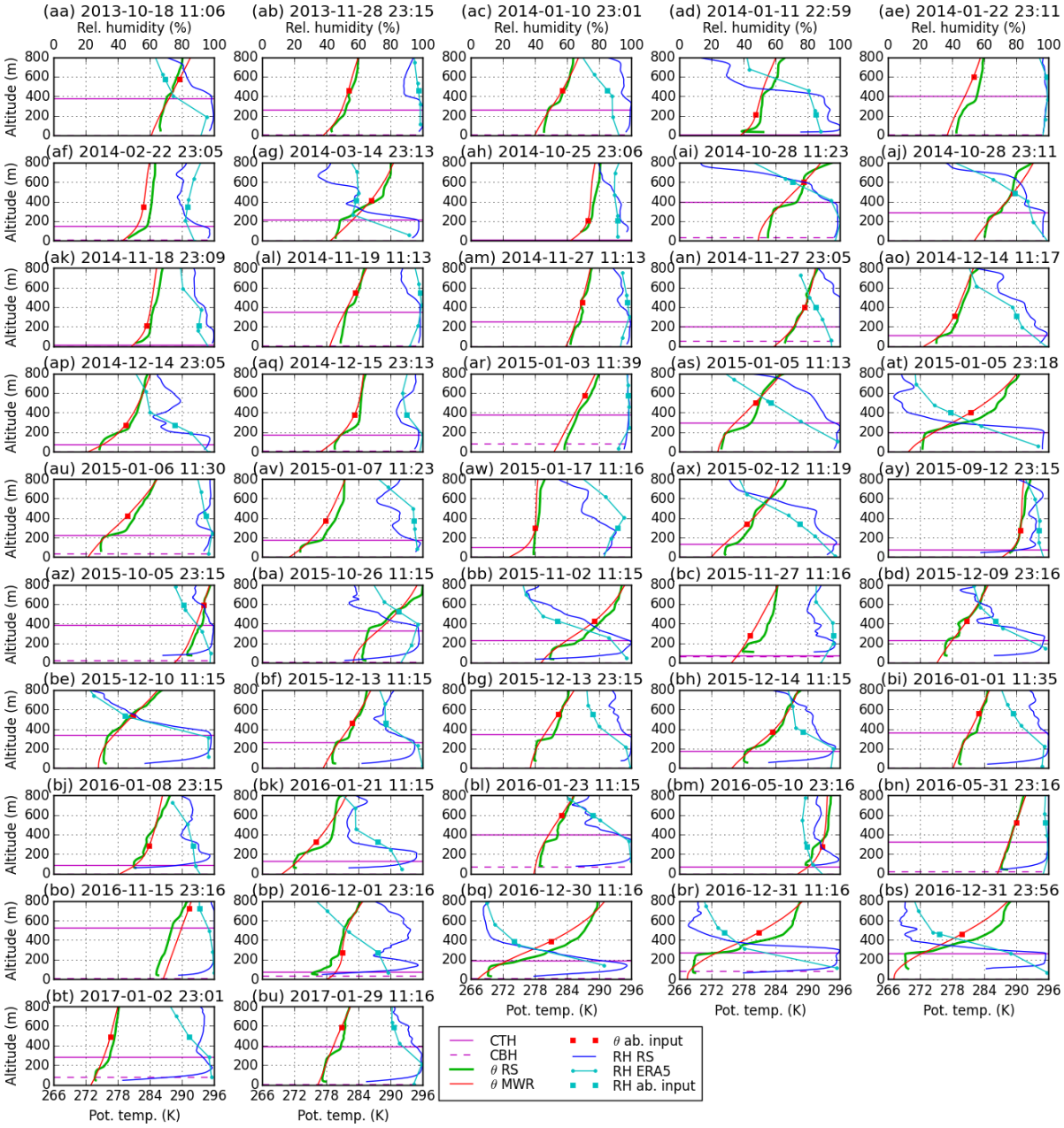

Figure 5.26: Profiles of potential temperature (θ) and relative humidity (RH) measured by 47 radiosondes launched at Trappes in the period 2013–2017, during fog at SIRTA, or during very low stratus with CBH $<$ 130 m and CTH $<$ 600 m, less than 6 h before or after a fog event (RS). This is compared to the simultaneous profiles of potential temperature retrieved by the MWR, and to the humidity profile interpolated in time from ERA5 for a 1° x 1° domain around SIRTA. The horizontal dashed and solid lines mark the cloud base and cloud top, respectively, measured at SIRTA. The red and cyan squares mark the values 200 m above fog top, which are used in the entrainment parametrisation (section 5.3.3) for the potential temperature and relative humidity at h_{ab}, respectively.

estimate, since the sharp inversion is not captured by the MWR. By applying the value 200 m above the fog top, we get a value closer to the potential temperature observed by the radiosonde directly above the inversion. However, there are also cases where the atmosphere has important stratification in the following few hundred metres above the inversion, and in these cases the value applied will overestimate the actual stability directly at fog top, even if the value agrees with the potential temperature of the radiosonde 200 m above fog top (e.g. (ag),(bh),(bq)). Overall, the uncertainty in the entrainment term due to the input parameter θ^+ is relatively small compared to the uncertainty related to the validity of the entrainment scheme, but it will cause an underestimation of the entrainment in some cases of gradually increasing potential temperature above fog top.

To evaluate the input relative humidity above fog top, we consider the difference between the humidity taken from ERA5 200 m above fog top (cyan square) and the humidity a few tens of metres above the fog top in the radiosonde. This value should be compared to the relative humidity closely above the fog, but sufficiently high that it is not already influenced by mixing with the fog, which is likely to be a few tens of metres above the fog top. In some cases, the humidity appears to drop rather abruptly at the fog top (e.g. (ah), (ap), (at), (ba) in Fig. 5.26), but in most cases the decrease is relatively gradual. The relative humidity applied in the conceptual model is therefore usually lower compared to what is observed closely above the fog top by the radiosonde (e.g. (as),(bb),(bg),(bh), and in particular (br)), but there are also some cases where it is too high (e.g. (av),(ba),(bc)). There are also cases where they are close, such as (ab), (aj), and (bf) (NB: we do not compare the ERA5 to the radiosonde at the same level, but we compare the cyan square to the value of the RS RH profile closely above the inversion in the RS θ profile). The distinction of a thin layer above the fog top from the rest of the atmosphere can be very important, as seen in the very stable cases at the end of December 2016 ((bq),(br),(bs)). These radiosondes indicate that there is a narrow layer between the inversion and the drop in humidity (only a few tens of metres thick), which may still limit the loss of LWP by entrainment while allowing a strong radiative cooling due to the low IWV (as discussed in W18). Of course, it could also be that this layer is created by the exchange between the fog and the dry air above (entrainment zone). Overall, the application of the ERA5 humidity seems to give an underestimation of the humidity of the air with which the fog mixes in most cases, which typically amounts to 10–20 %, in some cases much more. This uncertainty in relative humidity above fog top strongly limits the accuracy of the estimate of LWP loss by entrainment. The too weak entrainment velocity and the too low relative humidity above probably compensate each other to give values of entrainment loss of LWP which are not too far from its real magnitude, but both need to be improved in order to give a better estimate in each particular case.

When using the ERA5, a horizontal average is performed over a domain of 1° x 1°, corresponding to about 110 km x 70 km. This domain contains 4 x 4 columns of the ERA5 data (which have a resolution of 0.25°). The spread of the relative humidity within this domain can be an indicator of how uncertain the value exactly above our location is. Figure 5.27a shows the time-average during each of the fog events of the spread of $RH(h_{ab})$ in this horizontal domain of ERA5. The standard deviation is typically from 1 to 8 %, so there is relatively important variability within the domain, but this is still much smaller than the uncertainty found in Fig. 5.26.

All in all, the current calculation of the entrainment velocity and its impact on the LWP has low confidence. Important improvements need to be carried out before the impact of entrainment on the CTH and LWP can be estimated with confidence. It is in particular the formulation of the

entrainment parametrisation which needs to be adjusted to match fog. Likely the input parameters are the right ones, but the entrainment efficiency and possibly other parameters need to be modified. For the entrainment velocity, we could already have a reliable quantification if the parametrisation was fitted to fog, since it is only weakly sensitive to the relative humidity above (Fig. 5.9c). For the effect of entrainment on LWP, it is also necessary to have better information about the humidity in the layer above fog top, which might require new measurement techniques.

5.6.4 Subsidence

The horizontal variability of vertical velocity gradient within the ERA5 domain is shown in Fig. 5.27b. The standard deviation is usually similar to the mean value, which means that both positive and negative velocities typically occur within the domain, and whether there is upward motion or subsidence can be uncertain. However, there are also many cases, especially for subsidence, where the spread is smaller than the mean value and there is therefore more confidence that the airmass is indeed descending. Figure 5.27c compares the value of dw/dz obtained when using the 950 hPa level in the reanalysis rather than the 975 hPa level. The 975 hPa level is located 100–350 m above the SIRTA ground during the fog events, while the 950 hPa level is about 220 m higher (not shown). The correlation is good (0.95), indicating that the subsidence is consistent throughout the first 500 m of the atmosphere, so that the value taken at 975 hPa can be assumed to be relatively representative for the cloud top even if the fog layer is thick; at least the sign, while the magnitude is rather sensitive to which level is used. Given the rather large spread in the horizontal domain and the sensitivity to the level used, we consider the subsidence effect on CTH and LWP only to have medium confidence.

5.6.5 Deposition

As discussed in section 5.3.5, the contribution to deposition from turbulent interception is a very difficult quantity to estimate, due to its small magnitude and large variability in space. The sedimentation contribution can be validated with the FM-120, as far as the sedimentation rate calculated from FM-120 at 4 m can be assumed to represent the deposition due to sedimentation. The comparison of the sedimentation calculated from visibility vs calculated from FM-120 shows a large spread (Fig. 5.28). Clearly the combined uncertainty in estimating LWC from visibility and then F_{sed} from LWC makes the final estimate imprecise. The RMS deviations are 5.28, 2.65 and 1.14 g m^{-2} h^{-1} for the data with visibility $<$200 m, 200–500 m and $>$500 m, respectively. Thus, the spread is in the order of 50 % of the estimated value both for high and low values of visibility. The general overestimation of F_{sed} can be attributed to the overestimation of LWC with Eq. (2.4) (Fig. 2.11). Thus, the deposition term is at best only a rough estimate with low confidence.

The deposition estimate might be improved by including more explanatory variables, such as the wind speed or the Doppler velocity from cloud radar. However, a reliable way to measure the total deposition term would be necessary in order to validate (discussed in section 6.3).

5.7 Synthesis

- The lifting of the fog base from the ground can be largely explained by the evolutions of the parameters LWP and CTH, because there is a relationship between the CTH and the critical amount of LWP needed for the fog to fill the layer between the surface and the CTH. The model

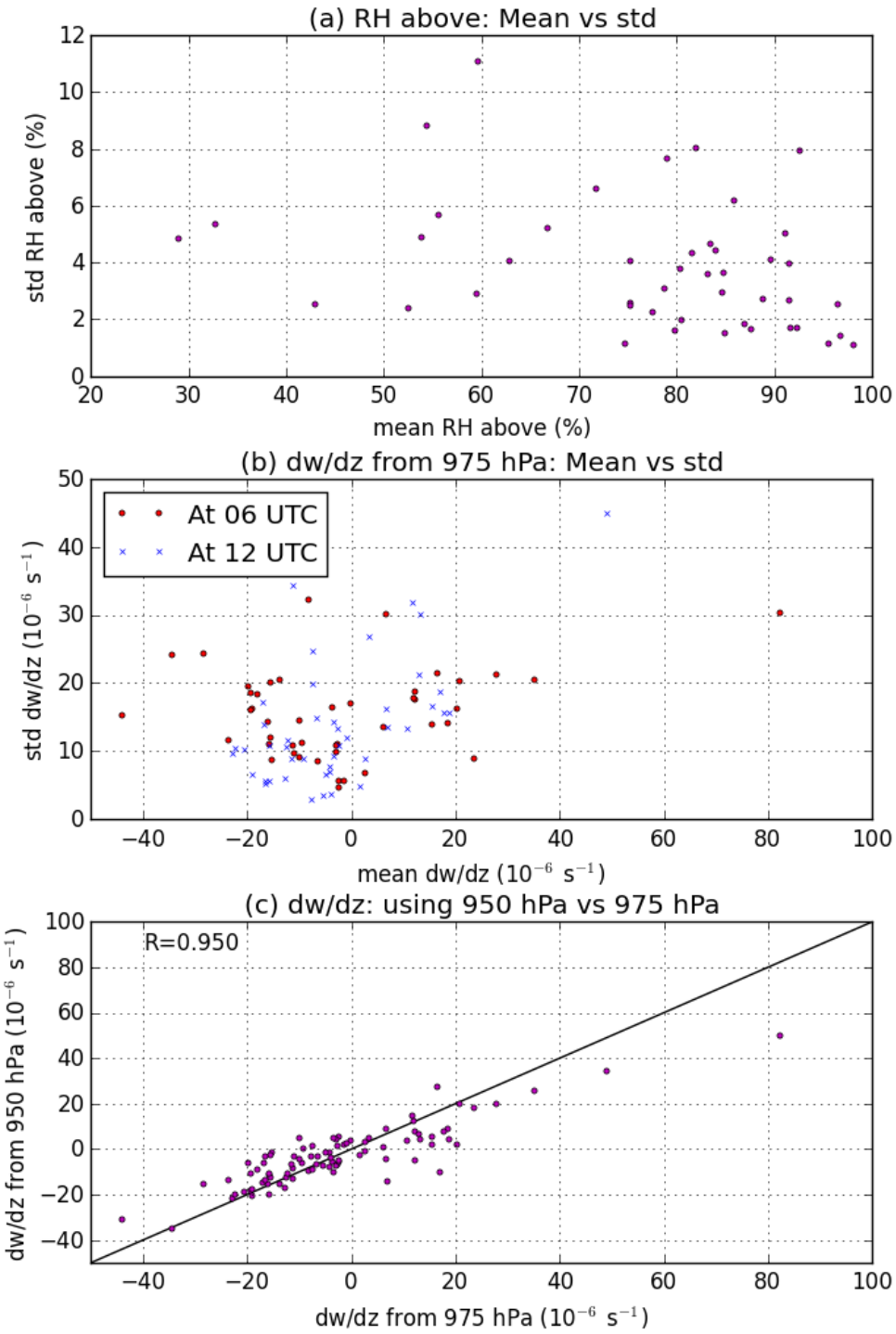

Figure 5.27: Variability within the 1° x 1° domain from ERA5 used for the conceptual model (which contains 4 x 4 cells), for each of the 45 morning fog events: (a) Relative humidity 200 m above fog top: standard deviation vs mean value in the horizontal domain, both averaged in all time blocks from sunrise to dissipation. (b) Vertical gradient in large-scale vertical velocity ($\frac{dw}{dz}$), calculated from the 975 hPa pressure level (see section 5.3.4): standard deviation vs mean value in the horizontal domain, at 6 UTC and at 12 UTC. (c) Comparison between the value for $\frac{dw}{dz}$ obtained using the horizontal mean data at 950 hPa vs at 975 hPa (at 6 and 12 UTC), with indicated correlation coefficient. (NB: One data point (13 Sept 2015 12 UTC) is far outside the shown range in panels b-c (values of 150–200·10^{-6} s^{-1}). This data point is still included in the correlation – if excluded, correlation is 0.85.)

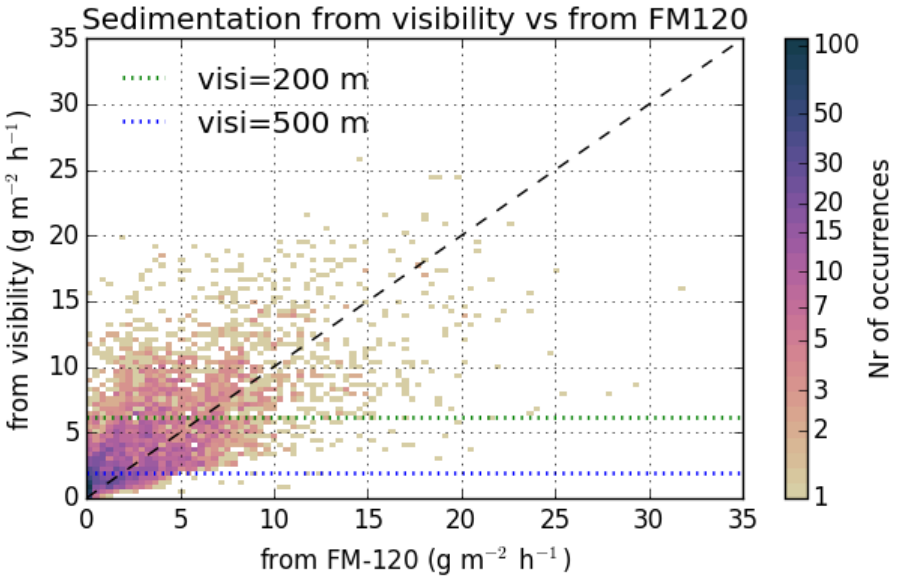

Figure 5.28: For the 64 fog cases with FM-120, the sedimentation rate F_{sed} calculated from the DSD of FM-120 vs the F_{sed} calculated from visibility using Eqs. (2.4), (5.47). The horizontal green and blue dashed lines mark the values of F_{sed} predicted when visibility is 200 m and 500 m, respectively.

of Cermak and Bendix (2011) (CB2011) describes well how this critical LWP changes with CTH, both for thin (100 m) and thick (400 m) fog layers (when we set $\beta_1 = 0.3$) . The negativity of the CBH calculated by the CBH CB2011 model indicates how large margin the fog currently has from dissipating, given that the estimates of LWP and CTH are reliable. To understand when the fog dissipates, it is therefore primarily these two parameters and their evolutions that must be understood.

- We developed a diagnostic conceptual model which estimates the tendencies in CTH and LWP due to six local processes (LW radiation, SW radiation, surface turbulent heat fluxes, deposition, entrainment and subsidence), using as input the observations from 8 different instruments and 2 parameters from a reanalysis. This model is applied to 45 fog events present at sunrise, to analyse the different evolutions in CTH and LWP in these events.
- An important seasonality in the dissipation time is found among the 45 events. A likely explanation for this is the important impact of the solar angle on the LWP loss terms of SW absorption in the fog and surface heat fluxes, and possibly also to some extent the entrainment.
- The calculated entrainment velocity is correlated with the observed vertical evolution of CTH, indicating that the parameters used in the entrainment parametrisation (especially the stratification above fog top) are relevant for the CTH development.
- The persistent fog events (which last all day) exhibit more frequent and stronger subsidence than the other morning fog cases. However, we showed that this is not directly due to the subsidence velocity, which actually reduces the LWP more than it reduces the critical LWP through the lowering of CTH. The subsidence in itself therefore weakly favours fog dissipation. It is therefore likely that other factors which occur together with subsidence can explain the link between subsidence and fog persistence.
- The radar reflectivity and its vertical profile vary importantly between the fog events, and it also

changes during the fog in several cases. In some of the events, the profile of radar reflectivity is modified before or during dissipation, with the max-value moving closer to the fog top, associated with a decrease of the reflectivity in the lower layers of the fog. This is interpreted as a lack of big droplets near the surface, due to the evaporation associated with the lifting of the fog base from the surface. The vertical profiles of reflectivity in fog should be further investigated to find out in more detail which microphysical processes it traces and how it can be used to understand the life cycle of fog.

- The conceptual model has several limitations which need to be addressed if the model is to explain a larger part of the observed tendencies in LWP and CTH. The main points that need to be improved regarding the local processes are: (1) The clouds above need to be better detected (requiring sufficient sensitivity of the cloud radar), and their opacities need to be estimated from the cloud radar measurements (requiring an appropriate parametrisation). While this requirement is mainly related to the calculation of radiative processes, the detection of liquid clouds above the fog is also important for determining when the MWR LWP retrieval, which used in the CB2011 model, is reliable. (2) The Bowen ratio needs to be better estimated, in order to estimate the LWP loss from surface fluxes. (3) The entrainment scheme must be adjusted to produce correct entrainment velocity for fog; comparisons with the LES indicate that the entrainment velocity is underestimated by a factor 2–3, while the increase in entrainment velocity from decreased stratification is well captured. (4) The humidity above fog top needs to be better quantified. (5) The effect of deposition is not sufficiently captured by the visibility, and more comprehensive parametrisations, such as described in Katata (2014), could be tested.
- The observed evolutions of LWP and CTH in the analysed case studies also suggest that non-local processes, such as advection and horizontal heterogeneity, have important impact on the two parameters. This is indicated both by the variability on hourly scale which is too large to be explained by local processes, and by the cases where the tendency changes importantly without evidence for a change in the local processes[4]. The model should therefore also take into account the spatial variability and horizontal advection (of LWP and CTH) to understand the observed evolutions of LWP and CTH.

[4]The latter situations can of course also be due to insufficient observation of the key parameters in the local processes, such as the Bowen ratio and humidity above fog top, which may change with time.

Chapter 6

Conclusions and outlook

This thesis was motivated by the need for improved forecasts of continental fog dissipation and the contribution that ground-based remote sensing instruments can give to observe and understand the processes responsible for the dissipation. The objectives were to quantify the impacts of each of the local processes (radiative, dynamical and microphysical) on the fog liquid water path (LWP) and on the fog dissipation, which parameters cause these impacts to vary, and how to detect this variability with observations.

The investigations have resulted in many interesting answers, and especially we have been able to point to several parameters which importantly impact the fog dissipation and should be further explored in future work. These conclusions, which will be detailed below, were obtained thanks to the large amount of fog observational data available from the SIRTA atmospheric observatory (Palaiseau, France), which allowed statistical studies of many different fog parameters which have clarified the role of several fog processes. It is especially the remote sensing observations (cloud radars and microwave radiometers (MWR)) which have allowed new insights, by providing continuous time series of cloud-base height (CBH), cloud-top height (CTH) and LWP, together with the radiosonde profiles. Numerical simulations were also important for quantifying the impacts of the observed variability on the processes which affect the fog dissipation. One of the main conclusions to draw is that processes at fog top can be at least as important as the processes near the ground for fog dissipation, and that more observations of the layer above fog top are needed to quantify the processes responsible for fog dissipation.

We will now go through the main conclusions. Section 6.1 concludes on the observed patterns of fog dissipation and the relationship found between LWP and fog thickness, section 6.2 provides conclusions from our investigations about the processes affecting the evolution of the fog layer, while perspectives for future work are given in section 6.3.

6.1 Observed patterns in continental fog dissipation

The 7 years with 250 fog events at SIRTA observatory (4 years with cloud radar data) allowed a statistical study of the macroscopic properties of the fog layers and the way fog dissipates. The most frequent dissipation time is around sunrise or in the following 4 hours (section 2.2). The fog events dissipating at night are usually short-lived (<3 h) compared to those dissipating after sunrise. Moreover, we also showed that the majority of the fog events dissipating after sunrise transitions into a low stratus which lasts for at least 2 h (below 400 m). Our investigations have therefore focussed on understanding the factors which determine when the cloud base lifts from the ground, thus leading to

fog dissipation:

- **Critical LWP:** We found that the lifting of fog into stratus can in most cases be explained by a deficit in LWP relative to fog thickness: the higher the fog top, the more LWP is needed for the fog to stay at the surface (section 5.2). This critical LWP can be well described by the model of LWC profile of Cermak and Bendix (2011, CB2011) with $\beta_1 = 0.3$, both for thin fog (100 m) and thick fog (400 m). The critical LWP increases more than linearly with CTH, being 6 g m^{-2} at 100 m, 29 g m^{-2} at 200 m, and 131 g m^{-2} at 400 m. Fog dissipation therefore depends to the first order on LWP and CTH, which together determine the CBH. In 1/3 of the fog events, the LWP increases at dissipation (section 2.5.1), which can be explained by CTH increasing simultaneously (section 5.2). The tracked LWP and CTH do in some cases evolve gradually, allowing an anticipation of the time of dissipation. However, their tendencies are more often irregular and abrupt. The evolutions of LWP and CTH therefore need to be understood and predicted in order to anticipate fog dissipation.
- **Tracking LWP and CTH:** The combination of ceilometer, cloud radar and MWR can track the evolutions of these two parameters to diagnose the dissipation of fog layers. The CTH is derived from the cloud radar (section 2.3), the LWP from the MWR (section 2.5.1), and the actual CBH is observed by the ceilometer and used to evaluate the lifting of the fog into stratus diagnosed by the CB2011 model. A cloud radar with high vertical resolution is essential for such an analysis, since it is the only instrument which can determine the CTH with precision. The cloud radar used in this study has a very low blind-zone, which is also necessary to be able to detect the CTH of thin fog. The cloud radar is also necessary to detect the higher clouds which may contain liquid water and therefore cause bias in the MWR LWP retrieval.
- **Profile of radar reflectivity:** We performed and analysed three field campaigns where an in situ particle counter was lifted by a tethered balloon in the range 0–300 m in fog which was simultaneously measured with the cloud radar (Dupont et al., 2018). The results show that the radar reflectivity can be related to LWC with a similar relationship to what is found for other clouds. The vertical profile of radar reflectivity also shows a variety of patterns during fog (Fig. 5.5). In particular, in several fog events the radar reflectivity decreases when the fog base lifts from the ground, and the altitude of the max value of the reflectivity moves upwards towards the fog top, which indicates that droplet sizes decrease in the lower levels (Fig. 5.19). In other situations, the max value is in the middle of the fog layer, which indicates important downward transport of the larger droplets. The magnitude of reflectivity in the fog is mostly in the range -40 to -15 dBZ (when there is not rain), and sensitivity and calibration are important to detect the whole profile and its absolute magnitude, as shown by the comparison of two generations of the cloud radar system (section 2.4.2).

6.2 Understanding the evolutions of LWP and CTH

Given that the two main parameters impacting fog dissipation are the LWP and CTH, we have investigated how these variables are impacted by different processes. Since the SIRTA observatory observes the vertical profile in detail, we have focussed on the local processes that occur in the 1D atmospheric column. To understand how the radiative, dynamical and microphysical processes impact LWP and CTH in different situations, we applied two comprehensive models. The radiative processes

were studied using the radiative transfer code ARTDECO, detailed in our first paper (Wærsted et al., 2017, W17, provided in section 3.1), and the dynamical and microphysical processes were studied with the large-eddy simulation (LES) model DALES, detailed in a second paper (Wærsted et al., 2018, W18, provided in section 4.1). These modelling studies allowed an interpretation of the variability we observe. The main findings are summarised and shown schematically in Table 6.1, complemented by the results of some other studies. Our findings are further described in the bullet points below.

Based on these findings, a conceptual model was developed to estimate the tendencies of LWP and CTH directly from observations (section 5.3). It uses 12 parameters derived from observations at the SIRTA observatory (screen temperature, fog base and top, clouds above, LWP, IWV, MWR temperature profile, surface net short-wave (SW) and long-wave (LW) radiation, ground heat flux, aerodynamic resistance, and visibility) and two parameters obtained from the reanalysis ERA5 (relative humidity above fog top, and large-scale vertical velocity).

- **LWP equation:** We developed a conceptual framework to understand the impacts of the processes on LWP (detailed in section 3.3 of W18 and in section 5.3 of the thesis). Assuming that the fog layer is saturated and well-mixed, it is reduced to a zero-dimensional system, based on the method by Van der Dussen et al. (2014) adjusted to fog. The well-mixed assumption is reasonable for thick fog, especially after sunrise, due to the destabilisation processes, confirmed by evidence of saturated adiabatic fog profiles from radiosondes in day and night (section 2.6). This diagnostic method takes into account the temperature dependency of the evaporative effects of heat and water vapour fluxes, and it allowed us to quantify the impact of each process on the LWP and to study the sensitivity of these impacts to varying boundary conditions. We showed that this method successfully closes the LWP budget of the modelled fog in the LES (W18).
- **LW radiation:** Using the comprehensive radiation code ARTDECO, we quantified the radiative cooling in fog by LW radiation and its variability (W17). When the fog is opaque to LW radiation (LWP $>\approx$ 30 g m^{-2}), LW cooling at fog top produces 40–70 g m^{-2} h^{-1} of liquid water when the sky is clear above. This is sufficient to renew the fog LWP in 0.5–2 h, making it the main process for maintaining the fog water against other processes which deplete it. The variability in the production is due to the integrated water vapour (IWV) above fog top, fog temperature and inversion strength above. When $LWP <\approx$ 30 g m^{-2}, the fog is semi-transparent to LW radiation and the cooling is therefore weaker and depends importantly on LWP. Since the fog statistically has LWP $<$ 30 g m^{-2} h^{-1} nearly half the time (section 2.5.1), the dependency of the LW cooling on LWP is very relevant for its LWP budget. When higher clouds appear above the fog, the LWP production from LW radiative cooling is importantly reduced. Even semi-transparent clouds reduce drastically the production of LWP. The effect is much stronger for a low cloud than a high cloud, since it is warmer. Sensitivity studies showed that a cloud at 2 km can reduce the LW cooling to zero when its optical depth is 4 or more, while an ice cloud at 10 km only reduces it by 20–30 %. The key parameters affecting this production by LW cooling can be observed by a cloud radar (CTH, clouds above) and a MWR (LWP, IWV, stratification).
- **SW radiation:** The impact of SW radiation after sunrise was also studied using the ARTDECO code (W17). The absorption in fog of SW radiation constitutes a sink of LWP with a magnitude reaching 5–15 g m^{-2} h^{-1} near winter midday, increasing with fog LWP, and it can be enhanced importantly by absorbing aerosols (a population of urban aerosols with dry aerosol optical depth

of 0.15 and single scattering albedo of 0.82 caused an increase of 100 %, while the more typical conditions of aerosol optical depth 0.05 caused a 30 % increase). In average, the SW radiation at the surface can be reproduced by the delta-Eddington scheme by assuming a number concentration of 200 cm^{-3} and an extinction by non-activated aerosols of 0.01 m^{-1}, found by comparing modelled and measured SW radiation at the surface (sections 3.2.2, 3.3). This indicates that the droplet number concentration increases with height, since typical measurements at 4 m (by FM-120) show that the number concentration is mostly below 150 cm^{-3} (Fig. 2.10).

- **Surface turbulent heat fluxes:** The turbulent heat fluxes from the surface are likely the most important sink of the fog LWP after sunrise, and we estimated its impact to 10–30 g m^{-2} h^{-1} for solar zenith angles corresponding to winter midday (≈70°, or $\mu_0 \approx 0.3$) (Fig. 5.14c). The impact that these fluxes have on LWP is sensitive to the Bowen ratio. Using the LES model, we found that the Bowen ratio in fog is sensitive to the liquid water present on the surface, which enhances the latent heat flux and thereby delays dissipation. The delay was 85 min in our sensitivity test comparing a dry surface (but with high soil moisture below) with a surface of which 50 % is covered by liquid (W18). An important seasonal cycle is found in the dissipation time of fog present at sunrise (Fig. 5.1), with several events near the winter solstice lasting the entire day, which does not occur in other seasons. This seasonality is likely due to the weaker insolation at winter solstice, which limits the LWP loss from surface fluxes, as well as the loss from SW absorption (Fig. 5.15bc).
- **Entrainment:** Entrainment is an important process for fog dissipation, since it can act both to increase CTH and decrease LWP. Using LES, we found evidence that the observed variability (from 47 radiosondes) in stratification and humidity above fog top has an important impact on the time of dissipation (W18). A strong stratification above fog top inhibits the vertical development of CTH, thereby delaying the lifting of the CBH. In our sensitivity test, the dissipation time was delayed by 90 min in a run with strong stratification ($d\theta$=11 K) relative to a run with weak stratification ($d\theta$=4 K) (see Fig. 3 in W18 for a definition of $d\theta$ and its observed variability). Dry air above fog top enhances the loss of LWP by entrainment (up to 30 g m^{-2} h^{-1}, as opposed to only a few g m^{-2} h^{-1} when the air above is near saturation), thereby causing an earlier lifting of the CBH (70 min earlier in our sensitivity test with the LES), even when the entrainment velocity is not much affected. We further calculated the entrainment velocity in many observed cases with an entrainment parametrisation using the stratification and buoyancy production in the fog layer (based on the parametrisation of Gesso et al. (2014), section 5.3.3). We found that the entrainment velocity calculated using this method is correlated to the observed evolution of CTH in the fog events after sunrise, although there is a large spread which can be due to advection (section 5.4.3).
- **Subsidence:** Both negative and positive large-scale vertical velocity occur during the fog events at SIRTA (from ERA5), but negative velocity (subsidence) is slightly more frequent (Fig. 4.1a). It is rarely more than 10–20 m h^{-1} at fog top, which corresponds to a gain or loss of LWP of about 10 g m^{-2} h^{-1} or less (Fig. 5.14fh). Because subsidence reduces both CTH and LWP, the effect on fog dissipation is not very strong. Both the LES model (section 4.2) and the CB2011 model (section 5.3.4) indicate that a negative large-scale velocity (subsidence) weakly favours earlier fog dissipation, because the reduction in LWP caused by subsidence is slightly stronger than the reduction in critical LWP through CTH reduction. Nevertheless, the fog events which

Process / Key parameter	Observation technique	CTH	LWP	CBH	Reference
LW cooling		→ ↗	↗ ↘	↘ ↗	***TT (W17)***
fog LWP(+)	MWR	→	↗	↘	
clouds above (–)	cloud radar	→	↘	↗	
IWV above (–)	MWR + cloud radar	→	↘	↗	
fog-top temperature (+)	cloud radar + 2-m temp.	→	↗	↘	
stratification above (–)	MWR + cloud radar	→	↘	↗	
SW absorption		→ ↘	↘ ↗	↗ ↘	***TT (W17)***
solar elevation angle (+)	calculated	→	↘	↗	
LWP (+)	MWR	→	↘	↗	
absorbing aerosols (+)	sun photometer (before fog)	→	↘	↗	
clouds above (–)	cloud radar	→	↗	↘	
Surface turbulent heat fluxes		→ ↗	↘ ↘	↗ ↗	***TT***
surface net radiation (+)	pyrano- & pyrgeometers	→ ↗	↘ ↘	↗ ↗	TT (W17)
solar elevation angle (+)	calculated	→	↘	↗	
LWP (–)	MWR	→	↗	↘	
clouds above (–)	cloud radar	→	↗	↘	
Bowen ratio (SH/LE) (+)	eddy covariance / scintillometer	→ →	↘ →	↗ →	TT (W18)
liquid on surface (–)		→	↗	↘	W18
soil moisture⋆ (–)	soil moisture sensor	→	↗	↘	MB17
soil/veg. heat storage (–)	heat flux sensor	→ ↘	↗ ↘	↘	
Subsidence		↘	↘	↗	***TT***
negative w_{ls} at fog top (+)	NWP	↘	↘	↗	
Entrainment		↗	↘	↗	***TT (W18)***
w_e (+)		↗	↘	↗	G14
stratification above (–)	MWR	↘	↗	↘	TT (W18)
buoyancy (+)		↗	↘	↗	G14
wind shear at CTH⋆ (+)	sodar	↗	↘	↗	B16
RH_{ab} (–)	radiosonde	→	↘	↗	TT (W18)
Deposition		→	↘	↗	
LWC near surface (+)	granulometer / visibility	→	↘	↗	K14
big droplets (+)	granulometer / Doppler cloud radar	→	↘	↗	TT / D12
10-m wind speed⋆ (+)	anemometer	→	↘	↗	K14
surface properties⋆		variable impacts			K14

Table 6.1: Summary of the impacts of each local process on the CTH and LWP of the fog, and consequently on its CBH (↗ means an increase, ↘ means a decrease, and → that it does not have a direct impact). For each process, the key parameters that impact the process are indicated, followed by (+) if they enhance the process or (–) if they inhibit the process, when they increase in magnitude. Some of the key parameters also have parameters which can be used to estimate them if they are not directly observed (indicated by a further indent in the table). The importance of the impacts on CTH, LWP and CBH of each parameter are indicated by the length of the arrow. Also indicated are the (measurement) techniques which can be used to observe each parameter, and where the importance of this parameter was studied (TT = this thesis, W17 = Wærsted et al. (2017), W18 = Wærsted et al. (2018), B16 = Bergot (2016), D12 = Dupont et al. (2012), G14 = Gesso et al. (2014), K14 = Katata (2014), MB17 = Maronga and Bosveld (2017)). For subsidence, the effects are opposite of what is shown if the large-scale vertical velocity is positive. The buoyancy is a special case, as its magnitude depends on the first three processes of the table (heat fluxes from radiation and the surface, see Fig. 5.7). This indirect effect of the first three processes is indicated with red arrows. The red arrows are not repeated for all the key parameters of these processes, to limit the complexity of the table. A star marks parameters that have not been studied in this thesis.

persist for the entire day have systematically subsidence, and stronger subsidence than the other events (Fig. 5.16b). This correlation between subsidence and persistence is likely related to other synoptic conditions occurring together with subsidence.

6.3 Perspectives

This thesis has performed a quantitative analysis of the LWP budget and cloud-top evolution of fog and attempted to explain the observed evolutions of LWP and CTH with the local processes. We have discovered that some important parameters need to be better quantified than what is possible with the current observations, and we have also found evidence that processes that we do not currently account for have an important impact on the evolutions of many of the fog events. There are therefore several possible tracks to follow for further advancing our understanding of processes driving fog dissipation.

- **Non-local processes:** Observed fog cases show that the LWP and CTH often change abruptly and have tendencies that likely cannot be explained by the local processes. This indicates that observations of the non-local processes are needed to better understand the fog evolution. Therefore, a next step could be to integrate the conceptual framework into an NWP model (in a similar way as was done in the LES in W18), which also can take into account the advection and horizontal heterogeneities. The SIRTA column could be used as an evaluation and a separate quantification of the impacts of the local processes. The horizontal variability in cloud thickness and LWP can also be studied using geostationary satellites and a scanning cloud radar.
- Spatial variability of LWP and CTH are likely due to spatial variability in the processes that determine these two parameters. Such variability could be due to differences in surface properties (albedo, heat capacity, soil moisture, water on the surface) which could affect the surface available energy and the Bowen ratio, thereby impacting the LWP budget through the surface flux term and also the entrainment velocity through buoyancy. The heterogeneous surface conditions will also impact fog formation time and spatial extent (Gultepe et al., 2007), which affects the LWP and CTH variability as well. The variability could also be due to the upper fog boundary: if the stratification and humidity varies in the horizontal, it could lead to variability in LWP and CTH through entrainment. This heterogeneity might be further increased by the feedbacks in LW radiation (LW cooling increasing with LWP) and SW radiation (more radiation reaching the surface where the fog LWP is lower). The understanding of horizontal variability of fog could be improved by documenting the variability in the properties at fog top and at the surface. Nevertheless, LES simulations have shown that important horizontal variability in LWP and dissipation time can also occur without any heterogeneity of the boundary conditions (Bergot, 2016).
- **Cloud radar evolutions:** The cloud radar is found to be a key instrument for analysing the fog, since it detects the cloud top, clouds above and gives a vertical profile which is related to the droplet sizes. However, some improvements would make it even more useful. Firstly, an increased sensitivity would let the cloud radar detect all important clouds that impact the LW radiative cooling and the MWR LWP retrieval. The sensitivity of the BASTA-SIRTA cloud radar deployed until 2016 was insufficient to detect clouds with small droplet sizes, which can affect the LW radiative cooling of the fog. The BASTA-MOBILE, installed in the 2016–17 season, has

significantly improved sensitivity. It should be investigated whether the present sensitivity of BASTA is sufficient to detect all important clouds.

- Secondly, a scanning capability of the radar, i.e. being able to rotate to measure in several different directions, would allow a better documentation of the spatial variability of fog and to further reduce the blind-zone relative to vertical observation. The scanning capability might also give a better indication of the cloud cover above fog top in cases when it is fractional.
- Thirdly, an analysis of the Doppler spectrum of the backscattered signal could provide additional information about the microphysical properties in the fog, and possibly the turbulent structures (see separate point above turbulence observations below).
- **Cloud retrievals:** To better quantify the radiative impacts of the detected clouds above the fog, an algorithm for a rough estimate of the optical depth of a cloud based on its radar observations (altitude, thickness, reflectivity, Doppler velocity) should be developed. An improved sensitivity is important for this sort of retrieval, since the clouds need to be clearly observed with a consistent backscatter if a robust interpretation of these signals is to be performed.
- The profile of reflectivity is related to the microphysical properties of the fog layer, in particular to the sizes of the droplets at different altitudes in the fog. The important variability that we found in this profile during fog (Fig. 5.5) might provide an additional information about the sedimentation processes which could improve the CB2011 model of critical LWP (more sedimentation might allow a thicker fog for a given LWP). Furthermore, the relationship between reflectivity and LWC (section 2.4.3), although only approximate, can be valuable to estimate the LWP in situations where the MWR LWP is perturbed by higher liquid water clouds. For the retrieval of LWC, it is important that the cloud radar is calibrated. The SIRTA observatory currently works on developing and testing reliable and robust methods for calibrating cloud radars.
- **The Bowen ratio:** The eddy-covariance measurements at SIRTA cannot close the surface energy balance sufficiently to conclude on the Bowen ratio during fog (W18). Since we also found similarly insufficient closure for another atmospheric observatory (Cabauw, the Netherlands) for a similar late autumn period as the one considered in W18, it seems to be an issue not only for the SIRTA location. The Bowen ratio in fog has not received much attention in previous studies of fog, but our findings of how sensitive the LWP budget is to it shows that it merits more attention. Our result that water on the ground inhibits fog dissipation needs to be evaluated by observational studies. It would also be very helpful if a measurement technique could quantify the Bowen ratio during fog with precision, as this would allow a validation of the estimated impact of the surface turbulent heat fluxes on LWP in our conceptual model. We could then also find out how much variability in this process can be attributed to variations in the Bowen ratio which are not captured by the current method where we use the Penman-Monteith equation with a constant c_{dry} (section 5.3.2). New instruments could be deployed to better monitor the temporal and spatial variability of the heat fluxes at the surface and along the vertical, such as scintillometers. This might allow for a better quantification of the surface energy balance in fog, which may vary importantly in the horizontal due to variability in e.g. soil moisture and surface liquid water.
- **Entrainment:** The entrainment parametrisation applied in our conceptual model was origi-

nally developed for stratocumulus layers, and by comparing with the entrainment produced by the LES, we found that the entrainment rate is underestimated by the parametrisation. The entrainment velocity is 2–3 times larger in the LES than when the same profiles are put into the parametrisation. However, the relative increase in entrainment velocity due to a decreased stratification is very similar in the parametrisation and the LES (Fig. 5.25). This indicates that the entrainment parametrisation needs to be adjusted to work correctly for fog but that the dependency on stratification is already correctly captured. To get an entrainment parametrisation which produces reliable values for fog, the coefficients of the parametrisation could be adjusted by sensitivity studies with an LES model. Preferably, this modified entrainment parametrisation should be validated using observations by cloud radar and MWR during fog, but it would not be trivial since effects of advection would have to be corrected for in some way, since we found that advection can hide the observed entrainment signal (section 5.4.3).

- The impact of entrainment on the fog LWP depends importantly on the humidity in the layer directly above fog top. The humidity of this layer cannot currently be observed by remote sensing instruments with sufficient resolution, neither by the MWR (not sufficient vertical resolution) nor by differential absorption lidars (signal attenuated by the fog). The documentation of the humidity of this layer, either in situ by instruments lifted by drones/balloons or by some novel remote sensing technique, would be useful for understanding how strongly the entrainment affects the LWP of the fog.
- **Deposition:** The deposition is a difficult process to quantify because it is weak and heterogeneous, and our current formula using only visibility is clearly not very precise. However, there are parametrisations in the literature that could be tested, which would introduce more explanatory variables, such as the wind speed (Katata, 2014). The Doppler velocity of the cloud radar could likely be used as an indicator for cases with important sedimentation. However, to be able to evaluate the parametrisations, measurements of deposition are needed. Deposition can be measured by the eddy covariance method, using high-frequency LWC measurements (e.g. Degefie et al., 2015), or by weighing of different vegetation samples (Trautner and Eiden, 1988; Tav et al., 2018). The challenges with such measurements are (1) the representativeness of the measured flux for the whole fog–surface interface (both in the horizontal and vertical), and (2) the incapacity to separate deposition from evaporation, since droplets may evaporate below the altitude of eddy-covariance measurements, and net increase in deposited mass is offset by the surface evaporation. The second point is especially relevant for daytime fog, since the surface is heated.
- **Turbulence observations:** During the work with this thesis, we considered also the remote sensing of turbulent structures in the fog, but we did not advance sufficiently on this track to produce results to be shown in the thesis. However, the preliminary investigations showed that the active profiles might provide interesting information. The Doppler velocity, which from our radar is available at 12.5 m vertical resolution and 12 s temporal resolution, can reveal oscillating patterns of up- and downdrafts in the fog. The variance of the Doppler velocity may describe the activity level of the large eddies in the fog, which we found to vary importantly during the life cycle of a fog event (not shown). Wind variance products from the sodar could also be used to characterise the turbulence in the fog layer. The sodar would also be valuable for measuring the wind shear at fog top, which is an aspect of the entrainment which has not been much

investigated in this thesis, although our test in W18 indicates that it is much less important than the buoyancy. Retrievals of fog-top wind shear will usually not be available from Doppler lidars due to attenuation in the fog, making the sodar the appropriate instrument. To study the fog-top wind shear, it is important that the sodar has a sufficient vertical range, preferably at least 500 m, in order to reach the fog-top, which is frequently as high as 300–400 m (see Fig. 2.9), and the layer of wind shear above.

The points mentioned above are all possible tracks that could merit attention and help advance even further our understanding of fog processes and our capacity to observe them.

Table of symbols and acronyms

Here follows an alphabetic list of definitions of the symbols and acronyms used in this thesis. The symbols starting with a Greek letter are at the end. Some symbols that are only used in one particular section are not included in this table; their explanation can be found in the concerned sections.

Symbol	**Meaning**
AOD	aerosol optical depth
ARTDECO	the radiative transfer code applied in W17
BASTA	the cloud radar used in this thesis (Delanoë et al., 2016)
BL	the atmospheric boundary layer
CB2011	The LWC model of Cermak and Bendix (2011) applied with $\beta_1 = 0.3$ (section 5.2)
CBH	cloud-base height
CBH CB2011	CBH calculated with the model of CB2011
CCN	cloud-condensation nucleus
C_{LW}	integrated condensation rate in fog due to LW cooling (g m^{-2} h^{-1}) (W17)
C_{rad}	condensation rate due to radiative cooling (g m^{-3} h^{-1}) (W17)
CTH	cloud-top height
c_{dry}	fraction of the surface not covered by liquid, in surface parametrisation (section 5.3.2)
c_{liq}	$1 - c_{dry}$
c_p	specific heat capacity of air (1004 J kg^{-1} K^{-1})
D	droplet diameter
DALES	the LES model used in W18
D_{eff}	effective diameter (section 1.2.3)
D_{min}, D_{max}	lowest and highest diameter considered to be droplets (section 1.2.3)
DSD	droplet size distribution (section 1.2.3)
$d\theta$	stratification at fog top, measured as difference in θ between screen level and 200 m above fog top
E	surface evaporation rate (g m^{-2} h^{-1})
E_a	vertically integrated evaporation rate of the fog (g m^{-2} h^{-1})
ECMWF	European Centre for Medium-Range Weather Forecasts
ERA5	a reanalysis created by the ECMWF
E_{SW}	integrated evaporation rate in fog due to absorption of SW radiation (g m^{-2} h^{-1}) (W17)
e_a	water vapour pressure in the air

e_s	saturation water vapour pressure
F_{dep}	flux of mass deposition of droplets on the surface (g m^{-2} h^{-1})
F_l	vertical flux of liquid water at fog top or base (g m^{-2} h^{-1}) (W18)
FM-120	an instrument measuring the DSD of fog (Table 2.1)
FMCW	frequency-modulated continuous wave technique (Delanoë et al., 2016)
F_{net}	net radiative flux (SW or LW)
F_{sed}	downward sedimentation flux of droplet mass (g m^{-2} h^{-1})
G	heat flux into the ground (W m^{-2})
g	acceleration of gravity (9.81 m s^{-2})
HATPRO	the model of MWR used in this thesis
h	fog-top height
IWV, IWV$_{ab}$	integrated water vapour in the whole atmospheric column, and above the fog (kg m^{-2})
k_{St}	Stokes' constant for droplet fall velocity (Eq. 5.45)
LAI	leaf–area index
LES	large-eddy simulation
LH	Latent heat flux (W m^{-2})
LOAC	light optical aerosol counter (Renard et al., 2016)
LW	long-wave (radiation)
LWC	liquid water content (g m^{-3})
LWP	liquid water path (vertical integral of LWC, g m^{-2})
LWP^{crit}	critical LWP for the fog to stay at the surface, according to the CB2011 model (section 5.2)
LWP^{mod}	modelled LWP with the CBH CB2011 model (section 5.2)
L_v	specific heat of vaporisation ($2.5 \cdot 10^6$ J kg^{-1})
MWR	microwave radiometer
N_c	droplet number concentration
NWP	numerical weather prediction
$n(D)$	droplet size distribution function (section 1.2.3)
$n(r)$	As $n(D)$, but defined w.r.t. radius instead of diameter
OD	optical depth
p	air pressure
Q_{ext}	extinction efficiency of droplets ($Q_{ext} \approx 2$) (section 1.2.3)
q_l	liquid water mixing ratio (g kg^{-1})
q_{sat}	saturation specific humidity (g kg^{-1})
q_v	specific humidity (g kg^{-1})
RH	relative humidity
RMS	root-mean-square
R_d	ideal gas constant for dry air (287.0 J kg^{-1} K^{-1})
$R_{net}/R_{net,s}$	net radiation (SW+LW) absorbed at the surface (W m^{-2})
R_v	ideal gas constant for water vapour (461.5 J kg^{-1} K^{-1})
r	droplet radius
r_a	aerodynamic resistance (s m^{-1}) (section 5.3.2)

r_e/r_{eff}	effective radius (r_{eff}=$D_{eff}/2$)
r_s	surface resistance (s m^{-1}) (section 5.3.2)
SH	sensible heat flux (W m^{-2})
SIRTA	Site Instrumental de Recherche par Télédétection Atmosphérique (section 2.1), the observatory from which the observations used in this thesis come
SW	short-wave (radiation)
SW_0	incoming direct SW radiation at fog top in the SW parametrisation (W m^{-2}) (section 3.2.2)
s	change of e_s with temperature (Pa K^{-1})
T	(air) temperature
T_a	screen-level air temperature
T_c	temperature of a cloud above the fog
TKE	turbulent kinetic energy (m^2 s^{-2})
UTC	Coordinated Universal Time
Vis	visibility (distance) (m)
W17	Wærsted et al. (2017), provided in section 3.1
W18	Wærsted et al. (2018), provided in section 4.1
w_e	entrainment velocity (see section 5.3.3)
w_{ls}	large-scale vertical velocity
Z	radar reflectivity (mm^6 m^{-3}) (Eq. 2.1)
z_b	cloud-base height
z_t	cloud-top height
α_{ext}	extinction coefficient (m^{-1}) (visible wavelengths)
β	subadiabaticity coefficient (see section 5.2)
Γ_s	saturated adiabatic lapse rate (K m^{-1})
γ	psychrometric constant: $\gamma \equiv \frac{c_p p}{\epsilon L_v}$
ϵ	R_d/R_v
ϵ_c	emissivity (in LW) of a cloud above the fog
ϵ_f	emissivity (in LW) of the fog
θ	potential temperature
θ_v	virtual potential temperature
κ	Increase of adiabatic LWC with height (g m^{-4}) (see section 5.2)
μ_0	cosine of the solar zenith angle
ρ_a	air density (kg m^{-3})
ρ_l	liquid water density (ρ_l = 10^3 kg m^{-3})
ρ_s	saturation water vapour density (g m^{-3})
σ	Stefan-Boltzmann's constant (5.67·10^{-8} W m^{-2} K^{-4})
σ_g	geometric standard deviation in the log-normal DSD

Bibliography

American Meteorological Society (2017). "Fog", "Haze", "Raindrop", "Visibility", Glossary of Meteorology. [Available online at http://glossary.ametsoc.org/wiki/Fog]. Accessed: 2018-07-09.

Atlas, D. (1954). The estimation of cloud parameters by radar. *Journal of Meteorology*, 11(4):309–317. https://doi.org/10.1175/1520-0469(1954)011<0309:TEOCPB>2.0.CO;2.

Barrie, L. and Schemenauer, R. (1986). Pollutant wet deposition mechanisms in precipitation and fog water. *Water, Air, and Soil Pollution*, 30(1-2):91–104.

Bergot, T. (2013). Small-scale structure of radiation fog: a large-eddy simulation study. *Quarterly Journal of the Royal Meteorological Society*, 139(673):1099–1112. https://doi.org/10.1002/qj.2051.

Bergot, T. (2016). Large-eddy simulation study of the dissipation of radiation fog. *Quarterly Journal of the Royal Meteorological Society*, 142(695):1029–1040. https://doi.org/10.1002/qj.2706.

Bergot, T., Terradellas, E., Cuxart, J., Mira, A., Liechti, O., Mueller, M., and Nielsen, N. W. (2007). Intercomparison of single-column numerical models for the prediction of radiation fog. *Journal of applied meteorology and climatology*, 46(4):504–521. https://doi.org/10.1175/JAM2475.1.

Błaś, M., Sobik, M., Quiel, F., and Netzel, P. (2002). Temporal and spatial variations of fog in the Western Sudety Mts., Poland. *Atmospheric Research*, 64(1-4):19–28. https://doi.org/10.1016/S0169-8095(02)00076-5.

Boris, A. J., Napolitano, D. C., Herckes, P., Clements, A. L., and Collett Jr, J. L. (2018). Fogs and air quality on the Southern California Coast. *Aerosol and Air Quality Research*, 18(1):224–239. https://doi.org/10.4209/aaqr.2016.11.0522.

Brenguier, J.-L., Pawlowska, H., Schüller, L., Preusker, R., Fischer, J., and Fouquart, Y. (2000). Radiative properties of boundary layer clouds: Droplet effective radius versus number concentration. *Journal of the atmospheric sciences*, 57(6):803–821. https://doi.org/10.1175/1520-0469(2000)057%3C0803:RPOBLC%3E2.0.CO;2.

Brown, R. and Roach, W. T. (1976). The physics of radiation fog: II–a numerical study. *Quarterly Journal of the Royal Meteorological Society*, 102(432):335–354. https://doi.org/10.1002/qj.49710243205.

Caumont, O., Cimini, D., Löhnert, U., Alados-Arboledas, L., Bleisch, R., Buffa, F., Ferrario, M. E., Haefele, A., Huet, T., Madonna, F., et al. (2016). Assimilation of humidity and temperature observations retrieved from ground-based microwave radiometers into a convective-scale NWP model. *Quarterly Journal of the Royal Meteorological Society*, 142(700):2692–2704. https://doi.org/10.1002/qj.2860.

Cermak, J. and Bendix, J. (2011). Detecting ground fog from space – a microphysics-based approach. *International journal of remote sensing*, 32(12):3345–3371. https://doi.org/10.1080/01431161003747505.

Conzemius, R. J. and Fedorovich, E. (2006). Dynamics of sheared convective boundary layer entrainment. Part II: Evaluation of bulk model predictions of entrainment flux. *Journal of the atmospheric sciences*, 63(4):1179–1199. https://doi.org/10.1175/JAS3696.1.

Degefie, D., El-Madany, T.-S., Hejkal, J., Held, M., Dupont, J.-C., Haeffelin, M., and Klemm, O. (2015). Microphysics and energy and water fluxes of various fog types at SIRTA, France. *Atmospheric research*, 151:162–175. https://doi.org/10.1016/j.atmosres.2014.03.016.

Delanoë, J., Protat, A., Bouniol, D., Heymsfield, A., Bansemer, A., and Brown, P. (2007). The characterization of ice cloud properties from Doppler radar measurements. *Journal of Applied Meteorology and Climatology*, 46(10):1682–1698. https://doi.org/10.1175/JAM2543.1.

Delanoë, J., Protat, A., Vinson, J.-P., Brett, W., Caudoux, C., Bertrand, F., Parent du Chatelet, J., Hallali, R., Barthes, L., Haeffelin, M., and Dupont, J.-C. (2016). BASTA: A 95-GHz FMCW Doppler Radar for Cloud and Fog Studies. *Journal of Atmospheric and Oceanic Technology*, 33(5):1023–1038. https://doi.org/10.1175/JTECH-D-15-0104.1.

Dollard, G., Unsworth, M., and Harve, M. (1983). Pollutant transfer in upland regions by occult precipitation. *Nature*, 302(5905):241.

Dong, X. and Mace, G. G. (2003). Profiles of low-level stratus cloud microphysics deduced from ground-based measurements. *Journal of Atmospheric and Oceanic Technology*, 20(1):42–53. https://doi.org/10.1175/1520-0426(2003)020%3C0042:POLLSC%3E2.0.CO;2.

Duntley, S. Q. (1948). The reduction of apparent contrast by the atmosphere. *JOSA*, 38(2):179–191. https://doi.org/10.1364/JOSA.38.000179.

Dupont, J., Haeffelin, M., Stolaki, S., and Elias, T. (2016). Analysis of dynamical and thermal processes driving fog and quasi-fog life cycles using the 2010–2013 ParisFog dataset. *Pure and Applied Geophysics*, 173(4):1337–1358. https://doi.org/10.1007/s00024-015-1159-x.

Dupont, J.-C. and Haeffelin, M. (2008). Observed instantaneous cirrus radiative effect on surface-level shortwave and longwave irradiances. *Journal of Geophysical Research: Atmospheres*, 113(D21). https://doi.org/10.1029/2008JD009838.

Dupont, J.-C., Haeffelin, M., Drobinski, P., and Besnard, T. (2008). Parametric model to estimate clear-sky longwave irradiance at the surface on the basis of vertical distribution of humidity and temperature. *Journal of Geophysical Research: Atmospheres*, 113(D7). https://doi.org/10.1029/2007JD009046.

Dupont, J.-C., Haeffelin, M., Protat, A., Bouniol, D., Boyouk, N., and Morille, Y. (2012). Stratus–fog formation and dissipation: a 6-day case study. *Boundary-layer meteorology*, 143(1):207–225. https://doi.org/10.1007/s10546-012-9699-4.

Dupont, J.-C., Haeffelin, M., Wærsted, E., Delanoe, J., Renard, J.-B., Preissler, J., and O'Dowd, C. (2018). Evaluation of fog and low stratus cloud microphysical properties derived from in situ sensor, cloud radar and SYRSOC algorithm. *Atmosphere*, 9(5):169. https://doi.org/10.3390/atmos9050169.

ECMWF (2016). *IFS Documentation Cy43r1*, chapter "Part IV: Physical processes". ECMWF.

Elias, T., Haeffelin, M., Drobinski, P., Gomes, L., Rangognio, J., Bergot, T., Chazette, P., Raut, J.-C., and Colomb, M. (2009). Particulate contribution to extinction of visible radiation: pollution, haze, and fog. *Atmospheric Research*, 92(4):443–454. https://doi.org/doi:10.1016/j.atmosres.2009.01.006.

Fabbian, D., de Dear, R., and Lellyett, S. (2007). Application of artificial neural network forecasts to predict fog at Canberra International Airport. *Weather and forecasting*, 22(2):372–381. https://doi.org/10.1175/WAF980.1.

Fox, N. I. and Illingworth, A. J. (1997). The retrieval of stratocumulus cloud properties by ground-based cloud radar. *Journal of Applied Meteorology*, 36(5):485–492. https://doi.org/10.1175/1520-0450(1997)036<0485:TROSCP>2.0.CO;2.

Gaussiat, N., Hogan, R. J., and Illingworth, A. J. (2007). Accurate liquid water path retrieval from low-cost microwave radiometers using additional information from a lidar ceilometer and operational forecast models. *Journal of Atmospheric and Oceanic Technology*, 24(9):1562–1575. https://doi.org/10.1175/JTECH2053.1.

Gesso, S. D., Siebesma, A., de Roode, S., and van Wessem, J. (2014). A mixed-layer model perspective on stratocumulus steady states in a perturbed climate. *Quarterly Journal of the Royal Meteorological Society*, 140(684):2119–2131. https://doi.org/10.1002/qj.2282.

Gultepe, I., Müller, M. D., and Boybeyi, Z. (2006). A new visibility parameterization for warm-fog applications in numerical weather prediction models. *Journal of applied meteorology and climatology*, 45(11):1469–1480. https://doi.org/10.1175/JAM2423.1.

Gultepe, I., Pearson, G., Milbrandt, J., Hansen, B., Platnick, S., Taylor, P., Gordon, M., Oakley, J., and Cober, S. (2009). The fog remote sensing and modeling field project. *Bulletin of the American Meteorological Society*, 90(3):341–360. https://doi.org/10.1175/2008BAMS2354.1.

Gultepe, I., Tardif, R., Michaelides, S. C., Cermak, J., Bott, A., Bendix, J., Müller, M. D., Pagowski, M., Hansen, B., Ellrod, G., Jacobs, W., Toth, G., and Cober, S. G. (2007). Fog research: A review of past achievements and future perspectives. *Pure and Applied Geophysics*, 164(6-7):1121–1159. https://doi.org/10.1007/s00024-007-0211-x.

Guyot, G., Gourbeyre, C., Febvre, G., Shcherbakov, V., Burnet, F., Dupont, J.-C., Sellegri, K., and Jourdan, O. (2015). Quantitative evaluation of seven optical sensors for cloud microphysical measurements at the Puy-de-Dôme Observatory, France. *Atmospheric Measurement Techniques*, 8(10):4347–4367. https://doi.org/10.5194/amt-8-4347-2015.

Haeffelin, M., Barthès, L., Bock, O., Boitel, C., Bony, S., Bouniol, D., Chepfer, H., Chiriaco, M., Cuesta, J., Delanoë, J., Drobinski, P., Dufresne, J.-L., Flamant, C., Grall, M., Hodzic, A., Hourdin, F., Lapouge, F., Lemaître, Y., Mathieu, A., Morille, Y., Naud, C., Noël, V., O'Hirok, B., Pelon, J., Pietras, C., Protat, A., Romand, B., Scialom, G., and Vautard, R. (2005). SIRTA, a ground-based atmospheric observatory for cloud and aerosol research. In *Annales Geophysicae*, volume 23, pages 253–275. hal-00329353.

Haeffelin, M., Bergot, T., Elias, T., Tardif, R., Carrer, D., Chazette, P., Colomb, M., Drobinski, P., Dupont, E., Dupont, J. C., Gomes, L., Musson-Genon, L., Pietras, C., Plana-Fattori, A., Protat, A., Rangognio, J., Raut, J.-C., Rémy, S., Richard, D., Sciare, J., and Zhang, X. (2010). Parisfog: shedding new light on fog physical processes. *Bulletin of the American Meteorological Society*, 91(6):767–783. https://doi.org/10.1175/2009BAMS2671.1.

Haeffelin, M., Dupont, J.-C., Boyouk, N., Baumgardner, D., Gomes, L., Roberts, G., and Elias, T. (2013). A comparative study of radiation fog and quasi-fog formation processes during the ParisFog field experiment 2007. *Pure and Applied Geophysics*, 170(12):2283–2303. https://doi.org/10.1007/s00024-013-0672-z.

Haeffelin, M., Laffineur, Q., Bravo-Aranda, J.-A., Drouin, M.-A., Casquero-Vera, J.-A., Dupont, J.-C., and De Backer, H. (2016). Radiation fog formation alerts using attenuated backscatter power from automatic lidars and ceilometers. *Atmospheric Measurement Techniques*, 9(11):5347–5365. https://doi.org/10.5194/amt-9-5347-2016.

Hautière, N., Labayrade, R., and Aubert, D. (2006). Real-time disparity contrast combination for onboard estimation of the visibility distance. *IEEE Transactions on Intelligent Transportation Systems*, 7(2):201–212. https://doi.org/10.1109/TITS.2006.874682.

Heus, T., Van Heerwaarden, C. C., Jonker, H. J., Siebesma, A. P., Axelsen, S., Van Den Dries, K., Geoffroy, O., Moene, A. F., Pino, D., De Roode, S. R., and others (2010). Formulation of the Dutch Atmospheric Large-Eddy Simulation (DALES) and overview of its applications. *Geoscientific Model Development*, 3(2):415. https://doi.org/10.5194/gmd-3-415-2010.

Horvath, H. and Noll, K. E. (1969). The relationship between atmospheric light scattering coefficient and visibility. *Atmospheric Environment (1967)*, 3(5):543–550. https://doi.org/10.1016/0004-6981(69)90044-4.

Hu, Y. and Stamnes, K. (1993). An accurate parameterization of the radiative properties of water clouds suitable for use in climate models. *Journal of climate*, 6(4):728–742. https://doi.org/10.1175/1520-0442(1993)006%3C0728:AAPOTR%3E2.0.CO;2.

Jarvis, P. (1976). The interpretation of the variations in leaf water potential and stomatal conductance found in canopies in the field. *Phil. Trans. R. Soc. Lond. B*, 273(927):593–610.

Katata, G. (2014). Fogwater deposition modeling for terrestrial ecosystems: A review of developments and measurements. *Journal of Geophysical Research: Atmospheres*, 119(13):8137–8159. https://doi.org/10.1002/2014JD021669.

Klemm, O., Schemenauer, R. S., Lummerich, A., Cereceda, P., Marzol, V., Corell, D., Van Heerden, J., Reinhard, D., Gherezghiher, T., Olivier, J., et al. (2012). Fog as a fresh-water resource: overview and perspectives. *Ambio*, 41(3):221–234. https://doi.org/10.1007/s13280-012-0247-8.

Köhler, H. (1936). The nucleus in and the growth of hygroscopic droplets. *Transactions of the Faraday Society*, 32:1152–1161. https://doi.org/10.1039/tf9363201152.

Koračin, D., Dorman, C. E., Lewis, J. M., Hudson, J. G., Wilcox, E. M., and Torregrosa, A. (2014). Marine fog: A review. *Atmospheric Research*, 143:142–175. https://doi.org/10.1016/j.atmosres.2013.12.012.

Koračin, D., Lewis, J., Thompson, W. T., Dorman, C. E., and Businger, J. A. (2001). Transition of stratus into fog along the California coast: Observations and modeling. *Journal of the atmospheric sciences*, 58(13):1714–1731. https://doi.org/10.1175/1520-0469(2001)058%3C1714:TOSIFA%3E2.0.CO;2.

Kotthaus, S., O'Connor, E., Münkel, C., Charlton-Perez, C., Haeffelin, M., Gabey, A. M., and Grimmond, C. S. B. (2016). Recommendations for processing atmospheric attenuated backscatter profiles from Vaisala CL31 ceilometers. *Atmospheric Measurement Techniques*, 9(8):3769–3791. https://doi.org/10.5194/amt-9-3769-2016.

Larson, V. E., Kotenberg, K. E., and Wood, N. B. (2007). An analytic longwave radiation formula for liquid layer clouds. *Monthly weather review*, 135(2):689–699. https://doi.org/10.1175/MWR3315.1.

Liou, K.-N. (2002). *An introduction to atmospheric radiation*, volume 84. Academic press, 2 edition.

Löhnert, U., Turner, D., and Crewell, S. (2009). Ground-based temperature and humidity profiling using spectral infrared and microwave observations. Part I: Simulated retrieval performance in clear-sky conditions. *Journal of Applied Meteorology and Climatology*, 48(5):1017–1032. https://doi.org/10.1175/2008JAMC2060.1.

Long, C. N. and Ackerman, T. P. (2000). Identification of clear skies from broadband pyranometer measurements and calculation of downwelling shortwave cloud effects. *Journal of Geophysical Research: Atmospheres*, 105(D12):15609–15626. https://doi.org/10.1029/2000JD900077.

Maalick, Z., Kühn, T., Korhonen, H., Kokkola, H., Laaksonen, A., and Romakkaniemi, S. (2016). Effect of aerosol concentration and absorbing aerosol on the radiation fog life cycle. *Atmospheric Environment*, 133:26–33. https://doi.org/10.1016/j.atmosenv.2016.03.018.

Maier, F., Bendix, J., and Thies, B. (2013). Development and application of a method for the objective differentiation of fog life cycle phases. *Tellus B: Chemical and Physical Meteorology*, 65(1):19971. https://doi.org/10.3402/tellusb.v65i0.19971.

Maronga, B. and Bosveld, F. (2017). Key parameters for the life cycle of nocturnal radiation fog: a comprehensive large-eddy simulation study. *Quarterly Journal of the Royal Meteorological Society*. https://doi.org/10.1002/qj.3100.

Martucci, G. and O'Dowd, C. (2011). Ground-based retrieval of continental and marine warm cloud microphysics. *Atmospheric Measurement Techniques*, 4(12):2749–2765. https://doi.org/10.5194/amt-4-2749-2011.

Matrosov, S. Y., Uttal, T., and Hazen, D. A. (2004). Evaluation of Radar Reflectivity–Based Estimates of Water Content in Stratiform Marine Clouds. *Journal of Applied Meteorology*, 43(3):405–419. https://doi.org/10.1175/1520-0450(2004)043%3C0405:EORREO%3E2.0.CO;2.

Mazoyer, M. (2016). *Impact du processus d'activation sur les propriétés microphysiques des brouillards et sur leur cycle de vie*. PhD thesis, Institut National Polytechnique de Toulouse, France.

Mazoyer, M., Lac, C., Thouron, O., Bergot, T., Masson, V., and Musson-Genon, L. (2017). Large eddy simulation of radiation fog: impact of dynamics on the fog life cycle. *Atmospheric Chemistry and Physics*, 17(21):13017. https://doi.org/10.5194/acp-17-13017-2017.

Menut, L., Mailler, S., Dupont, J.-C., Haeffelin, M., and Elias, T. (2014). Predictability of the meteorological conditions favourable to radiative fog formation during the 2011 ParisFog campaign. *Boundary-layer meteorology*, 150(2):277–297. https://doi.org/10.1007/s10546-013-9875-1.

Monteith, J. (1965). Evaporation and environment. p. 205–234. In *In GE Fogg (ed.) The state and movement of water in living organisms. Symp. of Soc. Exp. Biol. no. XIX, Swansea, UK. 8–12 Sept. 1964. Cambridge Univ. Press, Cambridge, UK.*

Nakanishi, M. (2000). Large-eddy simulation of radiation fog. *Boundary-layer meteorology*, 94(3):461–493. https://doi.org/10.1023/A:1002490423389.

Pasini, A., Pelino, V., and Potestà, S. (2001). A neural network model for visibility nowcasting from surface observations: Results and sensitivity to physical input variables. *Journal of Geophysical Research: Atmospheres*, 106(D14):14951–14959. https://doi.org/10.1029/2001JD900134.

Prata, A. (1996). A new long-wave formula for estimating downward clear-sky radiation at the surface. *Quarterly Journal of the Royal Meteorological Society*, 122(533):1127–1151. https://doi.org/10.1002/qj.49712253306.

Price, J. (2011). Radiation fog. Part I: observations of stability and drop size distributions. *Boundary-layer meteorology*, 139(2):167–191. https://doi.org/10.1007/s10546-010-9580-2.

Price, J., Porson, A., and Lock, A. (2015). An observational case study of persistent fog and comparison with an ensemble forecast model. *Boundary-Layer Meteorology*, 155(2):301–327. https://doi.org/10.1007/s10546-014-9995-2.

Renard, J.-B., Dulac, F., Berthet, G., Lurton, T., Vignelles, D., Jégou, F., Tonnelier, T., Jeannot, M., Couté, B., Akiki, R., Verdier, N., Mallet, M., Gensdarmes, F., Charpentier, P., Mesmin, S., Duverger, V., Dupont, J.-C., Elias, T., Crenn, V., Sciare, J., Zieger, P., Salter, M., Roberts, T., Giacomoni, J., Gobbi, M., Hamonou, E., Olafsson, H., Dagsson-Waldhauserova, P., Camy-Peyret, C., Mazel, C., Décamps, T., Piringer, M., Surcin, J., and Daugeron, D. (2016). LOAC: a small aerosol optical counter/sizer for ground-based and balloon measurements of the size distribution and nature of atmospheric particles – Part 1: Principle of measurements and instrument evaluation. *Atmospheric Measurement Techniques*, 9(4):1721–1742. https://doi.org/10.5194/amt-9-1721-2016.

Roach, W. (1995). Back to basics: Fog: Part 2 — the formation and dissipation of land fog. *Weather*, 50(1):7–11. https://doi.org/10.1002/j.1477-8696.1995.tb06053.x.

Rogers, R. R. and Yau, M. K. (1989). *A short course in cloud physics*. Elsevier, 3 edition.

Rose, T., Crewell, S., Löhnert, U., and Simmer, C. (2005). A network suitable microwave radiometer for operational monitoring of the cloudy atmosphere. *Atmospheric Research*, 75(3):183–200. https://doi.org/10.1016/j.atmosres.2004.12.005.

Sauvageot, H. and Omar, J. (1987). Radar reflectivity of cumulus clouds. *Journal of Atmospheric and Oceanic Technology*, 4(2):264–272. https://doi.org/10.1175/1520-0426(1987)004%3C0264:RROCC%3E2.0.CO;2.

Seely, M. and Henschel, J. R. (1998). The climatology of Namib fog. In *Proceedings of the First International Conference on Fog and Fog Collection*, pages 19–24.

Steeneveld, G. J., Ronda, R. J., and Holtslag, A. a. M. (2015). The Challenge of Forecasting the Onset and Development of Radiation Fog Using Mesoscale Atmospheric Models. *Boundary-Layer Meteorology*, 154(2):265–289. https://doi.org/10.1007/s10546-014-9973-8.

Stevens, B. (2002). Entrainment in stratocumulus-topped mixed layers. *Quarterly Journal of the Royal Meteorological Society*, 128(586):2663–2690. https://doi.org/10.1256/qj.01.202.

Tardif, R. and Rasmussen, R. M. (2007). Event-based climatology and typology of fog in the New York City region. *Journal of applied meteorology and climatology*, 46(8):1141–1168. https://doi.org/10.1175/JAM2516.1.

Tav, J., Masson, O., Burnet, F., Paulat, P., Bourrianne, T., Conil, S., and Pourcelot, L. (2018). Determination of fog-droplet deposition velocity from a simple weighing method. *Aerosol and Air Quality Research*, 18:103–113. https://doi.org/10.4209/aaqr.2016.11.0519.

Trautner, F. and Eiden, R. (1988). A measuring device to quantify deposition of fogwater and ionic input by fog on small spruce trees. *Trees*, 2(2):92–95.

Van der Dussen, J., De Roode, S., and Siebesma, A. (2014). Factors controlling rapid stratocumulus cloud thinning. *Journal of the Atmospheric Sciences*, 71(2):655–664. https://doi.org/10.1175/JAS-D-13-0114.1.

van Oldenborgh, G. J., Yiou, P., and Vautard, R. (2010). On the roles of circulation and aerosols in the decline of mist and dense fog in Europe over the last 30 years. *Atmospheric Chemistry and Physics*, 10(10):4597. https://doi.org/10.5194/acp-10-4597-2010.

Vautard, R., Yiou, P., and Van Oldenborgh, G. J. (2009). Decline of fog, mist and haze in Europe over the past 30 years. *Nature Geoscience*, 2(2):115. https://doi.org/10.1038/NGEO414.

Wood, R. (2012). Stratocumulus clouds. *Monthly Weather Review*, 140(8):2373–2423. https://doi.org/10.1175/MWR-D-11-00121.1.

Wærsted, E. G., Haeffelin, M., Dupont, J.-C., Delanoë, J., and Dubuisson, P. (2017). Radiation in fog: quantification of the impact on fog liquid water based on ground-based remote sensing. *Atmos. Chem. Phys.*, 17(17):10811–10835. https://doi.org/10.5194/acp-17-10811-2017.

Wærsted, E. G., Haeffelin, M., Steeneveld, G.-J., and Dupont, J.-C. (2018). Understanding the dissipation of continental fog by analysing the LWP budget using LES and in situ observations. *In review in the Quarterly Journal of the Royal Meteorological Society*.

Yang, Y., Liu, X., Qu, Y., Wang, J., An, J., Zhang, Y., and Zhang, F. (2015). Formation mechanism of continuous extreme haze episodes in the megacity Beijing, China, in January 2013. *Atmospheric Research*, 155:192–203. https://doi.org/10.1016/j.atmosres.2014.11.023.

Zhou, B. and Ferrier, B. S. (2008). Asymptotic analysis of equilibrium in radiation fog. *Journal of Applied Meteorology and Climatology*, 47(6):1704–1722. https://doi.org/10.1175/2007JAMC1685.1.

Résumé

Le brouillard cause des dangers pour les activités humaines par la réduction de la visibilité, en particulier en augmentant le risque d'accidents de transport. Le cycle de vie du brouillard est piloté par des processus radiatifs, dynamiques et microphysiques qui interagissent de manière complexe qui n'est pas encore entièrement compris. L'amélioration de la compréhension de ces processus et la capacité de prévision de la formation et la dissipation des brouillards est donc un objectif pour la science atmosphérique. Cette thèse analyse le cycle de vie des brouillards continentaux en région parisienne, en utilisant plusieurs instruments de télédétection installés à l'observatoire atmosphérique SIRTA. Nous investigons la dissipation du brouillard après le lever du soleil et les processus concernés. Pendant 4 ans, plus de 100 évènements de brouillard sont documentés par observations de l'altitude de la base du brouillard/nuage (CBH) (par télémètre), l'altitude du sommet du brouillard (CTH) et des nuages qui apparaissent au-dessus (par radar nuage), et le contenu intégré d'eau liquide (LWP) (par radiomètre micro-onde (MWR)). Quand il est combiné avec le radar nuage, le MWR peut également restituer la colonne intégrée de vapeur d'eau (IWV) au-dessus du brouillard et la stratification thermique de la couche au-dessus du brouillard.

La plupart des événements de brouillard se dissipe par lever du CBH sans que le nuage s'évapore complètement, parfois même sans une réduction du LWP. Ceci est expliqué par une augmentation du CTH, ce qui peut favoriser la dissipation. En fait, en appliquant le modèle de Cermak and Bendix (2011), nous avons trouvé que le LWP et le CTH sont les paramètres principaux expliquant le CBH et donc la dissipation du brouillard. Pour chaque CTH, il y a une valeur critique que le LWP doit dépasser pour que le brouillard reste au sol. Ce LWP critique augmente plus que linéairement avec le CTH, et nous l'avons estimé à 6 g m^{-2} h^{-1} pour un CTH de 100 m, 29 g m^{-2} h^{-1} à 200 m, et 131 g m^{-2} h^{-1} à 400 m, quand la température du brouillard est 5 °C. Afin de mieux comprendre la dissipation, nous nous concentrons sur les impacts des processus physiques sur LWP et CTH. En appliquant un code de transfert radiatif et un modèle de simulation de grands tourbillons (LES), les impacts sur les deux paramètres par le rayonnement long-wave (LW), le rayonnement short-wave (SW), les flux turbulents de chaleur de la surface, l'entrainement au sommet, la subsidence grande-échelle et le dépôt de gouttelettes sont quantifiés. Nous étudions également les paramètres qui causent de la variabilité dans ces impacts. Pour pouvoir calculer les impacts sur le LWP du brouillard par des flux de chaleur et d'humidité, un cadre conceptuel basé sur l'hypothèse que la couche de brouillard est bien mélangée est appliqué.

Les processus radiatifs sont étudiés avec le code de transfert radiatif ARTDECO. Le refroidissement radiatif au sommet du brouillard constitue une source de LWP de 40–70 g m^{-2} h^{-1} quand le brouillard est opaque par rapport au rayonnement LW (LWP $>\approx$ 30 g m^{-2}) et quand il n'y a pas des nuages au-dessus. Ce refroidissement est le processus principal de production de LWP et il peut renouveler le LWP du brouillard en 0.5–2 h. Sa variabilité est principalement due à la température du sommet du

brouillard et l'humidité au-dessus. Les nuages qui arrivent au-dessus du brouillard réduisent fortement la production de LWP, notamment des nuages bas : un nuage avec une épaisseur optique de 4 situé à 10 (2) km peut causer une réduction de 30 (100) %. Quand le brouillard est semi-transparent au rayonnement LW (LWP $<\approx 30$ g m^{-2}), ce qui est le cas pour presque la moitié de la base de données, la production augmente fortement avec le LWP. La perte de LWP par absorption de rayonnement solaire par le brouillard est 5–15 g m^{-2} h^{-1} près de midi en hiver, augmentant avec l'épaisseur du brouillard, mais elle peut augmenter de 100 % en présence d'une forte quantité d'aérosols absorbants (le cas testé: une population d'aérosols urbains avec une épaisseur optique sèche de 0.15 et un albédo de diffusion simple de 0.82).

Nos résultats indiquent que le réchauffement par le brouillard à travers l'absorption de rayonnement SW à la surface est le processus dominant de perte de LWP après le lever du soleil. Elle peut atteindre 20–30 g m^{-2} h^{-1} (selon nos simulations LES), mais sa grandeur est sensible au rapport de Bowen. Cependant, les observations des flux turbulent de la surface dans le brouillard ne sont pas suffisamment précises pour déterminer le rapport de Bowen. Son importance pour le bilan LWP du brouillard montre qu'une amélioration de la compréhension et l'observation du rapport de Bowen dans le brouillard devrait faire l'objet de futures recherches. À travers son impact sur le rapport de Bowen, l'eau liquide présente à la surface peut être un facteur important pour la persistance du brouillard le matin ; dans notre étude LES, le brouillard s'est dissipé 85 min plus tard dans une simulation dans laquelle 50 % la surface était couverte par l'eau liquide, par rapport à une simulation sans eau liquide à la surface.

Des observations par radiosondes montrent la variabilité de la stratification thermique et l'humidité dans la couche au-dessus du CTH. Avec le LES, nous avons trouvé une sensibilité importante du développement vertical du CTH à cette variabilité observée dans la stratification. En augmentant l'entrainement, une stratification faible peut mener à une dissipation plus tôt, par (1) une plus forte réduction de LWP par le mélange avec l'air au-dessus, particulièrement si l'air est sec, et (2) une augmentation du CTH. La dissipation est 90 min plus tôt dans une simulation avec une faible stratification par rapport à une simulation avec une forte stratification. La variabilité de la stratification observée par les radiosondes est reproduite suffisamment bien par le MWR pour permettre une observation continue de ce paramètre. La variabilité de l'humidité au-dessus du brouillard a aussi un impact important sur la dissipation : dans une simulation dans laquelle l'air au-dessus est sec, le brouillard se dissipe 70 min plus tôt que dans une simulation avec de l'air près de la saturation au-dessus. L'air plus sec a causé une perte de LWP plus rapide, permettant un lever du brouillard en stratus plus tôt. Cependant, l'effet de l'humidité au-dessus est sensible aux détails du profil d'humidité, parce que le refroidissement radiatif est également renforcé par une atmosphère plus sèche.

Afin d'investiguer les résultats présentés ci-dessus pour un plus grand nombre de cas de brouillard, un modèle conceptuel est développé. Ce modèle utilise 12 paramètres calculés à partir des observations par radar nuage, radiomètre micro-onde, télémètre, radiomètres à bandes larges, anémomètre sonique, fluxmètre du sol et diffusomètres, et 2 paramètres obtenu des réanalyses ERA5, pour calculer les impacts sur le LWP et le CTH de chacun des six processus locaux (rayonnement LW, rayonnement SW, flux de chaleur de la surface, entrainement, subsidence, dépôt). Le modèle est appliqué à 45 cas où le brouillard est présent au lever du soleil.

Une variabilité importante entre les cas dans le rayonnement, le taux d'entrainement et les flux de chaleur de la surface est trouvée. Cette variabilité peut expliquer une partie des différences observées dans les évolutions des brouillards. En particulier, la saisonnalité observée dans l'heure de dissipation,

avec les brouillards proches du solstice d'hiver durant plus longtemps, parfois même toute la journée, peut être liée à la plus faible insolation à proximité du solstice d'hiver, ce qui limite la perte de LWP par les processus liés au rayonnement solaire. Une corrélation est trouvée entre la vitesse d'entrainement calculée (par le schéma de Gesso et al. (2014)) et le développement vertical observé du CTH, même si il est clair que l'advection impacte fortement les changements du CTH. Le schéma d'entrainement reproduit également l'effet de la stratification sur le CTH trouvé avec le modèle LES, mais la vitesse d'entrainement est généralement sous-estimée par rapport au LES, ce qui montre qu'il faut ajuster le schéma pour une meilleure application aux brouillards. La vitesse verticale grande-échelle dans le brouillard prend des valeurs positives presqu'autant que des valeurs négatives, mais les cas les plus persistants sont systématiquement caractérisés par la subsidence. Nous montrons que la subsidence en elle-même ne favorise pas la persistance, parce que son effet de réduction de LWP (par réchauffement adiabatique et divergence) est plus fort que son effet de réduction du LWP critique (par affaissement du CTH). Donc, la corrélation entre la persistance et la subsidence est probablement due aux autres facteurs synoptiques qui ont lieu en même temps que la subsidence.

Tandis que les termes de rayonnement sont plutôt robustes, plusieurs des autres termes dans le modèle conceptuel comportent des incertitudes importantes, ce qui pourrait être amélioré dans le futur. Nous trouvons également des indications que l'advection et les hétérogénéités horizontales jouent un rôle important dans les évolutions de LWP et CTH, car ils évoluent souvent d'une manière qui ne peut pas s'expliquer par les processus locaux. Par conséquent, nous suggérons d'inclure l'effet de l'advection, modélisé ou observé, dans le modèle conceptuel.

Finalement, le profil vertical de la réflectivité radar dans le brouillard, qui peut être étudié en détail grâce à la haute résolution et la petite zone aveugle de notre radar nuage, démontre une grande variabilité. La réflectivité dans les couches de brouillard prend normalement des valeurs entre -40 et -15 dBZ. La valeur maximale du profil vertical se trouve parfois près du CTH, souvent pendant ou juste avant la dissipation par lever de la base. Cette forme du profil indique un déficit de grandes gouttelettes dans les basses couches du brouillard. Dans d'autres situations, la réflectivité est plus forte et atteint sa valeur maximale près du centre du brouillard, ce qui indique une sédimentation plus importante de grandes gouttelettes. Avec les données de trois vols sous ballon captif d'un compteur de particules dans le brouillard (altitude 0–300 m), il est également montré qu'une relation approximative entre le contenu en eau liquide et la réflectivité radar existe dans le brouillard, comme a été montré pour d'autres nuages bas dans le passé. Les profils de réflectivité radar peut donc fournir des informations des propriétés microphysiques du brouillard.

Par conséquent, les radars nuage Doppler, les radiomètre micro-onde et les télémètres sont trois instruments essentiels pour fournir des observations détaillées de variables clés – à la base, à l'intérieur, au sommet et au-dessus du brouillard – qui sont critiques pour mieux comprendre le cycle de vie des brouillards continentaux.

université PARIS-SACLAY
ÉCOLE DOCTORALE
Sciences mécaniques et énergétiques, matériaux et géosciences (SMEMAG)

Titre : Description des processus physiques pilotant le cycle de vie de brouillards radiatifs et des transitions brouillard–stratus basée de modèles conceptuels

Mots clés : brouillard, dissipation de brouillard, télédétection, radar nuage, modèle conceptuel, modèle LES

Résumé : Le brouillard cause des dangers pour les activités humaines par la réduction de visibilité, ce qui fait l'amélioration des prévisions du brouillard un objectif scientifique. Pendant 4 ans, plus de 100 événements de brouillard sont documentés à l'observatoire atmosphérique SIRTA par observations de sa base (par télémètre), son sommet (CTH) et les nuages au-dessus (par radar nuage), et le contenu intégré d'eau liquide (LWP) (par radiomètre micro-onde (MWR)). La dissipation du brouillard peut être expliquée en premier ordre par le CTH et le LWP. Pour mieux comprendre l'évolution de ces deux paramètres, les processus physiques qui les impactent sont étudiés.
En utilisant le code de transfert radiatif ARTDECO, la production d'LWP par refroidissement radiatif au sommet du brouillard est quantifiée à 40–70 g m^{-2} h^{-1} quand le brouillard est opaque (LWP $>\approx$ 30 g m^{-2}). Les nuages au-dessus du brouillard réduisent fortement la production, en particulier les nuages bas. Le réchauffement par absorption de rayonnement solaire à la surface est le premier processus de perte d'LWP après le lever du soleil, mais sa magnitude est sensible au rapport de Bowen.
Des simulations LES montrent une sensibilité importante à la stratification et l'humidité au-dessus du brouillard : en augmentant l'entrainement, une stratification faible au sommet peut accélérer la dissipation par (1) plus de perte d'LWP par l'entrainement de l'air non-saturé, et (2) par un développement vertical du CTH menant au lever de la base.
Un modèle conceptuel est développé pour calculer les impacts au LWP et CTH de chaque processus (rayonnement, flux de la surface, entrainement, subsidence, dépôt) directement à partir des observations, afin d'étendre notre analyse à plus de cas. On observe également un changement de la forme du profil de reflectivité radar à la dissipation dans plusieurs cas, ce qui peut être lié à l'absence de grandes gouttelettes dans les basses couches. Donc, par leur observation du développement du sommet, le LWP, la stratification, et le profil de réflectivité, le radar nuage et le MWR donnent des informations qui peuvent potentiellement anticiper la dissipation du brouillard.

Title : Description of physical processes driving the life cycle of radiation fog and fog–stratus transitions based on conceptual models

Keywords : fog, fog dissipation, remote sensing, cloud radar, conceptual model, LES model

Abstract : Fog causes hazards to human activities due to the reduction of visibility, and improving the forecasts of fog formation and dissipation is therefore an objective for research. Over a 4-year period, more than 100 fog events are documented at the SIRTA atmospheric observatory by observing fog base (by ceilometer), fog top (CTH) and higher clouds (by cloud radar), and the liquid water path (LWP) (by microwave radiometer (MWR)). We find that the dissipation of fog into stratus can be explained to the first order by the CTH and LWP, and we therefore focus on quantifying the processes driving the evolutions of these two parameters.
Using the radiative transfer code ARTDECO, we find that the radiative cooling at fog top can produce 40–70 g m^{-2} h^{-1} of LWP when the fog is opaque (LWP $>\approx$ 30 g m^{-2}) (production is lower for thin fog). Clouds above the fog will strongly reduce this production, especially low clouds. Heating due to solar radiation absorbed at the surface is found to be the dominating process of LWP loss after sunrise, but its magnitude is sensitive to the Bowen ratio.
Using the LES model DALES, we find a strong sensitivity of the fog dissipation to the observed variability in the stratification and humidity above fog top. By enhancing entrainment, a weak stratification can lead to earlier fog dissipation by (1) more depletion of LWP by mixing with unsaturated air, especially if the air is dry, and (2) vertical development of the fog top leading to lifting of the fog base.
A conceptual model which calculates the impacts on LWP and CTH of the six local processes (long-wave and short-wave radiation, surface heat fluxes, entrainment, subsidence and deposition) directly from observations is developed, in order to extend the analysis to more cases. We also find that the shape of the profile of radar reflectivity often changes during dissipation, which might be related to the evaporation of droplets in the lower levels of the fog. Hence, by observing the cloud top development, the stratification, the LWP and the profile of reflectivity, the cloud radar and MWR provide information that has potential for anticipating fog dissipation.

Université Paris-Saclay
Espace Technologique / Immeuble Discovery
Route de l'Orme aux Merisiers RD 128 / 91190 Saint-Aubin, France